Dissertation

submitted to the

Combined Faculties of the Natural Sciences and Mathematics

of the Ruperto-Carola-University of Heidelberg, Germany

for the degree of

Doctor of Natural Sciences

Put forward by

Maddalena Giulini

born in Milan, Italy

Oral examination: 18 January 2017

Search for the supersymmetric top quark partner with the HEPTopTagger algorithm in proton-proton collisions at $\sqrt{s} = 8$ TeV with the ATLAS detector

Referees: Prof. Dr. André Schöning
Prof. Dr. Stephanie Hansmann-Menzemer

Abstract

In this thesis, the search for direct pair production of the supersymmetric top quark partner with the HEPTopTagger algorithm is presented. An integrated luminosity of 20.3 fb^{-1} of proton-proton collision data at $\sqrt{s} = 8$ TeV collected by the ATLAS detector at the Large Hadron Collider is used. The top squark, $\tilde{t}_1$, is assumed to decay into a top quark and a neutralino, $\tilde{\chi}_1^0$, with $BR(\tilde{t}_1 \to t\tilde{\chi}_1^0) = 100\%$. The analysis targets the fully hadronic final state: the HEPTopTagger is employed to reconstruct the hadronically decaying top quarks with $p_{\mathrm{T}} > 200$ GeV; the M_{T2} variable together with the missing transverse momentum is used to measure the momentum imbalance of the undetected neutralinos.

In order to reliably apply the HEPTopTagger to search for the top squark, its performance is studied in a sample enriched in top quark pairs in the lepton+jets channel. The efficiency of identifying moderate to high p_{T} top quarks is measured to vary from 10% to 45%. A novel method is developed to estimate in-situ the uncertainty on the energy scale of the subjets, representing the top quark decay products. The simulation has been found to be a reliable tool to predict the Standard Model background and the HEPTopTagger can be safely employed in the search for top partners.

In the search for direct top squark pair production, no significant excess over the Standard Model background expectation is found, and exclusion limits are set as a function of the top squark and neutralino masses. Top squark masses between $250 - 720$ GeV are excluded for neutralino masses of a few tens of GeV.

Kurzfassung

In dieser Arbeit wird die Suche nach direkter Paarproduktion des supersymmetrischen Partners des Top Quarks mit dem HEPTopTagger-Algorithmus unter Verwendung von Proton-Proton-Kollisionsdaten entsprechend einer integrierten Luminosität von 20.3 fb^{-1}, die bei $\sqrt{s} = 8$ TeV vom ATLAS-Detektor am Large Hadron Collider aufgezeichnet wurden, vorgestellt. Es wird angenommen, dass das Top Squark, $\tilde{t}_1$, mit $BR(\tilde{t}_1 \to t\tilde{\chi}_1^0) = 100\%$ in ein Top Quark und ein Neutralino, $\tilde{\chi}_1^0$, zerfällt. Die Analyse konzentriert sich auf den vollständig hadronischen Endzustand. Der HEPTopTagger wird verwendet, um hadronisch zerfallendende Top Quarks mit $p_{\mathrm{T}} > 200$ GeV zu rekonstruieren und die M_{T2} Variable wird zusammen mit dem fehlenden transversalen Impuls verwendet, um das Impulsungleichgewicht aufgrund der undecktierten Neutralinos zu messen.

Um den HEPTopTagger in der Suche nach dem Top Squark zuverlässig anwenden zu können, wird seine Leistungsfähigkeit in einem Datensatz untersucht, der mit Top-Quarkpaaren im Lepton+Jets-Kanal angereichert ist. Die gemessene Effizienz der Identifizierung von Top Quarks mit niedrigem und hohem p_{T} variiert zwischen 10% und 45%. Eine neue Technik wird entwickelt, um in-situ die Unsicherheit auf die Energieskala der Subjets, die die Top-Quark-Zerfallsprodukte darstellen, abzuschätzen. Die Simulation hat sich als zuverlässiges Mittel zur Vorhersage des Standardmodell-untergrundes erwiesen und der HEPTopTagger kann bei der Suche nach Top Squarks sicher eingesetzt werden.

In der Suche nach Top-Squark-Paaren wird kein signifikanter Überschuss im Vergleich zur Standardmodell-untergrunderwartung gefunden und Ausschlussgrenzen werden als Funktion der Top-Squark- und Neutralino-Massen gesetzt. Top-Squark-Massen zwischen $250 - 720$ GeV sind für Neutralino-Massen von wenigen Dutzend GeV ausgeschlossen.

Contents

Introduction

The Standard Model (SM) has been shown to be the most comprehensive and predictive theory of elementary particle physics so far. The discovery of the so long-sought-after Higgs boson by the ATLAS and CMS experiments at the Large Hadron Collider [1, 2] represents its last success. Nevertheless, the SM leaves compelling questions unanswered, including the hierarchy problem, the matter-antimatter asymmetry and the nature of dark matter, and leaves room for physics beyond the SM (BSM).

The search for new physics phenomena is one of the primary goals of the Large Hadron Collider. It has been designed to collide protons at unprecedented high energies (up to a centre of mass energy of $\sqrt{s} = 14$ TeV) and luminosities. Thanks to the sizeable amount of data collected by the ATLAS detector, a large variety of BSM theories, predicting TeV scale particles, are currently under investigations. Most of these models aim to provide a solution to the hierarchy problem, which regards the quadratically divergent corrections to the Higgs boson mass, and the tremendously large fine tuning needed to account for a Higgs boson mass of 125 GeV, if no new physics phenomena appear before the Planck scale at 10^{19} GeV.

The top quark plays a crucial role in these models. Due to its large Yukawa coupling, the top loop dominates the divergent corrections to the Higgs boson mass. Many models predict the existence of top quark partners, which provide a cancellation to the large top loop contribution. The minimal supersymmetric extension of the SM, one of the most promising candidates of new physics theories, predicts the existence of a boson partner for every SM fermion and vice versa. In particular, two scalar partners for the top quark with large mass splitting are foreseen, and the lightest of the two top partners, called stop $\tilde{t}_1$, is expected to be the lightest of the quark partners by many models.

If kinematically allowed, the top quark is expected to be among the decay products of new particles. The decay signature of hadronically decaying top quarks, $t \to bW \to bq'\bar{q}$, consists of collimated bundle of particles combined into jets. As new particles are searched for at the TeV scale, the top quarks in the final state are expected to be produced with large transverse momentum, p_{T}. The decay products of top quarks with large p_{T} are collimated and their reconstruction by means of standard techniques, consisting in assigning a small radius jet to each of the three quarks, $bq'\bar{q}$, becomes unfeasible. Specialised techniques for boosted top quark reconstruction are essential to considerably enhance the significance of searches for new heavy particles. New methods have been developed in the past few years to identify

and reconstruct boosted top quarks. The top decay products may be contained in a single large and massive jet, called large-R jet. By looking into the internal structures of large-R jets it is possible to discriminate those originating from the top quark decay against those originating from a gluon or a light quark. Among these methods, the HEPTopTagger algorithm [3, 4] is capable to tag and to reconstruct the kinematics of top quarks over the widest range of the top transverse momentum down to 200 GeV, and it provides significant background rejection power.

Before the HEPTopTagger algorithm can be used in physics analyses, it is fundamental to assess how well the simulation describes the measured outcome of the algorithm and to evaluate the systematic uncertainties connected to the HEPTopTagger usage. In this thesis, a data sample enriched in hadronically decaying top quarks is used for this purpose. The data has been collected in 2012 by ATLAS at a centre of mass energy of $\sqrt{s} = 8$ TeV corresponding to an integrated luminosity of 20.3 fb^{-1}. The top quark sample is obtained by selecting those events with a top-antitop pair in the ℓ+jets channel, with one top quark decaying semi-leptonically $t \to Wb \to \ell\nu b$ and the other hadronically, requiring exactly one lepton (electron or muon), missing transverse momentum, b-tagged small-R jets, and a large-R jet. A novel method, first suggested in [5], is developed in order to evaluate in-situ the energy scale uncertainty of subjets reconstructed within the HEPTopTagger, exploiting the very clean top mass peak. The simulated outcome of the HEPTopTagger is compared in data and simulation, and the efficiency of tagging large-R jets originating from hadronically decaying top quarks is measured. The outcome of the performance measurement of the HEPTopTagger together with other top tagging techniques has been published in [6].

Thanks to its wide range of sensitivity in transverse momentum and its significant discrimination power, the HEPTopTagger is the best suited algorithm to investigate new models with final state top quarks produced with moderate to very large transverse momentum ($p_{\mathrm{T}} > 200$ GeV). The HEPTopTagger is employed in this thesis to search for the top squark using the full $\sqrt{s} = 8$ TeV proton-proton collision dataset. In R-parity conserving models, the stop is produced in pairs at the LHC and its decay mode ($\tilde{t}_1 \to t\tilde{\chi}_1^0$), into a top quark and a neutralino, $\tilde{\chi}_1^0$, the lightest supersymmetric particle, is kinematically allowed if the stop-neutralino mass difference is larger than the top quark mass. If this mass difference is sizeable, the final state top quarks are produced with moderately large transverse momentum. The channel with both top quarks decaying hadronically has the advantage that the kinematics of the two tops can be fully reconstructed and the missing transverse momentum only depends on the neutralino pair kinematics. The HEPTopTagger application can enhance the significance of analogous searches [7]. The analysis strategy of this thesis, similar to the one proposed in [4, 8], has been defined to target signal models with small $\tilde{\chi}_1^0$ masses and heavy stops, with mass of several hundreds of GeV. The final goal is to quantify the sensitivity improvements of the search by employing the HEPTopTagger algorithm.

The Standard Model and theories beyond the SM, with special emphasis on supersymmetry, are summarised in chapter 1. The ATLAS experiment is described in chapter 2. The same chapter details the simulated samples and the uncertainties, concerning the ℓ+jets analysis of the HEPTopTagger performance and the search for the direct stop pair production. The HEPTopTagger algorithm, explained in chapter 3, is validated in the ℓ+jets channel in chapter 4. The search for the direct stop pair production in the fully hadronic final state of a top-neutralino pair is detailed in chapter 5.

Chapter 1

Standard Model and beyond

The laws of nature are governed by four forces: the gravitational, the strong, the electromagnetic and the weak force.

The Standard Model (SM) theory represents a fundamental step in the attempt to unify these forces, started at the end of the 1960s [9–12]. Its success is based on the unification of the electromagnetic, the weak and the strong force under the same comprehensive quantum field theory description through local gauge invariance. On the experimental side, the SM has been accurately verified in quantitative tests, and has provided crucial predictions of the existence and properties of the three massive vector bosons. The latest triumph of the Standard Model is the discovery of the Higgs boson in 2012 by ATLAS and CMS with mass at about 125 GeV [1, 2], decades after it was predicted [13–15].

Although well established, the SM seems not to be the ultimate theory. There are observed phenomena, which are not explained or considered in the SM, like neutrino masses, matter-antimatter asymmetry and dark matter. Other outstanding theoretical issues remain unsolved: gravity is not included in the quantum field theory description; the SM Higgs mass receives large quantum corrections, leading to the *gauge hierarchy* problem; the three gauge coupling constants seem to get closer at high energies, but they do not meet, leading to the open issue of describing the three gauge interactions with only one force via the so called *Grand Unified Theories*.

Many theories beyond the Standard Model, like supersymmetric ones, may provide an answer to one or more of these open questions. In these theories the top quark plays a special role, as it is the heaviest fundamental particle, discovered so far.

The formulation of the Standard Model is described in section 1.1; the following references are used for the SM overview [16–20]. The theoretical concepts concerning physics at hadron colliders are reported in section 1.2. The phenomenology of the top quark is described in section 1.3, following the review [21]. An outlook on theories beyond the Standard Model, with particular emphasis on Supersymmetry is given in section 1.4.1.

1.1 Standard Model of particle physics

The elementary particles so far discovered are divided in fermions and bosons. Quarks and leptons, as well as their anti-particles, have spin 1/2 and belong to the first group. They are the constituents of ordinary matter. Quarks, contrary to leptons, participate in strong interactions. Both classes of fermions appear in three different *generations*:

$$\text{leptons: } \begin{pmatrix}\nu_e\\ e^-\end{pmatrix} \quad \begin{pmatrix}\nu_\mu\\ \mu^-\end{pmatrix} \quad \begin{pmatrix}\nu_\tau\\ \tau^-\end{pmatrix}$$
$$\text{quarks: } \begin{pmatrix}u\\ d\end{pmatrix} \quad \begin{pmatrix}c\\ s\end{pmatrix} \quad \begin{pmatrix}t\\ b\end{pmatrix}$$

where "ν_ℓ" stays for neutrino of the $\ell = e, \mu, \tau$ species, e^- for electron, μ^- for muon, τ^- for tau, the quarks appear in six different flavours: "*u*", *up*-quark; "*d*", *down*-quark; "*c*", *charm*-quark, "*s*" for *strange*-quark, "*t*" for *top*-quark, "*b*" for *bottom*-quark. The anti-particles are omitted for simplicity. The up-type quarks, *u, c, s*, have electric charge +2/3, the down-type quarks (*d, s, b*) have electric charge -1/3. The neutrinos are electrically neutral. The down-type leptons are charged, with negative unitary charge and they are commonly referred to as charged leptons. The anti-particle of these fermions have the same mass, same lifetime and opposite electric charge of the corresponding particle. Being subject to the strong force, quarks form bound states called hadrons. The hadrons are subdivided in *baryons*, formed by three quarks or three anti-quarks, and *mesons*, bound states of quark-antiquark pairs.

The bosons that acts as mediators of the interactions are the massive W^+, W^-, Z^0, and the massless photon, γ, and gluon, g.

The Standard Model is the theory that better describes the interactions among all the elementary particles, except for gravity, within the context of quantum field theory. The principle that drives the description of the fundamental interactions is the *local gauge invariance*, i.e. the assumption that the Lagrangian does not change under a set of transformations which are space-time dependent. To satisfy the principle of local gauge invariance of the free Dirac field Lagrangian, the fermions need to couple with the boson fields, interaction mediators.

Among the theories of elementary particle dynamics the simplest is *Quantum Electrodynamics*, which is invariant under local phase transformations of the group U(1) (section 1.1.1).

The extension of the gauge principle to non-Abelian groups, i.e. noncommutative groups, for example to SU(2)⊗U(1), allows the formulation of the electroweak theory (section 1.1.2). This theory on its own does not foresee mass terms for the weak gauge fields and for the fermions, which preserve the symmetries. The BEH-mechanism, through the spontaneous symmetry breaking of $\mathrm{SU(2)}\otimes\mathrm{U(1)_Y}$ to $U(1)_{\mathrm{em}}$[1], gener-

[1]The subscript Y of $\mathrm{U(1)_Y}$ corresponds to the weak hypercharge, the subscript em to the

ates masses for the $W^{\pm}$, Z^0 bosons, makes the inclusion of fermionic mass terms possible and predicts the existence of a massive scalar particle, called *Higgs boson* (section 1.1.3).

The strong force has been formulated as a non-Abelian gauge theory, with local invariance under $SU(3)_C$ transformations as stated by the theory of quantum chromodynamics (section 1.1.4)

The $SU(3)_C \otimes SU(2) \otimes U(1)_Y$ gauge theory and the BEH-mechanism define the Standard Model of particle physics.

1.1.1 Quantum electrodynamics

All the particles that carry the electromagnetic charge are subject to the electromagnetic interaction. The mediator of this interaction is the photon, which is massless.

The Lagrangian of a free Dirac field, ψ, of mass m is:

$$\mathscr{L}_{\text{Dirac}} = \bar{\psi}(i\partial\!\!\!/ - m)\psi$$

where the first term represents the kinetic energy and the second is the mass term[2].

The Lagrangian of a free electromagnetic field, A^μ, describing the photon as a massless vector field, consists of the kinetic energy term:

$$\mathscr{L}_{\text{EM}} = -\frac{1}{4}(F_{\mu\nu})^2 \tag{1.1}$$

with the electromagnetic field tensor defined as $F_{\mu\nu} \equiv \partial_\mu A_\nu - \partial_\nu A_\mu$.

To describe the interaction between the electromagnetic field and the Dirac field, the two Lagrangians, $\mathscr{L}_{\text{Dirac}}$ and $\mathscr{L}_{\text{EM}}$, can be combined with the addition of the interaction term to give the Lagrangian of quantum electrodynamics (QED):

$$\mathscr{L}_{\text{QED}} = \bar{\psi}(iD\!\!\!/ - m)\psi - \frac{1}{4}(F_{\mu\nu})^2$$

with $D_\mu \equiv \partial_\mu + ieA_\mu$, the *gauge covariant derivative*, which includes the interaction term. $\mathscr{L}_{\text{QED}}$ is symmetric under local transformation of the abelian U(1) group. This means that the Lagrangian is invariant under the phase rotation which transforms the fields:

$$\psi(x) \to e^{-ie\alpha(x)}\psi(x) \tag{1.2}$$

$$A_\mu(x) \to A_\mu(x) + \partial_\mu \alpha(x) \tag{1.3}$$

where e is the Dirac field charge, and $\alpha(x)$ is a real arbitrary differentiable function of x.

electromagnetic charge, and C to the colour charge

[2]In this chapter the following notation is employed. $\partial\!\!\!/ \equiv \gamma^\mu \partial_\mu$ where γ^μ are the gamma matrices with $\mu = 0, 1, 2, 3$ and ∂_μ is the partial derivative with respect to x^μ, $\partial_\mu \equiv \frac{\partial}{\partial x^\mu}$; a summation over repeated indexes (e.g. $^\mu$) is implied. $\bar{\psi}$ is the product of $\psi^\dagger$, Hermitian conjugate of ψ, and γ_0: $\bar{\psi} \equiv \psi^\dagger \gamma^0$.

From another point of view, the electromagnetic field, A^μ, appears, once the U(1) gauge invariance of the free Dirac field Lagrangian is imposed.

1.1.2 Electroweak model

All quarks and leptons are subject to the weak interactions. The mediators are the three massive vector bosons: the electrically charged W^+ and W^- bosons, and the electrically neutral Z^0 boson.

Depending on the electromagnetic charge of the mediator, it is possible to distinguish between *neutral current* processes (where the Z^0 boson is involved) and *charged current* ones (with the exchange of the W^+ or W^- boson). Processes in which both hadrons and leptons are present, are called *semileptonic processes*; in case either only leptons or only hadrons are involved, the processes are referred to as *leptonic* or *non-leptonic processes*, respectively.

The formulation of the electroweak theory requires the extension of the QED local gauge invariance principle to unitary groups of larger degree. The generalisation of this principle to any continuous symmetry group was performed by Yang and Mills. In the electroweak theory case, the starting point is the invariance of the Lagrangian under SU(2), *weak isospin* group. A doublet of Dirac fields defined as:

$$\Psi = \begin{pmatrix} \psi_1 \\ \psi_2 \end{pmatrix}$$

transforms in the spinor representation of SU(2) according to:

$$\Psi \rightarrow \exp\left(ig\alpha^i(x)\frac{\tau^i}{2}\right)\Psi \tag{1.4}$$

where g is the coupling constant, $\alpha^i(x)$, with $i = 1, 2, 3$, are three arbitrary real differentiable functions of x, τ^i represents the *i-th* Pauli matrix, satisfying the commutation relation $[\tau^i, \tau^j] = 2i\epsilon^{ijk}\tau_k$, with $j, k = 1, 2, 3$. The SU(2) transformation acting on the field doublet Ψ is a local transformation which mixes the doublet components.

Three vector fields, W^i_μ are needed to preserve the SU(2) symmetry, one for each generator of the SU(2) group. The covariant derivative replacing the simple partial derivative is:

$$D_\mu = \partial_\mu + igW^i_\mu\frac{\tau^i}{2} \ .$$

The Lagrangian invariant under SU(2),

$$\mathscr{L} = \bar{\Psi}(i\not{D} - m)\Psi,$$

is adjusted to take into account experimental observation of particle interactions. The weak interactions violate parity and reveal a "V-A" (vector minus axial) structure. This means that the interactions involve only the "left-handed" component

of the Dirac field, ψ. The "left-handed" and "right-handed" fields, ψ_{L} and ψ_{R} respectively, are defined to be the chirality states of ψ, and are the eigenstates of the projection operators P_{L} and P_{R}:

$$\psi_{\mathrm{L}} = P_{\mathrm{L}}\psi \qquad P_{\mathrm{L}} \equiv \frac{(1-\gamma_5)}{2} \tag{1.5}$$

$$\psi_{\mathrm{R}} = P_{\mathrm{R}}\psi \qquad P_{\mathrm{R}} \equiv \frac{(1+\gamma_5)}{2} \tag{1.6}$$

where $\gamma^5 = i\gamma^0\gamma^1\gamma^2\gamma^3$.

The charged current processes couple neutrinos to charged leptons, or up-type quarks to down-type quarks. Thus, the field doublet, called *weak isospinor*, is identified with

$$\Psi_{\mathrm{L}} = \begin{pmatrix} \nu_{\mathrm{L}}^{\ell} \\ \ell_{\mathrm{L}} \end{pmatrix} \qquad \text{or} \qquad \Psi_{\mathrm{L}} = \begin{pmatrix} u_{\mathrm{L}} \\ d'_{\mathrm{L}} \end{pmatrix}^{3}.$$

The field Ψ_{L} transforms as in equation 1.4 under local SU(2) transformations, while the right-handed Dirac fields being singlet do not change under SU(2). The interaction term of the doublet Ψ_{L} to the three vector bosons, W_μ^i, appears from the requirement of SU(2) gauge invariance:

$$\mathscr{L}_{\mathrm{W}} = -gW_\mu^i \bar{\Psi}_{\mathrm{L}}\gamma_\mu \frac{\tau^i}{2}\Psi_{\mathrm{L}}.$$

The right-handed fields, which are SU(2) singlets, do not couple to the W_μ^i gauge bosons.

To interpret the gauge bosons as the particle mediators of the charged current interaction, the gauge fields W_μ^+ and W_μ^-, defined as:

$$W_\mu^{\pm} = \frac{1}{\sqrt{2}}(W_\mu^1 \mp iW_\mu^2) \tag{1.7}$$

are used in place of W_μ^1 and W_μ^2 with the corresponding matrix combination:

$$\tau^{\pm} = \frac{1}{2}(\tau^1 \pm i\tau^2)$$

The remaining vector field, W_μ^3 identifies a neutral current term, connecting ν_{L}^{ℓ} with $\bar{\nu}_{\mathrm{L}}^{\ell}$ and ℓ_{L} with $\bar{\ell}_{\mathrm{L}}$. It cannot be identified with the photon because W_μ^3 couples to ν_{L} and ℓ_{L} with opposite charges. However, the second term, connecting ℓ_{L} with $\bar{\ell}_{\mathrm{L}}$, is a part of the electromagnetic current, apart from a constant factor. To include the electromagnetic interaction in the Lagrangian, the invariance under U(1) is required, and the gauge field, B_μ, appears to preserve the symmetry. This transforms as in equation 1.3, with $g'Y$ coupling constant of B_μ with each Dirac field ψ. Y is the weak hypercharge and takes different values with respect to the field it is associated to (left-handed or right-handed fermion, charged lepton or neutrino).

[3] d'_{L} is the field resulting from the application of the CKM matrix to the down-type quark. A detailed review on the CKM matrix can be found in [21]

The interaction term of the electroweak Lagrangian becomes:

$$\mathscr{L}_{\mathrm{I}} = -\frac{g}{\sqrt{2}}\sum_i \bar{\Psi}^i_{\mathrm{L}}\gamma_\mu\tau^+\Psi^i_{\mathrm{L}}W^+_\mu - \frac{g}{\sqrt{2}}\sum_i \bar{\Psi}^i_{\mathrm{L}}\gamma_\mu\tau^-\Psi^i_{\mathrm{L}}W^-_\mu \tag{1.8}$$

$$- gW^3_\mu\sum_i \bar{\Psi}^i_{\mathrm{L}}\gamma_\mu\frac{\tau_3}{2}\Psi^i_{\mathrm{L}} \tag{1.9}$$

$$- \frac{g'}{2}B_\mu\Big(\sum_i Y_{i_{\mathrm{L}}}\bar{\Psi}^i_{\mathrm{L}}\gamma_\mu\Psi^i_{\mathrm{L}} + \sum_j Y_{j_{\mathrm{R}}}\bar{\psi}^j_{\mathrm{R}}\gamma^\mu\psi^j_{\mathrm{R}}\Big) \tag{1.10}$$

where the first row represents the charged current terms and the second and third are neutral currents, i indicates the doublet species and j the fermion. The gauge fields has to transform as well in order for the total Lagrangian, sum of the free-Dirac Lagrangian and $\mathscr{L}_{\mathrm{I}}$, to be gauge invariant under $\mathrm{SU}(2)\otimes\mathrm{U}(1)_{\mathrm{Y}}$.

Under the hypothesis that B_μ and W^3_μ are a composition of the A_μ and Z_μ fields, with mixing angle θ_{W}, called *Weinberg angle*:

$$B_\mu = A_\mu\cos\theta_{\mathrm{W}} - Z_\mu\sin\theta_{\mathrm{W}}$$

$$W^3_\mu = A_\mu\sin\theta_{\mathrm{W}} + Z_\mu\cos\theta_{\mathrm{W}}$$

the exact fermion couplings to the photon, identified with the field A_μ, are imposed:

$$Qe = gT^3\sin\theta_{\mathrm{W}} + \frac{g'}{2}Y\cos\theta_{\mathrm{W}}$$

where T^3 corresponds to the $\frac{\tau_3}{2}$ weak isospin for Ψ_{L}, and T^3 is zero for its right-handed components. By convention, $Y_{\ell_{\mathrm{L}}}$ is chosen to be -1. From the known couplings of the photons to the fermions it follows that $g\sin\theta_{\mathrm{W}} = g'\cos\theta_{\mathrm{W}} = e$, $Y_{\ell_{\mathrm{R}}} = -2$ and $Y_{\nu_{\mathrm{R}}} = 0$. The following relation is thus valid:

$$Q = T^3 + \frac{Y}{2}$$

with Q being a conserved quantity, and T^3 the weak isospin.

$\mathscr{L}_{\mathrm{I}}$, expressed in terms of the physical fields, is hence:

$$\begin{aligned}\mathscr{L}_{\mathrm{I}} = &-\frac{g}{\sqrt{2}}\sum_i \bar{\Psi}^i_{\mathrm{L}}\gamma_\mu\tau^+\Psi^i_{\mathrm{L}}W^+_\mu - \frac{g}{\sqrt{2}}\sum_i \bar{\Psi}^i_{\mathrm{L}}\gamma_\mu\tau^-\Psi^i_{\mathrm{L}}W^-_\mu \\ &- e\sum_j Q_j\bar{\psi}_j\gamma^\mu\psi_j A_\mu \\ &- \frac{g}{2\cos\theta_{\mathrm{W}}}\sum_j \bar{\psi}_j\gamma^\mu\big((T^3_j - 2Q_j\sin^2\theta_{\mathrm{W}}) - T^3_j\gamma^5\big)\psi_j Z_\mu\end{aligned}$$

where the index i denote the flavour of a doublet and j the flavour of a fermion.

The Lagrangian of the free vector boson fields, where the masses of the gauge bosons are assumed to be zero, is in analogy to the electromagnetic field kinetic term of equation 1.1:

$$\mathscr{L}_{\mathrm{B}} = -\frac{1}{4}B_{\mu\nu}B^{\mu\nu} - \frac{1}{4}G_{i\mu\nu}G^{\mu\nu}_i.$$

The generalisation of the field tensor $F_{\mu\nu}$ to the W_i^μ case requires an additional term in order to preserve the gauge invariance under SU(2). Thus, $B^{\mu\nu}$ and $G_i^{\mu\nu}$ are defined as:

$$\begin{aligned} B^{\mu\nu} &\equiv \partial^\nu B^\mu - \partial^\mu B^\nu \\ G_i^{\mu\nu} &\equiv F_i^{\mu\nu} + g\epsilon_{ijk} W_j^\mu W_k^\nu \\ F_i^{\mu\nu} &\equiv \partial^\nu W_i^\mu - \partial^\mu W_i^\nu . \end{aligned}$$

The direct consequence of the second term in the definition of $G_i^{\mu\nu}$ is the appearance of interactions terms of the bosons among themselves in the free boson Lagrangian. Contrary to the photon field, which does not carry electromagnetic charge, the W_i^μ fields carry weak isospin charge.

1.1.3 Spontaneous electroweak symmetry breaking

No mass terms for the gauge bosons and the fermions have been considered so far. A Lagrangian which would include the mass of these fields could be:

$$m_W^2 W_\mu^+ W^{-\mu} + \frac{1}{2} m_Z^2 Z_\mu Z^\mu$$

for the boson fields; and

$$-m_f \bar{\psi}_f \psi_f$$

for the fermion fields.

However, these terms would not be $\mathrm{SU(2)}\otimes\mathrm{U(1)_Y}$ gauge invariant. Either the masses of the fields are zero, which is the case only for the photon, or a mechanism is needed which introduces the field masses but preserves the invariance under $\mathrm{SU(2)}\otimes\mathrm{U(1)_Y}$. This effect is given by the *spontaneous symmetry breaking* mechanism, also referred to as the *BEH-mechanism* (from the names of Brout-Englert-Higgs).

Spontaneous symmetry breaking occurs in a system defined by a Lagrangian which is symmetric under a group of transformations. If the lowest energy level of the system is degenerate, the ground state is not unique. As soon as a specific ground state is selected, the system is no longer symmetric under the group transformations and thus its symmetry is spontaneously broken. In field theory, if the vacuum expectation value is different from zero and is not invariant under the symmetry transformations, a particular vacuum state can be chosen. A scalar field is needed for the vacuum states under the assumption of Lorentz invariance. The Goldstone model is the simplest example of a theory which reveals spontaneous symmetry breaking. This model is defined by the Lagrangian:

$$\mathscr{L} = \partial^\mu \phi^* \partial_\mu \phi - V(|\phi|^2) \tag{1.11}$$

$$V(|\phi|^2) = \mu^2 |\phi|^2 + \lambda |\phi|^4 \tag{1.12}$$

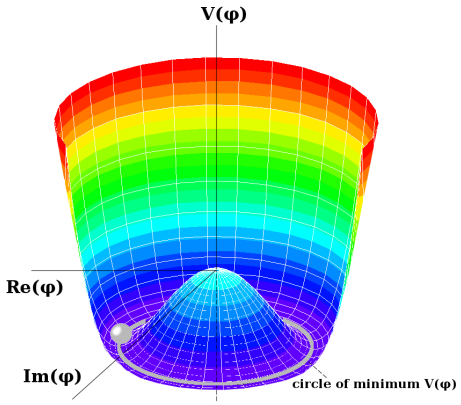

Figure 1.1: Potential $V(\phi)$ as a function of the real and imaginary component of ϕ.

where $\phi(x)$ is a complex scalar field and μ^2 and λ are real parameters. The Lagrangian is invariant under global U(1) phase transformations. If $\mu^2 < 0$, the potential has the form illustrated in figure 1.1 with an infinite number of minima:

$$\phi_{\text{min}} = \left(\frac{-\mu^2}{2\lambda}\right)^{1/2} e^{i\theta}, \quad 0 \leq \theta < 2\pi.$$

If a particular θ is chosen, symmetry is spontaneously broken. For example, a vacuum state with a real expectation value can be selected:

$$\phi_{\text{min}} = \left(\frac{-\mu^2}{2\lambda}\right)^{1/2} = \frac{1}{\sqrt{2}} v$$

and $\phi(x)$ can be expressed in terms of the real fields $\sigma(x)$ and $\eta(x)$

$$\phi = \frac{1}{\sqrt{2}}(v + \sigma + i\eta).$$

The Lagrangian expressed in terms of σ and η is composed of their free Lagrangian terms and other terms which concern the interactions among themselves. The outcome of the spontaneous symmetry breaking mechanism consists of two real scalar fields: σ with mass $\sqrt{(2\lambda v^2)}$; and the massless η, called *Goldstone boson*, which is not observed in nature.

If the U(1) gauge invariance is imposed on the Goldstone model Lagrangian of equation 1.12, the gauge field A_μ is introduced to preserve the symmetry in the definition of the covariant derivatives. After the spontaneous symmetry breaking occurs, the interaction of A_μ with the field ϕ produces the appearance of a mass term for the real vector field A_μ. The invariance under U(1) gauge transformations allows to find a gauge which transforms ϕ into a real field. In this so called *unitary gauge*, the field η can be discarded.

The spontaneous breaking of the U(1) symmetric Lagrangian of a complex scalar field and a massless real vector field leads to a Lagrangian for a real scalar field and

a massive real vector field. This effect is the so called BEH-mechanism, and the massive scalar boson associated to σ is the Higgs boson.

By extending the BEH-mechanism to the Lagrangian invariant under $\mathrm{SU(2)}\otimes\mathrm{U(1)_Y}$, the weak isospin doublet of the scalar fields $\phi_a(x)$ and $\phi_b(x)$ is defined as:

$$\Phi(x) = \begin{pmatrix} \phi_a(x) \\ \phi_b(x) \end{pmatrix}$$

The $\mathrm{SU(2)}\otimes\mathrm{U(1)_Y}$ symmetric Lagrangian for Φ is as in 1.12, but with the substitution of $\phi \to \Phi$ and $\partial_\mu \to D_\mu = \partial_\mu + ig\frac{\tau^i}{2}W^i_\mu + ig'YB^\mu$. The ground state of this Lagrangian can be chosen to be:

$$\Phi_0 = \begin{pmatrix} 0 \\ v/\sqrt{2} \end{pmatrix}, \quad \text{with} \quad v = \left(\frac{-\mu^2}{\lambda}\right)^{1/2}.$$

In order not to break the electromagnetic gauge invariance and to ensure that the photon is massless, the value of 1 is assigned to the hypercharge Y of the Higgs field and the lower component of Φ is neutral.

Additional $\mathrm{SU(2)}\otimes\mathrm{U(1)_Y}$ gauge invariant terms can be added to the electroweak Lagrangian by taking into account the Yukawa interaction between fermions and the Higgs doublet. For example, the Lagrangian for the charged leptons is:

$$\mathscr{L} = -g_\ell(\bar{\Psi}^\ell_{\mathrm{L}}\psi^\ell_{\mathrm{R}}\Phi + \Phi^\dagger\bar{\psi}^\ell_{\mathrm{R}}\Psi^\ell_{\mathrm{L}}) \tag{1.13}$$

In the unitary gauge, the Φ field becomes

$$\Phi = \frac{1}{\sqrt{2}}\begin{pmatrix} 0 \\ v+h \end{pmatrix}$$

with $h(x)$, being a real field. In this gauge, the up-component of the covariant derivative acting on Φ is $\frac{i}{2}vgW^+_\mu$ which results in a Lagrangian mass term for the fields $W^\pm$ with mass $m_W = \frac{1}{2}vg$. In a similar way, the down component has a term $\frac{i}{2\sqrt{2}}v\frac{Z^\mu}{\cos\theta_{\mathrm{W}}}$ which is connected to the mass term Lagrangian $\frac{1}{2}m_Z^2Z_\mu Z^\mu$ with $m_Z = m_W/\cos\theta_{\mathrm{W}}$. Moreover the Lagrangian terms of equation 1.13 expressed in terms of the unitary gauge gives raise to the fermion mass term with $m_\ell = vg_\ell/\sqrt{2}$.

Other terms, which have not been mentioned, lead to the interaction among the gauge boson fields, the Higgs boson h and the fermions themselves. The vacuum expectation value v is obtained from the Fermi constant, G_F, determined experimentally:

$$v = (\sqrt{2}G_F)^{-1/2} \approx 246 \text{ GeV}, \quad G_F = \frac{\sqrt{2}}{8}\frac{g^2}{m_W^2}$$

In conclusion, the application of the BEH-mechanism to the Lagrangian with $\mathrm{SU(2)}\otimes\mathrm{U(1)_Y}$ symmetry, spontaneously broken to $U(1)_{\mathrm{em}}$, leads to terms with non-vanishing masses of the $W^\pm$ and Z^0 bosons, to mass terms for the fermions and to the prediction of a massive scalar boson, the Higgs boson.

1.1.4 Quantum Chromodynamics

After the discovery of the neutron in 1935 by Chadwick, it was clear that two different nuclear forces were involved in the nucleus dynamics: unstable nuclei are subject to decay via weak processes; but the force that holds the nucleus together is the *strong force*.

Yukawa was the first one to propose a theory of the strong force (in 1934): the attraction between protons and neutrons is due to the exchange of a meson. Yukawa predicted the mass of the strong force mediator to be approximately 200 GeV by realising that this mass is inversely proportional to the force range, which is of the order of 1 fm for nuclear forces. This meson, called pion, was eventually discovered in 1947 with a mass at about 140 GeV.

Many more hadrons have been discovered since then. Gell-Mann provided a structure to organise all the discovered particles into geometrical patterns according to their mass, electric charge, and *strangeness*, a particle property conserved in strong interactions but not in weak ones. The explanation for this complex structure was independently provided by Gell-Mann and Zweig: the hadrons were not fundamental particles, but they were composed of quarks with spin 1/2.

Two characteristics of the quark dynamics were puzzling. Isolated quarks have never been observed: they are subject to "quark confinement". Baryons with three quarks with the same flavour and same spin seemed to violate Pauli's principle.

The model, which satisfactory describes the strong interactions, is based on the non-abelian gauge theory with the group SU(3). The model of strong interactions is called *quantum chromodynamics* (QCD), since the charge of the theory is called *colour*. The quarks appear in the triplet representation of SU(3), i.e. in three different colour states.

The quark confinement requires that free hadronic states are only colour singlets. The Pauli principle is not violated because the colour wave function of the baryons is totally antisymmetric.

A triplet of Dirac fields, ψ_i, is defined as

$$\Psi = \begin{pmatrix} \psi_1 \\ \psi_2 \\ \psi_3 \end{pmatrix}$$

The Lagrangian of the free Dirac field triplet Ψ is invariant under transformations of the SU($n = 3$) group. T^a are the $n^2 - 1 = 8$ generators of the group with index $a = 1, ...8$. The generators satisfy the commutation relation

$$[T^a, T^b] = if^{abc}T^c$$

with f^{abc} being the structure constants of the SU(3) algebra. After requiring the Lagrangian to retain invariance under local transformations, eight vector gauge bosons A^a_μ, called *gluons*, are introduced. The SU(3) gauge invariant QCD Lagrangian is:

$$\mathscr{L}_{\mathrm{QCD}} = -\frac{1}{4}F_a^{\mu\nu}F^a_{\mu\nu} + \sum_{\mathrm{f}}\left(\bar{\Psi}^{\mathrm{f}}(i\partial\!\!\!/ - m_{\mathrm{f}})\Psi^{\mathrm{f}} - g_{\mathrm{S}}\bar{\Psi}^{\mathrm{f}}T^a A\!\!\!/_a \Psi^{\mathrm{f}}\right) \tag{1.14}$$

$$F^a_{\mu\nu} = \partial_\mu A^a_\nu - \partial_\nu A^a_\mu - g_{\mathrm{S}}\sum_{b,c} f_{abc}A^b_\mu A^c_\nu \tag{1.15}$$

where g_{S} is the strong coupling constant and f is the index running over the quark flavours. The first term describes the gluon dynamics. The consequences of gluons carrying non-zero colour charges are the impossibility to observe them as isolated free particles, due to colour confinement, and the existence of gluon self-interaction terms. The last term represents the quark-gluon interaction. The strong coupling constant of this interaction is independent of the quark flavour and thus the flavour number $N_{\mathrm{f}} \equiv N(\mathrm{f}) - N(\bar{\mathrm{f}})$, defined as the difference between the number of quarks and antiquarks of flavour f, is conserved.

Another striking feature of QCD is the *asymptotic freedom*, which allows to treat quarks and gluons as free particles at high energies or short ranges. Before going into the detail of the asymptotic freedom, the phenomenon of *scaling* is described. It was observed in deep inelastic scattering processes (DIS) at the end of the 1960s. DIS processes are the collisions of leptons with a nucleon target, resulting in numerous massive particles in the final state. The *parton model* was proposed by Bjorken and Feynman to describe the structure of the proton as a loosely bound collection of a few constituents. In this picture, the lepton scatters from one of these partons.

The dimensionless Bjorken variables are used to describe the kinematics of the scattering process:

$$x \equiv \frac{Q^2}{2p\cdot q} \qquad y \equiv \frac{q\cdot p}{k\cdot p} \tag{1.16}$$

where p is the nucleon four-momentum, q is the four-momentum transferred to the nucleon with $Q^2 = -q^2$, and k is the incoming lepton four-momentum. Under the hypothesis of negligible mass of the lepton and of the hypothetical parton and that the electron-parton scattering is elastic, x corresponds also the longitudinal fraction of the proton momentum carried by the parton in the electron-proton centre of mass frame.

Bjorken predicted that in the high energy limit, the leading order differential cross section of DIS processes in terms of x and y given by the parton model is:

$$\frac{d^2\sigma}{dxdy} = \sum_f x f_f(x) Q_f^2 \frac{2\pi\alpha^2 s}{Q^4}[1 + (1-y)^2] \tag{1.17}$$

where $f_f(x)$ is the *parton distribution function* (PDF), such that $f_f(x)dx$ is the probability of finding the parton of f species with x longitudinal fraction of the proton momentum. The first order dependence of $f_f(x)$ solely on x and not on Q^2 coincides with the concept of Bjorken scaling, observed in DIS processes at SLAC with an

accuracy of 10% for large values of Q. Bjorken scaling implies that the structure of the proton is the same independently from the energy of the electromagnetic probe and suggests that the lepton is scattered by pointlike constituents.

The observation of the Bjorken scaling reinforced the need to have a field theory description of the strong force that becomes weak at high energies and thus is asymptotically free. The theory of quantum chromodynamics, being a non-Abelian gauge theory, reveals asymptotic freedom. QCD theory is a renormalisable field theory, if all the ultraviolet divergences can be absorbed by a redefinition of the coupling constants and the fields. The dependence of physical quantities on the ultraviolet cutoff M is eliminated by the redefinition of the coupling constant α in terms of the renormalised coupling constant α_{ren} and the finite scale μ_{R}, called *renormalisation scale*: $\alpha_{\text{ren}} = \alpha_{\text{ren}}(\alpha, M/\mu_{\text{R}})$ and $\alpha = \alpha(\alpha_{\text{ren}}, M/\mu_{\text{R}})$. In order to leave physical quantities invariant under μ_{R} variations, α_{ren} has to vary as well. The evolution of the coupling constant as a function of the scale μ_{R} is expressed via the renormalisation group equation in terms of the β function, which depends only on the renormalised coupling constant:

$$\frac{\mathrm{d}\alpha_{\text{ren}}}{\mathrm{d}\log\mu_{\text{R}}^2} = \beta(\alpha_{\text{ren}}) \tag{1.18}$$

$$\beta(\alpha_{\text{ren}}) = -b_0\alpha_{\text{ren}}^2 - b_1\alpha_{\text{ren}}^3 + \mathscr{O}(\alpha_{\text{ren}}^4) \tag{1.19}$$

$$b_0 = \frac{11N_c - 2n_f}{12\pi} \tag{1.20}$$

where N_c is the number of colours, n_f is the number of active flavours. The solution of the differential equation requires a boundary value usually taken at the Z boson mass scale. From figure 1.2 it can be seen that the evolution of the coupling constant α_S leads to asymptotic freedom, becoming smaller as higher energies are probed. This effect is due to the value of b_0: being positive, the evolution of α_{ren} is characterised by a negative slope at higher scales.

1.2 Physics at the Large Hadron Collider

At the Large Hadron Collider (LHC) protons have been collided at energies ranging from a few TeV up to 13 TeV. The interactions with large momentum exchange between constituents of the two colliding protons, referred to as *hard interactions*, can be described by the perturbative expansion of QCD. The parton model, which represents hadrons as being made of quark-, antiquark-, gluon-constituents, generically referred to as partons, is used to make quantitative predictions at parton level of observables like cross sections, angular and momentum distributions, and so on. Under the assumption that the proton-proton interaction is hard and parton binding effects are negligible, the cross section for a scattering process which results in the final state X can be factorised in terms of a partonic scatter cross section $\hat{\sigma}$ and

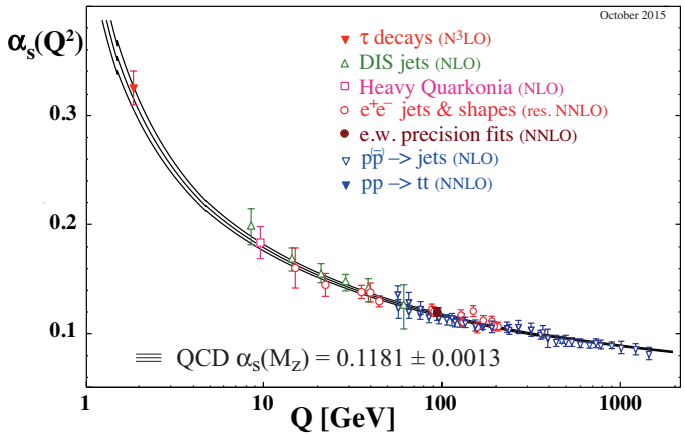

Figure 1.2: Measurement summary of α_s as a function of the energy scale Q. In brackets the order of α_s extraction in perturbative QCD is indicated: next-to-leading order (NLO); next-to-next-to leading order (NNLO); NNLO matched with resummed next-to-leading logarithms (res. NNLO); or next-to-NNLO (N^3LO). Figure from [21].

factors for the flux of interacting partons as follows:

$$\sigma(pp \to XY) = \int_0^1 \mathrm{d}\, x_1 \int_0^1 \mathrm{d}x_2 \sum_{i,j} f_i(x_1, \mu_F^2) f_j(x_2, \mu_F^2) \hat{\sigma}_{ij\to X}(x_1 x_2 s, \alpha_s(\mu_R^2), \mu_R, \mu_F) \sigma_{p_{1r}p_{2r}\to Y}, \tag{1.21}$$

where two protons, with four-momentum P_1 and P_2 and energy P, collide. The sum runs over all the possible initial state partons i, j, representing gluons, quarks and anti-quarks. The energy fraction of the parton i (j) with respect to the proton is x_1 (x_2). The partonic centre of mass energy is $\hat{s} = x_1 x_2 s$, where $s = (P_1 + P_2)^2$ is the proton-proton centre of mass energy square. The probability to find a parton i with an energy fraction x in a proton is described in terms of the PDFs $f_i(x, \mu_F^2)$. The PDFs depend on the *factorisation scale* μ_F, according to the Dokshitzer-Gribov-Lipatov-Altarelli-Parisi (DGLAP) equation [22–24]. $\hat{\sigma}_{ij\to X}$ is the short distance cross section of the parton i interacting with parton j producing the system X. It can be calculated as a perturbative expansion in α_s. The *underlying event* cross section, $\sigma(p_{1r}p_{2r} \to Y)$, is due to the interaction of the residual parts of the two protons, p_{1r} and p_{2r}, not directly involved in the hard scatter resulting in a hadronic final state Y.

1.2.1 Simulation

The partons produced in the hard scatter immediately initiate a process, called *parton shower*, of radiating low-energy and collinear gluons. Afterwards partons evolve into hadrons in a process called *hadronization*. The transition of a system of partons into confined hadrons is described by models which take into account non-perturbative effects. In order to describe the final state particles realistically and to make theoretical predictions, Monte Carlo (MC) simulation programs are used.

An event is generated by a MC program by randomly defining the kinematics and partonic channels of a hard scattering process. The cross section of a hard process is generated by MCs at leading order (LO). Afterwards the parton shower follows: gluons randomly split into a quark-antiquark pair or quarks randomly emit gluons. Each emission and splitting is generated at a lower scale than the previous one. If the radiation comes from the partons leaving the hard collision, it is referred to as final state radiation (FSR). Radiation emitted by the incoming particles is referred to as initial state radiation (ISR). As soon as the energy scale approaches 1 GeV, the hadronization model is employed to transform partons into hadrons. The scattering between the proton remnants is also used to simulate the underlying event (UE), consisting of a $2 \to 2$ scattering at the GeV scale. Free parameters are tuned to better model the observation.

In addition to UE, a similar soft contribution to the event, called pileup, is given by additional simultaneous proton-proton interactions, as the protons are collided in bunches. The pileup is modelled by overlaying with simulated inelastic proton-proton scattering events.

After hadronization the decay of all the particles present in the event occur until only stable particles are left. These are defined as particles with a lifetime τ in the laboratory system such that $c\tau > 10\,mm$ [21]. The simulation at the experimental level is achieved by propagating stable particles through the ATLAS detector by the GEANT4 software toolkit [25] within the ATLAS simulation framework [26], where the particle interactions with the detector material and the signal formation are simulated. The same algorithm used for data is employed for the reconstruction in the simulation.

1.3 Top quark phenomenology

The top quark is the heaviest particle known and was the last quark to be discovered in 1995 at the Tevatron [27, 28]. Its phenomenology depends mainly on its large mass. Combined ATLAS measurements report a top mass value of $m_t = 172.84 \pm 0.70$ [29]. It decays into a real W boson. Its life time, of the order of 10^{-25} s, is so short that its decay occurs before it can hadronise, with the hadronization time of QCD being of the order of 10^{-24} s, and the distance between the production and the decay vertices of the order of 10^{-16} m. Thus, the top quark is a unique laboratory for studying the properties of a bare quark free from non-perturbative effects of QCD confinement.

Its Yukawa coupling with the Higgs boson is very close to unity:

$$g_t = \sqrt{2}\frac{m_t}{v} \approx 1.$$

For this reason, which is connected to its large mass, the top quark plays a crucial role in the Higgs physics and also in new physics models, as described in section 1.4

1.3.1 Top quark production and decay

At hadron colliders, the top quark is mainly produced in pair through the gluon-gluon fusion process, $gg \to t\bar{t}$ and through the quark-antiquark annihilation process $q\bar{q} \to t\bar{t}$. At the LHC, where the colliding particles are protons, gluon-gluon fusion is the leading process contributing from 80 to 90% of the total production cross section for proton-proton centre of mass energy from 7 to 14 TeV.

One top quark can be also produced alone via electroweak interactions in the so called, *single-top* production. Although suppressed by the weak coupling constant with respect to the strong $t\bar{t}$ production, single top production has a considerable cross section, since it is kinematically enhanced. The production occurs via three production mechanisms. The leading one is called the t-channel: the top quark is produced in association with another quark, $qb \to q't$ via the mediation of a virtual t-channel W boson. The sub-leading production process occurs via the s-channel, in which a virtual W boson is exchanged in the s-channel. In this case a single top quark is produced in association with a b-quark, via the process $q\bar{q}' \to t\bar{b}$. The final state of the last production channel is composed of the single top quark in association with a W boson. For this process a gluon interacts with a b-quark either directly or via the exchange of a virtual top quark.

The top quark decay width and its decay modes are determined by the fact that the top quark mass is larger than the sum of the W boson and b quark masses and by the CKM element $|V_{tb}| \gg |V_{td}|, |V_{ts}|$. Thus, the Wb final state is dominant. For a value of the top pole mass, m_t, of 173.3 GeV/c^2 and $\alpha_s(M_Z) = 0.118$ the width is 1.35 GeV/c^2 and the corresponding lifetime is at about 0.5×10^{-24}s.

The W decay modes, that characterise the top quark final state, are divided in *hadronic* decays into a quark-antiquark pair $BR(W \to q_1\bar{q}_2) \approx 2/3$; and *leptonic* decays into a lepton-neutrino pair with branching ratio $\sum_{l=e,\,\mu\,\tau} BR(W \to l\bar{\nu}_l) \approx 1/3$. If the charged lepton is a tau, in turn, it decays 35% of the time into a final state with an electron or a muon plus neutrinos. The final state with a leptonically decaying tau is accounted for in experimental measurements with electron and muon final states, as the leptonic tau decay signature is almost identical to the $W \to e/\mu\nu$ one. Concerning the remaining 65% of the time, the τ decays into hadrons and a neutrino.

Events containing $t\bar{t}$ pair production can be divided into three classes depending on the number of leptons in the final state. The most probable $t\bar{t}$ channel, which occurs to 45.7% of the time, is fully hadronic: $t\bar{t} \to W^+(q\bar{q}')b\,W^-(q''\bar{q}''')\bar{b}$. The final state quarks hadronise and evolve into jets of hadrons. The channel with slightly lower probability is the so called l+jets channel, with only one charged lepton, l, in the final state, occurring 43.8% of the time. The remaining decay channel is the dilepton channel, with two charged leptons in the final state, corresponding to 10.5% of the cases.

1.4 Physics beyond the Standard Model

The most fundamental question that theories beyond the SM seek to answer, concerns the electroweak symmetry breaking sector.

In the SM, the scalar mass of the Higgs boson is affected by large quantum corrections from the coupling with fermions. In particular, the largest contribution comes from the massive top quark. The physical value of the Higgs boson mass is:

$$m_h^2 \approx m_{h0}^2 - \frac{|g_f|^2}{8\pi^2} N_c^f \int^{\Lambda} \frac{\mathrm{d}^4 p}{p^2} \approx m_{h0}^2 - \frac{g_f^2}{8\pi^2} N_c^f \Lambda^2 \tag{1.22}$$

where m_h is measured to be approximately at 125 GeV [30], m_{h0} is the bare Higgs boson mass and the remaining term is the 1-loop correction, $m_{h\,1-\mathrm{loop}}$, N_c^f is the number of colours, g_f is the Yukawa coupling of the fermion f to the Higgs boson, and Λ is the upper energy scale limit of validity of the SM. If Λ is assumed to be the Planck scale, $m_{\mathrm{Pl}} = (G_N)^{-1/2} \approx 10^{19}$ GeV, at which the magnitude of the gravitational interaction of particles becomes of the order of the gauge interactions, an *unnatural* fine-tuning of the Higgs boson bare mass is required in order to cancel the large radiative corrections. The gauge hierarchy problem concerns the huge difference between the Higgs boson mass and the Planck scale.

The top quark plays a crucial role in searches for physics beyond the Standard Model (BSM). Theory models, which address the naturalness problem, foresee a direct connection between new physics and the top quark. For example, the Little Higgs and Composite Higgs models are based on a spontaneously broken global symmetry, leading to a pseudo-Goldstone Higgs boson. These theories predict vector-like quarks, in particular vector-like top partners, which behave like the top quark apart from the electroweak couplings. The couplings of these vector-like top partners to top quarks is large, giving the top quark a decisive role in the search for these new particles. In other models the electroweak symmetry breaking is a dynamical mechanism where top quarks are directly involved. In *topcolor*, for example, a new strong gauge force which couples preferentially to the third generation quarks is the source of a low energy condensate of top-antitop pair which breaks the SM $\mathrm{SU(2)}\otimes\mathrm{U(1)_Y}$ symmetry. In *topcolor-assisted technicolor*, a heavy Z' boson is predicted which couples especially to third generation quarks.

The gauge hierarchy problem is also addressed by supersymmetric models. These models are discussed in section 1.4.1 and [20, 21, 31, 32] are used as references.

1.4.1 Supersymmetry

The SM Lagrangian is invariant under transformation of the Poincaré group. A non-trivial extension of the space-time symmetries is called *supersymmetry* (SUSY), which transforms fermions into bosons and vice versa. This symmetry was born in the generalisation of the Coleman-Mandula theorem, which states that it is not possible to non-trivially combine Lorentz invariance and an internal symmetry for physical

theories. However, the theorem was found not to hold any more for supersymmetries with fermionic generators, defined by anticommutative relations. A supersymmetric generator, Q, is an operator which commutes with the Hamiltonian and carries half-integer spin, in the simplest case $1/2$, in order to convert bosonic into fermionc states and vice versa:

$$Q|\text{Boson}\rangle = |\text{Fermion}\rangle, \qquad Q|\text{Fermion}\rangle = |\text{Boson}\rangle. \tag{1.23}$$

This operator, Q_α with $\alpha = 1, 2$ is defined by spinor components, which are left-handed, while its Hermitian conjugates $Q^\dagger_\beta$ are right-handed. The anticommutator transforms under Lorentz transformations:

$$\{Q_\alpha, Q^\dagger_\beta\} = 2\sigma^\mu_{\alpha,\beta} P^\mu \tag{1.24}$$

$$\{Q_\alpha, Q_\beta\} = \{Q^\dagger_\alpha, Q^\dagger_\beta\} = 0 \tag{1.25}$$

$$[P^\mu, Q_\alpha] = [P^\mu, Q^\dagger_\alpha] = 0 \tag{1.26}$$

where P^μ is the total energy-momentum, which commutes with Q. The single-particle states are represented by *supermultiplets*, containing both fermion and boson states, which are *superpartners* of each other. Since Q commutes also with $-P^2$ and the generator of gauge transformations, particles of the same supermultiplet must have equal masses, the same electric charges, weak isospin and colour degrees of freedom. Moreover the number of fermion and boson degrees of freedom must be equal. The *scalar* supermultiplet is composed of a single Weyl fermion with two degrees of freedom and two real scalars combined into a complex scalar field. While the *gauge* supermultiplet is formed by a massless spin-1 boson and a Weyl fermion. The phenomenological implication of supersymmetry is that for every fermion (leptons and quarks), which appears in the left-handed or right-handed component, two complex scalar partner are predicted, one for each Weyl spinor. These scalar partners are called *sfermions* (*slepton* and *squarks*), denoted by the symbol $\widetilde{\ }$: for example, the superpartners of the left-handed and right-handed parts of the top quark Dirac field are called left- and right-handed *stop*s, $\widetilde{t}_\text{L}$ and $\widetilde{t}_\text{R}$.

In the minimal supersymmetric extension of the SM (MSSM) the existence of an additional Higgs doublet is predicted, resulting in two $SU(2)_L$ doublets $H_u = (H^+_u, H^0_u)$ and $H_d = (H^0_d, H^-_d)$, the first one giving masses to the up-type fermions and the second to the down-type fermions. Their spin-1/2 superpartners are called higgsinos.

The particle content in the MSSM is composed of three families for each quark and lepton supermultiplets, two chiral Higgs supermultiplets, eight gluon gauge supermultiplets and four electroweak gauge supermultiplets.

In the MSSM Lagrangian renormalisable gauge-invariant terms not conserving the baryon number and the lepton number could be present. Their inclusion in the theory would lead to an unstable proton, which could decay into a lepton and a meson. Measurements of the proton lifetime set a lower limit of the order of 10^{29} years

[21], resulting in strong constraints on the proton decay. A new discrete symmetry, called R-parity, is thus included in the MSSM defined for each particle as:

$$P_R = (-1)^{3(\mathrm{B-L})+2s}$$

where B is the baryon number, L is the lepton number, s is the spin of the particle. SM particles have even R-parity, while all squarks, sleptons, gauginos and higgsinos, generically referred to as *sparticles*, have odd R-parity. If R-parity is conserved, sparticles cannot mix with SM particles and in every interaction vertex an even number of sparticles must be foreseen. Thus, only even number of sparticles can be produced at the LHC. The most relevant phenomenological implication of R-parity conservation is the stability of the lightest supersymmetric particle (LSP), which should be present in the final state of every sparticle decay. If the LSP has neutral electric charge, it interacts only weakly with matter and, thus constitutes a good dark matter candidate.

The presence of extra particles with respect to the SM leads to an interesting behaviour of the gauge couplings in the MSSM at high energies. The SM contains three independent gauge couplings, g, g' and g_S. An appealing idea would be that the three gauge symmetries $\mathrm{SU(3)_C}\otimes\mathrm{SU(2)}\otimes\mathrm{U(1)_Y}$ are subgroups of a larger symmetry group, like SU(5), that is spontaneously broken at very high energies into $\mathrm{SU(3)_C}\otimes\mathrm{SU(2)}\otimes\mathrm{U(1)_Y}$. In such a SU(5) theory, with coupling constant g_5, the following relation would be valid

$$g_5 = g_S = g = \sqrt{\frac{5}{3}}g'.$$

According to the SM, the extrapolation of the coupling constant from a scale of m_Z up to very high energies results in values that come close to each other without converging. However, the MSSM particle content leads to the gauge coupling unification at a scale $m_{\mathrm{GUT}} \approx 10^{16}$ GeV, called Grand Unification scale. The evolution of α_a^{-1}, where $\alpha_a = g_a^2/4\pi$, and $g_1 = \sqrt{5/3}g'$, $g_2 = g$ and $g_3 = g_S$, as a function of the energy scale Q is compared between the SM and the MSSM predictions in figure 1.3 [32].

If SUSY were unbroken, the squarks and sleptons would have the same mass as their SM fermionc partners. The direct consequence of an unbroken supersymmetric Lagrangian is that the Yukawa couplings for fermionic fields y_f and for scalar fields y_S satisfy the relation $y_S = |y_f|^2$, and thus the quadratic divergences in the Higgs mass vanishes to all orders in perturbation theory as they cancel through the opposite contributions between fermions and bosons. However, squarks and sleptons should have already been detected if they had masses of the order of the SM particle ones. Since none of them have been found so far, if nature is supersymmetric, SUSY must be broken in the vacuum state. Under the hypothesis that even a broken SUSY has to provide a cancellation to the quadratic corrections to the Higgs mass, SUSY should be *softly* broken. Given the largest mass scale associated to the softly symmetry

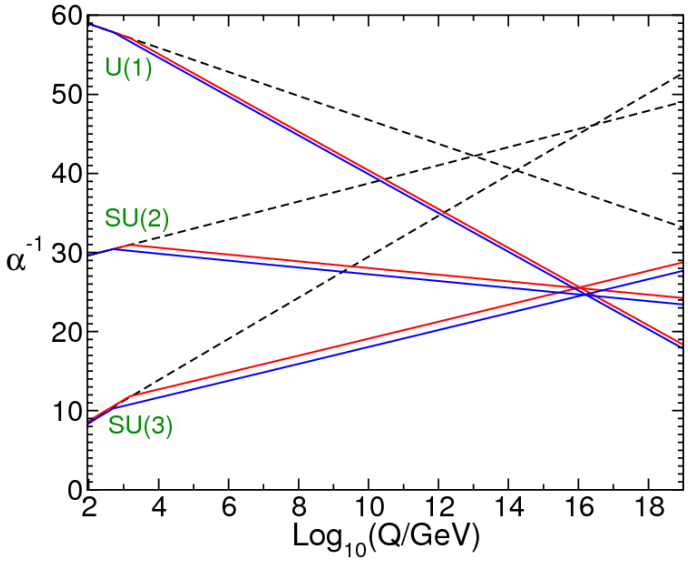

Figure 1.3: Extrapolation as a function of the energy scale Q of the $g_1 = \sqrt{5/3}g'$, $g_2 = g$ and $g_3 = g_S$ coupling constants, expressed with respect to $(\alpha_a)^{-1} = (g_a^2/4\pi)^{-1}$, using the β functions calculated in the context of the MSSM or SM particle content represented with solid and dashed lines respectively. Figure from [32].

breaking terms, m_{soft}, the corrections to the Higgs mass are of the form:

$$\Delta m_h^2 \approx m_{\text{soft}}^2 \left(\frac{\ln(\Lambda/m_{\text{soft}})}{16\pi^2} \right).$$

m_{soft} should be of the order of 1 TeV to provide corrections to the Higgs mass of the order of the vacuum expectation value.

After symmetry breaking, mixing can occur between electroweak gauginos and higgsinos as well as within sets of squarks, sleptons and Higgs scalars with the same electric charge, R-parity and colour quantum numbers. Concerning the Higgs sector, the two complex $SU(2)_L$-doublets are composed of eight scalar degrees of freedom. After electroweak symmetry breaking five Higgs mass eigenstates survive: h, SM-like Higgs; H, heavy CP-even boson mixing with the state h; a CP-odd state A; and two charged Higgs bosons, $H^{\pm}$, with the same mass.

Higgsinos and electroweak gauginos mix between themselves after electroweak symmetry breaking. The resulting four mass eigenstates from the mixing of neutral higgsinos, $\widetilde{H}_u^0$ and $\widetilde{H}_d^0$, and neutral gauginos, $\widetilde{B}$ and $\widetilde{W}^0$ are the *neutralinos*: $\widetilde{\chi}_1^0$, $\widetilde{\chi}_2^0$, $\widetilde{\chi}_3^0$ and $\widetilde{\chi}_4^0$. In a similar way the positively (negatively) charged higgsino, $\widetilde{H}_u^+$ ($\widetilde{H}_d^-$) mix with the $\widetilde{W}^+$ ($\widetilde{W}^-$) wino to form the charginos, $\widetilde{\chi}_1^+$ and $\widetilde{\chi}_2^+$ ($\widetilde{\chi}_1^-$ and $\widetilde{\chi}_2^-$).

Most of the mixing angle between sleptons, sneutrinos and squarks is foreseen to be very small. A significant mixing is expected among the third-generation $(\widetilde{t}_L, \widetilde{t}_R)$, $(\widetilde{b}_L, \widetilde{b}_R)$ and $(\widetilde{\tau}_L, \widetilde{\tau}_R)$ pairs, which are characterised by large Yukawa couplings. On the contrary, the first- and second families of squarks and leptons are expected to have a negligible mixing and to be almost mass degenerate due to their negligible Yukawa coupling.

The phenomenological particle set of the MSSM is composed of the mass states of table 1.1.

Names $P_R=+1$	Names $P_R=-1$	$P_R=+1$ particles	$P_R=-1$ sparticles	$P_R=-1$ mass eigenstates
quarks	squarks	$u_L\ u_R\ d_L\ d_R$	$\widetilde{u}_L\ \widetilde{u}_R\ \widetilde{d}_L\ \widetilde{d}_R$	(same)
		$c_L\ c_R\ s_L\ s_R$	$\widetilde{c}_L\ \widetilde{c}_R\ \widetilde{s}_L\ \widetilde{s}_R$	(same)
		$t_L\ t_R\ b_L\ b_R$	$\widetilde{t}_L\ \widetilde{t}_R\ \widetilde{b}_L\ \widetilde{b}_R$	$\widetilde{t}_1\ \widetilde{t}_2\quad \widetilde{b}_1\ \widetilde{b}_2$
leptons	sleptons	$\nu_L, e_L\ e_R$	$\widetilde{\nu}_e\ \widetilde{e}_L\ \widetilde{e}_R$	(same)
		$\nu_\mu\ \mu_L\ \mu_R$	$\widetilde{\nu}_\mu\ \widetilde{\mu}_L\ \widetilde{\mu}_R$	(same)
		$\nu_\tau\ \tau_L\ \tau_R$	$\widetilde{\nu}_\tau\ \widetilde{\tau}_L\ \widetilde{\tau}_R$	$\widetilde{\nu}_\tau\ \widetilde{\tau}_1\ \widetilde{\tau}_2$
gluon	gluino	g	$\widetilde{g}$	(same)
Higgs-es	Higgsinos	$H_u^+\ H_d^-\ H_u^0\ H_d^0$	$\widetilde{H}_u^+\ \widetilde{H}_d^-\ \widetilde{H}_u^0\ \widetilde{H}_d^0$	$\widetilde{\chi}_1^+\ \widetilde{\chi}_1^-\ \widetilde{\chi}_1^0\ \widetilde{\chi}_2^0$
W/B bosons	winos, binos	$W^\pm\ W^0\ B^0$	$\widetilde{W}^+\ \widetilde{W}^-\ \widetilde{W}^0\ \widetilde{B}^0$	$\widetilde{\chi}_2^+\ \widetilde{\chi}_2^-\ \widetilde{\chi}_3^0\ \widetilde{\chi}_4^0$

Table 1.1: MSSM particle content. R-parity odd and even states are reported, together with the mass eigenstates of the R-parity odd states. The mixing of H_u^+, H_d^-, H_u^0 and H_d^0 into h, A, H, $H^\pm$ is not reported in this table. For each chiral super-multiplet there is a corresponding anti-particle multiplet of charged conjugated fermions and their associated scalar partners.

Depending on the values of the masses and mixing parameters the sparticle mass spectrum can have large variations. However, some general features, which often recur in several models are:

- the LSP is the lightest neutralino $\tilde{\chi}_1^0$;
- the gluino is predicted to be much heavier than the lighter neutralinos and charginos;
- the first and second family squarks are almost degenerate and the left-handed squarks are likely to be heavier than the right-handed ones.
- due to their large mixing effects, the lighter stop $\widetilde{t}_1$ and the lighter sbottom $\widetilde{b}_1$ are probably the lightest squarks
- the stau is expected to be the lightest charged slepton;
- the h SM-like Higgs is expected to be much lighter than the other Higgs mass eigenstates.

With respect to the structure of the soft supersymmetry breaking terms, several models have been suggested with different sets of parameters, which reduce the MSSM parameter space. The resulting supersymmetric particle spectrum depends

only on a relatively small number of input parameters. However, the large number of models with different theoretical descriptions of the symmetry breaking sector makes it difficult to interpret experimental results in term of each model. Thus, for experimental tests simplified models [33] are used in order to focus only on a reduced set of hypothetical supersymmetric particles. The signal process is characterised by the production of a specific sparticle pair each decaying into a chain defined by only few dominant decay modes. With this approach the masses of SUSY particles are considered as free parameters.

Phenomenology of the top scalar partner

Supersymmetric models predict the existence of two scalar partners of the top quark, $\widetilde{t}_R$ and $\widetilde{t}_L$, each associated either to the right- or the left- handed chiral component of the top quark. They significantly mix to form the mass eigenstates $\tilde{t}_1$ and $\widetilde{t}_2$, where the first is much lighter than the second.

Concerning SUSY models with R-parity conservation, a pair of stop squarks could be produced at the LHC via gluon-gluon or quark-antiquark fusion. The production cross section depends only on the $\tilde{t}_1$ mass to leading order. It is calculated with PROSPINO [34, 35] in $p-p$ collisions at $\sqrt{s} = 8$ TeV to next-to-leading order in the strong coupling constant with the resummation of soft gluon emission at next-to-leading-logarithmic accuracy (NLO+NLL)[36–38] and it is shown in figure 1.4(a).

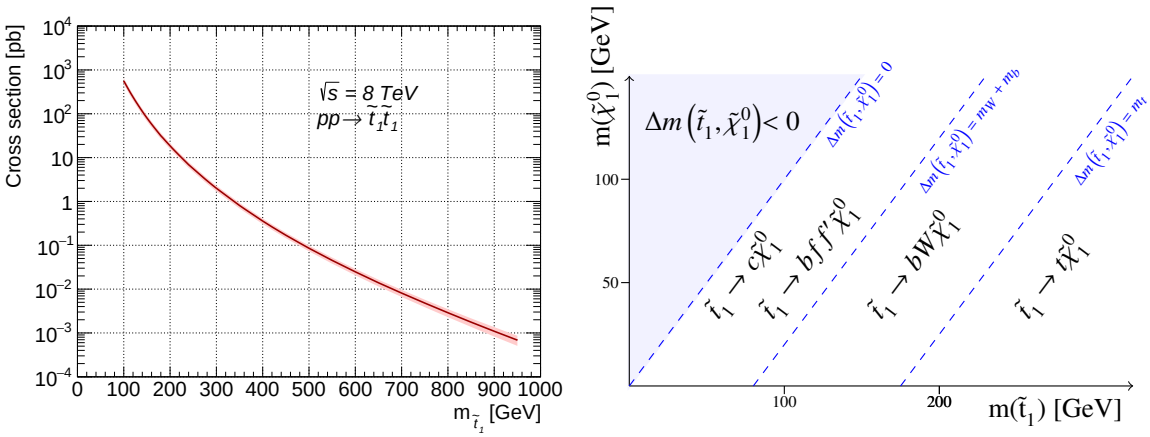

(a) (b)

Figure 1.4: (a) and (b) from [39]. (a) Cross section at $\sqrt{s} = 8$ TeV of the direct stop pair production process. (b) Dominant stop decay channels with respect to the stop mass and the neutralino mass.

After the stop is pair produced, the decay chain leads to a final state with neutralinos and SM particles. Which SM particles are involved in the final state depends principally on the $\tilde{t}_1$ mass, $m_{\tilde{t}_1}$, and the neutralino mass, $m_{\tilde{\chi}^0_1}$, or more precisely on their difference $\Delta m(\tilde{t}_1, \tilde{\chi}^0_1) = m_{\tilde{t}_1} - m_{\tilde{\chi}^0_1}$, as can be seen in figure 1.4(b).

This difference reveals the energy left to produce the remaining decay products: if $\Delta m(\tilde{t}_1, \tilde{\chi}_1^0)$ is larger than the top quark mass, m_t, the decay $\tilde{t}_1 \to t\tilde{\chi}_1^0$ is the favoured one.

Chapter 2

The ATLAS experiment at the Large Hadron Collider

The Large Hadron Collider (LHC) [40] at the European Organisation for Nuclear Research (CERN) is the largest experiment ever built and able to explore new high energy regimes. The LHC has been built to accelerate and collide protons or heavy ions at unprecedented energies. The experience and knowledge acquired with preceding high energy colliders like the Tevatron [41] and HERA [42] has been applied in the design and construction of the LHC.

Four large experiments have been engineered according to specific physics requirements. Two general purpose experiments, ATLAS (A Toroidal LHC ApparatuS) [43] and CMS (Compact Muon Solenoid) [44], have been built to unveil the electroweak symmetry breaking mechanism, and to probe new reachable high energy scales searching for hints of Physics Beyond the Standard Model. The LHCb (Large Hadron Collider beauty) experiment [45] is devoted to investigate the phenomenology of the b-quark, measuring with high precision rare decays of B hadrons and the CP violation in order to search for indirect evidence of new physics. ALICE (A Large Ion Collider Experiment) [46] has been built to study the physics of strongly interacting matter and of the quark-gluon plasma in heavy ion collisions, especially lead-lead collisions provided by the LHC at a maximum design ion beam energy of 2.76 TeV/nucleon.

After a brief description of the Large Hadron Collider machine in section 2.1, the ATLAS detector is presented in section 2.2. The Run 1 data taking conditions are reported in section 2.3. The ATLAS trigger system is described in section 2.4. Objects used in physics analyses are reconstructed from the signals of one or more sub-detectors, as explained in section 2.5. The Monte Carlo simulation used to model the background and the systematic uncertainties which concern the analyses of this thesis are described in sections 2.6 and 2.7, respectively.

2.1 The Large Hadron Collider

The following description is focused on proton-proton collisions and [40, 47] are used as references. The LHC consists of a two-ring tunnel of about 27 km formerly built for LEP [48], equipped with superconducting magnets for the particle bending. As

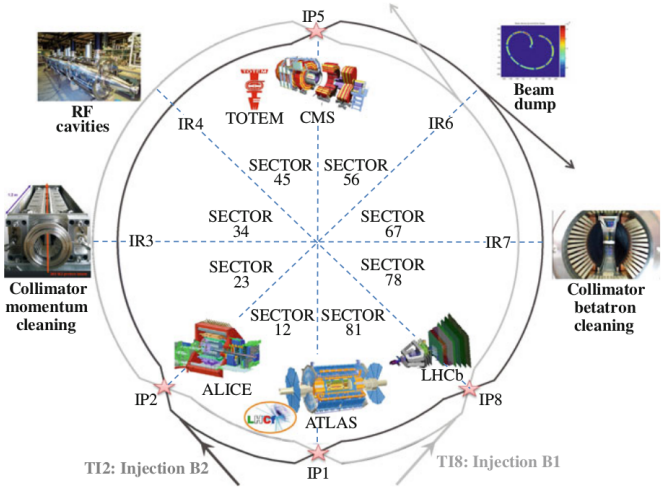

Figure 2.1: Schematic of the LHC structure from [47].

depicted in figure 2.1, the LHC machine consists of eight arcs connected by eight straight sections corresponding to the insertion regions (IRs). The ATLAS and CMS detectors are located in the two opposite high-luminosity interaction points (IPs). In the regions contiguous to ATLAS, two additional IPs are located where the ALICE and LHCb detectors are installed together with the beam injection systems. On the four remaining IR the storage ring hardware for the 400 MHz radio frequency, the collimation, the beam extraction and the dump systems are placed. The beam crossing occurring at the four IPs leads to two trajectories of the same size for the two beams. The LHC is designed to accelerate protons up to an energy of 7 TeV, thanks to the superconducting dipole magnets with nominal field strength of 8.3 T. Magnets with "twin-aperture" are placed in a common return yoke and cryostat in order to have a compact layout, fitting in the tunnel with a diameter of about 4 m. The beam optics is characterised by the standard FODO lattice: repeated groups of two quadrupole magnets, one focusing and the other defocusing, separated by three dipoles which bend the beam. Superconducting correction coils are included. The beam stability is achieved by the presence of multipole compensation coils, which correct for multipole errors of the main magnets.

The proton beams are provided to the LHC by an injector chain formed by several accelerating stages, as displayed in figure 2.2. Protons are produced in Linac2 and accelerated up to 750 keV. Protons are transferred to the Proton Synchrotron Booster (PSB), formed by four stacked rings, and reach energies of about 1 GeV. The Proton Synchrotron (PS) accelerates protons up to energies of 26 GeV. Protons finally running in the Super Proton Synchrotron (SPS) reach energies of 450 GeV.

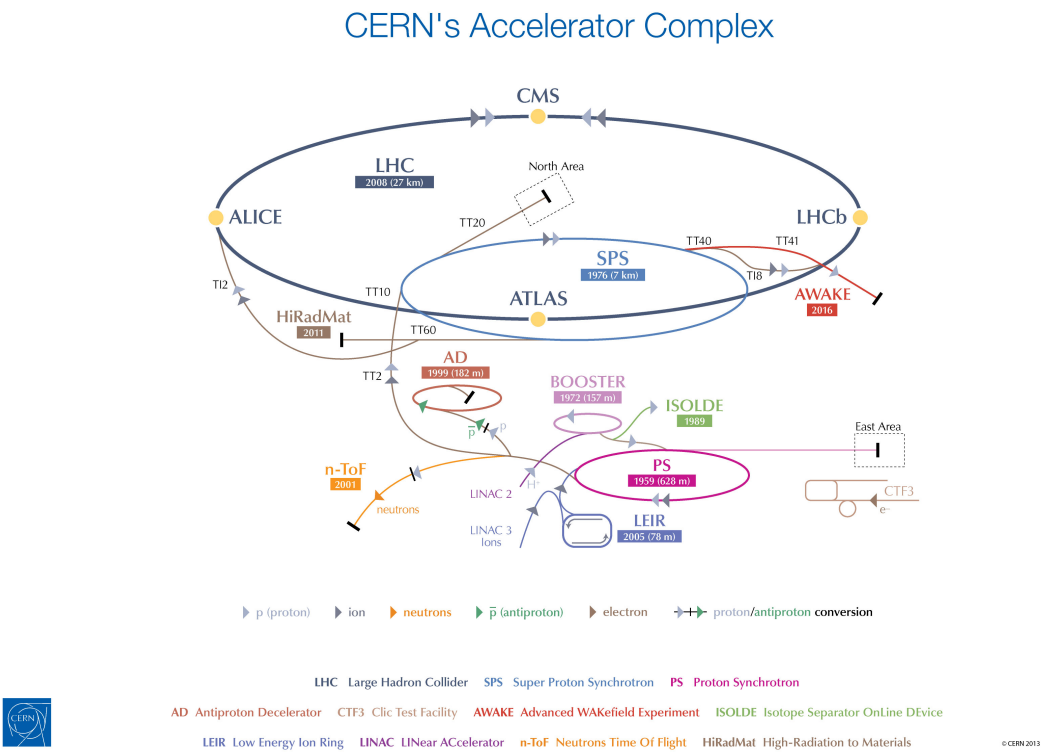

Figure 2.2: Schematic of the proton accelerator stages from [49].

Multiple bunch trains (up to 288) can be run and their collision occurs at the four IPs. The design bunch distance is 25 ns and a maximum of 2808 bunches per beam can circulate. Each bunch is composed of 1.15×10^{11} protons. The LHC can provide beam intensities corresponding to a instantaneous luminosity, $\mathcal{L}$, of $10^{34}\,\mathrm{cm}^{-2}\mathrm{s}^{-1}$. This luminosity, concerning a Gaussian transverse particle distribution, is given by the formula:

$$\mathcal{L} = \frac{N_1 N_2 f_{\mathrm{rev}} n_{\mathrm{b}}}{2\pi\sqrt{\sigma_{1x}^2 + \sigma_{2x}^2}\sqrt{\sigma_{1y}^2 + \sigma_{2y}^2}} \cdot F \cdot W \tag{2.1}$$

where N_1 and N_2 are the number of particles in the n_{b} colliding bunches of beam 1 and beam 2; f_{rev} is the ring revolution frequency and σ is the transverse beam size with respect to the horizontal (x) and vertical (y) plane for each of the two beams at the IP. The factors F and W are introduced to take into account the luminosity reduction due to a final crossing angle of the two beams and the transverse offset at the collision point, respectively. The peak luminosity in Run 1 has been $7 \times 10^{33}\,\mathrm{cm}^{-2}\mathrm{s}^{-1}$ for ATLAS and CMS. A lower luminosity has been provided to the specific purpose experiments, corresponding to typical values of $10^{32}\,\mathrm{cm}^{-2}\mathrm{s}^{-1}$ for LHCb and $10^{27}\,\mathrm{cm}^{-2}\mathrm{s}^{-1}$ for ALICE.

In physics analyses aiming to reconstruct and measure specific hard processes, the instantaneous luminosity is an important ingredient determining the size of the data sample. The rate of events, $\dot{N}_{\mathrm{event}}$, produced by the collisions of protons concerning

a certain process, with cross section σ_{event}, is given by:

$$\dot{N}_{\text{event}} = \sigma_{\text{event}} \times \mathcal{L}$$

The higher the instantaneous luminosity, the higher is the expected number of events per unit time. However, at higher luminosities a disadvantage has to be considered: the number of additional proton-proton interactions in the same collision of proton bunches is enhanced. These soft-interactions, characterised by low momentum transfer, are considered spurious with respect to the hard process of interest, and are referred to as *pileup*. The average number of interactions per bunch crossing, $\langle\mu\rangle$, depends on the instantaneous luminosity, $\mathcal{L}$, on the cross section of the inelastic proton-proton scattering, σ_{inel}[1], and the mean time interval between two bunch crossings, $\langle t\rangle$:

$$\langle\mu\rangle = \mathcal{L} \times \sigma_{\text{inel}} \times \langle t\rangle$$

The 2012 pileup conditions are represented by the distribution of the variable $\langle\mu\rangle$ in figure 2.3. On average the pileup activity in 2012 corresponded to values of mean

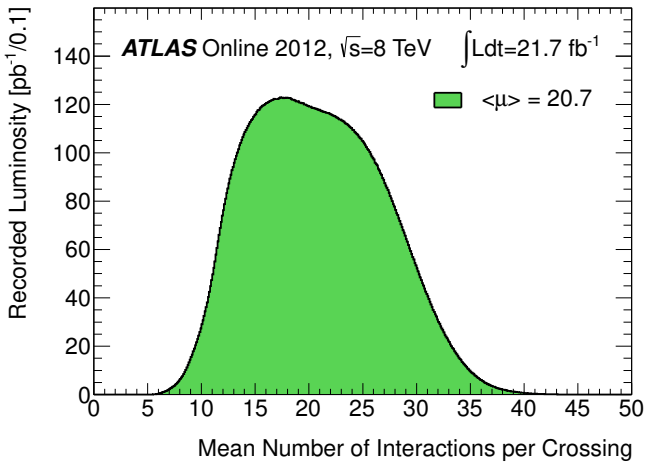

Figure 2.3: Luminosity weighted distribution of the average number of interactions per bunch crossing in 2012 from [50].

number of interactions per bunch crossing of $\langle\mu\rangle \approx 20.7$.

A distinction is made with respect to the pileup source. If additional proton-proton interactions occur in the same bunch-crossing as the one of interest, they are referred to as *in-time* pileup. Otherwise, if the additional collisions happen in bunch crossings before or after the one of interest, they are referred to as *out-time* pileup. In ATLAS, the liquid argon calorimeter sub-detector is characterised by a signal duration of about 600 ns. This time is much larger than the time spacing between two bunch crossing of 50 ns in 2012. Therefore, the detector is affected by signal residuals from proton collisions occurring in the 12 preceding bunch crossings.

[1] $\sigma_{\text{inel}} = 73$ mb for protons colliding at a centre of mass energy $\sqrt{s} = 8$ TeV.

2.2 The ATLAS detector

The ATLAS experiment has been designed to cover the full solid angle via a cylindrical structure with a central barrel and two endcaps to close the sides in order to detect particles with directions quite close to the beam pipe. It is built with a multi-layer structure of sub-detectors components with respect to the increasing radius from the interaction point, in order to provide precise measurements of different particle properties. Very close to the IP tracking detectors are placed within a strong magnetic field to measure the kinematics of charged particles coming from the IP. The tracking system is then surrounded by the electromagnetic and hadronic calorimeters to measure the energies of electrons, photons and hadrons. The farthest sub-detectors from the IP are the muon chambers for muon identification and reconstruction.

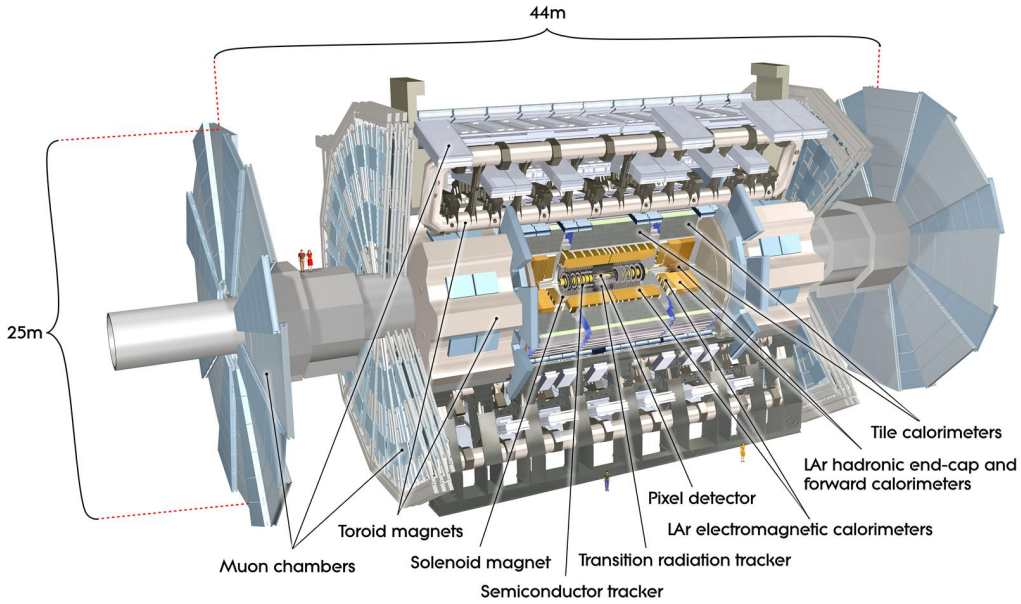

Figure 2.4: Sketch of the ATLAS detector from [51].

2.2.1 ATLAS coordinates

The coordinate system of the ATLAS detector has its origin in the nominal interaction point. The plane which is transverse to the beam direction is defined to be the x-y plane, with the positive x- and y-axis pointing in the direction of the centre of the LHC ring and upwards, respectively. The z-axis coincides with the direction of the beam. Polar coordinates are also defined: the azimuthal angle ϕ in the x-y plane starting from the x axis and the polar angle θ from the z-axis. The coordinate θ is often replaced by the pseudorapidity η [2], defined as $\eta = -\ln\tan(\theta/2)$. η is

[2]The pseudorapidity η coincides with the rapidity $y = \frac{1}{2}\ln\frac{E+p_L}{E+p_L}$, where p_L is the longitudinal particle momentum, in the limit of a massless particle.

used together with ϕ to define the direction of a vector in the detector. The angular distance ΔR between two trajectories ($i = 1, 2$), with (η_i, ϕ_i) coordinates, is defined as the distance in the $\eta - \phi$ plane:

$$\Delta R = \sqrt{\Delta\eta^2 + \Delta\phi^2} \tag{2.2}$$

$$\Delta\phi = \phi_1 - \phi_2 \tag{2.3}$$

$$\Delta\eta = \eta_1 - \eta_2. \tag{2.4}$$

The transverse momentum, $\vec{p}_{\mathrm{T}}$, is defined by the momentum components in the $x-y$ plane and its magnitude is $p_{\mathrm{T}} = \sqrt{p_x^2 + p_y^2}$.

2.2.2 Inner detector

The inner detector (ID) provides accurate track reconstruction within $|\eta| < 2.5$ in a high track multiplicity environment of about 1000 tracks and determines the positions of primary and secondary vertices. This information is of fundamental importance for electron identification, heavy-flavour and τ lepton tagging. A precise measure of the track momentum is achieved by detectors with fine granularity, immersed in an axial 2 T magnetic field generated by a solenoid of length 5.3 m and diameter of 2.5 m. Three layers of pixel detectors are placed close to the beamline, at a radial distance of about 45 mm up to 242 mm, surrounded by four layers of silicon microstrip trackers (SCT), occupying the space region from a radius of 255 mm up to 549 mm. Straw tubes of the Transition Radiation Tracker fill the remaining space within the solenoid. The pixels and SCT, divided into barrel and end cap regions, consists of concentric cylinders around the beam axis with respect to the barrel layers, while the endcap layers are formed by discs placed in the transverse plane. Pixel sensors, which are placed from the beamline, have a nominal size of 50×400 μm^2 with a total of 80.4 million readout channels.

The SCT barrel is composed of four layers of small angle stereo microstrip detector modules with pairs of single-sided sensors glued back-to-back. They measure the $R - \phi$ coordinates. The endcap region is characterised by a set of strips displaced radially and a set of stereo strips at an angle of 40 mrad. The total number of readout channels is about 6.3 million.

The TRT is composed of 4 mm diameter straw tubes parallel to the beam axis in the barrel region and perpendicular in the endcap regions. $R - \phi$ information is given by the TRT up to $|\eta| < 2.0$. The readout system is composed of approximately 351000 readout channels.

The layout of the subdetectors with the exception of the TRT barrel is shown in figure 2.5. The track reconstruction in the barrel region typically relies on 3 pixel hits, 8 SCT hits and about 30 TRT hits.

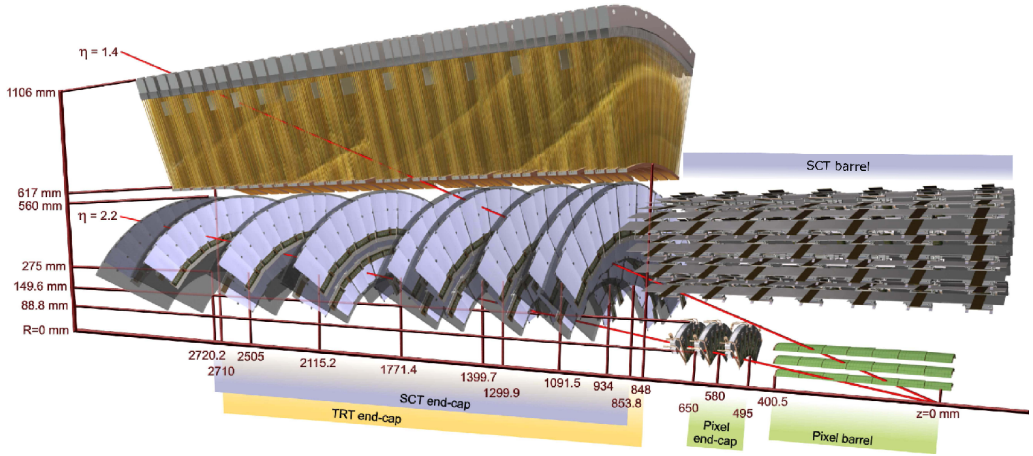

Figure 2.5: Sketch of the ATLAS inner detector crossed by two 10 GeV tracks with $\eta = 1.4$ and $\eta = 2.2$. The TRT barrel detector is omitted in the picture. Figure from [52].

2.2.3 Calorimeter

The calorimeter system in ATLAS consists of electromagnetic and hadronic sampling calorimeters covering a region of $|\eta| < 4.9$, see figure 2.6. Its transversal size corresponds to radiation lengths (X_0) greater than 22 (24) and the active calorimeter hadronic interaction lengths, λ, of 9.7 (10) in the barrel (endcaps).

The electromagnetic calorimeter (EM) is characterised by high granularity for electron and photon identification and reconstruction. It is divided into a barrel part covering the pseudorapidity range $|\eta| < 1.475$ and two endcaps within $1.375 < |\eta| < 3.2$. The first is composed of two identical half-barrels, the second is divided in two coaxial wheels. The EM calorimeter is a sampling liquid-argon (LAr) calorimeter which uses lead as an absorber and has accordion-shaped kapton electrodes. The detector part covering $|\eta| < 2.5$ is divided in three longitudinal layers (strip, middle and back layer) and is finely segmented in the lateral direction to provide accurate information on EM shower properties. The middle layer, which collects most of the high energy EM showers, has $\eta \times \phi$ size of 0.025×0.025. The strip layer is composed of strips segmented in the η-direction with coarser ϕ granularity. The back layer collects the energy deposits of the EM shower tail. In the pseudorapidity region $|\eta| < 1.8$ a thin presampler is located to correct for fluctuation of electron and photon energy losses. Between the barrel and endcap there is a transition region, within $1.37 < |\eta| < 1.52$, with a large amount of dead material in front of the first active calorimeter layer.

The hadronic calorimeter is characterised by coarse granularity which provides the reconstruction of energy deposits combined in jets. It is divided into three parts: one located in the central barrel region, $|\eta| < 0.8$; and two extended barrel regions within $0.8 < |\eta| < 1.7$. The hadronic calorimeter technology consists of three layers of scintillator-tile/steel calorimeter (Tile) azimuthally divided in 64 modules with angular aperture of $\pi/32$ rad.

Two regions within $1.5 < |\eta| < 3.2$ are instrumented by liquid-argon/copper calorimeter modules forming the hadronic endcap calorimeters. These consists of two wheels per endcap located directly behind the EM calorimeter endcap. Each wheel is formed by 32 identical wedge-shaped modules and is divided in two segments in depth.

The region $3.1 < |\eta| < 4.9$ is covered by the forward liquid-argon/copper and liquid-argon tungsten calorimeter modules providing electromagnetic and hadronic energy measurements, respectively.

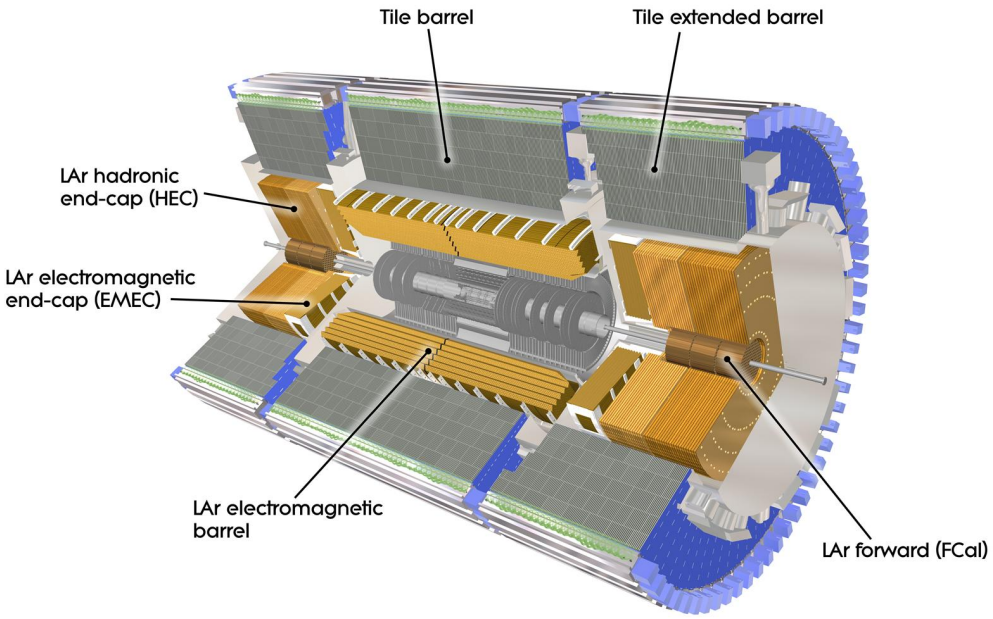

Figure 2.6: Illustration of the ATLAS calorimeter from [51].

2.2.4 Muon spectrometer

In order to identify and reconstruct muons, a muon spectrometer (MS) system has been built in the outermost part of ATLAS. Its acceptance extends up to $|\eta| = 2.7$. As shown in figure 2.7, the MS consists of a barrel composed of cylindrical layers around the beam axis, covering the region of $|\eta| < 1.05$, and two endcap sections perpendicular to the beam. The MS is immersed in a magnetic field with a bending integral of about 2.5 Tm in the barrel and up to 6 Tm in the endcaps which is generated by a system of three large superconducting air-core toroid magnets, one large barrel toroid placed within the $|\eta| < 1.4$ region and two endcap magnets placed in the $1.6 < |\eta| < 2.7$ region. The generated magnetic field is mostly orthogonal to the muon trajectories. Three doublet layers of Resistive Plate Chambers (RPC) in the $|\eta| < 1.05$ region and three triplet and doublet layers of Thin Gap Chambers in the $1.0 < |\eta| < 2.4$ region provide fast $\eta - \phi$ position measurements for trigger decisions. Three layers of Monitored Drift Tube (MDT) Chambers for $|\eta| < 2$ and

two layers of MDT together with one layer of cathode strip chambers in the $2.0 < |\eta| < 2.7$ region provide precise muon momentum reconstruction through six to eight η measurements along the muon trajectory.

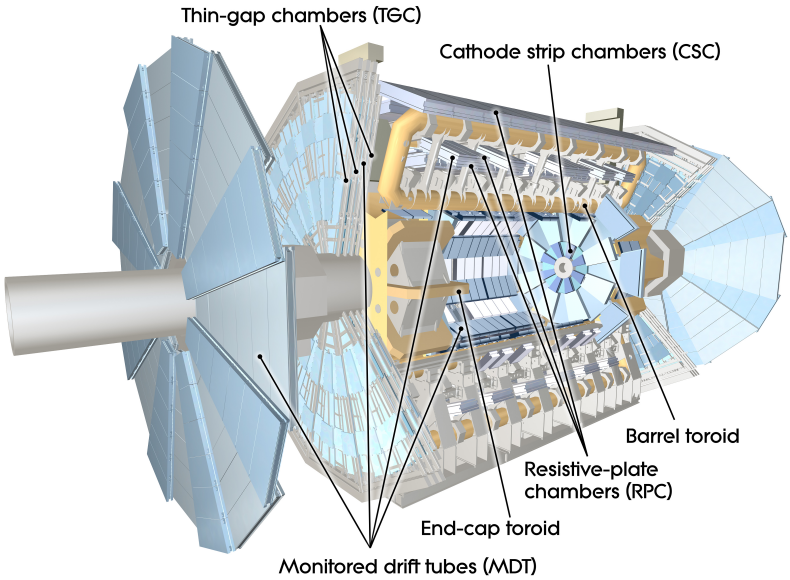

Figure 2.7: ATLAS muon sub-system schematic from [53].

2.3 Run 1 data-taking

After the first collisions with unsqueezed beams, delivered on 30 March 2010, and the first year of beam commissioning in 2010, the ATLAS Run 1 data-taking started, and it lasted until 17 December 2012. In 2011 the LHC entered its first year of high luminosity running providing proton-proton collisions at a centre of mass energy of $\sqrt{s} = 7$ TeV. The bunch spacing was reduced to 50 ns with up to 1380 bunches per beam. Afterwards the bunch intensity was increased with the corresponding ramp-up of the luminosity. A luminosity peak of $3.6 \times 10^{33}\,\mathrm{cm}^{-2}\mathrm{s}^{-1}$ was achieved at the end of 2011. The instantaneous luminosity evolution from 2010 to 2012 is shown in figure 2.8.

In 2012 the beam energy was increased to provide proton-proton collisions at $\sqrt{s} = 8$ TeV. The bunch spacing remained unchanged with respect to 2011 with about 1380 bunches per beam. The bunch intensity was raised up to 1.7×10^{11} protons per bunch, more than the design bunch intensity. However, the LHC running conditions have been very stable and a maximum luminosity of $7.7 \times 10^{33}\,\mathrm{cm}^{-2}\mathrm{s}^{-1}$ was reached.

The integrated luminosities delivered to ATLAS is shown in figure 2.9 for the years 2011 and 2012. The delivered luminosity, consisting of collisions from the start of stable beams until the request of LHC to put the ATLAS detector in a safe standby mode have been of 5.46 fb^{-1} and 22.8 fb^{-1} in the years 2011 and 2012 respectively.

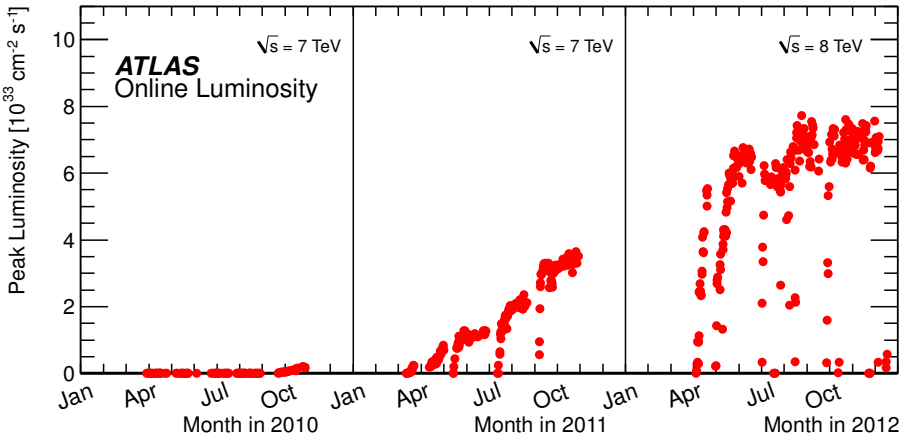

Figure 2.8: Peak instantaneous luminosity of proton-proton collisions delivered to ATLAS as a function of the time. The picture is divided with respect to the proton collision year 2010, 2011 and 2012. Figure from [50].

A small part of these luminosities has not been recorded due to data acquisition inefficiency and due to the time needed to ramp the high-voltage and to turn on the preamplifiers of the tracking system. After data reprocessing, the quality of data is verified to be good for physics. A fraction of 89.9% and 95.5% of the recorded data has been certified as good for physics in 2011 and 2012 respectively, resulting in 4.57 fb^{-1} and 20.3 fb^{-1} integrated luminosity proton-proton collision data collected at $\sqrt{s} = 7$ TeV and $\sqrt{s} = 8$ TeV.

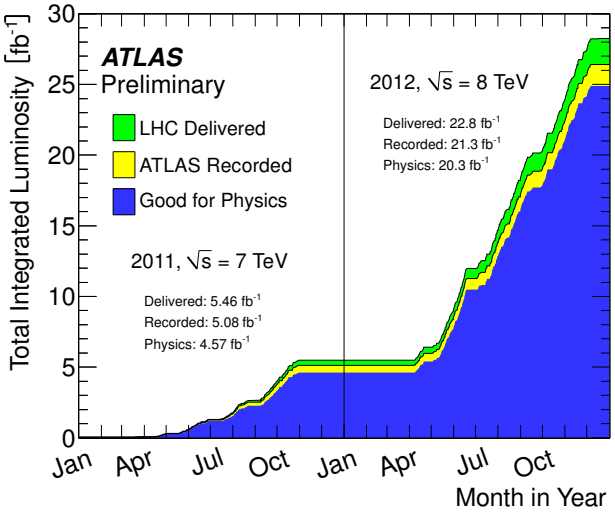

Figure 2.9: Integrated luminosity as a function of time, delivered to ATLAS in green, recorded by ATLAS in yellow and certified for physics analyses as good quality data in blue. Figure from [50].

After the first long shutdown (LS1) started on 14 February 2013 and ended at the beginning of 2015, Run 2 began with proton-proton collision data collected at $\sqrt{s} = 13$ TeV.

2.4 Trigger system

During Run 1, three distinct sequential trigger levels were used to reduce the rate of events to read out and store [54].

The hardware based Level 1 trigger (L1) exploited coarse granularity data coming from the muon spectrometer to identify high transverse-momentum muons and the calorimeter subdetectors for the selection of events with electrons, photons, jets, τ-leptons decaying hadronically and large missing transverse energy. The rate was reduced from the nominal 40 MHz bunch crossing rate to 20-75 kHz. Regions of Interest (RoIs) were defined by the L1 trigger. These are $\eta - \phi$ regions where interesting physics objects are identified. The trigger decision was made in less than 2.5 μs. Due to this constrained latency, the tracking information from the inner detectors could not be read out at this level.

The Level 2 trigger (L2) and the Event Filter (EF) were the two high level trigger (HLT) systems, which ran on large farm processors, and they selected events with a rate around 400 Hz to record on line. The L2 was the first trigger level that could access the partial information at full resolution from the Inner Detector (ID) and from the other subdetectors in the L1 selected RoIs (around 2% of the total volume). It reduced the trigger rate to few kHz with a decision time less than 100 ms. The full detector data of events selected by the L2 , was read out and processed within a few seconds by the EF, which used offline analysis procedures to reconstruct and base its event selection on physics objects like leptons, photons and jets, and global quantities such as missing transverse momentum.

Data events selected by the trigger system are subdivided in specific data *streams*. Four main physics data streams are present in ATLAS: one regarding events with reconstructed electron or photon trigger objects, one collecting events with muon trigger objects, one grouping events selected by jet, tau and missing transverse energy triggers, and events with only very soft collisions belong to the minimum bias stream. Overlap between different streams is allowed.

The configuration of the trigger system is based on a trigger menu. It defines all the triggers used to select and record data. These are grouped in different classes: triggers selecting events with at least one trigger object belong to the *single object trigger* class; triggers selecting events with two or more reconstructed objects at trigger level are grouped in the *multiple object trigger* class if the objects are of the same type, otherwise they belong to the *combined triggers* if the object type is different; triggers using the information from two or more RoIs belong to the class of *topological triggers*.

2.5 Object reconstruction

The accurate reconstruction and identification of particles and jets by the ATLAS detector is of primary importance for physics analyses and depends on the oper-

ational performance of each sub-detector and on the algorithms which transform the raw sub-detector measurements into particle objects used in physics analyses. Fully reconstructed final states consist of: collections of individual particle objects like electrons, photons, muons, and taus; bundles of hadrons, reconstructed as jets; and the missing transverse energy, measuring the transverse momentum imbalance resulting from the reconstructed objects.

The reconstruction strategy is presented regarding these objects used in the analyses reported in this thesis: tracks, electrons, muons, topological clusters combined into jets and missing transverse momentum.

2.5.1 Tracks

Charged particle tracks with transverse momentum $p_{\mathrm{T}} > 500$ MeV and $|\eta| < 2.5$ are reconstructed in the ID. The reconstruction of these tracks [55, 56] starts from the identification of clusters from raw hits. A point in the three dimensional space is directly calculated for each pixel hit, while a pair of clusters from each side of an SCT module form a single space point.

Tracks for physics analyses originate mainly from primary particles with lifetimes grater than 3×10^{-11} s either promptly produced in the proton proton interaction or from the decay of short lifetime (smaller than 3×10^{-11} s) particles. They are reconstructed with an inside-out pattern recognition algorithm, which starts from the space points close to the interaction point up to the TRT. Three space points in the silicon layers define a track seed. A road is constructed from the seeds in order to find, moving outwards, other hits associated to the track. The extension of the track candidate to the TRT is tested. From the final collection of hits a track fitter extracts the track parameters and removes overlapping tracks. These tracks are required to have $p_{\mathrm{T}} > 400$ MeV. At this step, the hits used in each reconstructed track are removed from the hits list.

Afterwards a back-tracking sequence starts form a seed in the TRT and perform an extrapolation inside to the silicon layers taking into account only the remaining hits. With the back-tracking sequence, most of the secondary particles, coming from the interaction of the primary ones, are reconstructed.

The track information is used to reconstruct primary vertices [57]. A primary vertex finding algorithm associates reconstructed tracks to the vertex candidates. A vertex fitting algorithm reconstructs the vertex position and its error matrix. Afterwards, tracks associated to the primary vertex are refitted in order to constrain them to originate from the reconstructed vertex.

2.5.2 Electrons

Electrons are reconstructed from energy deposits in the EM calorimeter, *EM clusters*, associated with a track in the inner detector [58–60]. A grid of towers is defined in the $\eta - \phi$ plane with size $\Delta\eta^{\mathrm{tower}} \times \Delta\phi^{\mathrm{tower}} = 0.025 \times 0.025$ in order to characterise the

event energy distribution. This size corresponds to the EM middle layer granularity. The energy associated to each tower is calculated by summing the energy of the cells belonging to the tower in all longitudinal layers. If a cell corresponds to more than one tower, its energy is uniformly distributed among the associated towers. A sliding-window algorithm [61] searches for seed clusters with a minimum energy of 2.5 GeV within a window of 3×5 towers in the $\eta - \phi$ space. Loose shower shape requirements are applied to select those seed clusters to be matched to tracks. A candidate electron track is reconstructed via pattern recognition [62] and via a track fit using the ATLAS global χ^2 track fitter [63]. If the standard pion hypothesis used in track reconstruction fails, the electron hypothesis is employed. The track is matched to the EM cluster if it points towards it (approximately $\Delta\eta < 0.05$ and $\Delta\phi < 0.05 - 0.2$ between the track and the cluster). The parameters of the electron-track candidate are re-estimated with an electron track fitter, the Gaussian Sum Filter algorithm [64]. If more than one track is associated to the electron, the discrimination criteria for the optimal track choice are at first based on the number of hits in the Pixel detector and then on the angular distance between the track and the EM cluster.

Each track-cluster combination is considered an electron candidate, whose energy and position is readjusted to take into account contribution coming from other cells. The cluster energy is calibrated to weight the contribution from each of the three EM layer. Electron candidate energy in data is corrected with factors derived by in situ measurements in $Z \to ee$ events, while it is smeared in simulated events. The final candidate four-momentum is defined by the energy of the cluster, by the η and ϕ of the track.

Longitudinal and transverse shapes of the electromagnetic showers in the calorimeters together with track quality requirements and particle identification using the TRT are used in order to discriminate electrons from other particles, producing hadronic jets, and to reject electrons from photon conversion or from semileptonic heavy flavour decays.

In order to be selected as signal electrons in the ℓ+jets analysis of chapter 4, reconstructed electrons are required to be in a region of $|\eta| < 2.47$ and outside of the calorimeter transition regions $1.37 < |\eta| < 1.52$ between the calorimeter barrel and the endcap. Only reconstructed electrons with transverse energy $E_{\mathrm{T}} > 25$ GeV are taken into account, where E_{T} is calculated from the energy of the cluster E_{cluster} and the direction of the associated track η_{track}: $E_{\mathrm{T}} = E_{\mathrm{cluster}}/\cosh\eta_{\mathrm{track}}$. Their longitudinal impact parameter to the primary vertex should be less than 2 mm to match the electron to the collision vertex. An $\eta - \phi$ cone is defined around the direction of the electron track. Its size shrinks for higher electron E_{T}, as $\Delta R = 10\ \mathrm{GeV}/E_{\mathrm{T}}$. If the sum of the track p_{T} within this cone is less than 5% of the transverse energy of the reconstructed electron, the reconstructed electron is considered isolated.

Selection criteria which are looser in the the direct stop search than the ℓ+jets analysis are used for electron reconstruction. The transverse energy of the electron

candidates must exceed 10 GeV and requirements only on the hadronic leakage and on the shower shape variables are applied, corresponding to the "loose" selection described in [58, 60].

2.5.3 Muons

Reconstructed muons are categorised, depending on the available information from the ID, the MS and the calorimeter [65].

The categories of muons reconstructed from at most a pair of sub-detectors are: *stand-alone* muons, reconstructed only in the MS; *segment-tagged* muons or *calorimeter-tagged* muons, defined by a track in the ID identified as a muon which is associated with at least a track segment in the MDT or CSC chambers (segment-tagged) or with energy deposits compatible with a minimum ionising particle for the second type (calorimeter-tagged).

The main type with the highest muon purity consists of *combined* muons. An inner detector track is combined with one reconstructed in the muon spectrometer. Two different reconstruction strategies have been employed to reconstruct combined muons. Regarding the first one, the STACO algorithm is employed to perform a statistical combination of the parameters and covariance matrices of the two tracks. The resulting full track parameters define the muon object. Concerning the second strategy, *muid*, a global refit using hits from both the subdetectors is performed in order to obtain a muon candidate.

Kinematic requirements of the "muid" combined muon in the ℓ+jets analysis are: $|\eta| < 2.5$ and $p_{\mathrm{T}} > 25$ GeV. The compatibility of the muon originating from the primary vertex is defined by requiring that the longitudinal impact parameter related to the collision vertex is less than 2 mm, and the significance of the transverse impact parameter $d_0/\sigma_{d_0} < 3$. An isolation criterion very similar to the electron one is applied: the muon isolation cone size shrinks as function of p_{T}^{μ}, $\Delta R = 10\ \mathrm{GeV}/p_{\mathrm{T}}^{\mu}$, and the sum of the track p_{T} within this cone is less than 5% of the transverse energy of the reconstructed muon.

In the direct stop search, STACO combined and segment-tagged muons are selected as signal muons if they have a momentum greater than 10 GeV and pseudo-rapidity $|\eta| < 2.4$.

2.5.4 Topological clusters

The reconstruction of isolated hadrons, jets and hadronically decaying τ-leptons is performed via the association of topologically connected calorimeter cell signals, referred to as *topo-clusters* [66]. The strategy of the clustering algorithm aims to extract the significant signal from a background originating from electronic noise and other spurious fluctuations due to pileup. The reduction of the background contribution is possible thanks to the high calorimeter granularity, both in the fine lateral read-out segmentation and the subdivided longitudinal sampling layers which

allows for particle energy-flow patterns to be resolved. The signal reconstruction consists in the identification of three-dimensional confined energy structures from particle showers in the active calorimeter material.

The reconstruction of topo-clusters from calorimeter cells proceeds according to a spatial signal-significant criterion, which follows the pattern of particle showers. Each cell measurement is characterised by a signal significance defined as the ratio between the absolute signal value and the average expected noise. To a seed cell with high signal significance (greater than 4), topologically connected cells are associated if they satisfy the requirement of a signal significance greater than 2. Finally the direct neighbours with positive signal significance are added and the collection of the selected cells defines a proto-cluster. This procedure often leads to the formation of large proto-clusters. They cannot provide a good energy flow observation: they merge together cells with large signal significance and several local signal maxima surrounded by an envelope of cells with small signal significance. Proto-clusters with two or more local maxima are split in the three spatial dimensions by means of a cluster splitting algorithm, and topo-clusters are the results of this procedure.

Each topo-cluster can originate from the total or the fractional energy deposition of a single particle or the combined energy deposition of more particles. In fact hadronic showers subjected to large intrinsic fluctuations are affected by large variations in their shapes and compactness, contrary to compact and dense electromagnetic showers.

The energy scale of the topo-clusters so far considered is electromagnetic (EM scale). This scale is suited for the correct reconstruction of energy deposits from electrons and photons but does not include compensation for hadron signal loss. A *local hadronic calibration*, also referred to as local hadronic cell weighting (LCW), is applied to provide calorimeter clusters with well-estimated energy for physics object reconstruction. Properties of the topo-clusters can be used to extract information on the shower generating the cluster. The calibration scheme, derived from single pion (π^0 and $\pi^{\pm}$) simulations, takes into account these properties to identify the probability of the shower to be electromagnetic or hadronic and consequently to correct for effects of the non-compensating calorimeter response to hadrons, signal losses due to inactive material or to the intrinsic noise suppression of the clustering procedure.

2.5.5 Jets

After the production of quarks and gluons, their hadronization process occurs resulting in a collimated spray of hadrons, called *jet*. These quarks and gluons could directly come from the parton interaction, or from the decay of a heavy particle. Jet algorithms define a criterion to combine objects into different groups, with each group being a jet, and to evaluate the momentum of the original parton by combining the momenta of the associated final state objects into a jet. An algorithm is

well-defined if it can be described by partonic calculations, and if it can be applied on simulated particles, clusters or tracks, generically referred to as *constituents*, resulting in a common representation of all the jets in each event. If the constituents are generated particles, the clustered jets are called *particle jets* or *truth jets*; if either calorimeter clusters or tracks are combined by the algorithm, the resulting jets are called *calorimeter jets* and *track jets*, respectively. Among the jet algorithm properties infrared and collinear safety are the most important. These properties consist in the invariance of the final set of hard jets in an event under the addition of soft radiation or under the collinear splitting of an object. This invariance is needed in order not to be sensitive to the non-perturbative effects of QCD and to be compatible with the finite resolution and non-zero momentum thresholds of experimental measurements.

A specific category of algorithms is used at the LHC: the *sequential recombination* algorithms. They combine the four-momentum of the constituents into protojets in several sequential steps until the final jets are formed. The three most common recombination algorithms, called k_t [67–69], anti-k_t [70] and Cambridge Aachen (C/A) [71, 72] differ in the order, in which the constituents are combined. A measure d_{ij} defines which pair of objects i and j has to be merged. i and j are either constituents or in later stages of the algorithm protojets. The algorithm starts with a list of constituents; those having the lowest d_{ij} distance among all the possible pair combination are tested for merging: if d_{ij} is less than an upper value d_{iB}, than the (i, j) object pair is merged[3] into a protojet, and the (i, j) pair is replaced in the list of objects by the protojet; otherwise if $d_{ij} > d_{iB}$, i is identified as a jet and removed from the list of objects. The algorithm is recursively applied until only jets are left. The definitions of d_{ij} and d_{iB} are:

$$d_{ij} = \frac{\Delta R_{ij}}{R} \min({p_{\mathrm{T},i}}^a, {p_{\mathrm{T},j}}^a)$$
$$d_{iB} = {p_{\mathrm{T},i}}^a$$

where R is called distance parameter, a is 1 for k_t, $a = -1$ for anti-k_t and $a = 0$ for C/A. The distance parameter R represents the minimum angular distance between a jet and any other remaining object in the list not belonging to the jet. Since it can occur that very soft jets result from the clustering, if they are far away from other objects, a minimum transverse momentum is required on the final jets to ensure the jets to be theoretically well defined.

The anti-k_t jets are defined by the highest p_{T} constituents and are characterised by circular shapes. The k_t and C/A algorithms cluster the hardest and most separated objects last, respectively; thus, they provide useful information on the order in which pairs of objects are clustered, also referred to as *clustering history*, and on their jet substructures.

[3]The result of the i, j merging is the four-momentum sum of the two objects.

A further algorithm distinction is made: the description so far reported corresponds to the *inclusive* implementation of the recombination algorithms. A different approach, called *exclusive* clustering, can be employed if a fixed number of jets, N, parameter of the algorithm, is needed in the final state. The algorithm proceeds as for the inclusive algorithm, but the merging procedure does not stop when all the final objects have $d_{ij} > d_{iB}$, but when N protojets are left in the list of objects. These N protojets are the exclusive clustered jets.

The jet algorithms are implemented in the framework of FastJet [73]. The standard ATLAS jet reconstruction proceeds via the recombination of locally calibrated calorimeter topo-clusters by means of the anti-k_t algorithm with distance parameter $R = 0.4$. The reconstructed jets are referred to as small-R jets. These are mainly suited for the reconstruction of activity produced via the fragmentation of quarks and gluons, and for the identification of b-jets.

Small-R jets are calibrated to restore the energy scale to that of jets reconstructed from simulated stable particles [74]. The calibration procedure begins with the reduction of the pileup contribution via the so called *area correction* technique [75], which was originally proposed in [76]. This technique exploits the large correlation between the pileup contributing to the jet and the size of the jet, evaluated by its area[4] in the $\eta - \phi$ plane. The assumption is made that the pileup contribution in the calorimeter can be treated as a uniform diffuse energy deposition. An estimate of the pileup activity in each event is given by the median, ρ, of the jet p_{T} density distribution, defined as the ratio of the jet p_{T} over its area. To calculate ρ and to be sensitive to soft radiation, all the reconstructed jets in the event are taken into account without any lower limit in the jet p_{T} cut. The contribution of the pileup to each jet is reduced by subtracting from the jet p_{T} a quantity given by the product of the jet area and the median p_{T} density.

After the jet is area-corrected, its energy scale (JES) response is tuned to provide the expected particle jet response. Calibration constants are derived for this purpose by the comparison of the reconstructed jet energy with the corresponding particle-level jet in multi-jet simulation as a function of the energy and the jet η. An additional correction coming from in-situ measurements is applied [77].

In the ℓ+jets analysis the final small-R jet four-momentum is required to be $p_{\mathrm{T}} > 25$ GeV and $|\eta| < 2.5$. Low-p_{T} jets which lie in a region of $|\eta| < 2.4$ are required to have 50% of the p_{T} scalar sum of tracks in the jet, if any, to come from tracks associated with the primary vertex. This parameter, called *jet vertex fraction*, allows to suppress jets originating from pileup energy deposits. Small-R jets used in the direct stop search are required to have $p_{\mathrm{T}} > 35$ GeV and $|\eta| < 2.8$.

A b-tagging algorithm is applied to the small-R jets in order to identify those jets originating from the fragmentation of a b-quark [78]. This multivariate based

[4]The area of a jet is a measure of the limited region in the $\eta-\phi$ space such that if a soft particle is in that region, it is clustered into the jet. The jet area is dimensionless and in anti-k_t jets, which are characterised by circular shape, the jet area is approximately πR^2.

algorithm exploits the information of the secondary vertex and of the track impact parameters. Only jets within the acceptance of the inner detector ($|\eta| < 2.5$) are tested by the b-tagging algorithm. The working point used for this analysis corresponds to an average efficiency of 70% of tagging b-quark jets in a simulated $t\bar{t}$ sample and to a probability of rejecting c-jet (light flavour jets) of about 20% (1%).

A second category of jets is used to reconstruct the decay products of a hadronically decaying top quark in a large and massive jet, called *large-R jet*, used as input to the HEPTopTagger algorithm. The C/A jet algorithm with distance parameter $R = 1.5$ combines locally calibrated topo-clusters into large-R jets. Similarly to small-R jets, the contribution due to pileup effects is subtracted from the large-R jet four-momentum and the remaining energy is calibrated. Only large-R jets with $p_{\mathrm{T}} > 200$ GeV and $|\eta| < 2.0$ are taken into account.

2.5.6 Missing transverse momentum

The momentum conservation in the transverse plane with respect to the beam direction leads to the statement that the sum of the vectorial transverse momenta, $\vec{p_{\mathrm{T}}}$, of all the particles in the final state has to be zero. However, neutral weakly interacting particles, like neutrinos, escape the detector undetected. The resulting transverse momentum imbalance can be measured by the negative vector sum of the transverse momenta of all the reconstructed and calibrated physics objects [79], and is called missing transverse momentum $\vec{E}_{\mathrm{T}}^{\mathrm{miss}}$:

$$\vec{E}_{\mathrm{T}}^{\mathrm{miss}} = -\sum_{i\in\{\mathrm{e},\gamma,\mu\}} \vec{p}_{\mathrm{T}}^{\,\mathrm{i}} - \sum_{j\in\{\mathrm{jets}\}} \vec{p}_{\mathrm{T}}^{\,\mathrm{j}} + \vec{E}_{\mathrm{T}}^{\mathrm{miss\ cells}}. \tag{2.5}$$

Its magnitude is often referred to as missing transverse energy $E_{\mathrm{T}}^{\mathrm{miss}} = \sqrt{(E_x^{\mathrm{miss}})^2 + (E_y^{\mathrm{miss}})^2}$. The *electron term*, $-\sum_{i\in\{\mathrm{e}\}} \vec{p}_{\mathrm{T}}^{\,\mathrm{i}}$, is given by the transverse vectorial sum of electrons reconstructed with $p_{\mathrm{T}} > 10$ GeV. The contribution of photons with $p_{\mathrm{T}} > 10$ GeV, $-\sum_{i\in\{\gamma\}} \vec{p}_{\mathrm{T}}^{\,\mathrm{i}}$ is accounted in a similar way. The total muon contribution $-\sum_{i\in\{\mu\}} \vec{p}_{\mathrm{T}}^{\,\mathrm{i}}$ is the sum of reconstructed muon momenta with $p_{\mathrm{T}} > 5$ GeV and $|\eta| < 2.7$. The contribution of muon energy deposits in the calorimeter is taken into account with parametrised estimates to avoid double counting of a fraction of their momenta. Regarding the sum of the jet momenta, $\sum_{j\in\{\mathrm{jets}\}} \vec{p}_{\mathrm{T}}^{\,\mathrm{j}}$, only calibrated jets with $p_{\mathrm{T}} > 20$ GeV are taken into account. The remaining low-p_{T} jets and cluster cells not belonging to any other previous objects contribute to the $\vec{E}_{\mathrm{T}}^{\mathrm{miss\ cells}}$ term, called *soft term*.

Sources of missing transverse momentum due to mismeasurement, referred to as fake $E_{\mathrm{T}}^{\mathrm{miss}}$, arise from the undetection of particles going through regions not covered by detecting material, the p_{T} mismeasurement, miscalibration and misidentification of physics objects.

2.6 Sample simulation

The details of the simulated samples used in this thesis are reported. These samples are used to evaluate the signal prediction and the background expectation of the ℓ+jets channel of chapter 4 and of the search for direct production of a pair of SUSY top partners in the fully hadronic channel reported in chapter 5.

The details of the Monte Carlo samples concerning the generator, the hadronization, the parton shower, the underlying event modelling and their tune, with the parton distribution functions set employed, are summarised in table 2.1.

- $t\bar{t} \to (l\nu b)(q\bar{q}'b)$: pair production of top-antitop with one top decaying hadronically and one semi-leptonically with $l = e, \mu, \tau$. Different simulated samples are taken into account in order to evaluate the expected contribution and its systematic uncertainties. The nominal signal sample is simulated with POWHEG generator[80–83] interfaced with PYTHIA [84], and it is also referred to as the POWHEG+PYTHIA sample. A discrepancy between the $\sqrt{s} = 7$ TeV POWHEG+PYTHIA sample and the data collected at $\sqrt{s} = 7$ TeV was observed in the $t\bar{t}$ differential cross section measurement [85]. This discrepancy has been corrected for by applying a sequential reweighting of the top quark's and the $t\bar{t}$ system's transverse momenta, as explained in [86]. In the study of the HEPTopTagger performance using ℓ+jets events, the sample produced with the full detector response using GEANT4 [25] is employed. A sample with a parametrised description of the calorimeter response (fast simulation framework [87]) is used for the direct stop production search, as a larger amount of simulated events is needed. In order to evaluate the $t\bar{t}$ modelling systematic uncertainties, alternative samples are used. The generator uncertainties are evaluated with a sample produced with MC@NLO [88, 89] interfaced to Herwig [90]. The evaluation of the uncertainty related to the parton shower and hadronization simulation is obtained by comparing the nominal sample with the one generated with POWHEG interfaced to Herwig and Jimmy [91]. ACERMCs [92] samples are used to evaluate the effects related to the modelling variation of the QCD initial and final state radiation (ISR and FSR). These samples are interfaced with PYTHIA with different settings of the parton shower parameters to increase and decrease the ISR and FSR, within the range allowed by data [93]. To account for the PDF uncertainties, a sample generated with POWHEG, interfaced with PYTHIA, is produced with the HERAPDF set, instead of the nominal CT10 set. The $t\bar{t}$ cross section is $\sigma_{t\bar{t}} = 253^{+13}_{-15}$ pb for a top quark mass of 172.5 GeV/c^2. It has been calculated at next-to-next-to leading order (NNLO) in the strong coupling constant α_s including resummation of next-to-next-to-leading logarithmic (NNLL) soft gluon terms [94–99] with top++2.0 [100], using the MSTW 2008 NNLO PDF set. The fully hadronic final state of the top quark pair production has the same settings as the nominal l+jets $t\bar{t}$ sample.

- Single top: the processes in the s-, Wt-, and $t-$channels are generated with POWHEG interfaced with PYTHIA. The last process was simulated in the four-flavour (4F) scheme, in which the b-quarks are dynamically produced in the hard scatter and the b-quark is not considered an active flavour in the proton. The diagram-removal scheme [101] is used to get rid of the overlap between the Wt and $t\bar{t}$ production. The approximate NNLO cross section prediction [102–104] is used to normalise the single top processes.

- W+jets and Z+jets: production of a W or a Z boson in association with jets. In the ℓ+jets channel, W+jets and Z+jets samples are generated with ALPGEN interfaced with PYTHIA. In these samples, the final state consists of a vector boson and up to five additional partons, which are included in the calculation of the matrix element. The c quarks, $c\bar{c}$ and $b\bar{b}$ pairs which are produced among all the additional partons, are considered with their masses. The W+jets simulated events are weighted in order to predict the data charge asymmetry related to the W boson production, as explained in [105, 106].

  Concerning the stop search, samples generated with SHERPA [107] are used for the W+jets and Z+jets production. Up to four additional partons, taking into account also heavy flavour jets with massive b/c quarks, are included in the leading order matrix elements. The theoretical cross section of V+jets is used to normalise the samples. It is calculated with DYNNLO [108] with the MSTW 2008 NNLO [109] PDF set. A discrepancy in the reconstructed boson transverse momentum between data and simulation has been observed [110], and events are weighted with respect to the generated vector boson transverse momentum to correct for this difference [111].

- VV: diboson production, WW, WZ, ZZ. Events are generated with SHERPA and up to three additional partons are included in the matrix element, the cross section for the sample normalisation is calculated with MCFM [112] with MSTW 2008 NLO PDFs.

- $t\bar{t}V$: associated production of a top quark pair with a vector boson $V = Z, W$. This processes is simulated using MadGraph [113] interfaced with PYTHIA with up to two additional partons and it is normalised to the NLO cross section [114, 115].

- multijet: QCD processes generated with PYTHIA.

- $\tilde{t}_1\tilde{t}_1^* \rightarrow (t\tilde{\chi}_1^0)(\bar{t}\tilde{\chi}_1^0)$: direct production of a top supersymmetric partner pair, each decaying into a top quark and a neutralino, signal of the stop search. The signal samples are produced with Herwig++[116]. The phenomenology of the SUSY particle is described via simplified models, such that the neutralino is a pure bino and the decay of the $\widetilde{t}_R$ component of the $\tilde{t}_1$ to a right-handed top quark is enhanced. The parameters of these samples are the $\tilde{t}_1$ and $\tilde{\chi}_1^0$

masses. The cross section calculated to NLO in the strong coupling constant, with the additional resummation of soft gluon emission at next next-to-leading logarithmic accuracy (NLO+NLL) [36–38], is used to normalise the signal samples.

Simulated events are weighted in order to match the pileup data distribution.

type		generator	parton shower, hadronization UE model	UE tune	PDF set
$t\bar{t}$	nominal	POWHEG-BOX r2129	PYTHIA v6.426	Perugia 2011C [117]	CT10 [118]
	generator	MC@NLO v4.01	Herwig v6.520, Jimmy v4.31	AUET2 [119]	CT10
	PS	POWHEG-BOX r2330.3	Herwig v6.520, Jimmy v4.31	AUET2	CT10
	ISR/FSR	ACERMC v3.8	varied PS param, PYTHIA	AUET2B	CTEQ6L1 [120]
	PDF	POWHEG-BOX r2330.3	PYTHIA v6.427	Perugia 2011C	HERAPDF
single top		POWHEG-BOX	PYTHIA v6.426 and v6.427	Perugia 2011C	CT10(-F4)
W+jets (ℓ+jets)		ALPGEN v2.13	PYTHIA v6.426	Perugia 2011C	CTEQL1
W/Z+jets (SUSY)		SHERPA 1.4.1	SHERPA	AUET2B	CT10
VV		SHERPA 1.4.1	SHERPA	AUET2B	CT10
$t\bar{t}V$		MadGraph 5 v1.3.33	PYTHIA 6.426	AUET2B	CTEQ6L1
multijet		PYTHIA 8	PYTHIA	AU2	CT10
$\tilde{t}_1 \to t\tilde{\chi}_1^0$ (SUSY)		Herwig++ 2.5.2	Herwig	UEEE3	CTEQ6L1

Table 2.1: Simulated samples with detailed production information. Concerning the $t\bar{t}$ process, different samples are used either to estimate the nominal expected signal contribution or to estimate a particular modelling uncertainty. Its usage is specified in the table. In parenthesis it is indicated if a sample is employed only in the stop search or in the HEPTopTagger performance analysis in the ℓ+jets channel.

2.7 Systematic uncertainties

The systematic uncertainties, concerning the HEPTopTagger performance analysis in the ℓ+jets channel and the search for direct pair production of stops, are reported in this section. These uncertainties concern: the reconstruction of the HEPTopTagger candidate affected by uncertainties on the large-R jet and subjet energy scale and resolution; the reconstruction of small-R jets with uncertainties on the energy scale and resolution, and on the efficiency of being b-tagged. Reconstructed muons and electrons are affected by uncertainties on the momentum scale, resolution, and on their identification. If events are selected by single lepton triggers, an uncertainty on the trigger efficiency has to be taken into account. Uncertainties on the theory prediction of the background are considered. The integrated luminosity of the collected data is affected by an uncertainty.

Luminosity

A 2.8% relative uncertainty on the integrated luminosity is used. It was derived in November 2012 from a preliminary calibration of the luminosity scale beam-separation scans. The procedure, described in [121], consists in combining simultaneous precision measurements of the bunch current and of the transverse size of colliding bunches to finally estimate the luminosity and its accuracy.

b-tagging efficiency, *c*-jet mistag rate, *l*-jet mistag rate

The identification of b-tagged jets helps in the reduction of background. The efficiency of tagging a b-jet and the probability of mis-tagging as b-jet a jet containing a c hadron or a light-flavour parton, also referred to as *mistag rate* have been measured [78]. A sample of $t\bar{t}$ events with one or two leptons in the final state has been used to determine the former. The latter has been measured in multijet events. A calibration of the b-tagging efficiency and mis-tag probability has been provided as data-to-simulation scale factors. These were calculated in terms of the ratio between the observed efficiency (mistag rate) in data and the efficiency (mis-tag rate) predicted by simulation. Systematic uncertainties on the scale factors have been derived.

If b-tagged jets are included in the event selection, the b-tagging associated systematic uncertainties are fully specified by the systematic uncertainties on the scale factors. Hence, the measured scale factors with the corresponding systematic uncertainties are applied as corrections in order to evaluate the nominal and the $\pm\sigma$ uncertainty MC prediction.

Lepton reconstruction efficiency

Electron and muon objects are affected by uncertainties on the reconstruction and identification. These uncertainties are determined with tag-and-probe method using $Z \to ee$ and $Z \to \mu\mu$ samples [58, 59] and [65]. The reconstruction efficiency of muons with $p_{\mathrm{T}} > 10$ GeV is corrected by means of scale factors. These scale factors depend on the muon η and ϕ and are mainly close to one with few $\eta - \phi$ regions with 0.05 maximum deviation from one. The same approach is applied to correct the reconstruction and identification efficiency of electrons with transverse energy $E_{\mathrm{T}} > 7$ GeV. The scale factors, measured differentially in (E_{T}, η) bins of the electron object, are close to unity within 2%.

The muon and electron momentum scale and resolution have been measured and corrections have been derived together with uncertainties to be used in physics analyses. These uncertainties have been found negligible in the analyses of this thesis.

If a single lepton trigger is employed to select a ℓ+jets sample, scale factors are applied to correct discrepancies between the data and MC trigger efficiency.

Large-R and subjet energy scale

The HEPTopTagger algorithm identifies and reconstructs hadronically decaying top quarks, by looking into the substructure of a large-R jet. In particular, it extracts the large-R jet hard structures by filtering and recombining the large-R constituents into subjets. Both the large-R jet and the subjets are calibrated, as described in section 3.2.

The scale of the large-R jet energy is affected by an uncertainty which depends on the degree of accuracy of the jet p_{T} modelling. This uncertainty is derived using the *R-track double-ratio* method [122]. The quality of the calorimeter response simulation can be estimated by comparing the p_{T} of each calorimeter jet with the p_{T} of the associate track-jet. In fact, track jets provide a reliable momentum reference for each jet. The comparison between the momenta of the two kinds of jets is expressed by means of the r_{track} variable, defined as the ratio between the transverse momenta of the calibrated calorimeter jet, $p_{\mathrm{T}}^{\mathrm{jet}}$, and its associated track jet $p_{\mathrm{T}}^{\text{track jet}}$:

$$r_{\mathrm{track}} = \frac{p_{\mathrm{T}}^{\text{track jet}}}{p_{\mathrm{T}}^{\mathrm{jet}}}.$$

The data and MC distribution of r_{track} in several regions of large-R jet p_{T} are compared by evaluating the discrepancy between the average values, $\langle r_{\mathrm{track}}^{\mathrm{data}} \rangle$ in data and $\langle r_{\mathrm{track}}^{\mathrm{MC}} \rangle$ in simulation. In fact, the mean values of these distributions are supposed to be very similar in data and MC, if the detector response is well modelled. The data-MC agreement is measured through the double ratio:

$$R_{\mathrm{track}} = \frac{\langle r_{\mathrm{track}}^{\mathrm{data}} \rangle}{\langle r_{\mathrm{track}}^{\mathrm{MC}} \rangle}$$

Its deviation from unity, in addition to the propagation of the uncertainties on the tracking efficiency and the choice of the MC generator and PS, gives the measure of the relative calorimeter large-R jet p_{T} uncertainty. The relative p_{T} uncertainty is measured to vary from 2% for $p_{\mathrm{T}} < 400$ GeV up to 5% for $p_{\mathrm{T}} > 700$ GeV [123].

The uncertainty on the subjet momentum is estimated by means of an in situ technique which exploits the top mass peak, as described in section 4.2. The uncertainty on the subjet momentum varies between 4-10% for subjets with $p_{\mathrm{T}} < 50$ GeV and between 1-3% for subjets with $p_{\mathrm{T}} > 50$ GeV.

The uncertainties on the large-R jet and the subjet energy scales are assumed to be uncorrelated. The impact of each uncertainty in the analysis is evaluated by varying "up" and "down" the energy scale of the subjets and large-R jets independently and quantifying the effect of this variation on signal and background distributions or on the expected event yield.

Large-R jet and subjet energy resolution

In addition to the energy scale uncertainty, the energy of the large-R jet and of the subjet is affected by an uncertainty on the resolution.

The subjet energy resolution uncertainty was derived in a di-jet sample, studying the p_{T} balance of several C/A jet collections corresponding to different values of the distance parameter ($R = 0.2, 0.25, 0.3, \ldots, 0.6, 1.5$) [124]. The simulated calorimeter response is found to have a slightly better resolution than the observation. The difference between the measured resolution in data and MC is applied as an uncertainty on the jet resolution. Each jet is thus smeared with a Gaussian with mean at one and width given by the resolution calculated from the data-MC difference. The impact of the jet energy resolution uncertainty is evaluated by comparing the distribution obtained from smeared jets to the nominal distribution.

Small-R energy scale and resolution

The uncertainty on the energy scale of small-R jets reconstructed with the anti-k_t algorithm and distance parameter $R = 0.4$ is determined using a combination of techniques [74, 77, 125]. In situ techniques measure the uncertainty on the small-R jet p_{T} by analysing events where the jet p_{T} is balanced by a well-measured momentum of a reference object, like a photon or a Z boson. Other techniques measure the energy scale uncertainty using single isolated hadron calorimeter response. The measured uncertainty is 3% (4%) for jets with $p_{\mathrm{T}} < 30$ GeV and $|\eta| < 1.5$ ($|\eta| > 1.5$) and about 1% (3%) for higher p_{T} jets with $|\eta| < 1.5$ ($|\eta| > 1.5$).

As for the large-R jet and subjet energy resolution, the small-R jet energy resolution uncertainty is measured using the jet response asymmetry in dijet events [74]. The impact of the small-R jet energy resolution on the results of this thesis was found to be negligible.

Uncertainties on the theory prediction

The $t\bar{t}$ uncertainties on the theory prediction are divided in modelling uncertainties and uncertainties on the cross section, on the factorisation and renormalisation scale.

The modelling uncertainties are evaluated by comparing a pair of samples whose simulation process and tools are the same apart from the modelling part undergoing test. The uncertainty due to the choice of the parton shower is evaluated by comparing the nominal $t\bar{t}$ sample, generated with POWHEG interfaced to PYTHIA, to the sample generated with POWHEG but interfaced with Herwig. The difference between the predictions of the two simulated samples is symmetrised to obtain an "up" and "down" uncertainty evaluation:

$$\Delta n_{\mathrm{PS}}^{\mathrm{up(down)}} = {}^{+}_{(-)}(n_{\mathrm{Herwig}} - n_{\mathrm{PYTHIA}}),$$

where $\Delta n_{\mathrm{PS}}^{\mathrm{up(down)}}$ is the difference corresponding to the "up" ("down") uncertainty on the nominal number of counts, n_{PYTHIA}, with respect to those obtained from the sample with the Herwig PS, n_{Herwig}. This difference is used to estimate the impact of the parton shower uncertainty on the analysis results.

In a similar way, the uncertainties on the generator and on the PDF are accounted for, by comparing distributions of the MC@NLO sample with respect to the sample

generated with POWHEG interfaced to Herwig, and of the sample simulated with HERAPDF set with respect to the nominal sample.

The uncertainties on the modelling of initial and final state radiation are evaluated by comparing the ACERMC samples generated with different settings of the parton shower parameters to increase and decrease the ISR and FSR. These samples correspond to the "up" and "down" variation of the ISR/FSR modelling uncertainty. The relative ISR/FSR uncertainty is given by the difference between the number of events with more, n_{more}, and less ISR/FSR, n_{less}, divided by their sum. Thus the absolute uncertainty on the nominal event prediction, n_{nominal}, is:

$$\Delta n_{\text{ISR/FSR}}^{\text{up(down)}} = {}^{+}_{(-)} n_{\text{nominal}} \frac{n_{\text{more}} - n_{\text{less}}}{n_{\text{more}} + n_{\text{less}}}$$

The PDF and α_S uncertainties on the $t\bar{t}$ cross section, $\sigma_{t\bar{t}} = 253^{+13}_{-15}$ pb, were calculated using the PDF4LHC prescription [126] with the MSTW2008 68% CL NNLO [109, 127], CT10 NNLO [118, 128] and NNPDF2.3 5f FFN [129] PDF sets, added in quadrature to the scale uncertainty. An additional uncertainty of about 7 pb is added in quadrature to take into account ± 1 GeV top quark mass variations. The total realtive normalisation uncertainty is about $^{+6\%}_{-7\%}$.

The impact of the factorisation and renormalization scale on the phase space is evaluated by comparing dedicated $t\bar{t}$ samples where the scales are varied independently by a factor of 2 and 0.5. Only the renormalization scale has a non negligible impact in the phase space distribution.

Systematic uncertainties due to the modelling and normalisation of the V+jets background are evaluated comparing the prediction of the samples generated with SHERPA with the samples generated with ALPGEN.

The relative uncertainty on the single top production cross section is about 4% in the s- and t- channel [102, 104], and 7% in the Wt-channel [103].

The relative diboson cross section uncertainty, quadratic sum of scale and PDF+α_s, is estimated to be around 7% [130].

The dominant uncertainty on the $t\bar{t}+V$ background is on the NLO cross section and amounts to 22% relative uncertainty [114, 131].

The uncertainty on the direct stop production cross section is determined from an envelope of cross section predictions with different PDF sets, factorisation and renormalisation scale [35].

Chapter 3

HEPTopTagger

The last missing quark of the Standard Model (SM), the top quark, has been discovered at Tevatron after years of search in 1995.

Its extremely large mass and small lifetime makes it different from the other quarks: the top quark decays before hadronization and its coupling with the Higgs field is very close to unity.

The top quark plays a special role in searches for physics beyond the Standard Model. Many new physics models predict new heavy particles to couple to third generation quarks. As higher and higher mass scales are proven, top quarks in the final state are expected with larger transverse momentum, referred to as *boosted* tops.

The full-hadronic decay mode of the top is defined by the presence of three quarks in the final state and it is characterised by a *three-prong* signature. After their hadronization, the produced spray of particles are recollected into jets. If the transverse momentum of the original top is small, *resolved* techniques can be employed to reconstruct the top quark. These consist in assigning a small-R jet to each top decay product, and in reconstructing the top kinematic from the three reconstructed small-R jets. As soon as the top quark transverse momentum exceeds its rest mass these classical techniques are not adequate any more. The more boosted the top quark is, the more collimated its final decay products become.

Nevertheless, information about the top quark three-prong decay is not completely lost, if a large-R jet, which contains the final decay products, is reconstructed. In fact, very useful information can be extracted by looking into the momentum and spatial distribution of the large-R jet constituents. Over the last few years, many *top tagging* techniques have been developed to study how this substructure information can be used to discriminate large-R jets originating from top quark decays with respect to those from hard light quarks and gluons, also referred to as *QCD jets*.

Not only can a simple identification of the origin of the jet be extracted looking into substructure, but also the kinematic information of the original particle can be reconstructed. The HEPTopTagger algorithm [3, 4] is one of the most complete top tagging techniques for the identification and reconstruction of boosted hadronically

decaying top quarks.

This chapter reports the explanation of the HEPTopTagger algorithm. Thus, only hadronically decaying top quarks are taken into account: $t \to bq\bar{q}'$.

3.1 The HEPTopTagger algorithm

The idea behind the HEPTopTagger algorithm is to identify the hard substructures of a massive large-R jet. The compatibility of these hard subjets with the top quark decay products is then verified.

If top quarks are produced with moderate or high transverse momentum, i.e. $p_{\mathrm{T}} > 200$ GeV, all the directions of the top decay products lie in a cone of decreasing aperture with the rise in top quark p_{T}. This trend can be observed in figure 3.1(a) and (b). For top quarks with p_{T} in the range 200-300 GeV the maximum angular distance, ΔR, among the three top decay products is on average around 1.5, while the minimum angular distance is smaller than 1. The decrease in the minimum angular separation, which drops below 0.5 for top quarks with $p_{\mathrm{T}} > 400$ GeV, denotes the difficulty in disentangling each decay product by means of separated standard jets with $R = 0.4$, as done by resolved techniques, and the need of substructure techniques for this high p_{T} regime.

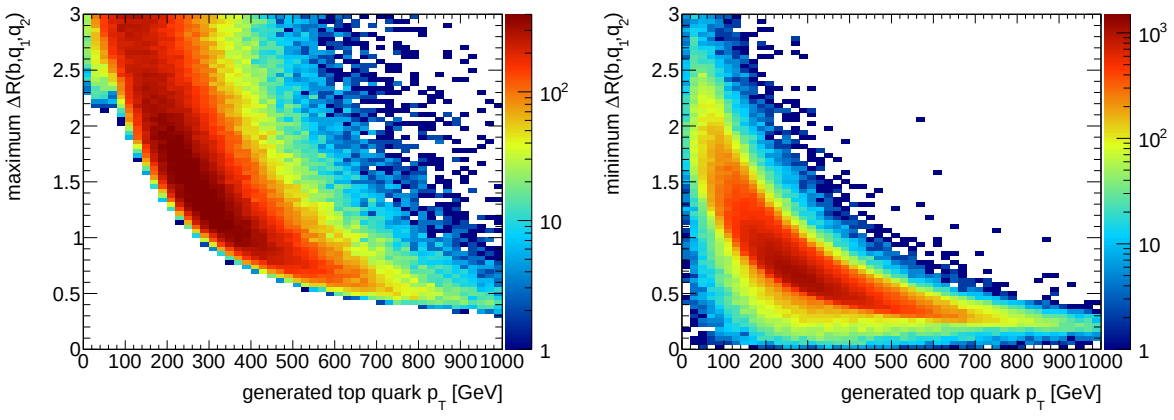

(a) (b)

Figure 3.1: Maximum (a) and minimum (b) angular distance ΔR between the three quark decay products of top quarks in a SUSY signal sample with two top quarks in the final state produced by the decay of two SUSY top partners.

The distribution of the maximum angular distance among the three quarks in the low p_{T} region is characterised by long tails towards large ΔR values, as shown in figure 3.1(a): a non-negligible fraction of low p_{T} top quarks will have one of the decay products outside a large-R jet, with distance parameter $R \sim 1.5$.

According to a specific top p_{T} range of interest, a particular jet distance parameter R can be chosen, such that a large fraction of top quarks have their three decay products reconstructed in the same jet. At the same time R cannot take an arbitrary

large value, otherwise the jet would be affected by huge contribution of pileup or other processes not directly related to the top quark decay. In order to be sensitive to the moderately boosted regime ($p_{\mathrm{T}} > 200$ GeV), the distance parameter of the large-R jet is chosen to be $R = 1.5$.

Large $R = 1.5$ jets reconstructed with the C/A algorithm are used as input to the HEPTopTagger algorithm. The C/A recombination algorithm, explained in section 2.5.5, clusters the protojets with larger angular distance last and allows the HEPTopTagger algorithm to have access to the clustering history. The most distant protojets are identified in each backward step of the recombination history. The constituents of these large-R jets at the experimental level are locally calibrated topological clusters.

The HEPTopTagger algorithm combines different procedures to identify and reconstruct top quarks starting from the large-R jet constituents and clustering history. These are the mass drop criterion [132], the filtering technique, and kinematic-based requirements. The HEPTopTagger has internal parameters that can be optimised for the specific analysis. The values of the parameters, used in this thesis, are listed in table 3.1, and their definition is given in the following.

parameter	value
m_{cut}	50 GeV
$R_{\mathrm{filt}}^{\mathrm{max}}$	0.25
N_{filt}	5
f_{W}	15%

Table 3.1: The HEPTopTagger parameter settings used in this thesis.

Mass drop criterion

Declustering backwards through the clustering history of the large-R jet, the two protojets which were clustered last are obtained and the mass balance of these is verified. If the one with the leading mass carries more than 80% of the initial parent jet mass the other is discarded. The procedure continues recursively until the remaining protojets have mass smaller than a parameter m_{cut}.

For example in figure 3.2(a), a large-R jet associated to a simulated hadronically decaying top quark undergoes the procedure of the mass drop criterion. The constituents of the four final protojets, labelled as **a**, **b**, **c**, and **d**, which survive the $m_{\mathrm{cut}} > 50$ GeV requirement, are shown in the $\eta - \phi$ plane as squares with size proportional to their energy.

Filtering procedure

The following step takes place on every combination of three protojets, called triplet, among the ones surviving the mass drop procedure. The triplet constituents (topological clusters) are recombined with the C/A algorithm using a distance parameter

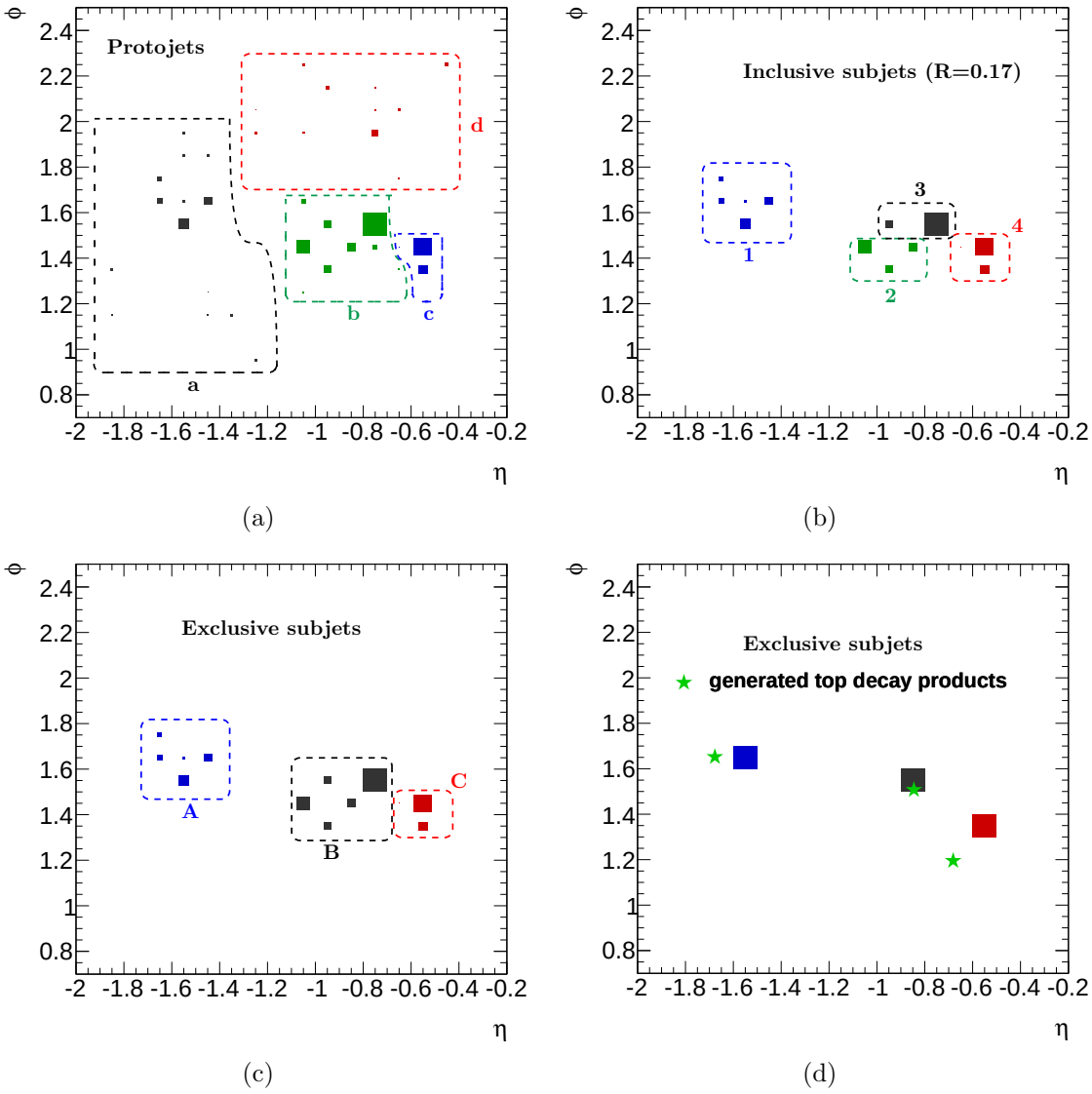

Figure 3.2: $\eta - \phi$ distribution of clusters of a tagged large-R jet originating from a hadronically decaying top quark, corresponding to different steps of the HEPTopTagger algorithm. The size of the squares is proportional to the energy of the clusters. After the mass drop criterion, the constituents of the resulting protojets are shown in different colours (a). The clusters associated to the inclusive and exclusive subjets are shown in different colours in figure (b) and (c), respectively. The $\eta - \phi$ coordinates of the final exclusive subjets and of the three decay products of the generated top quark are displayed in figure (d).

R_{filt} which varies for each triplet and amounts to half of the minimum separation among the three protojets but does not exceed the $R_{\text{filt}}^{\text{max}}$ parameter value. At most N_{filt} resulting hardest subjets, called *inclusive subjets* are kept and their invariant mass is determined. It corresponds to the reconstructed top mass associated to the triplet. After this procedure the pileup and underlying event contribution is highly reduced. Thus, the invariant mass of the resulting top candidate should not be sensitive to this soft contribution. The triplet and its inclusive subjets, whose associated invariant mass is closest to the mass of the top quark, is chosen as final triplet.

In the example of figure 3.2, the constituents of the triplet, formed by **a**, **b** and **c** protojets of figure (a), are filtered with R_{filt} =0.17. In figure 3.2(b), the resulting four inclusive subjets, labelled as **1**, **2**, **3**, and **4**, are used to determine the mass of the reconstructed top. In this example, the **a**, **b**, **c** triplet is the one that gives the reconstructed mass closest to the top mass.

Compatibility with a top quark decay

The constituents of the final inclusive subjets are recombined into exactly three subjets, called *exclusive subjets*, using the exclusive C/A algorithm.

The inclusive subjet constituents are reclustered into the **A**, **B**, and **C** exclusive subjets (figure 3.2(c)). In figure 3.2(d), the reconstructed exclusive subjets are compared to the three generated quarks of the top decay in the $\eta - \phi$ coordinates.

The exclusive subjets, which should correspond to the three jets originated from the three top quark decay products, are used to test the compatibility with the 3-prong pattern of the top decay, by applying kinematic requirements. One of the constraint regards the compatibility of two subjets with a W decaying into two quarks. At least one of the three exclusive subjet pairs must have the invariant mass in the W mass range, 80.4 GeV $\cdot$ $(1 \pm f_{\text{W}})$. The invariant mass, m_{123}, is given by the sum of the three exclusive subjets four-momentum, p_1, p_2 and p_3, in decreasing order of the transverse momentum:

$$m_{\text{top}}^2 = m_{123}^2 = (p_1 + p_2 + p_3)^2 \tag{3.1}$$

$$= m_{12}^2 + m_{13}^2 + m_{23}^2 \tag{3.2}$$

where m_{12} is the invariant mass of the leading and subleading exclusive subjet four-vector sum, m_{13} of the leading and lowest p_{T} exclusive subjets and m_{23} of the sub-leading and lowest p_{T} exclusive subjets. This equality, in the limit of negligible invariant masses of the subjets, can be described as a sphere with $m_{123} = m_{\text{top}}$ radius. Every point on this sphere corresponds to a specific top quark kinematic and it is univocally defined by two parameters, which could be for example the $\cos\theta$, with θ polar angle, and the azimuthal angle ϕ:

$$\theta = \arctan\left(\frac{m_{13}}{m_{12}}\right) \quad \text{and} \quad \phi = \frac{m_{12}}{m_{123}}$$

In this coordinate system, the requirement that at least one of the subjet pair has to be compatible with a W decay causes the signal large-R jets, originating

from hadronically decaying top quarks, to gather within an "A"-shaped region, figure 3.3(a), while QCD jets lie in the low $\arctan(m_{13}/m_{12})$ or low m_{23}/m_{123} phase space, figure 3.3(b). The additional requirements of $0.2 < \arctan(m_{13}/m_{12}) < 1.3$, of $m_{23}/m_{123} > 0.35$ and that the reconstructed mass is close to m_{top}, reduces significantly the multijet background. The thick line contours of figure 3.3 denote the candidates which are tagged by the HEPTopTagger.

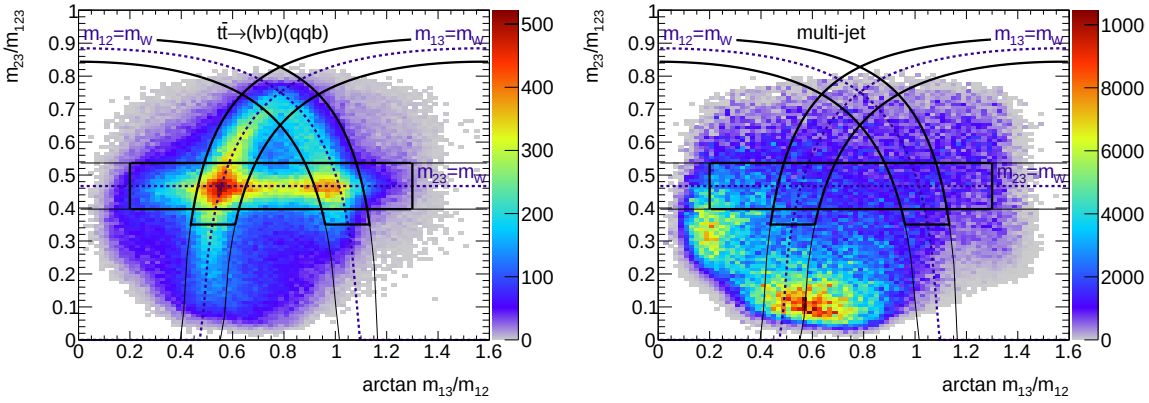

(a) (b)

Figure 3.3: Distribution of the mass ratio m_{23}/m_{123} with respect to $\arctan(m_{13}/m_{12})$ for large-R jets associated to hadronically decaying top quarks of the $t\bar{t} \to (l\nu b)(qqb)$ process (a), and large-R jets from background multijet events (b).

3.2 HEPTopTagger in ATLAS

In ATLAS the constituents of large-R jets are locally calibrated topological clusters. These clusters can originate from the deposition of particles from the hard process, or from pileup and underlying events, not related to the physics process of interest. The reconstructed four-momentum of a large-R jet is heavily affected on the latter spurious contribution. The area correction technique, described in section 2.5.5, reduces it, by subtracting to the jet p_{T} a quantity proportional to the jet area times the average p_{T} density of the event. Afterwards, the energy of the large-R is calibrated. The calibration constants are derived by comparing the reconstructed jet energy with the corresponding particle-level jet in multijet simulation. A minimal transverse momentum of 180 GeV is required for the calibrated large-R jet to be tested by the HEPTopTagger.

The inclusive and exclusive HEPTopTagger subjets are first calibrated, then only those with $p_{\text{T}} > 20$ GeV are kept. The area correction procedure is not applied to these subjets, because the HEPTopTagger filtering step reduces by itself a substantial amount of the pileup contribution.

Chapter 4

HEPTopTagger performance in the ℓ+jets channel

It is important to validate the performance and the simulation modelling of the HEPTopTagger algorithm in a data sample pure in hadronically decaying top quarks, before applying it in physics analyses. An enriched sample of pair produced top quarks, where one top quark decays semi-leptonically and the other hadronically, is exploited for this purpose. This sample is obtained by selecting those events with exactly one lepton [1], missing transverse momentum, b-tagged small-R jets, and a large-R jet. The event selection is detailed in section 4.1.

Since a very pure reconstructed top quark mass peak is obtained, the uncertainty on the momentum scale of the HEPTopTagger subjets can be constrained by comparing the data mass distribution with the Monte Carlo prediction, as discussed in section 4.2.

In section 4.3, the enriched $t\bar{t}$ data sample is used to validate the simulation prediction of the internal variables of the HEPTopTagger.

The measurement of the algorithm efficiency of tagging hadronically decaying top quarks is reported in section 4.4. Finally, the dependence of the reconstructed top mass with respect to different pileup conditions is studied in section 4.5.

The studies described in this chapter have been published in [6].

4.1 Selection and samples

The dataset used in this analysis was collected in 2012 by the ATLAS experiment and corresponds to an integrated luminosity of 20.3 fb^{-1} of proton-proton collisions at a centre of mass energy of $\sqrt{s} = 8$ TeV.

A sample enriched in $t\bar{t}$ events is used, in order to study the performance of the HEPTopTagger algorithm in data. Such a signal rich sample is obtained by selecting events with a single isolated lepton, electron or muon, and hadronic activity: large-R

[1] In the conventional ATLAS nomenclature leptons, ℓ, are electrons and muons, while the neutrinos, being undetected, are not included in the lepton definition. Taus are usually not considered in the ℓ category, since they in turn decay hadronically or leptonically.

jets and b-tagged jets. This channel, called ℓ+jets channel ($\ell = e, \mu$), aims to collect events where a top quark pair is produced, with the final production of a W decaying leptonically and the other W decaying hadronically, see figure 4.1.

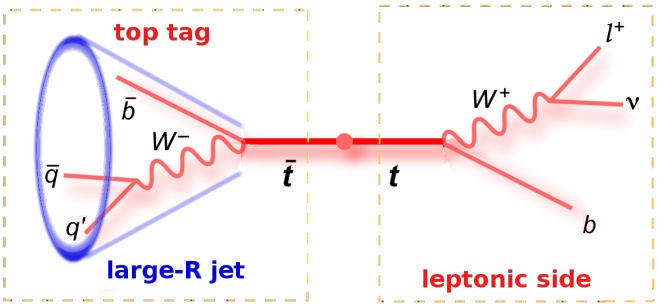

Figure 4.1: The top quark pair production in the ℓ+jets channel, described by the process $t\bar{t} \to (W^+b)(W^-\bar{b}) \to (\ell^+\nu b)(q\bar{q}'\bar{b})$. The leptonic side is characterised by the presence of a lepton, a neutrino and a b-quark, reconstructed as a lepton candidate, missing transverse momentum and a b-tagged jet. The hadronically decaying top quark can appear as a large-R jet which might be top-tagged.

4.1.1 Monte Carlo simulation

The main SM processes characterised by the presence of exclusively one prompt lepton and jets in the final state are: $t\bar{t} \to (l\nu b)(qqb)$[2], single top production, and W+jets. The contribution of other SM processes like multi-jet, Z+jets is negligible after the application of the selection described in section 4.1.5.

The signal for this analysis consists of $t\bar{t}$ events with a large-R jet originating from a hadronically decaying top quark. The background is composed of non-$t\bar{t}$ events with QCD large-R jets, as for the W+jets process, and from $t\bar{t}$ and single top events, where the large-R jet is not associated to any hadronically decaying top quark, referred to as "not matched" $t\bar{t}$ background.

These SM processes are simulated using Monte Carlo (MC) generators. Detailed information regarding the generator, the parton shower (PS), the underlying event (UE) modelling, and the parton density function (PDF), used to produce the MC samples, are described in section 2.6.

4.1.2 Quality requirements

A baseline quality selection identical to most analyses is applied. It requires data collection with complete functionality of all subdetectors during stable beam conditions and the rejection of events contaminated by detector noise. At least one primary vertex should be reconstructed close to the LHC beam spot position from at least five associated inner detector tracks with $p_{\mathrm{T}} > 400$ MeV. If the event contains more than one reconstructed primary vertex, these are ordered in descending $\sum p^2_{\mathrm{T,track}}$

[2] In the MC sample production l can be an electron, a muon or a tau.

and the first one is taken as the primary vertex, the process originated from. Events where the primary vertex comes from non collision events are rejected. Those events containing at least one fully calibrated anti-k_t $R = 0.4$ jet with $p_{\mathrm{T}} > 20$ GeV with bad calorimeter conditions are rejected.

4.1.3 Electron and muon triggers

The data sample corresponding to events with an electron in the final state is called electron channel. These events are collected with electron triggers, which select events where electromagnetic calorimeter energy clusters are found. These clusters, which define the electron trigger objects, are characterised by electron-like shower shapes and a matched track in the inner detector. Data are collected by a first trigger, which requires an electron object of medium quality, with transverse energy (E_{T}^{e}) greater than 24 GeV and the associated track to be isolated. In addition to this, a second trigger is used to recover some of the efficiency for high-p_{T} electrons. This has looser requirements on the electron trigger object, for example, no track isolation is required, but the E_{T}^{e} threshold is 60 GeV.

The data of the muon channel are collected by muon triggers. These require the presence of at least one muon trigger object, which is reconstructed using tracks identified in the muon spectrometer and in the inner detector. Events of the muon-channel data sample pass at least one of the following single muon triggers: the lowest unprescaled one selects events with isolated muon objects with $p_{\mathrm{T}}^{\mu} > 24$ GeV; a second trigger has a p_{T} threshold of 36 GeV with no isolation requirement.

In both electron and muon channels, the inclusive disjuction of two triggers provide a uniform efficiency for offline lepton objects with transverse momentum $p_{\mathrm{T}} > 25$ GeV.

4.1.4 Object reconstruction

Small-R jets, large-R jets, missing transverse momentum, and electron and muon objects are used in this analysis. Their main selection criteria are summarised in table 4.1. A more detailed description of their reconstruction is given in section 2.5.

muon $p_{\mathrm{T}}^{\mu} >$	25 GeV
electron $E_{\mathrm{T}}^{e} >$	25 GeV
small-$R = 0.4$ anti-k_t jet $p_{\mathrm{T}} >$	25 GeV
small-$R = 0.4$ anti-k_t jet $\lvert\eta\rvert <$	2.5
large-$R = 1.5$ C/A jet $p_{\mathrm{T}} >$	200 GeV
large-$R = 1.5$ C/A jet $\lvert\eta\rvert <$	2.0
$E_{\mathrm{T}}^{\mathrm{miss}} >$	20 GeV

Table 4.1: Main selection criteria for the object reconstruction.

An overlap of physics objects can happen. Therefore a procedure to assign calorimeter deposits or tracks only to one reconstructed object is necessary.

While the algorithm for the $E_{\mathrm{T}}^{\mathrm{miss}}$ determination has its own overlap removal procedure, electrons, muons and jets need a specific one optimized for the regime where the two top quarks have a moderate or high p_{T} [133].

After the reconstruction of electrons, if for any of them there is a close-by jet with $\Delta R < 0.4$, the electron four-vector is subtracted from the close-by jet. If the electron is close to the recalculated jet, $\Delta R < 0.2$, the electron is removed and the jet is considered with its original four-momentum in the analysis. In case the electron and the jet are far from each other, i.e. $\Delta R > 0.2$, they are treated as separated objects and the kinematic variables of the jet is updated to the electron-subtracted one.

Reconstructed muons are removed if their angular distance from a small-R jet is such that $\Delta R < 0.04 + 10\ \mathrm{GeV}/p_{\mathrm{T}}^{\mu}$. This p_{T}^{μ} dependent requirement ensures not to lose efficiency in the reconstruction of events with high p_{T} top quarks.

4.1.5 ℓ+jets selection

Exactly one muon, matched with the object that fired the trigger, and no electrons are required for the muon channel, and vice versa for the electron channel. This selected lepton will be used as a reference for subsequent requirements.

Among those events containing one single isolated lepton, the ones with one leptonically decaying W boson needs to be selected. Therefore $E_{\mathrm{T}}^{\mathrm{miss}}$ coming from the undetected neutrino is required to be grater than 20 GeV. The transverse mass of this W candidate is defined as

$$M_{\mathrm{T}}^{W} = \sqrt{2p_{\mathrm{T}}^{\ell} E_{\mathrm{T}}^{\mathrm{miss}} (1 - \cos\Delta\phi)}\,, \tag{4.1}$$

where $\Delta\phi$ is the azimuthal angle between the vectors of the transverse lepton momentum $\vec{p_{\mathrm{T}}}^{\ell}$ and of $\vec{E}_{\mathrm{T}}^{\mathrm{miss}}$. The requirement of $E_{\mathrm{T}}^{\mathrm{miss}} + M_{\mathrm{T}}^{W} > 60$ GeV is applied.

Events are selected if they contain at least one large-R jet far from the region, where the isolated lepton is reconstructed. This large-R jet is probably originating from the hadronic decay of a top quark with moderate transverse momentum. The leading large-R jet, among those far away from the lepton, i.e. $\Delta R > 1.5$, is taken into account for the subsequent analysis.

The selection based simply on the leptonic W boson candidate and a distant large-R jet does not help in rejecting one of the main background components, the W+jets process. By requiring that a small-R jet should be reconstructed within $\Delta R < 1.5$ from the lepton, the amount of remaining W+jets is reduced by two-thirds, while the $t\bar{t}$ only by one-quarter. If this jet is b-tagged, the W+jets contamination decreases even more and becomes approximately 10% of the total selected events.

An additional requirement of a second b-tagged jet is applied in specific parts of this analysis. This small-R jet lies in the spatial region of the large-R jet, by

requiring its angular distance from the lepton to be greater than 1.5. After this requirement, the W+jets contribution becomes almost negligible.

All of the above-mentioned requirements, summarised in Table 4.2, are effective in reducing another particular background source, which consists in $t\bar{t}$ events where the selected large-R jet originates from event hadronic activity different from a hadronically decaying top quark.

Trigger	single lepton (μ or e)
Number of ℓ	1
$E_{\mathrm{T}}^{\mathrm{miss}}$	> 20 GeV
$E_{\mathrm{T}}^{\mathrm{miss}} + M_{\mathrm{T}}^{W}$	> 60 GeV
Number of large-R jets	≥ 1
$\Delta R(\ell, \text{large-}R \text{ jet})$	> 1.5
b-jet with $\Delta R(\ell, b\text{-jet}) < 1.5$	≥ 1

Table 4.2: Selection criteria before the HEPTopTagger application.

4.2 Subjet energy scale uncertainty

As described in section 3.2, the energy and momentum of the subjets reconstructed by the HEPTopTagger algorithm are calibrated with energy and η dependent functions.

A procedure for the uncertainty determination of the subjet energy scale is described in this section. The events selected for this study are coming only from the muon channel where at least one b-tagged jet is reconstructed close to the muon. The requirement of a second b-tagged jet is not applied in this study. In fact, after the application of the HEPTopTagger algorithm a very pure sample of $t\bar{t}$ events is obtained and the W+jets background contribution is almost negligible.

The four-momentum of the top candidate is given by the four-momentum sum of the calibrated inclusive subjets which pass the HEPTopTagger filtering procedure. Therefore, any change in the latter appears accordingly in the former. This feature is particularly visible in the HEPTopTagger top candidate mass distribution of figure 4.2(b), which is characterised by a peak at around 170 GeV. Any scaling of the subjet four-momenta determines a shift of the entire peak. Its position changes proportionally to the relative scaling of the subjets.

This peak structure can be exploited in order to constrain the energy scale uncertainty of the HEPTopTagger subjets. This idea was first suggested in [5].

The method proceeds as follows.

1. The p_{T}-energy scale of all the calibrated subjets reconstructed by the HEPTopTagger is varied in the simulation. For example, their four-momenta can be scaled constantly by 1.03, corresponding to a p_{T}-energy shift of +3%, as illustrated in figure 4.2(a).

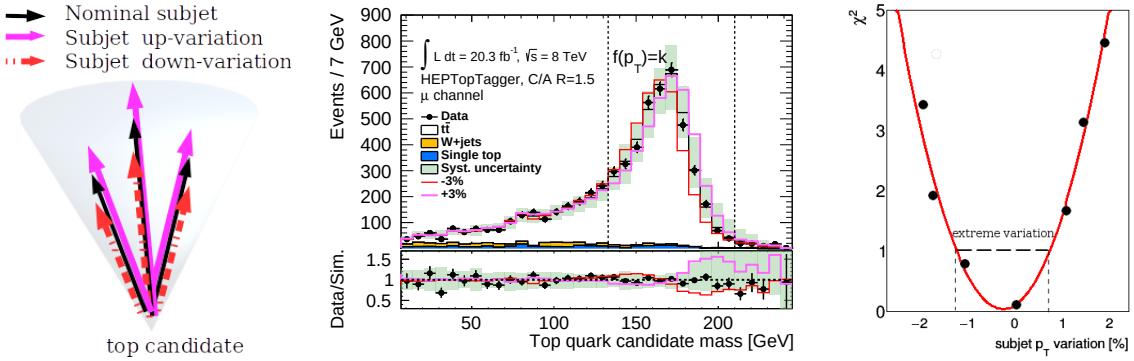

(a) (b) (c)

Figure 4.2: (a) Illustration of the HEPTopTagger subjet momentum variation. (b) Data and MC HEPTopTagger candidate mass distribution. The nominal and the varied distributions, where the p_{T} of the subjets have been scaled up or down by 3%, are shown in black line with green systematic error band, magenta think line and red thin, respectively. The data is represented in black points. In the bottom panel the ratio of the data and the nominal MC prediction is represented with black points, the ratio between the up (down) MC variation and the nominal MC is represented with magenta thick (red thin) lines. (c) Illustration of the extreme subjet variations obtained from the χ^2 distribution as a function of the subjet momentum variation.

2. The resulting top candidate mass distribution is compared with the data distribution and a χ^2 is calculated. In figure 4.2(b), the magenta top mass peak resulting from the 3% energy shift of the HEPTopTagger subjets moves to higher masses with respect to the nominal MC expectation, where no variation is applied. Similarly, if the subjets are scaled by 0.97, corresponding to a -3% shift, the peak moves to lower mass values. A χ^2 value is associated to each of these variations.

3. After taking into account different subjet variations, the constraint on the subjet p_{T} scale uncertainty is obtained by those extreme distributions that describe the data mass peak within the uncertainties. The extreme variations are determined from the χ^2 distribution as a function of the subjet variation, as illustrated in figure 4.2(c).

4.2.1 Subjet p_{T} scale variation

All the reconstructed subjet four-momenta related to a mass distribution are varied up or down in a correlated way:

$$p^{\nu} \rightarrow p^{\nu}\ (1 \pm f)\,, \tag{4.2}$$

where $f = f(p_{\mathrm{T}})$ specifies the relative shift that is applied to a subjet as a function of the subjet p_{T}. Three different functional forms are considered in order to take

into account possible dependencies of the relative p_{T} scale uncertainty on the subjet transverse momentum:

- $f = k_1\sqrt{p_{\mathrm{T}}}$: larger variation for high p_{T} subjets;
- $f = k_2$: the uncertainty is independent of the subjet p_{T};
- $f = k_3/p_{\mathrm{T}}$: larger variation for low p_{T} subjets;

where, k_1, k_2 and k_3 are constant parameters. These functional forms aim to describe different uncertainty configurations: the p_{T} dependence of the uncertainty is determined by the effect, contributing predominantly to the subjet p_{T} scale uncertainty. For example, the uncertainty could be dominated by effects due to pileup mismodelling leading to a relative uncertainty which is high for low p_{T} subjets, and small at high p_{T}, described by the $f = k_3/p_{\mathrm{T}}$ functional form. If the dominant source of the subjet p_{T} uncertainty is due to non-closure in the MC calibration, i.e. the calibrated subjet response is on average over- or underestimated compared to the particle jet scale, the subjet p_{T} scale uncertainty might be independent on the subjet p_{T} to a first approximation. If the miscalibration of very high p_{T} subjets dominates the uncertainty, for example, due to effects of jet collimation and merging, the $f = k_1\sqrt{p_{\mathrm{T}}}$ functional form would be the correct description of the subjet p_{T} scale uncertainty.

The functions corresponding to different k values, considered for the uncertainty estimate, are shown in figure 4.3.

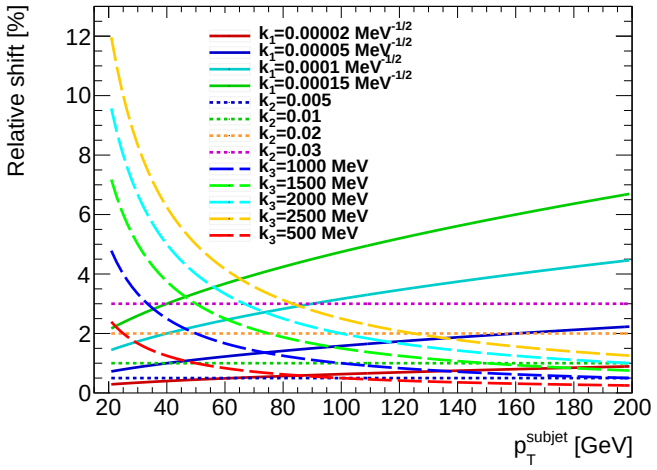

Figure 4.3: Several p_{T}-dependent relative variations used to study the uncertainty of the HEPTopTagger subjet p_{T} scale. The percentage relative shift applied to subjets is shown as a function of the subjet p_{T}. The values listed in the legend are the values of the parameter k.

4.2.2 Comparison of the data and Monte Carlo distributions after the subjet variation

A χ^2 value is calculated by comparing the data distribution and the simulated one after each subjet variation. In order to see the dependence of the subjet scale uncertainty with respect to the large-R jet p_{T} and η, this comparison is performed in four different regions. In particular the tagged large-R jet sample is divided in central and forward regions, with $|\eta^{\text{large-}R\text{ jet}}| < 0.7$ and $|\eta^{\text{large-}R\text{ jet}}| > 0.7$, respectively. These two are in turn divided in other two phase spaces, one characterised by large-R jets with $p_{\mathrm{T}} < 320$ GeV and the other with $p_{\mathrm{T}} > 320$ GeV, for a total of four regions.

For example, the top candidate mass distribution corresponding to the central regions for low p_{T} large-R jets and for high p_{T} ones is shown in figure 4.4(a) and 4.4(b), respectively. The main difference between the two is the width of the top mass peak. It is broader for the low p_{T} region, since the probability of one top decay product to be lost outside the large-R jet is higher. On the contrary, the decay products of more boosted top quarks are collimated enough to be well contained in the higher p_{T} large-R jets, determining a narrower top mass peak structure. In addition to the data and expected nominal MC distributions, the ones shown in red and magenta lines correspond to a subjet p_{T} shift of $f = k_3/p_{\mathrm{T}}$ where $k_3 = \pm 10^3$ MeV. In order to easily compare the impact of the different functional forms, the numerical value of the shift applied to a subjet of $p_{\mathrm{T}} = 100$ GeV, called *JES shift*, is used as reference for a specific variation instead of the k parameter value. The 100 GeV reference value is chosen, since it corresponds to the average p_{T} of the HEPTopTagger subjets. The relative shift of the top mass peak with respect to the nominal position is very close to the value of $f(p_{\mathrm{T}})|_{p_{\mathrm{T}}=100\text{ GeV}}$.

The varied and nominal distributions are then compared to data in the mass region $133 < m_{\text{top cand.}} < 210$ GeV and a χ^2 value is determined as follows. As expressed by equation 4.3, the squared difference of the expected number of events from the varied simulation $N_i^{t\bar{t}}$ and the measured number of data events N_i^{data} is weighted with respect to the quadrature sum of systematic uncertainties from the first $\Delta N_i^{t\bar{t}}$ and statistical uncertainty from the second ΔN_i^{data}. The sum over all i mass bins in the top candidate mass region $133 < m_{\text{top cand.}} < 210$ GeV is defined as the χ^2 associated to a varied MC distribution.

$$\chi^2 = \sum_{\text{bin } i} \frac{\left(N_i^{t\bar{t}} - N_i^{\text{data}}\right)^2}{(\Delta N_i^{\text{t}\bar{\text{t}}})^2 + (\Delta N_i^{\text{data}})^2} \tag{4.3}$$

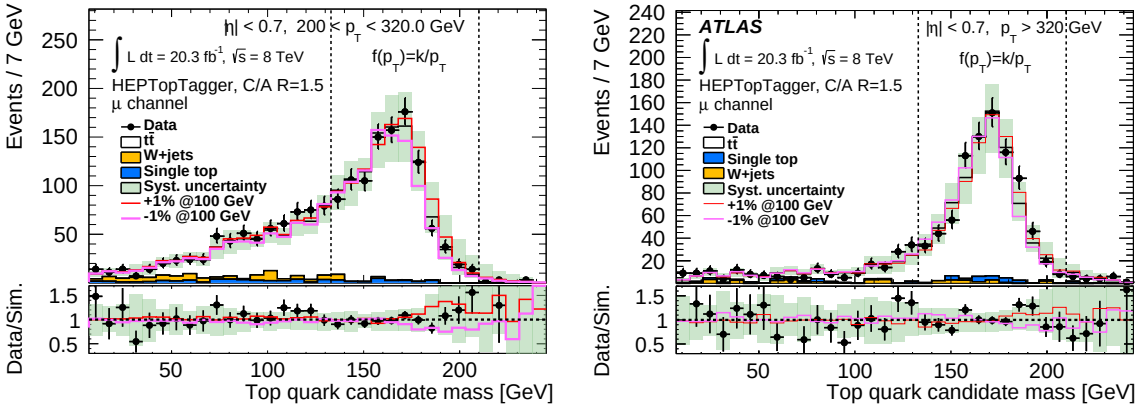

(a) $200 < p_{\mathrm{T}} < 320$ GeV and $|\eta| < 0.7$

(b) $p_{\mathrm{T}} > 320$ GeV and $|\eta| < 0.7$

Figure 4.4: Data/MC comparison of the HEPTopTagger top candidate mass distributions relative the central regions, $|\eta^{\text{large-}R\text{ jet}}| < 0.7$. Figure (b) from [6]. The style convention is identical to figure 4.2(b) but the red thin and magenta thick lines correspond to the MC variation of the subjet p_{T} with the $f(p_{\mathrm{T}}) = k/p_{\mathrm{T}}$ functional form, corresponding to a relative $\pm 1\%$ p_{T} shift for subjets with $p_{\mathrm{T}} = 100$ GeV.

4.2.3 Subjet p_{T} scale uncertainty estimate with χ^2 fit

The χ^2 value is calculated for every simulated variation using the three different functional forms, previously described, in the four $p_{\mathrm{T}} - \eta$ bins. The distribution of these values as a function of the corresponding JES shift can be fitted with a parabola.

The minimum of the parabola defines the minimum value, χ^2_{min}, and the optimal JES shift corresponds to the shift $\hat{f}$ such that $\chi^2(\hat{f}) = \chi^2_{\mathrm{min}}$. The uncertainty on $\hat{f}$ then is given by the $\sigma_{\hat{f}}$ value that satisfies the condition:

$$\chi^2(\hat{f} \pm \sigma_{\hat{f}}) = \chi^2_{\mathrm{min}} + 1$$

In this case $\sigma_{\hat{f}}$ is the uncertainty on the optimal JES shift $\hat{f}$. Ideally $\hat{f}$ should correspond to the nominal simulated distribution where no shift is applied: $\hat{f} = 0$. However, this condition is not met in most of the cases, as can be seen in figure 4.5 for the functional form $f = k_3/p_{\mathrm{T}}$ in the four $p_{\mathrm{T}} - \eta$ regions. Although the nominal subjet p_{T} scale is not optimal and a correction to this could be applied, this shift is included in the systematic uncertainty. Therefore, the estimate of the systematic uncertainty on the subjet p_{T} scale is the maximum between $|\hat{f} + \sigma_{\hat{f}}|$ and $|\hat{f} - \sigma_{\hat{f}}|$.

This estimate is obtained for the three different functional forms in the four $p_{\mathrm{T}} - \eta$ kinematic regions, and the values are summarised in table 4.3. The uncertainty on the p_{T} scale of the subjets is estimated to vary between 1.4% and 2.7% for $p_{\mathrm{T}} = 100$ GeV subjets.

In figure 4.6, the JES shift, summarised in table 4.3, is translated into functions with respect to the subjet p_{T} describing the subjet energy scale uncertainty.

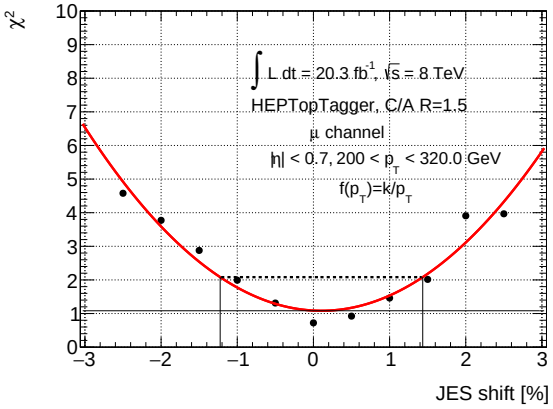

(a) $200 < p_{\mathrm{T}} < 320$ GeV and $|\eta| < 0.7$

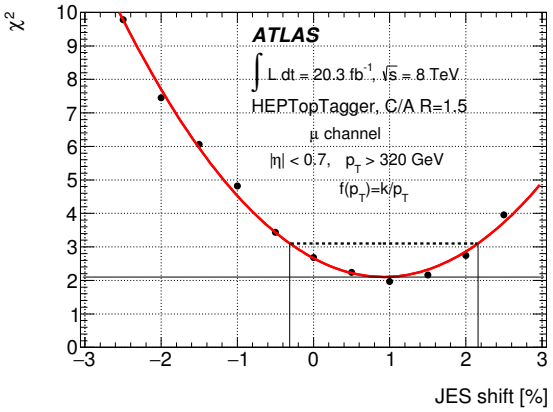

(b) $p_{\mathrm{T}} > 320$ GeV and $|\eta| < 0.7$

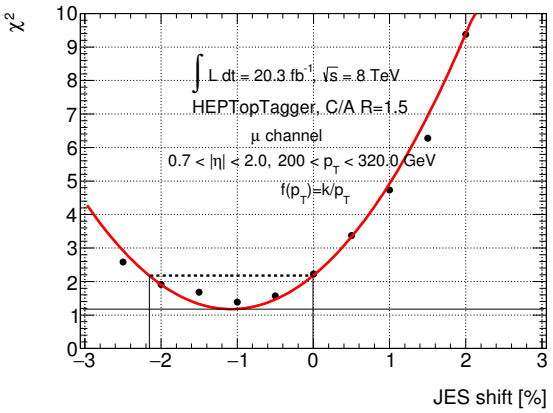

(c) $200 < p_{\mathrm{T}} < 320$ GeV and $0.7 < |\eta| < 2.0$

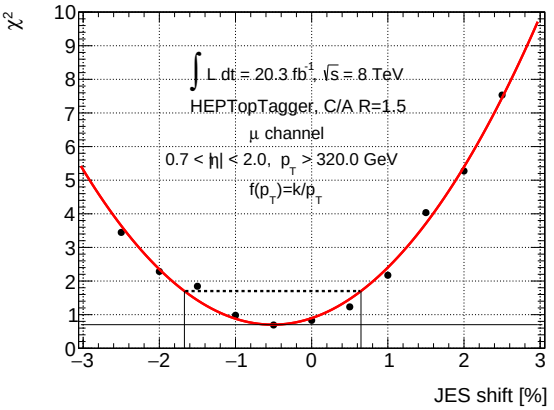

(d) $p_{\mathrm{T}} > 320$ GeV and $0.7 < |\eta| < 2.0$

Figure 4.5: χ^2 distributions corresponding to four large-R jet p_{T} $-\eta$ bins as a function of the relative p_{T} shift of subjets with $p_{\mathrm{T}} = 100$ GeV (JES shift) for C/A $R = 1.5$ large-R jets. The functional variation of the subjet four-momentum is $f(p_{\mathrm{T}}) = k/p_{\mathrm{T}}$. Figure (b) from [6].

subjet $p_{\mathrm{T}} = 100$ GeV	$200 < p_{\mathrm{T}} < 320$ GeV			$p_{\mathrm{T}} > 320$ GeV		
	$k_1\sqrt{p_{\mathrm{T}}}$	k_2	k_3/p_{T}	$k_1\sqrt{p_{\mathrm{T}}}$	k_2	k_3/p_{T}
$\lvert\eta\rvert < 0.7$	2.4%	2.1%	1.4%	2.2%	2.5%	2.2%
$0.7 < \lvert\eta\rvert < 2.0$	2.7%	2.4%	2.2%	2.0%	2.2%	1.7%

Table 4.3: Relative p_{T} scale uncertainty for HEPTopTagger subjets with $p_{\mathrm{T}} = 100$ GeV in different bins of large-R jet p_{T} and η for three different functional forms of the relative p_{T} variation.

To estimate the impact of the subjet energy scale on the results of physics analyses, the following procedure has to be performed. The impact of the HEPTopTagger subjet energy scale uncertainty on a sample of top candidates should be evaluated using the three different functional forms separately and applying both as up and down variations. The functional form, which gives the maximum deviation, is used to evaluate the systematic uncertainty.

In the following analyses, the functional form $f(p_{\mathrm{T}}) = k/p_{\mathrm{T}}$ has been found to be the dominant one and is used to evaluate the impact of the subjet p_{T} uncertainty. This is the case for all the physics processes where the top candidates are mainly reconstructed with a moderate momentum ($200 < p_{\mathrm{T}} < 400$ GeV).

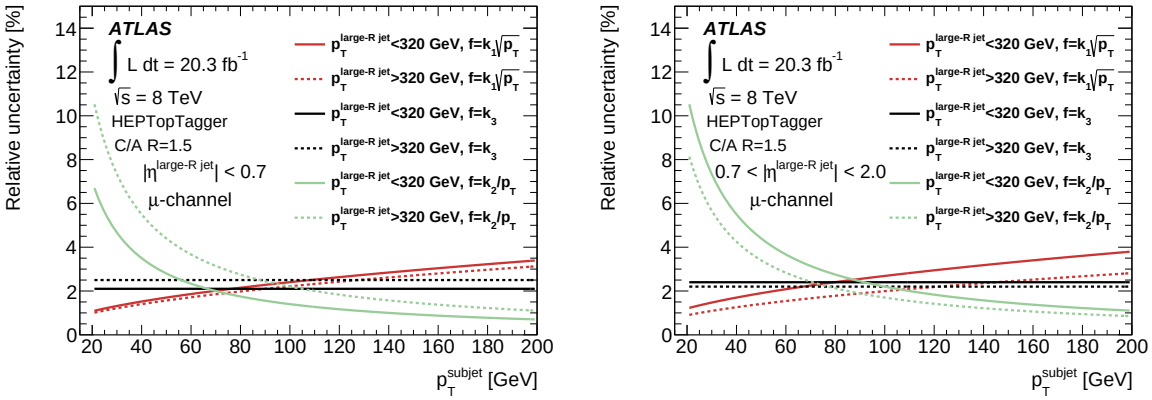

(a) $|\eta| < 0.7$ (b) $0.7 < |\eta| < 2.0$

Figure 4.6: Relative energy scale uncertainty as a function of the HEPTopTagger subjet p_{T} in different large-R jet p_{T} and η bins for three different functional forms. Figures from [6].

4.3 Validation of the HEPTopTagger in data

In order to study how well the simulation models the outcome of the HEPTopTagger, data and Monte Carlo distributions are compared for several variables before and after the application of the algorithm.

The selection described in section 4.1, including the second b-tag requirement, is applied. As can be see in figure 4.7(b), the selected sample is very pure of top quarks.

The fraction of W+jets events expected from the simulation is approximately 3%. The rest of the events contain real top quarks (6% single top and 91% $t\bar{t}$).

Although the sample of the selected events is very pure in top quarks, only a fraction of the leading large-R jets can be geometrically associated to top quarks decaying hadronically. If a generated top quark, which decays hadronically, is found within an angular distance of 1 from the large-R jet, $\Delta R(\text{large-}R \text{ jet, top}) < 1.0$, this jet and the corresponding event are defined as *matched*. Those which are *not matched* constitute a background for this analysis, aiming to select only large-R jets originating from hadronically decaying top quarks.

As can be seen from figure 4.7(a), the angular distance between the large-R jet and the lepton is a crucial requirement for the reduction of the unmatched $t\bar{t}$ background. For this reason the selected large-R jet in every event is the leading one among those which are reconstructed away from the lepton, i.e. $\Delta R(\ell, \text{large-}R \text{ jet}) > 1.5$.

The remaining unmatched large-R jets are mainly composed of a low number of hard subjets. The large-R jet constituents can be reclustered into very small C/A jets with distance parameter $R = 0.2$. The multiplicity distribution of the $R = 0.2$ jets with $p_{\mathrm{T}} > 20$ GeV is shown in figure 4.7(b). The matched large-R jets are mainly composed of at least two reconstructed $R = 0.2$ jets. On the contrary, the unmatched large-R jets are characterised by low multiplicity of hard structures.

Almost half of the unmatched large-R jets originates from one of the two b-quarks from the top decay, either because both top quarks decay semileptonically or because the hadronically decaying top quark has moderately low p_{T} ($p_{\mathrm{T}} \lesssim 200$ GeV). Its decay products are too apart to be reconstructed in a single large-R jet. The other half of events containing an unmatched large-R jet corresponds to events where the hadronically decaying top quark has low p_{T} ($p_{\mathrm{T}} \lesssim 100$ GeV) and the large-R jet originates from the non-top-quark hadronic activity in the event: the ISR or the underlying event.

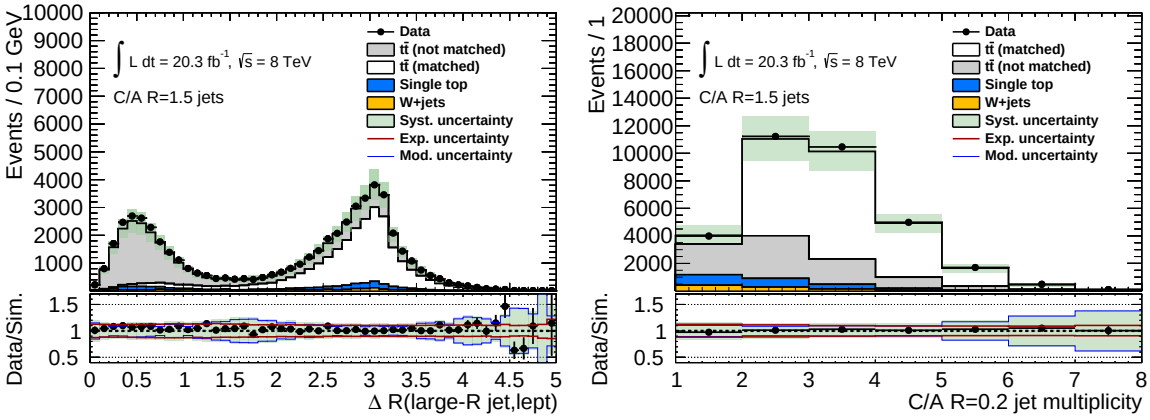

(a) (b)

Figure 4.7: Distribution of the angular distance between the leading large-R jet of the event and the lepton (a). After requiring that the large-R jet should be the leading one among those with the angular distance from the lepton greater than 1.5, (b) multiplicity distribution of C/A R=0.2 subjets reconstructed from the constituents of the large-R jet. The SM prediction is represented as a stacked histogram with green total uncertainty band (quadrature sum of statistical and systematic uncertainties) while the data distribution is overlaid as black points. The $t\bar{t}$ contribution is divided in events with the large-R jet matched to the hadronically decaying top quark (signal) and events in which the large-R jet does not originate from a hadronically decaying top quark (background). The lower panel shows the ratio between the data and the SM prediction. The contribution to the total systematic uncertainty (green band) is divided in experimental uncertainties (red line) and modelling uncertainties (blue line), whose definition is reported in section 4.3.1.

4.3.1 Impact of systematic uncertainties

The impact of the systematic uncertainties can be divided in experimental and modelling uncertainties.

Among the experimental uncertainties, the dominant ones are on: luminosity, lepton reconstruction efficiency, b-tagging efficiency, large-R jet energy scale (JES), large-R jet energy resolution (JER), subjet energy scale, subjet energy resolution.

Other experimental uncertainties were found to be negligible: the $E_{\mathrm{T}}^{\mathrm{miss}}$ reconstruction, the energy scale and resolution of the lepton and of the small-R jet.

The modelling uncertainties are related to the simulation of $t\bar{t}$ events and to the theory knowledge. The ones considered are: $t\bar{t}$ cross section; $t\bar{t}$ ISR/FSR; $t\bar{t}$ generator; $t\bar{t}$ parton shower; $t\bar{t}$ PDF; $t\bar{t}$ renormalization scale.

The way the uncertainties are evaluated is explained in section 2.7.

All these uncertainties affect the shape of several distributions in different ways. In order to evaluate the impact of the uncertainties before (pre-tag) and after (post-tag) applying the HEPTopTagger, the simulated yield of events passing the selection with the large-R jet far from the lepton is compared to the yield after a systematic

uncertainty variation. The impact on the pre-tag and post-tag event yield is given in table 4.4.

Systematic uncertainty	relative uncert. [%]	
	pre-tag	post-tag
Luminosity	2.8	2.8
b-tagging efficiency	7.5	7.3
c-jet mistag rate	1.2	0.6
l-jet mistag rate	0.6	0.3
lepton reconstruction efficiency	4.3	4.4
large-R jet JES	5.1	0.9
large-R jet JER	2.0	0.8
subjet energy scale	–	8.1
subjet energy resolution	–	1.9
$t\bar{t}$ cross section	5.4	5.7
$t\bar{t}$ ISR/FSR	1.8	7.6
$t\bar{t}$ generator	1.6	4.1
$t\bar{t}$ PDF	4.7	5.7
$t\bar{t}$ parton shower	6.5	2.7
$t\bar{t}$ renormalization scale	2.2	3.1

Table 4.4: Impact of systematic uncertainties on the simulated pre-tag and post-tag large-R jet yield. The numbers give in percentage the relative yield variation. The quoted values correspond to the absolute value of the maximum shift when applying "up" and "down" variations with respect to the nominal prediction.

The number of events before tagging is mainly affected by the uncertainties on the b-tagging efficiency, on the $t\bar{t}$ cross section normalisation, on the large-R jet energy scale, and on the parton shower with an impact of 7.5%, 5.4%, 5.1%, and 6.5%, respectively.

After the application of the HEPTopTagger, only those candidates with mass between 140 and 210 GeV are considered.

The total number of events containing a tagged large-R jet is not any more affected by the large-R jet energy scale uncertainty. The transverse momentum of the reconstructed top quark is generally smaller than the unfiltered large-R jet p_{T}. The tagger selects only those candidates with $p_{\mathrm{T}} > 200$ GeV. This requirement is more stringent than the one applied on the large-R jet p_{T}. Moreover, the HEPTopTagger is less efficient in tagging top quarks with moderate momentum ($p_{\mathrm{T}}^{\mathrm{top}} < 400$ GeV) with respect to those more boosted. Therefore, large-R jets with p_{T} close to the 200 GeV threshold have a low probability to be tagged. Hence, the large-R jet energy scale uncertainty becomes negligible in the post-tag region, and the dominant one becomes the uncertainty on the subjet energy scale. The major effect of the subjet energy scale uncertainty comes from the 20 GeV minimal p_{T} requirement applied both to calibrated inclusive and exclusive subjets. In fact when shifting "up" or "down" their four-momenta, if they are close to the 20 GeV p_{T} threshold they could increase

or decrease their transverse momentum by approximately 15%. Therefore low p_{T} subjets could be kept or discarded, leading to an increase or decrease in tagging probability.

Moreover the number of tagged large-R jets has a substantial dependence on the generator choice, the ISR/FSR modelling and the PDF, whose uncertainties are 4.1%, 7.6% and 5.7%, respectively.

4.3.2 Control distributions

The comparison of data-MC distributions for several variables before and after the application of the HEPTopTagger is performed in order to validate that the tagger output and its discriminant quantities are well described by the simulation.

The transverse momentum and the mass distributions of those large-R jets in input to the HEPTopTagger are shown in figures 4.8(a) and 4.8(b), respectively. The former is characterised by a steeply falling spectrum. The latter peaks at approximately 190 GeV, close to the top quark mass, but with a very broad structure due to the pileup and underlying event contamination. The distribution of large-R jet masses from not matched top quarks, single top and W+jets is shifted to lower values than the top quark mass. Both distributions are well described within the systematic uncertainties.

It can be observed from the data over simulation panel of figure 4.8(a), that the relative systematic uncertainties have a large dependence on the large-R jet p_{T}, and in particular they increase proportionally with the latter. These uncertainties are divided in experimental and modelling ones. The former is dominated by the contribution of the large-R jet energy scale uncertainty. This contribution rises with the large-R jet p_{T}: it is around 3% at 200 GeV and it becomes $\approx$ 20% for $p_{\mathrm{T}} >$ 500 GeV. The large p_{T} dependence of the uncertainty results from the large-R jet uncertainty measurement. As explained in section 2.7 this uncertainty is estimated using as a reference track jets. The dense jet environment enhances the chances that hits of two charged particles are reconstructed as a single track, leading to track jet momentum losses. This occurs especially in high p_{T} jets leading to a large effect of the large-R jet energy scale uncertainty at high large-R jet p_{T}. The modelling uncertainties increase as well with the transverse momentum of the large-R jet.

The distributions of $E_{\mathrm{T}}^{\mathrm{miss}}$ and M_{T}^{W} before tagging are shown in figures 4.8(c) and 4.8(d). Both are quite well described by the simulation within the systematic uncertainties. These uncertainties do not appear to have a dependence on either $E_{\mathrm{T}}^{\mathrm{miss}}$ or M_{T}^{W}. A peak close to the W boson mass is visible in the M_{T}^{W} distribution.

The application of the HEPTopTagger reduces prominently the background. In fact the W+jets process which contributes less than 1% can be neglected and the fraction of not matched $t\bar{t}$ events is reduced to 5%. The mass of the HEPTopTagger candidate distribution is shown in figure 4.9(a). The top mass distribution is more affected by systematic uncertainties in the region where the reconstructed top mass

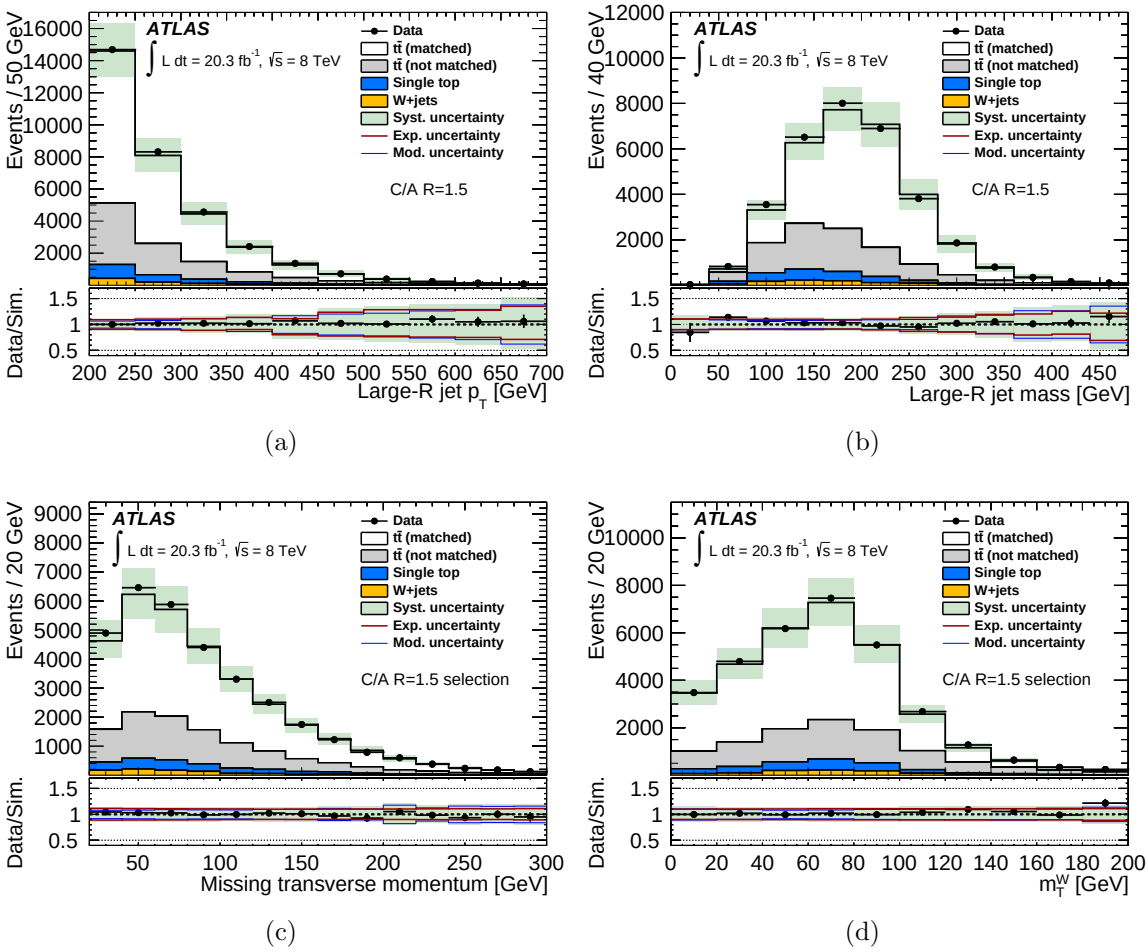

Figure 4.8: (a) and (b) large-R jet p_{T} and mass distribution before the application of the HEPTopTagger. $E_{\mathrm{T}}^{\mathrm{miss}}$and M_{T}^{W} quantities which are used in the baseline selection are shown in (c) and (d). The style convention is identical to figure 4.7. Figures (a), (b), (c) and (d) from [6].

is higher than the top quark mass (at 173 GeV). Here the systematic uncertainty on the HEPTopTagger subjet p_{T} resolution is the dominant one and it affects the shape and the peak width. In addition, the modelling of ISR and FSR influences both the number of tagged events and the HEPTopTagger mass shape.

The transverse momentum, the pseudorapidity and the azimuthal angle of the top candidate are shown in figure 4.9(b)-4.9(d). Two variables, $\arctan(m_{13}/m_{12})$ and m_{23}/m_{123}, used in the HEPTopTagger can be seen in figures 4.9(e) and 4.9(f), respectively. They help in the discrimination between a purely QCD three prong structure and the top decay one. The variable given by the ratio of the invariant mass of the two sub-leading subjets, m_{23}, and the invariant mass of the three top candidate subjets, m_{123}, is mainly close to the ratio of the W mass and the top mass, as can be seen from the peak in the distribution of figure 4.9(f). This feature suggests that the leading subjet is most probably originating from the b-quark.

Other variables related to the reconstruction of the top decay subjets can be

seen in figures 4.10(a)-4.10(f). The simulation distributions of the three top candidate subjet transverse momenta, figures 4.10(a)-4.10(c), agree well with the data. Similarly the maximum distance between the protojets of the triplet, figure 4.10(d), which gives the final top candidate is well modelled by the MC. These three protojets are the result of the mass drop procedure. The average distance is 1.3.

In figure 4.10(e), the distribution of the number of inclusive subjets used to reconstruct the top candidate mass and which are exclusively clustered into three top candidate decay subjets is shown. This quantity is very sensitive to the ISR and FSR modelling, to the generator, and also, to the detector response simulation. Although the total number of tagged large-R jet is the same, if the fast simulation is used, which is characterised by a simplified calorimeter description, the number of inclusive subjets can be lower than using the full complexity detector simulation. Regarding the experimental uncertainty the two that have the largest impact are the subjet energy resolution and scale uncertainties. The former does not affect the total number of tagged events, but it leads the distribution of the number of inclusive subjets to be shifted to higher values. The latter affects mainly the number of tagged large-R jets which are reconstructed from those characterised by three inclusive subjets.

A similar behaviour is related to the variable of figure 4.10(f), which counts the number of HEPTopTagger pre-candidates per large-R jet. There might be more than one combination of protojet triplets which lead to a plausible top candidate. Afterwards, the one with the mass closest to the top quark is chosen as a final candidate.

The simulation describe very well the data distributions of both the pre-tag and post-tag variables within the systematic uncertainties: the HEPTopTagger can be reliably used in physics analyses and the background expectation can be accurately estimated by means of the MC simulation.

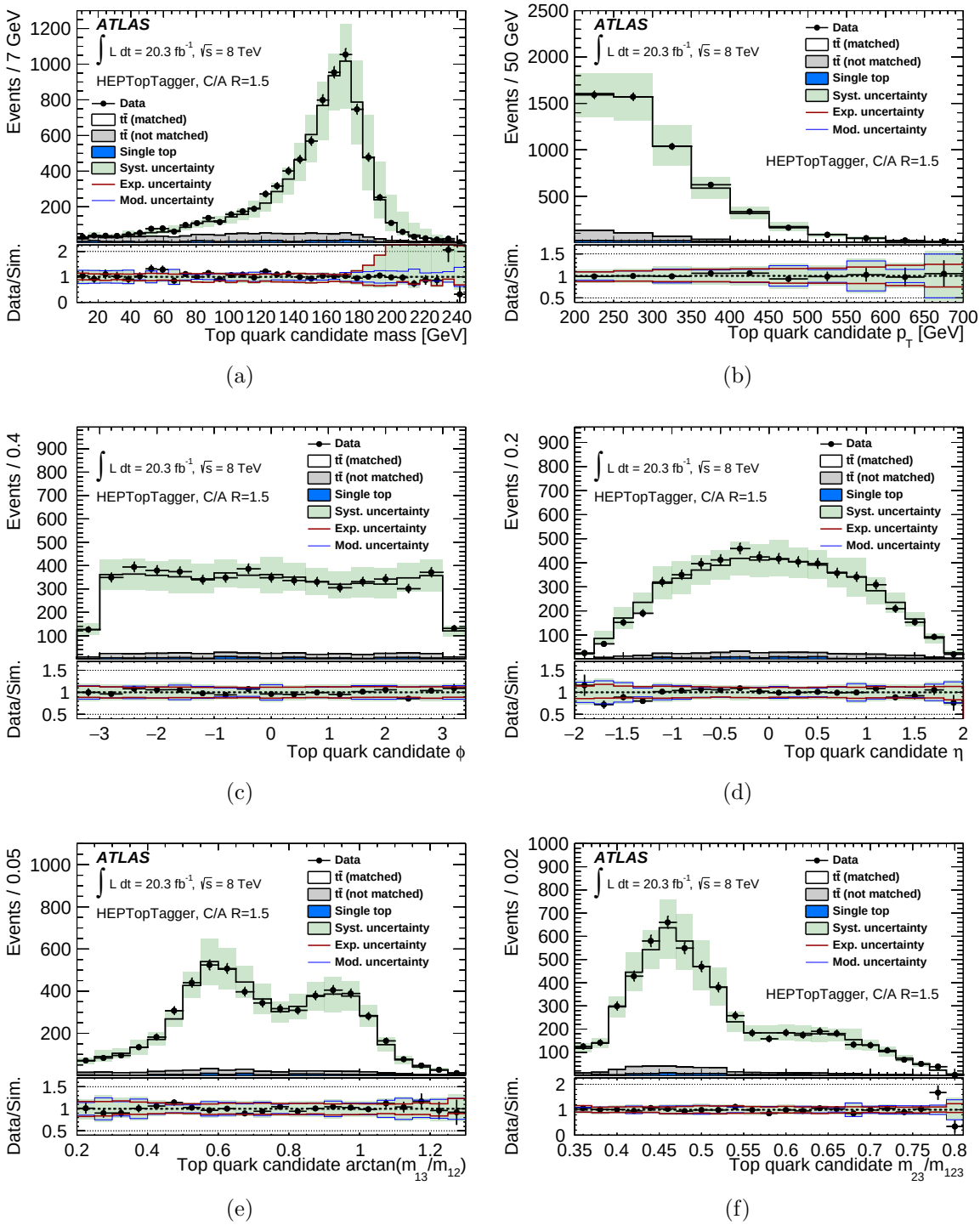

Figure 4.9: (a) Distribution of the HEPTopTagger candidate mass. Top candidates within the mass range 140−210 GeV are considered as tagged, and the distribution of their kinematic variables, p_{T}, ϕ and η, are shown in (b),(c) and (d). (e) and (f) distributions of the mass ratio quantities used by the HEPTopTagger algorithm to tag large-R jets. The style convention is identical to figure 4.7. Figures (a), (b), (e) and (f) from [6].

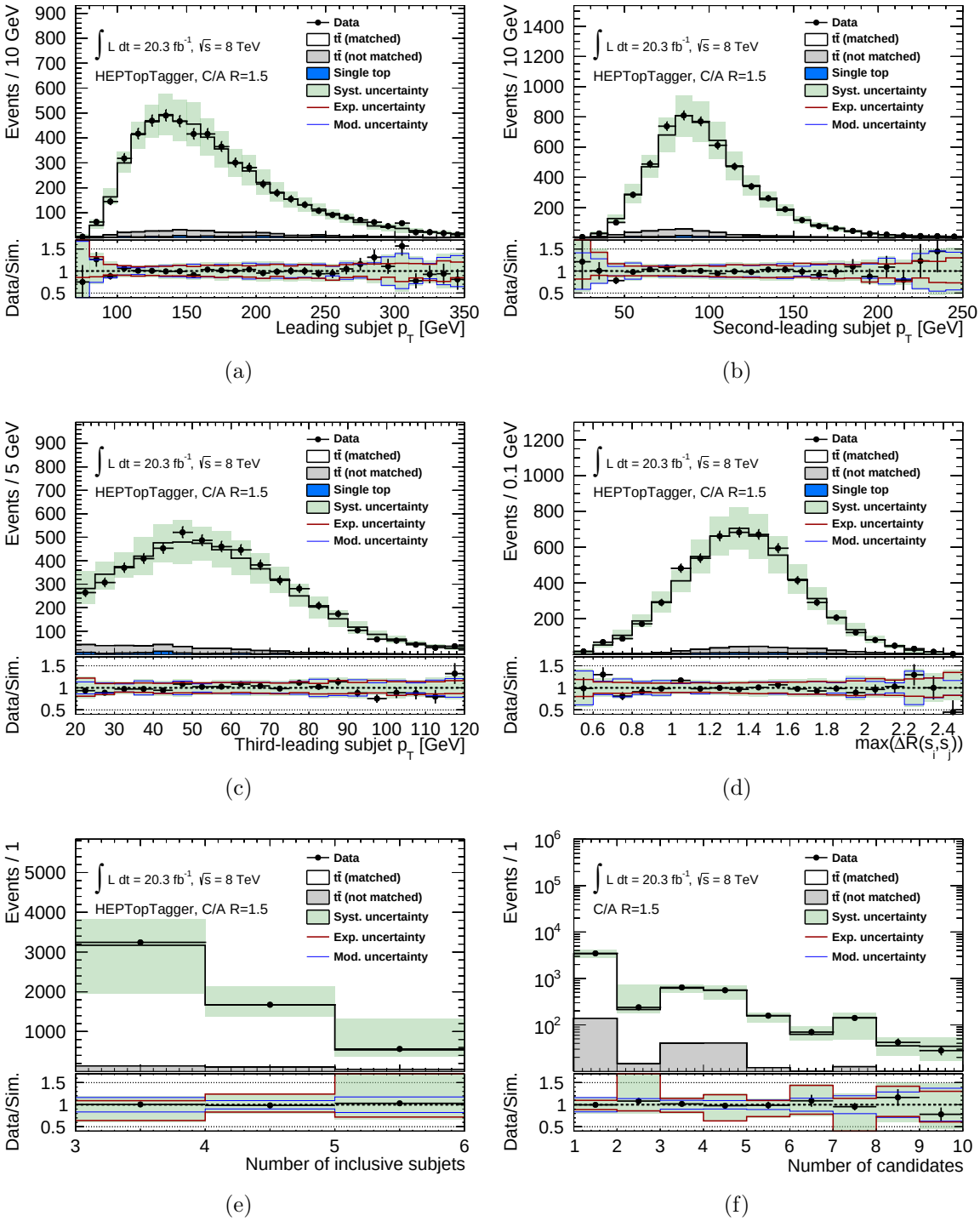

Figure 4.10: (a), (b) and (c) distributions of the leading, second and third leading exclusive subjets of the HEPTopTagger candidate, respectively. (d) Maximum distance distribution between the protojets of the triplet which gives the final top candidate. (e) Number of inclusive subjets distribution of the HEPTopTagger candidates. (f) Distribution of the number of HEPTopTagger candidates per large-R jet. The style convention is identical to figure 4.7.

4.4 HEPTopTagger efficiency measurement

The very pure top quark sample obtained with the ℓ+jets selection is used to measure the HEPTopTagger efficiency in data and to compare it with the simulation.

The HEPTopTagger efficiency is defined as the fraction of tagged over all large-R jets originating from hadronically decaying top quarks. The efficiency depends on the top quark momentum. Thus, it can be measured as a function of the large-R jet p_{T} and η.

The number of data large-R jets, matched with a top quark, in a particular p_{T} range before and after tagging is obtained by subtracting the simulated background. Thus, the HEPTopTagger efficiency in data for a certain large-R jet p_{T} range corresponding to bin i is defined as:

$$f_{\mathrm{data},i} = \left(\frac{N^{\mathrm{tag}}_{\mathrm{data}} - N^{\mathrm{tag}}_{t\bar{t}\text{ not matched}} - N^{\mathrm{tag}}_{\text{non-}t\bar{t}}}{N_{\mathrm{data}} - N_{t\bar{t}\,\text{not matched}} - N_{\text{non-}t\bar{t}}} \right)_i \tag{4.4}$$

As discussed previously, the background consists of those processes which are not $t\bar{t}$, i.e. W+jets and single top production, whose number of (tagged) large-R jets is $N^{(\mathrm{tag})}_{\text{non-}t\bar{t}}$, and of those $t\bar{t}$ (tagged) large-R jets not associated to any hadronically decaying top quark, amounting to $N^{(\mathrm{tag})}_{t\bar{t}\text{ not matched}}$ large-R jets. These counts are subtracted from the number of measured (tagged) large-R jets $N^{(\mathrm{tag})}_{\mathrm{data}}$.

Similarly the MC efficiency is calculated using the nominal $t\bar{t}$ POWHEG+PYTHIA sample:

$$f_{\mathrm{MC},i} = \left(\frac{N^{\mathrm{tag}}_{\mathrm{MC}}}{N_{\mathrm{MC}}} \right)_i \tag{4.5}$$

where $N^{(\mathrm{tag})}_{\mathrm{MC}}$ is the number of (tagged) large-R jets which are associated to hadronically decaying top quarks.

In figure 4.11 the data-MC efficiency comparison is shown as a function of the large-R jet p_{T} for two different η regions: $|\eta| < 0.7$ and $0.7 < |\eta| < 2.0$. The HEPTopTagger efficiency increases from 10% for large-R jet p_{T} in the range $200 - 250$ GeV, up to $\approx 50\%$ for $p_{\mathrm{T}} > 450$ GeV. The maximum large-R jet p_{T} bin is chosen with respect to the statistical error in data. Only bins with relative statistical uncertainty lower than 30% are shown.

The background subtracted data and the simulated efficiencies agree very well. Their ratio is compatible with unity within the uncertainties.

Integrating over p_{T} and η, the impact of the systematic uncertainties on the data and MC efficiency curves is determined and listed in table 4.5.

The data have systematic uncertainties due to the subtraction of the simulated background, which is affected by systematic uncertainty. The amount of subtracted events is different with respect to the pre-tag and post-tag regions. In fact, the background contribution post-tag is almost negligible. Therefore the systematic uncertainties of numerator and denominator do not cancel out. The ones that contribute

the most are those related to the modelling of the not-matched $t\bar{t}$, in particular related to the generator choice. In fact, the fraction of not-matched large-R jets is different for POWHEG and MC@NLO, determining a large uncertainty in the not-matched $t\bar{t}$ background subtraction from data.

However, most of the systematic uncertainties, which have a non-negligible impact on the pre-tag and post-tag large-R jet p_{T} distributions, cancel out for $f_{\mathrm{MC},i}$, with the exception of those that have a very different impact on the numerator and denominator. Among these the large-R jet energy scale has a non-negligible impact only in the pre-tag region, and vice versa for the subjet energy scale.

Since the systematic uncertainties are correlated for the data efficiency distribution and the simulated one, this correlation is taken into account. The total correlated uncertainty is shown as the blue band in the bottom panels of figure 4.11, which displays the ratio between the measured efficiency and the expected efficiency. The systematic uncertainties are larger than the statistical ones.

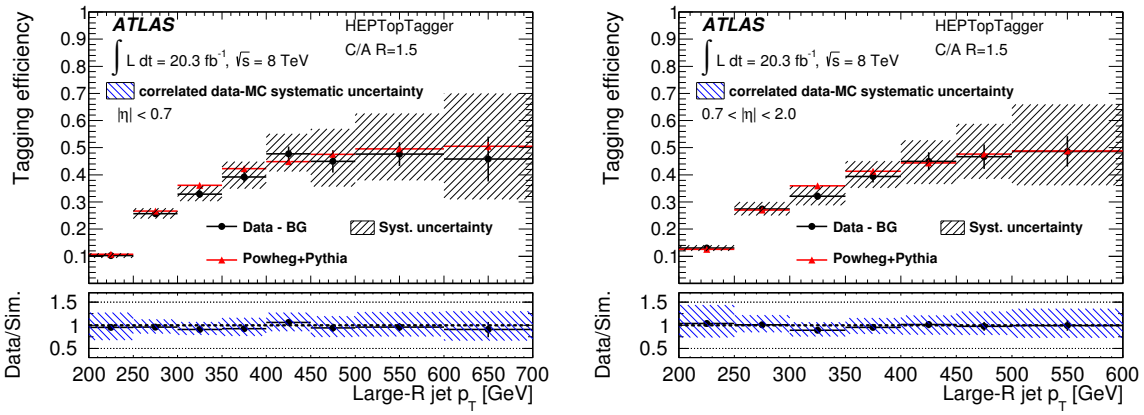

Figure 4.11: The HEPTopTagger efficiency f_{data} is represented by black points and compared with f_{MC}, red triangles, as a function of the large-R jet p_{T} for two bins of large-R jet pseudorapidity. The ratio $f_{\mathrm{data}}/f_{\mathrm{MC}}$ is shown in the bottom panels with an uncertainty band that takes into account the correlation between the numerator and denominator systematic uncertainties. Figure from [6].

uncertainty	$\lvert\eta\rvert < 2.0$ $\Delta f_{\text{data}}/f_{\text{data}}$ (%)	$\Delta f_{\text{MC}}/f_{\text{MC}}$ (%)
large-R jet energy scale	2.9	4.4
large-R jet energy resolution	1.5	0.1
luminosity	1.3	0.0
b-tagging efficiency	3.5	0.2
lepton reconstruction efficiency	2.0	0.0
$t\bar{t}$ cross section	2.0	0.0
$t\bar{t}$ ISR/FSR	3.2	3.6
$t\bar{t}$ generator	6.7	0.3
$t\bar{t}$ parton shower	1.7	2.9
$t\bar{t}$ PDF uncertainty	2.2	1.2
$t\bar{t}$ renormalization scale	0.6	0.5
subjet energy scale	1.1	8.3
subjet energy resolution	0.7	0.0
total	9.9	10.6

Table 4.5: Impact of systematic uncertainties on the p_{T}-integrated fraction of tagged large-R jets in data (from [6]) and simulation. The numbers give the absolute shift of the tagging fraction and correspond to the maximum shift when applying "up" and "down" variations with respect to the nominal prediction.

4.5 Pileup stability

Making use of the ℓ+jets selection, the stability of the HEPTopTagger against pileup can be studied in data and MC.

The effect that the pileup contribution has on the top candidate mass distribution can be observed in figure 4.12. The average HEPTopTagger mass in the window $140 < m_t < 210$ GeV is shown as a function of the average number of interactions per bunch crossing $\langle\mu\rangle$ and of the number of reconstructed primary vertices, N_{PV}.

The pileup dependence of the mass is rather small, but it is larger with respect to the N_{PV} compared to the dependence with respect to $\langle\mu\rangle$. This behaviour suggests that in a specific event the number of reconstructed primary vertices describes the amount of pileup better, compared to the average number of interactions per bunch crossing.

The data and MC points, which are consistent within the uncertainty, are fitted with a linear function. The increase in the reconstructed top mass is approximately of 1 GeV from low to high $\langle\mu\rangle$ conditions. While a shift of ≈ 2 GeV is observed in the average reconstructed mass of events with small N_{PV} with respect to those with large number of primary vertices.

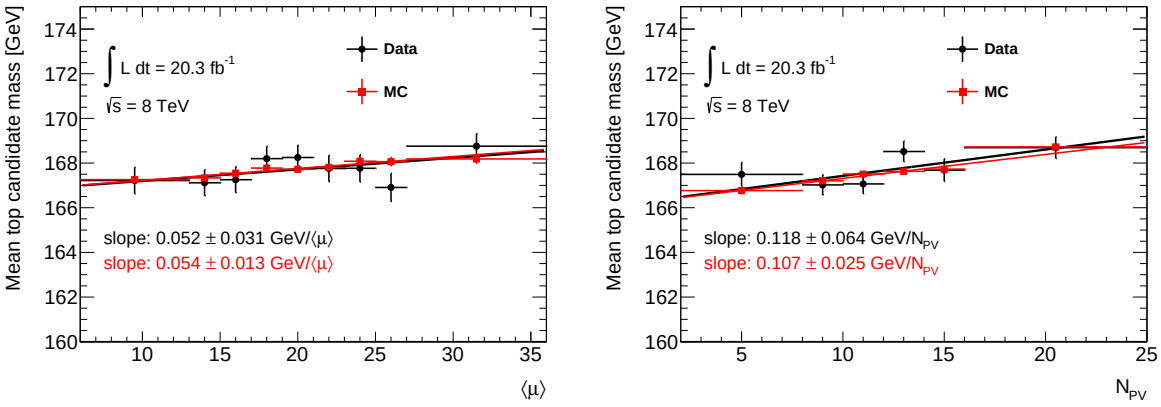

Figure 4.12: Average mass of the reconstructed HEPTopTagger top quark candidate in data (black points) and MC (red points) as a function of the average number of interactions per bunch crossing, $\langle\mu\rangle$, (left) and the number of reconstructed primary vertices, N_{PV}, (right) in events passing the ℓ+jets selection. The mass average is determined in the window $140 < m_t < 210$ GeV. The points are fitted with a linear function and the slope related to the data (MC) fit is displayed in black (red).

4.6 Summary and conclusions

The HEPTopTagger algorithm is used to identify and reconstruct hadronically decaying top quarks with $p_{\mathrm{T}} > 200$ GeV each contained in a large-R jet. The characterisation of this tagger is necessary before its application in physics analyses, for example in searches for physics beyond the SM with top quarks in the final state.

The performance of this algorithm has been studied in proton-proton collision data collected at a centre of mass energy of $\sqrt{s} = 8$ TeV corresponding to an integrated luminosity of 20.3 fb^{-1} [6]. An event sample enriched in $t\bar{t}$ events in the ℓ+jets channel has been selected by requiring one charged lepton, electron or muon, a large-R jet and b-tagged small-R jets. This sample has provided a sizeable fraction of large-R jets originating from hadronically decaying top quarks with a contamination from non-$t\bar{t}$ background less than 10%.

The large-R jet kinematic observables together with the variables used internally by the HEPTopTagger have been found to be well modelled by the simulation. The mass peak very pure of top quarks reconstructed by the HEPTopTagger has been employed to determine in situ the energy scale uncertainty of the HEPTopTagger subjets. The estimated uncertainty for the average p_{T} subjet, about $p_{\mathrm{T}} = 100$ GeV, is measured to be approximately 2.5%. A recipe for the determination of the contribution of this uncertainty in physics analyses has been developed.

The efficiency of tagging a jet containing a hadronically decaying top quark is measured in the ℓ+jets channel as a function of the large-R jet p_{T} in the central and forward η regions. On average about 10% (45%) of large-R jets with $p_{\mathrm{T}} \approx 200$ GeV ($p_{\mathrm{T}} \gtrsim 400$ GeV) associated to hadronically decaying top quarks are identified and

reconstructed by the algorithm. The dominant systematic uncertainty source comes from the modelling of the $t\bar{t}$ SM process. The measured and simulated efficiencies are consistent within a few percent.

This performance study has demonstrated the reliability of employing MC simulation to model and predict the output of the HEPTopTagger algorithm concerning large-R jets from hadronically decaying top quarks.

Chapter 5

Search for direct pair production of the SUSY top quark partner with the HEPTopTagger

Naturalness requires Supersymmetry to be unbroken above energy scales of a few TeV, implying that the mass difference between the top quark and the lightest of its scalar partners, the stop ($\tilde{t}_1$), should be of the order of 1 TeV: the stop could be accessible at the energies of the LHC. If R-parity is conserved, the stop can be produced in pairs at the LHC and the lightest supersymmetric particle (LSP), in many models corresponding to the neutralino ($\tilde{\chi}_1^0$), is stable and weakly interacting. As explained in section 1.4.1, the stop decay modes depend on its mass and the mass of the neutralino, being one of the final products of the stop decay chain. In models with the stop mass being much larger than the neutralino mass, the leading decay mode involves a top quark in the final state: $\tilde{t}_1 \to t\tilde{\chi}_1^0$.

Many analyses in ATLAS and CMS have been performed to look for direct stop production. Searches conducted at a centre of mass energy of $\sqrt{s} = 8$ TeV using a data sample corresponding to integrated luminosities of about 20 fb^{-1} have not revealed any signal [39, 134–138]. Under the assumption of BR($\tilde{t}_1 \to t\tilde{\chi}_1^0$) = 100%, stop masses in the range $200 - 700$ GeV and $200 - 755$ GeV have been excluded for small neutralino masses by ATLAS and CMS, respectively. The most recent searches are performed using data collected at $\sqrt{s} = 13$ TeV corresponding to an integrated luminosity of approximately 13 fb^{-1}. The ATLAS and CMS results improve the limits significantly compared to the 8 TeV analyses: stop masses up to 840 GeV (ATLAS) and 910 GeV (CMS) are excluded [139–146].

The majority of the ATLAS searches at $\sqrt{s} = 8$ TeV make use of resolved or semi-resolved techniques for the reconstruction of the top quarks. As soon as higher and higher stop masses are tested, the top quark in the final state is expected to be boosted enough to impede its reconstruction by means of standard techniques. The HEPTopTagger is perfectly suited to reconstruct the boosted hadronically decaying top quarks from the stop decays and to reject significantly non-top quark hadronic activity, as suggested in [4, 8].

In this chapter, the search for the direct production of a pair of top squarks, each decaying via $\tilde{t}_1 \to t\tilde{\chi}_1^0$, in the all hadronic final state with the HEPTopTagger algorithm is reported. The proton-proton collision data collected at $\sqrt{s} = 8$ TeV is used in this analysis.

The chapter is structured as follows. The HEPTopTagger performance in selecting signal events is studied in section 5.1. Common requirements are shared among the signal enriched regions. These concern the trigger, data quality and loose selection criteria specific to the signal topology under study. Altogether they are referred to as *baseline selection*, and are described in section 5.2. The description of the physics objects used in the analysis, like electrons, muons and jets is also reported in section 5.2. The analysis strategy is explained in section 5.3. It consists in the definition of *signal regions* with enhanced signal over background ratio and in the estimation of the main background sources by means of *control regions* in data. The procedure to statistically evaluate the outcome of the analysis is detailed in section 5.4. The impact of the systematic uncertainties is described in section 5.5 and the analysis results are reported in section 5.6 and 5.7. A comparison with the publicly available ATLAS results at $\sqrt{s} = 8$ TeV which searches for the direct stop production in the fully hadronic final state is discussed in section 5.8.

5.1 Study of the HEPTopTagger performance in simulated SUSY signal events

In this analysis the signature with two hadronically decaying top quarks and missing transverse momentum is considered. This top pair decay mode has two main advantages. Firstly, the fraction of events with both top quarks decaying hadronically is large, around 45%; secondly, the missing transverse momentum in signal events provides direct information on the transverse momentum of the neutralino pair system, as no neutrinos from the top quark decays are present.

The signature of the signal events in the detector is characterised by the presence of jets, some of which might be b-tagged, and large missing transverse momentum, as illustrated in figure 5.1.

Under the assumption that the mass difference between $\tilde{t}_1$ and $\tilde{\chi}_1^0$, $\Delta m(\tilde{t}_1, \tilde{\chi}_1^0) = m_{\tilde{t}_1} - m_{\tilde{\chi}_1^0}$, is much larger than the top quark mass, the tops in the final state are produced with moderate or high momentum. In figure 5.2 the transverse momentum of the top quark produced from a $\tilde{t}_1$ decay is shown for several $\tilde{t}_1$ and $\tilde{\chi}_1^0$ mass hypotheses. The larger the $\tilde{t}_1$ mass and $\Delta m(\tilde{t}_1, \tilde{\chi}_1^0)$ are, the higher the average of the generated top quark p_{T} is. The fraction of signal events having at least one top quark (both top quarks) in the final state with $p_{\mathrm{T}} > 200$ GeV is 90% (50%) for the signal sample with $(m_{\tilde{t}_1}, m_{\tilde{\chi}_1^0}) = (600, 1)$ GeV. In this regime, the hadronic decay products of the top quark start being collimated and might not be reconstructed as separate small-R jets. Therefore top tagging techniques for the reconstruction of these boosted top quarks are crucial to select signal events. In par-

ticular, the HEPTopTagger is well suited for this search [4, 8]. In fact, the algorithm reconstructs hadronically decaying top quarks with $p_{\mathrm{T}} > 200$ GeV from a large-R jet.

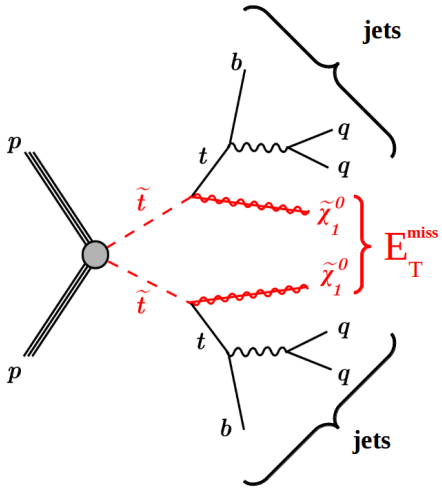

Figure 5.1: Sketch depicting the signature of signal events with a produced $\tilde{t}_1$ pair with each stop decaying via $\tilde{t}_1 \to t\tilde{\chi}_1^0$. The final state with two hadronically decaying top quarks and neutralinos are characterised by jets and missing transverse momentum.

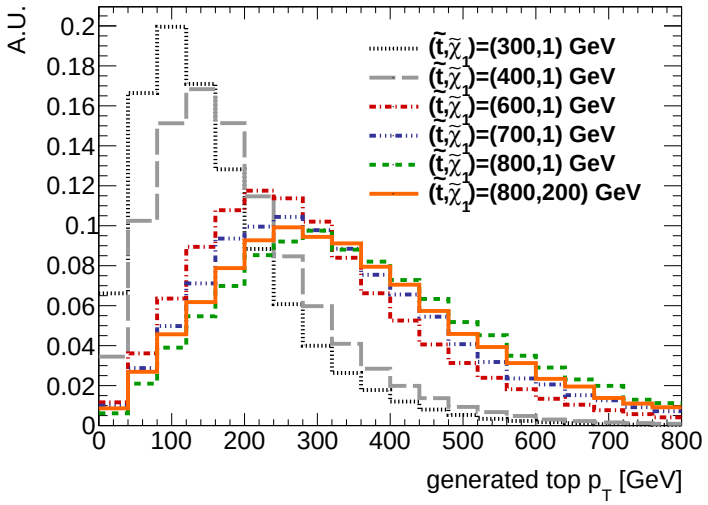

Figure 5.2: Transverse momentum distribution of top quarks from several signal models with different top squark and neutralino masses.

The performance of the HEPTopTagger in data and simulation has been studied in detail in the ℓ+jets channel, as reported in chapter 4. In that case, the hadronically decaying tops of $t\bar{t} \to (l\nu b)(qqb)$ events are mainly isolated, since the two top quarks are produced back-to-back. On the contrary, the two tops of the SUSY signal final state might be close to each other. The distributions of the angular separation between the two top quarks are compared in figure 5.3(a) for the $t\bar{t}$ process and the

signal with $(m_{\tilde{t}_1}, m_{\tilde{\chi}_1^0}) = (600, 1)$ GeV. The first is peaking at π and have less than 4% of events with a top quark angular separation $\Delta R < 1.5$, while the fraction of events with $\Delta R < 1.5$ is about 20% for the signal process. Hence, it is interesting to study the performance of the HEPTopTagger algorithm with respect to this SUSY signal topology.

The number of reconstructed large-R jets and the number of HEPTopTagger candidates depend on the transverse momentum of the two top quarks in each event. As illustrated in figure 5.3(b), the transverse momenta of the top quarks produced by the decay of a stop pair are mutually independent, while they are correlated in the $t\bar{t}$ process, see figure 5.3(c).

The performance of reconstructing one or two top tags in a signal sample with $(m_{\tilde{t}_1}, m_{\tilde{\chi}_1^0}) = (600, 1)$ GeV is discussed in the following.

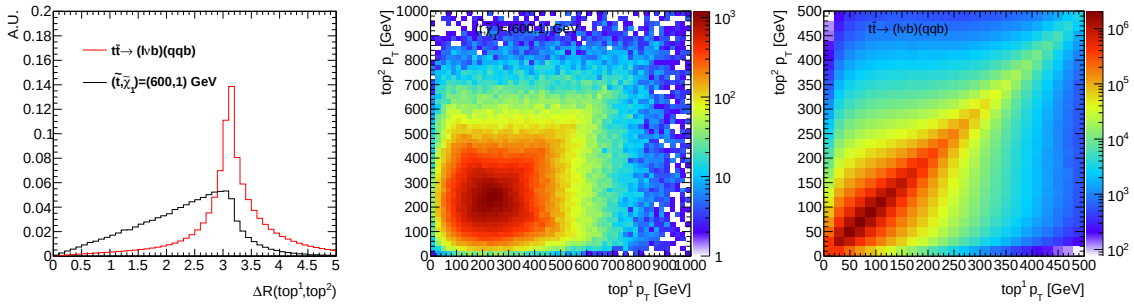

(a) (b) (c)

Figure 5.3: (a) Comparison of the ΔR angular distance distributions between the two top quarks, generically called top^1 and top^2, for the simulated $t\bar{t}$ process (red line) and the SUSY signal process with $(m_{\tilde{t}_1}, m_{\tilde{\chi}_1^0}) = (600, 1)$ GeV (black line). Correlation between the transverse momenta of the two top quarks in simulated signal (b) and $t\bar{t}$ events (c).

5.1.1 HEPTopTagger tagging efficiencies

The HEPTopTagger tagging efficiency is defined as the fraction of generated hadronically decaying top quarks with $|\eta| < 2$, such that a top candidate is found within an angular distance of $\Delta R(\text{gen. top, top cand.}) < 1$ from the generated top. This efficiency is highly dependent on the generated top quark transverse momentum. In figure 5.4(a), the probability of reconstructing a hadronically decaying top quark becomes higher with the transverse momentum of the top quark, $p_{\mathrm{T}}^{\mathrm{top}}$, and reaches a plateau of approximately 40% when $p_{\mathrm{T}}^{\mathrm{top}} > 400$ GeV. In fact the higher the top quark transverse momentum is, the more collimated its decay products are and the higher the probability of reconstructing all them together in a single large-R jet becomes. At low transverse momentum, the tagging efficiency is smaller for top quarks which are distant from other tops, i.e. $\Delta R > 2.0$. In fact, for low p_{T} tops, one decay product might be lost outside of the large-R jet, J, and therefore the probability of

tagging it is much smaller. But if a second top quark decays hadronically nearby, one of its decay products might be reconstructed in the large-R jet J, enhancing the chances of mis-reconstructing a top candidate in J.

In figure 5.4(b) the efficiency of tagging a moderately boosted top quark, with $p_{\mathrm{T}}^{\mathrm{top}} < 300$ GeV, significantly depends on the distance between the two hadronically decaying top quarks: it increases if the two are closer than the distance parameter $R = 1.5$ of the large-R jet.

Signal events are characterised by moderately large missing transverse momentum. The tagging efficiency is independent of this variable, see figure 5.4(c). The slight increase in tagging efficiency for moderate p_{T} top quarks ($200 < p_{\mathrm{T}} < 250$) does not directly depend on $E_{\mathrm{T}}^{\mathrm{miss}}$, but it is rather related to the lower average angular separation between the two tops in events with higher $E_{\mathrm{T}}^{\mathrm{miss}}$. The dependence of the average angular distance of the top quarks with respect to the event missing transverse momentum is represented in figure 5.4(d).

In every event it is possible that two top candidates are reconstructed. The double tagging efficiency is defined as the fraction of fully hadronic events with two top tags, with each tag being close to one of the two hadronically decaying top quarks ($\Delta R < 1.0$). In figure 5.5(a), its dependence with respect to the average top quark transverse momentum is shown. Contrary to what was observed for the efficiency of tagging only one top quark, the double tagging efficiency relative to top quarks with $p_{\mathrm{T}} < 400$ GeV decreases when the two top quarks are too close to each other 5.5(b): the reconstruction of two large-R jets becomes unfeasible when the two tops are too close.

5.1.2 M_{T2}, the *stransverse mass*

The kinematic information given by two reconstructed HEPTopTagger candidates is useful to construct a variable, called M_{T2} or *stransverse mass* [147–150], which aims to extract information regarding the pair-produced particle mass: the $\tilde{t}_1$ mass in the current search.

In general, the mass of a decaying particle can be calculated if the four-momenta of its daughters are known. If one of the decay products escape the detector, the missing momentum in the transverse plane is the only information that can be used to calculate the transverse mass of the original particle. For example, the transverse mass of the W boson, which undergoes a leptonic decay $W \to \ell\nu$, is defined as:

$$\begin{aligned} M_{\mathrm{T}}^{W} &\equiv \sqrt{(E_{\mathrm{T},\ell} + E_{\mathrm{T},\nu})^2 - (\vec{p}_{\mathrm{T},\ell} + \vec{p}_{\mathrm{T},\nu})^2} \\ &= \sqrt{m_\ell^2 + m_\nu^2 + 2(E_{\mathrm{T},\ell}E_{\mathrm{T},\nu} - \vec{p}_{\mathrm{T},\ell} \cdot \vec{p}_{\mathrm{T},\nu})}\,, \end{aligned} \tag{5.1}$$

where $E_{\mathrm{T}} = \sqrt{m^2 + p_{\mathrm{T}}^2}$, m_ℓ ($\vec{p}_{\mathrm{T},\ell}$) and m_ν ($\vec{p}_{\mathrm{T},\nu}$) are the masses (vectorial transverse momenta) of the charged lepton ℓ and of the neutrino ν, respectively. The

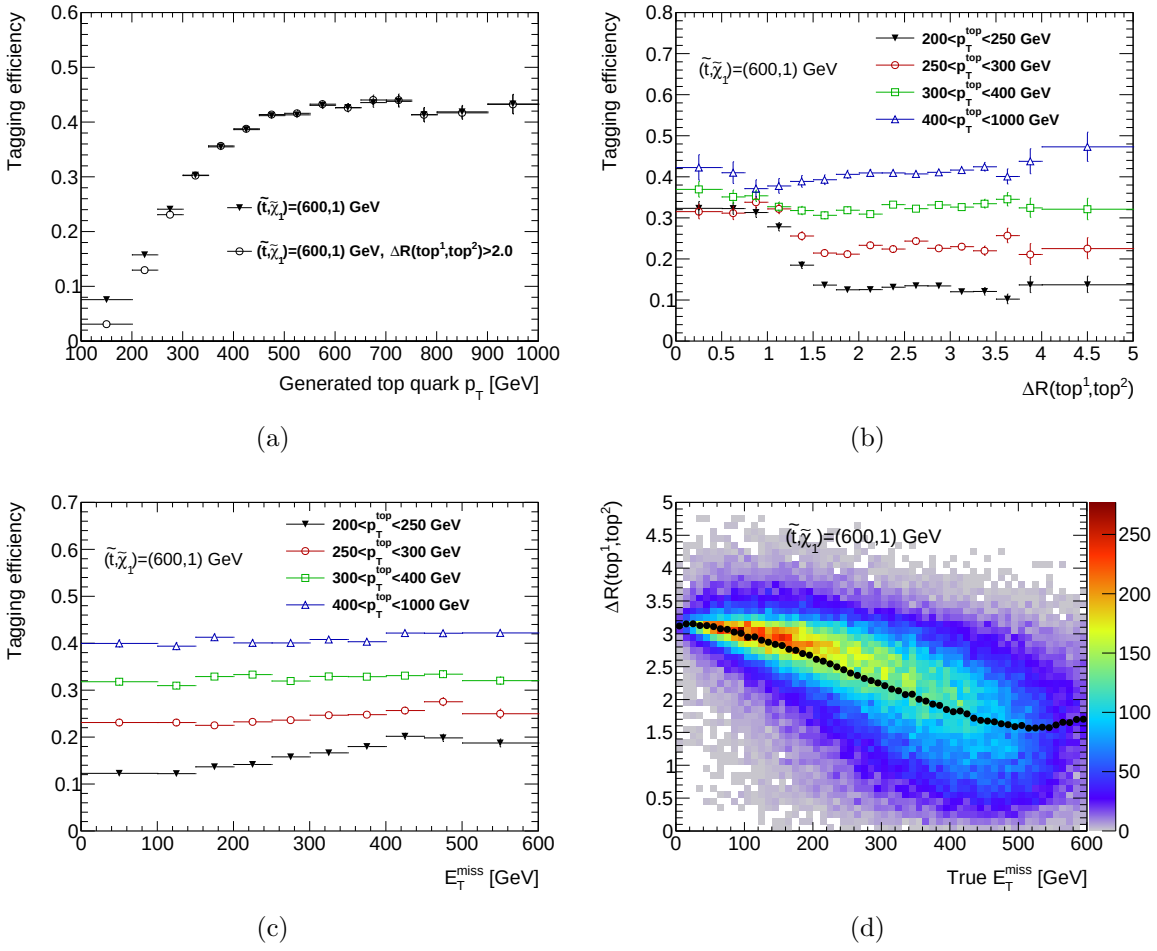

Figure 5.4: Distributions of the simulated $(m_{\tilde{t}_1}, m_{\tilde{\chi}_1^0}) = (600, 1)$ GeV signal sample. (a) Efficiency of tagging hadronically decaying top quarks with (without) an isolation requirement marked with empty circles (filled triangles) as a function of the generated top transverse momentum. Top-tagging efficiency as a function of the angular distance between the top quark pair in each event for different ranges of the generated top transverse momentum (b) and as a function of the event missing transverse momentum (c). (d) Correlation of the generated missing transverse momentum with respect to the angular distance between the two top quarks; the mean of the ΔR distribution as a function of the missing transverse momentum is overlaid as black points.

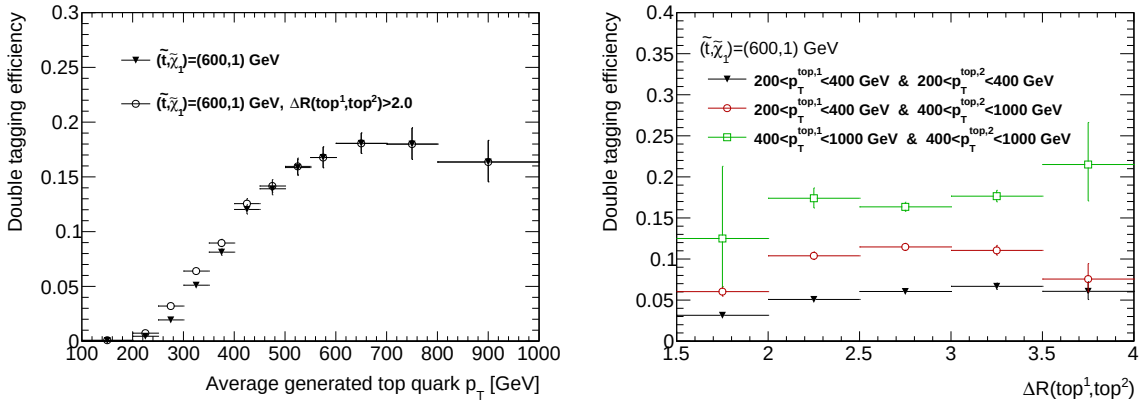

(a) (b)

Figure 5.5: Distributions of the simulated $(m_{\tilde{t}_1}, m_{\tilde{\chi}_1^0}) = (600, 1)$ GeV signal sample. (a) Efficiency of tagging both tops in events with two hadronically decaying top quarks with (without) an isolation requirement marked with empty circles (filled triangles) as a function of the generated top transverse momentum. Efficiency of tagging both tops as a function of the angular distance between the top quark pair in each event for different ranges of the generated top transverse momenta (b).

endpoint of the M_{T}^W distribution is the W boson mass, $M_{\mathrm{T}}^W \leq m_W$. Since m_ℓ and m_ν are negligible and $\vec{p}_{\mathrm{T},\nu} = \vec{E}_{\mathrm{T}}^{\mathrm{miss}}$, the equation 5.1 reduces to equation 4.1.

If the neutralino transverse momentum ($\vec{p}_{\mathrm{T},\tilde{\chi}_1^0}$) were known, the transverse mass of the $\tilde{t}_1$ particle, $M_{\mathrm{T}}^{\tilde{t}_1}$, could be calculated after the reconstruction of the top quark transverse momentum, $\vec{p}_{\mathrm{T},t}$. The same relation would be valid: $M_{\mathrm{T}}^{\tilde{t}_1}(\vec{p}_{\mathrm{T},t}, \vec{p}_{\mathrm{T},\tilde{\chi}_1^0}) \leq m_{\tilde{t}_1}$.

However, in the all-hadronic channel under study, the particles escaping the detectors are two neutralinos, $\tilde{\chi}_{1,a}^0$ and $\tilde{\chi}_{1,b}^0$ and their transverse momenta $\vec{p}_{\mathrm{T},\tilde{\chi}_{1,a}^0}$ and $\vec{p}_{\mathrm{T},\tilde{\chi}_{1,b}^0}$ cannot be individually assessed. The measured missing transverse momentum, $\vec{E}_{\mathrm{T}}^{\mathrm{miss}}$, carries the information only of the sum of their transverse momenta:

$$\vec{E}_{\mathrm{T}}^{\mathrm{miss}} = \vec{p}_{\mathrm{T},\tilde{\chi}_{1,a}^0} + \vec{p}_{\mathrm{T},\tilde{\chi}_{1,b}^0}. \tag{5.2}$$

This constraint allows the construction of a quantity, M_{T2}, which satisfies the relation $M_{\mathrm{T2}} \leq m_{\tilde{t}_1}$. In fact, the $(\vec{p}_{\mathrm{T},\tilde{\chi}_{1,a}^0}, \vec{p}_{\mathrm{T},\tilde{\chi}_{1,b}^0})$ parameter space is scanned with the constraint stated in equation 5.2, and the maximum value between the squared $\tilde{t}_1$ transverse masses, $(M_{\mathrm{T}}^{\tilde{t}_1}(\vec{p}_{\mathrm{T},t}, \vec{p}_{\mathrm{T},\tilde{\chi}_{1,a}^0}))^2$ and $(M_{\mathrm{T}}^{\tilde{t}_1}(\vec{p}_{\mathrm{T},t}, \vec{p}_{\mathrm{T},\tilde{\chi}_{1,b}^0}))^2$, is chosen. The minimum over several $(\vec{p}_{\mathrm{T},\tilde{\chi}_{1,a}^0}, \vec{p}_{\mathrm{T},\tilde{\chi}_{1,b}^0})$ points is defined as M_{T2}^2:

$$M_{\mathrm{T2}}^2 = \min_{\vec{E}_{\mathrm{T}}^{\mathrm{miss}} = \vec{p}_{\mathrm{T},\tilde{\chi}_{1,a}^0} + \vec{p}_{\mathrm{T},\tilde{\chi}_{1,b}^0}} \left(\max \left(\left(M_{\mathrm{T}}^{\tilde{t}_1}(\vec{p}_{\mathrm{T},t}, \vec{p}_{\mathrm{T},\tilde{\chi}_{1,a}^0})\right)^2, \left(M_{\mathrm{T}}^{\tilde{t}_1}(\vec{p}_{\mathrm{T},t}, \vec{p}_{\mathrm{T},\tilde{\chi}_{1,b}^0})\right)^2 \right) \right) \tag{5.3}$$

M_{T2} is derived under the assumption that both $\tilde{t}_1$ squarks decay in the same mode and under a $\tilde{\chi}_1^0$ mass hypothesis, chosen to be 1 GeV in this thesis for the M_{T2} calculation.

The distribution of the generated M_{T2} variable, constructed from the true missing transverse momentum and the simulated top quark four-momenta, referred to as *true* M_{T2}, for different $m_{\tilde{t}_1}$ and $m_{\tilde{\chi}_1^0}$ hypothesis is shown in figure 5.6. The samples with the $\tilde{\chi}_1^0$ mass of 1 GeV, assumed also for the M_{T2} calculation, have an endpoint at the generated $\tilde{t}_1$ mass. If $m_{\tilde{\chi}_1^0} > 1$ GeV, the endpoint does not correspond any more to the $\tilde{t}_1$ mass and the distribution is shifted to lower values of M_{T2}.

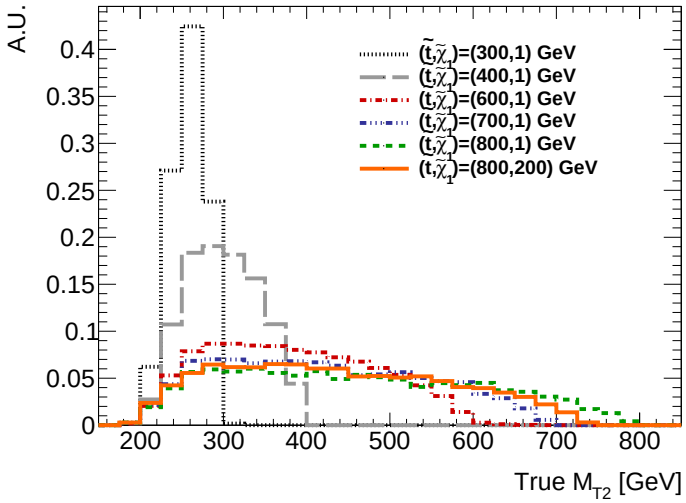

Figure 5.6: Distribution of the generated M_{T2} for different signal models.

At the experimental level, the calculation of the M_{T2} profits from the reconstruction of two HEPTopTagger candidates, which provide the top quark transverse momenta and masses needed in equation 5.3.

The dependence of the double tagging efficiency as a function of the M_{T2} is shown in figure 5.7(a). The correlation of M_{T2} with the angular distance between the two top quarks is illustrated in figure 5.7(b). Similarly to the missing transverse energy, on average the two top quarks are closer, the higher M_{T2} is, see figure 5.7(b). Therefore, if one of the two generated top transverse momenta is below 400 GeV the efficiency of tagging both quarks decreases with the increase of M_{T2} (figure 5.7(a)).

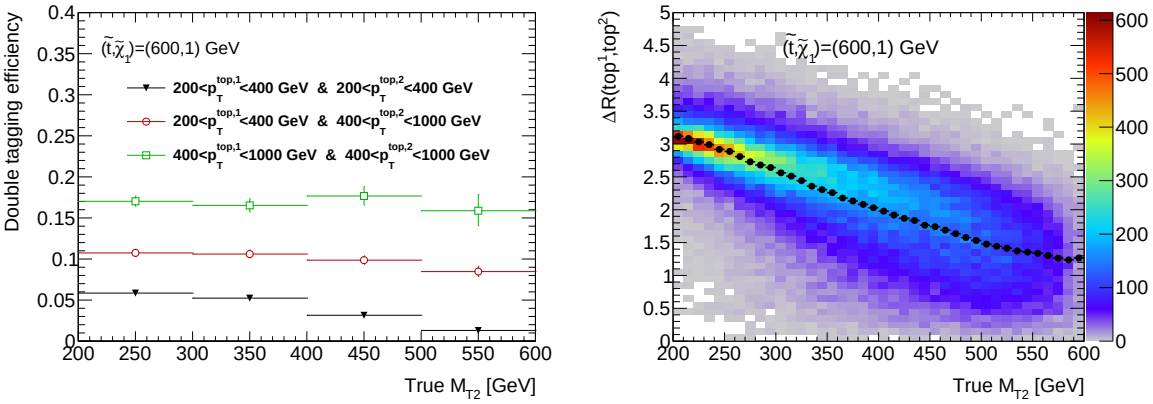

(a) (b)

Figure 5.7: Distributions of the simulated $(m_{\tilde{t}_1}, m_{\tilde{\chi}_1^0}) = (600, 1)$ GeV signal sample. (a) Efficiency of tagging both tops as a function of the M_{T2} calculated from generator level observables. (b) Correlation of M_{T2} with respect to the angular distance between the two top quarks (top^1 and top^2); the mean of the ΔR distribution as a function of M_{T2} is overlaid as black points.

5.1.3 M_{T2} resolution

The performance in the reconstruction of M_{T2} depends on the momentum resolution of the reconstructed top candidates. The HEPTopTagger reconstruction performance is studied in the signal sample with $(m_{\tilde{t}_1}, m_{\tilde{\chi}_1^0}) = (600, 1)$ GeV by comparing the candidate transverse momentum with respect to the associated generated top quark (ΔR(gen. top, top cand.) < 1.0). Only isolated hadronically decaying top quarks with $p_T > 200$ GeV are taken into account. The isolation criterion consists of requiring that no other top quark is found within an angular separation of 2.

The distribution of the ratio between the reconstructed and the generated top quark p_T is given for different ranges of the generated top quark p_T. The shape of the distribution is Gaussian between 0.8 and 1.2 and contains approximately 85% of the entries, but presents non-Gaussian tails outside this range. The mean and width (σ) parameters of the Gaussian fit performed in the central part of the distribution are shown in figure 5.8(a) and 5.8(b), respectively. The Gaussian mean is close to one over most of the p_T range. The resolution of the reconstructed top p_T improves with the increase in top p_T.

If two top quarks are reconstructed, M_{T2} can be calculated. The comparison between the reconstructed and true M_{T2} is shown in figure 5.9 for the signal sample with $(m_{\tilde{t}_1}, m_{\tilde{\chi}_1^0}) = (600, 1)$ GeV. A Gaussian fit of the reconstructed and true M_{T2} ratio is performed: on average the reconstructed M_{T2} is close to the true value with a resolution of approximately 7%.

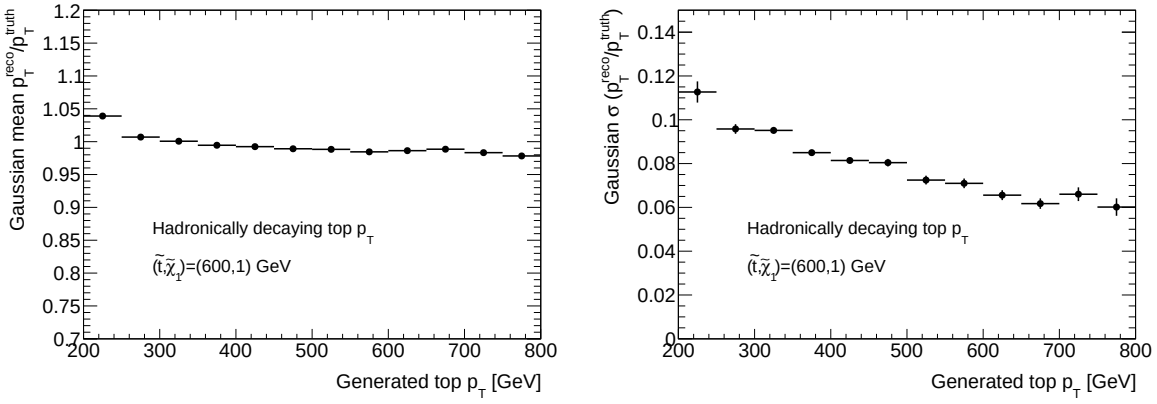

(a) (b)

Figure 5.8: Distributions of the simulated $(m_{\tilde{t}_1}, m_{\tilde{\chi}_1^0}) = (600, 1)$ GeV signal sample. Gaussian fit mean (a) and standard deviation (b) of the distribution of the reconstructed and generated top transverse momentum ratio as a function of the generated top p_{T}.

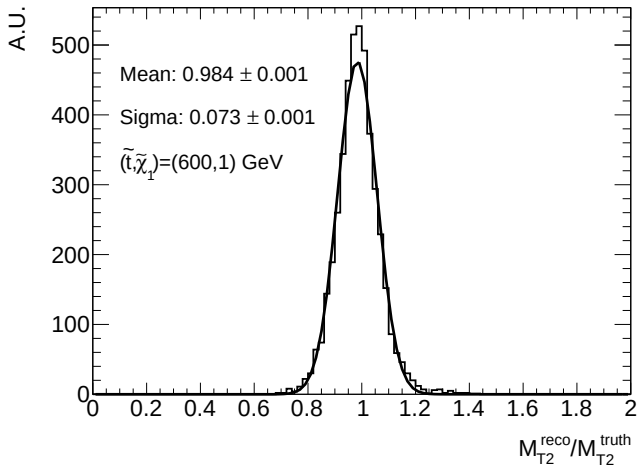

Figure 5.9: Distribution of the generated and reconstructed M_{T2} ratio. Superimposed is the Gaussian fit with 0.984 mean value and 0.073 standard deviation.

5.2 Object reconstruction and baseline event selection

The experimental signature for this search is characterised by large missing transverse momentum and hadronic activity, reconstructed as C/A jets with $R = 1.5$ and tagged by the HEPTopTagger. A baseline event selection in part identical to many all-hadronic ATLAS supersymmmetric searches is applied. In particular the baseline selection of this analysis is similar to the ATLAS one, published with data collected at $\sqrt{s} = 8$ TeV, targeting at the same signal process (direct stop pair production) in the all hadronic final state [7].

An integrated luminosity of 20 fb^{-1} of data is collected by a missing transverse energy trigger. The first level trigger selects events for which transverse vector sum of all trigger towers is larger than 40 GeV. Afterwards, events having an HLT missing transverse energy larger than 80 GeV, calculated using the vector sum of the calibrated clusters of calorimeter cells, are used for the analysis. This trigger reaches an efficiency greater than 98% for an offline reconstructed $E_{\mathrm{T}}^{\mathrm{miss}}$ of at least 150 GeV, as can be seen from figure 5.10.

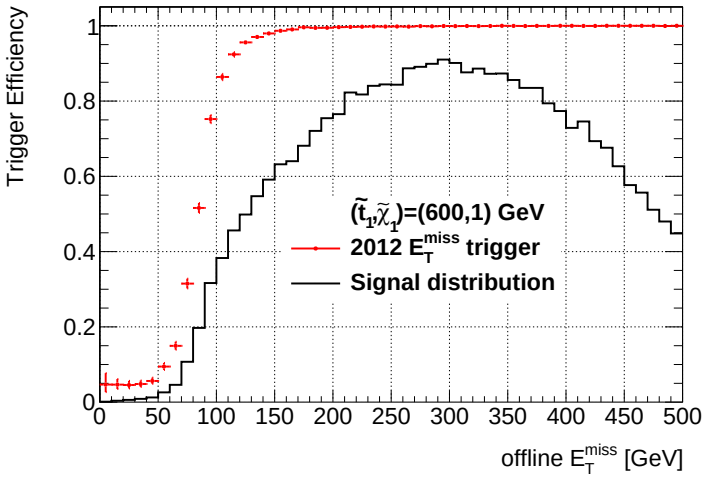

Figure 5.10: In red, simulated 2012 $E_{\mathrm{T}}^{\mathrm{miss}}$ trigger efficiency in a direct stop pair production sample for selected events with muon and electron veto and one large-R jet with $p_{\mathrm{T}} > 200$ GeV. The lowest unprescaled $E_{\mathrm{T}}^{\mathrm{miss}}$ trigger chain consists in $E_{\mathrm{T}}^{\mathrm{miss}} > 80$ GeV at the EF level, $E_{\mathrm{T}}^{\mathrm{miss}} > 45$ GeV at L2 and $E_{\mathrm{T}}^{\mathrm{miss}} > 40$ GeV at L1. The offline $E_{\mathrm{T}}^{\mathrm{miss}}$ distribution for the direct stop pair production is overlaid as a black line.

In addition to the quality requirements described in section 4.1.2, events with muons not originating from the interaction point, which might also be coming from cosmic rays, are discarded.

5.2.1 Monte Carlo samples

The simulation is used to describe the background and the signal distributions in this analysis. The background consists of processes characterised by the presence of large missing transverse energy and hadronic activity. These are:

- $t\bar{t} \to (l\nu b)(qqb)$: $l = e, \mu, \tau$;
- V+jets: $V = Z, W$ vector boson produced in association with jets;
- single top;
- VV: (ZZ, WW, ZW) diboson production;
- $t\bar{t}V$: associated production of a top quark pair and a vector boson.

The $t\bar{t}$ contribution in the fully hadronic final state is found negligible in this analysis.

The signal samples are generated according to the simplified model approach: the direct production of a stop pair is simulated in the $\tilde{t}_1 \to t\tilde{\chi}_1^0$ decay mode, with 100% branching ratio. The stop mass and the neutralino mass are the only free parameters of the model, and define univocally the signal sample. A collection of signal samples is generated covering a grid in the stop-neutralino mass plane, with stop mass ranging from 250 to 800 GeV with 50 GeV spacing and neutralino masses $m_{\tilde{\chi}_1^0} \geq 1$ GeV with 50 GeV spacing, such that $m_{\tilde{t}_1} - m_{\tilde{\chi}_1^0} > m_t$.

The detailed description of the MC settings (the generator, the parton shower, the underlying event modelling, and the set of PDFs), used to produce the samples, are described in section 2.6.

A preliminary comparison between the data and the MC expectation is performed in control regions, and the SM background yield is normalised to the theory cross sections. The full cross section description is given in section 2.6.

5.2.2 Object reconstruction

Electron and muon candidates, small-R jets which may be b-tagged, large-R jets and missing transverse momentum are the objects used in this analysis. Their reconstruction proceeds as explained in section 2.5. The main object requirements are summarised in table 5.1.

The overlap between reconstructed electrons, muons and jets is removed by considering the angular distance between the leptons and the jets. If a muon is found to be angularly close to the jet, $\Delta R(\mu, \text{jet}) < 0.4$ the first is discarded. An electron is rejected if its separation from a jet is $0.2 < \Delta R(e, \text{jet}) < 0.4$ or if it is close to a b-tagged jet with $\Delta R(e, \text{jet}) < 0.2$. Otherwise the calorimetric object is considered to be an electron.

muon $p_{\mathrm{T}}^{\mu} >$	10 GeV
loose electron $E_{\mathrm{T}}^{e} >$	10 GeV
small-$R = 0.4$ anti-k_t jet $p_{\mathrm{T}} >$	35 GeV
small-$R = 0.4$ anti-k_t (b-)jet $\lvert\eta\rvert <$	2.8 (2.5)
large-$R = 1.5$ C/A jet $p_{\mathrm{T}} >$	200 GeV
large-$R = 1.5$ C/A jet $\lvert\eta\rvert <$	2.0
$E_{\mathrm{T}}^{\mathrm{miss}} >$	150 GeV

Table 5.1: Main selection criteria for the object reconstruction.

5.2.3 Baseline selection

In order to select only events with hadronically decaying top quarks, those events containing reconstructed electrons or muons are vetoed ($N_e = 0$ and $N_\mu = 0$, being N_e and N_μ the number of reconstructed electrons and muons, respectively). The selected event fraction corresponds approximately to 60% of the total signal events.

The minimal offline $E_{\mathrm{T}}^{\mathrm{miss}}$ requirement consistent with the plateau region of the $E_{\mathrm{T}}^{\mathrm{miss}}$ trigger is 150 GeV. This reduces the fraction of signal events to 50%, with $(m_{\tilde{t}_1}, m_{\tilde{\chi}_1^0}) = (600, 1)$ GeV. This $E_{\mathrm{T}}^{\mathrm{miss}}$ requirement reduces the multijet background. However, a consistent fraction of multijet events are characterised by fake $E_{\mathrm{T}}^{\mathrm{miss}}$. If the reconstructed four-vector of a jet is mis-measured, a fake transverse momentum imbalance could lead to the selection of the multijet event. The jet term of equation 2.5 is the dominant component of the $E_{\mathrm{T}}^{\mathrm{miss}}$ calculation in such events characterised mainly by hadronic activity. Thus, the missing transverse momentum is most probably aligned with one of the highest-p_{T} small-R jets of the event. The absolute value of the jet-$E_{\mathrm{T}}^{\mathrm{miss}}$ angular separation, $\Delta\phi$, being the difference between the ϕ azimuthal angles of $\vec{E}_{\mathrm{T}}^{\mathrm{miss}}$ and of each of the three p_{T}-leading small-R jets, jet^0, jet^1 and jet^2, is small for multijet events, as can be seen in figure 5.11(a) and 5.11(b) for the second- and third-leading jet (jet^1 and jet^2). The $\Delta\phi$ distribution is different for the signal process where the reconstructed missing transverse momentum is mainly due to particles escaping the detector. Thus, the missing transverse momentum is not aligned with the three leading small-R jets. The requirement $|\Delta\phi(\mathrm{jet}^{0,1,2}, \vec{E}_{\mathrm{T}}^{\mathrm{miss}})| > \pi/5$ rejects most of the multijet background with a small impact on the signal acceptance.

The Standard Model background sources, which are left after the previous selection, are composed of those processes which are characterised by large missing transverse energy and hadronic activity. One of the major contributions is given by $t\bar{t} \to (l\nu b)(qqb)$, where l is most likely a τ lepton. The production of a vector boson (W or Z) in association with jets, or with $t\bar{t}$, contributes to the background predominantly in the $Z \to \nu\nu$ and $W \to \tau\nu$ channels. Finally, single top and diboson production processes are the remaining background sources.

C/A $R = 1.5$ jets are reconstructed and calibrated. The p_{T} distribution of the leading large-R jet is shown in figure 5.12(a). For low p_{T} large-R jets, the main detector systematic uncertainty is due to the small-R jet energy scale, which has an impact

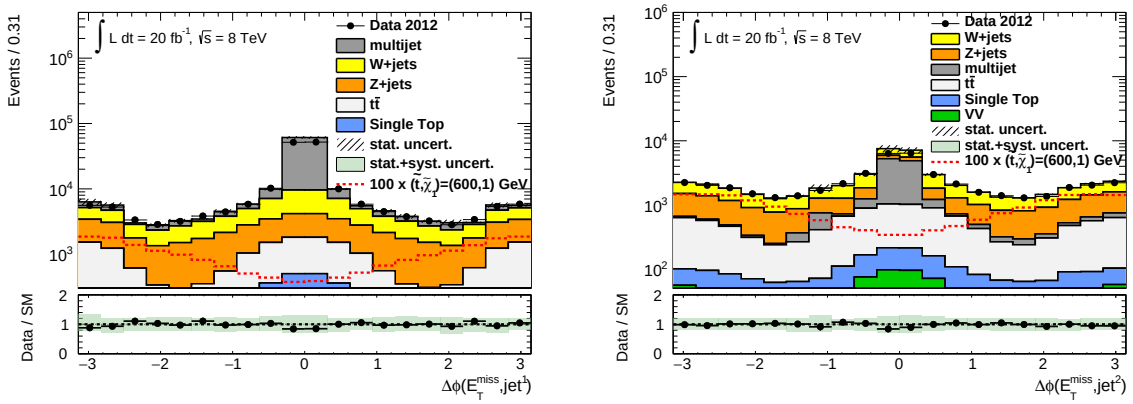

(a) (b)

Figure 5.11: Distributions of the azimuthal angular distance between the direction of the missing transverse momentum and the second-leading (a) and third-leading (b) small-R jet p_{T}. The requirement of $|\Delta\phi(\mathrm{jet}^0, \vec{E}_{\mathrm{T}}^{\mathrm{miss}})| > \pi/5$ and $|\Delta\phi(\mathrm{jet}^{0,1}, \vec{E}_{\mathrm{T}}^{\mathrm{miss}})| > \pi/5$ is applied to obtain the distribution in (a) and (b), respectively. The SM background prediction is represented as a stacked histogram while the data distribution is overlaid as black points. The signal expectation for the sample with $(m_{\tilde{t}_1}, m_{\tilde{\chi}_1^0}) = (600, 1)$ GeV is multiplied by a factor reported in the legend to improve visibility and is represented by a red dashed line. The lower panel shows the ratio between the data and the SM prediction and overlaid is the impact of the systematic and statistical uncertainties added in quadrature.

on the $E_{\mathrm{T}}^{\mathrm{miss}}$ reconstruction. On the contrary, the large-R jet energy scale uncertainty increases with the jet p_{T}, as described in section 4.3.2 concerning figure 4.8(a). The SM background p_{T} distribution is characterised by a steeply falling spectrum, while the signal p_{T} distribution has its maximum at approximately $p_{\mathrm{T}}^{\text{large-}R\text{ jet}} \sim 350$ GeV. Events containing a leading large-R jet with $p_{\mathrm{T}}^{\text{large-}R\text{ jet}} > 280$ GeV are selected. Approximately 25% of the so-far-selected signal events are rejected after this p_{T} requirement .

The missing transverse energy distributions in figure 5.12(b) have similar features to the leading large-R jet p_{T}. While the background is mainly characterised by low $E_{\mathrm{T}}^{\mathrm{miss}}$, large missing transverse energy identifies signal events.

Two hadronically decaying top quarks are produced in a signal event. Thus, it can happen that a second large-R jet is reconstructed. Its p_{T} distribution can be seen in figure 5.12(c). The sub-leading large-R jet has low transverse momentum for both signal and background processes.

The dominant background components before the requirement of a reconstructed HEPTopTagger candidate are Z+jets, W+jets, $t\bar{t}$, which contribute 35%, 35% and 21%, respectively, to the total expected background. After requiring the leading large-R jet to be tagged, the multijet background contribution becomes negligible, the $t\bar{t}$ becomes the dominant one, followed by Z+jets and W+jets. The percentage contributions of the different processes after the requirement of the leading large-R

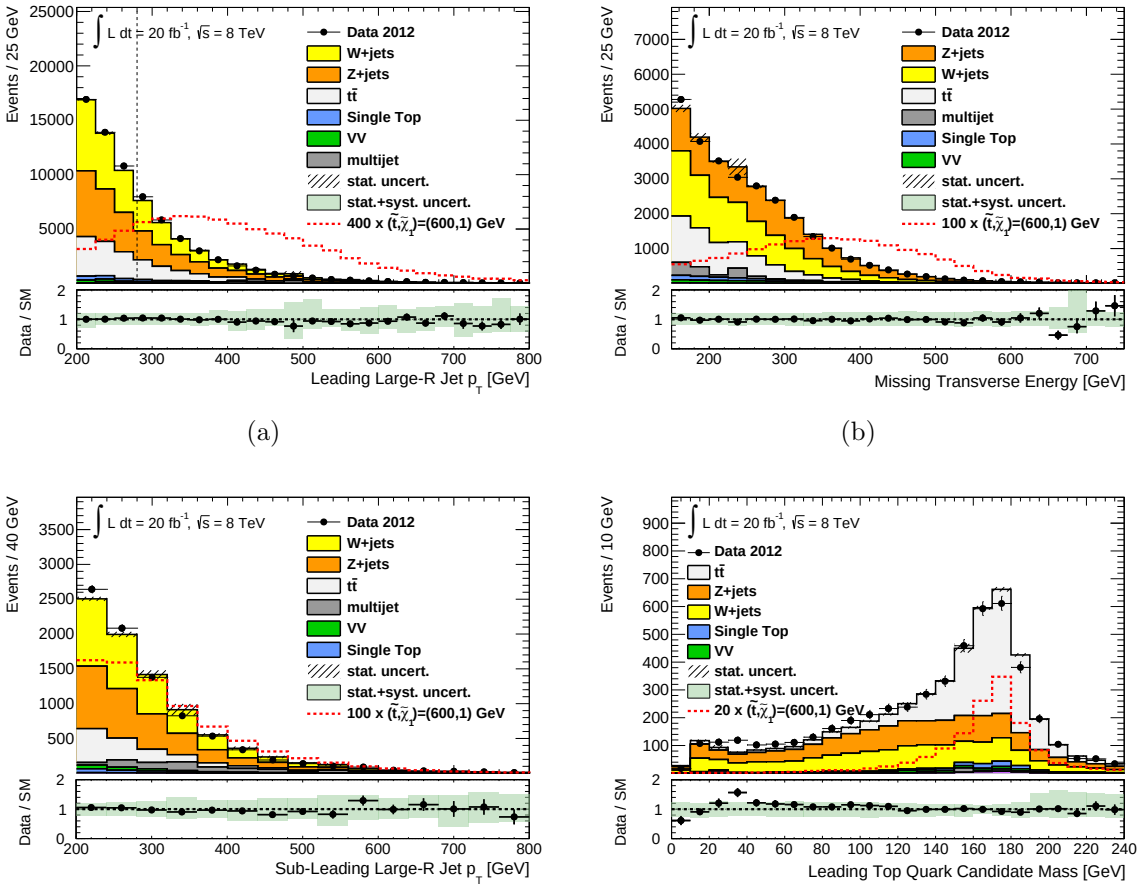

Figure 5.12: Distributions of the transverse momentum of the highest-p_{T} large-R jet (a), of $E_{\mathrm{T}}^{\mathrm{miss}}$ (b), of the transverse momentum of the second highest-p_{T} large-R jet (if reconstructed) (c), and of the top quark candidate mass reconstructed by the HEPTopTagger (d). The requirement on the top candidate mass window is not applied in figure (d). The style convention is identical to figure 5.11.

Process	Composition pre-tag	Composition post-tag
Z+jets	35%	18%
W+jets	35%	16%
$t\bar{t}$	21%	60%
multijet	4%	1%
Single top	2%	3%
VV	2%	2%
$t\bar{t}$ V	$< 1\%$	$< 1\%$
total expected events in 20 fb^{-1}	$\sim 28 \times 10^3$	$\sim 3 \times 10^3$

Table 5.2: Relative contribution of different background sources express in percentage after the quality, the trigger, the missing transverse energy and the large-R jet requirements, referred to as pre-tag. Concerning the post-tag column the additional requirement of a reconstructed HEPTopTagger candidate is applied. The sum of the contributions is 100%.

jet p_{T} to be greater than 280 GeV, *pre-tag*, and after an HEPTopTagger candidate is found in the event, *post-tag*, are shown in table 5.2.

The HEPTopTagger candidate mass distribution, reconstructed from the constituents of the leading large-R jet, is shown in figure 5.12(d). The signal distribution peaks at the top quark mass with a full width at half maximum of about 30 GeV, similarly to the $t\bar{t}$ background, where a hadronically decaying top quark is reconstructed. The distributions of W+jets and Z+jets which do not contain any top quark decay are characterised by a broader structure. In this analysis, the $\arctan(m_{13}/m_{12})$ is required to be in the range (0.3, 1.2), with respect to what was described in section 3.1, as it leads to a reduction of the non-top quark background with a negligible effect on the signal efficiency. The large-R jet is tagged by the HEPTopTagger, if the top candidate mass is within the $(140, 210)$ GeV mass window.

The baseline requirements are summarised in table 5.3 with the corresponding efficiency loss for the signal sample with $(m_{\tilde{t}_1}, m_{\tilde{\chi}_1^0}) = (600, 1)$ GeV. Events with final state top quarks decaying semileptonically are included. The main reduction of the signal acceptance is given as expected by the lepton veto, and by the requirement of a reconstructed HEPTopTagger candidate. Concerning the $(m_{\tilde{t}_1}, m_{\tilde{\chi}_1^0}) = (600, 1)$ GeV signal sample, the signal rate is approximately reduced by a factor of ten.

Selection	Fraction of events $(m_{\tilde{t}_1}, m_{\tilde{\chi}_1^0}) = (600, 1)$ GeV
Quality requirements	98%
$N_e = 0$ & $N_\mu = 0$	61%
$E_{\mathrm{T}}^{\mathrm{miss}}$ trigger	57%
$E_{\mathrm{T}}^{\mathrm{miss}} > 150$ GeV	50%
$\lvert\Delta\phi(\mathrm{jet}^{0,1,2}, \vec{E}_{\mathrm{T}}^{\mathrm{miss}})\rvert > \pi/5$	42%
large-R jet, $p_{\mathrm{T}} > 280$ GeV	33%
HEPTopTagger candidate $p_{\mathrm{T}} > 200$ GeV	13%

Table 5.3: Baseline selection criteria with the corresponding fraction of selected events (always with respect to the total events in the signal sample including those with final state top quarks decaying semileptonically.). The signal sample considered has $(m_{\tilde{t}_1}, m_{\tilde{\chi}_1^0}) = (600, 1)$ GeV. For each row, the left column selection criteria in upper rows are applied in logical conjunction (AND).

5.3 Analysis strategy

The signature of the signal process is similar to other SM processes with much larger cross sections. A tight selection has to be applied in order to maximise the sensitivity of this search. Regions of phase space are defined to select a significant excess of predicted signal events with respect to the expected background. These signal regions (SRs) are described in section 5.3.1.

Two approaches are taken into account to estimate the background, as explained in section 5.3.2. The contribution to the SRs of those SM processes with a small cross section is predicted by the simulation yields normalised to the theory cross section. A more robust approach is used to estimate the impact of the main background sources: $t\bar{t}$ and V+jets. Control regions (CRs) enriched in these types of processes are defined in order to extract normalisation factors by comparing the data and the simulated distributions. Systematic uncertainties related to these background sources are then constrained in these regions. The outcome of the background estimation is probed in validation regions (VRs), defined to be kinematically close to the SRs, as described in section 5.3.3.

A likelihood fit is performed to test the background-only hypothesis or the signal-plus-background hypothesis and to extract the final result. The contribution of signal and background processes are simultaneously taken into account in the three different types of regions. Normalisation factors for simulated background processes and constraints on systematic uncertainties are extracted from the fit. The fit and the hypothesis testing are described in section 5.4.

5.3.1 Signal regions

The search for the fully hadronic final state of the $\tilde{t}_1 \to t\tilde{\chi}_1^0$ pair production, where the $\tilde{t}_1$ is heavy and much heavier than the $\tilde{\chi}_1^0$, can benefit significantly by the selection of events with large M_{T2}. The discrimination power of this variable is illustrated in figure 5.13, where the background distribution represented by the $t\bar{t} \to (l\nu b)(qqb)$ process is compared to several signal samples. The majority of $t\bar{t}$ background events can be rejected by requiring $M_{\mathrm{T2}} > 300$ GeV while keeping a large fraction of signal events. Moreover, the larger the $\Delta m(\tilde{t}_1, \tilde{\chi}_1^0)$ mass difference is, the more substantial the separation between the signal and the background distributions results.

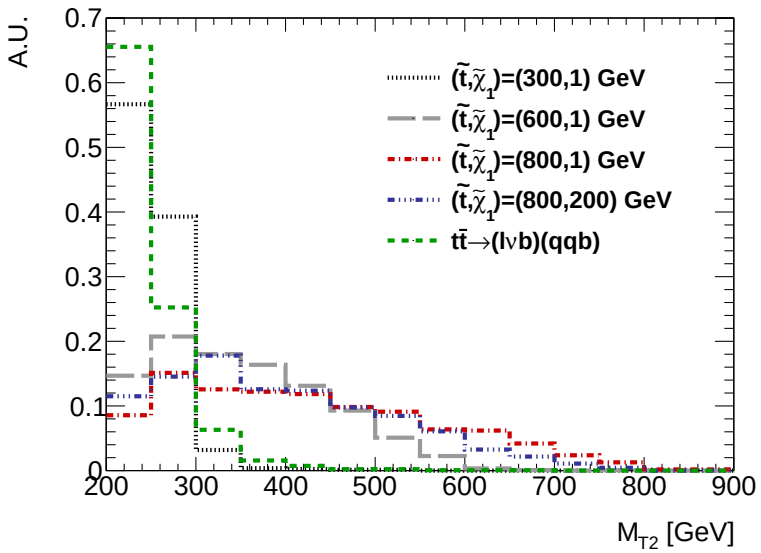

Figure 5.13: Distribution of the reconstructed M_{T2} for events of different signal models containing two hadronically decaying top quarks and for events of the $t\bar{t} \to (l\nu b)(qqb)$ background.

The M_{T2} calculation requires the four-momentum reconstruction of two top quarks, provided by the HEPTopTagger. However, it can be noticed in figure 5.14(a) that the fraction of selected signal events is largely reduced after the requirement of two top tags. Most of the sub-leading top quark transverse momenta are below 200 GeV for small $\tilde{t}_1$ masses ($m_{\tilde{t}_1} \lesssim 400$ GeV), while they mainly have p_{T} between 100 and 300 GeV for $m_{\tilde{t}_1} \sim 600-700$ GeV, see figure 5.14(b). Only those signal samples with large $\tilde{t}_1$ masses, $m_{\tilde{t}_1} \gtrsim 700$ GeV, have the majority of the events with both top quarks boosted enough to have chances of being tagged by the HEPTopTagger.

The experimental sensitivity to the $\tilde{t}_1$ pair production can be enhanced by taking into account also events where only one top tag is reconstructed. Three signal regions, differing in the number of reconstructed large-R jets and top candidates, are then defined: the first, SR1, composed of events with two top-tagged large-R jets; the second, SR2, with two large-R jets of which exclusively one is top-tagged; and the third, SR3, with exclusively one large-R jet, which is top-tagged. The SRs are separately optimized using additional variables in order to reduce the background

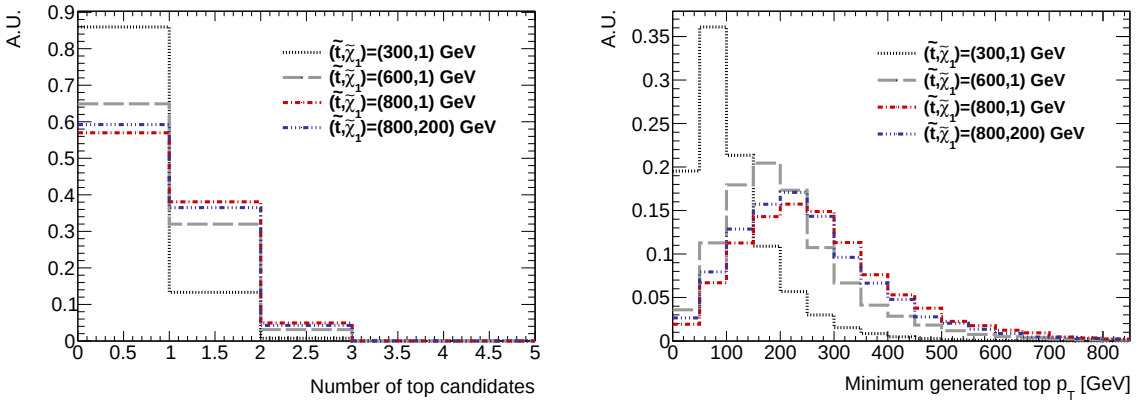

(a) (b)

Figure 5.14: Distributions of the number of HEPTopTagger candidates (a) and of the minimum generated p_{T} top quark (b) for events of different signal models containing two hadronically decaying top quarks.

contamination and enhance the ratio $S/\sqrt{B}$, where S is the number of signal events and B the number of expected background events.

Two HEPTopTagger candidates: signal region SR1

The first event category, referred to as SR1, is selected by requiring two reconstructed HEPTopTagger top candidates. The leading large-R jet as input to the algorithm is required to have $p_{\mathrm{T}} > 280$ GeV and the sub-leading is required to have $p_{\mathrm{T}} > 200$ GeV. Their four-momenta are used to calculate the M_{T2} variable. Events with $E_{\mathrm{T}}^{\mathrm{miss}} > 275$ GeV and $M_{\mathrm{T2}} > 300$ GeV are kept. The signal acceptance of SR1 is 0.7% in the signal sample with $(m_{\tilde{t}_1}, m_{\tilde{\chi}_1^0}) = (600, 1)$ GeV.

The distributions of the missing transverse energy and the M_{T2} are shown in figure 5.15.

Single HEPTopTagger candidate and a second large-R jet: signal region SR2

For those events where the leading top quark is moderately boosted, $p_{\mathrm{T}} > 300$ GeV, and the transverse momentum of the subleading one is slightly higher than 200 GeV, it is rather unlikely that both top quarks are reconstructed. These events can be selected by requiring one top candidate corresponding to one generated top and an untagged large-R jet originating from some decay products of the other generated top quark. Events belong to the second signal region, SR2, if they contain at least two reconstructed large-R jets, one with $p_{\mathrm{T}} > 280$ GeV and the other with $p_{\mathrm{T}} > 200$ GeV, and only one of them is top-tagged.

The requirement of only one HEPTopTagger candidate does not provide enough rejection power to be sensitive to the signal process. The presence of a b-tagged small-R jet is additionally required. Most of the Z+jets and W+jets events,

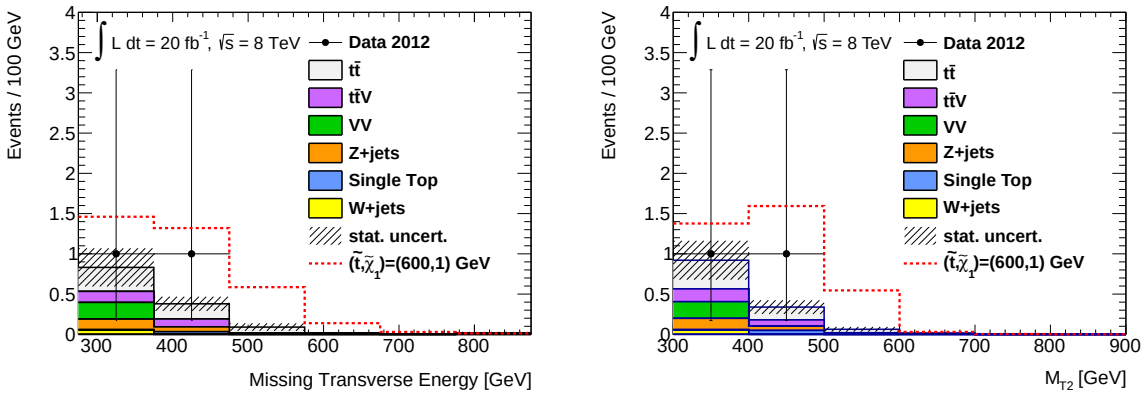

(a) (b)

Figure 5.15: SR1 distributions of $E_{\mathrm{T}}^{\mathrm{miss}}$ (a) and M_{T2} (b). The SM background prediction is represented as a stacked histogram with an error band of the simulation statistical uncertainty while the data distribution is overlaid as black points. The signal expectation for the sample with $(m_{\tilde{t}_1}, m_{\tilde{\chi}_1^0}) = (600, 1)$ GeV is represented by a red dashed line.

which mainly do not have b-tagged jets, are rejected. The transverse mass, $M_{\mathrm{T}}^{\mathrm{b,min}} = \sqrt{2p_{\mathrm{T}}^{b} E_{\mathrm{T}}^{\mathrm{miss}}(1 - \cos\Delta\phi(\vec{p}_{\mathrm{T}}^{\,b}, \vec{E}_{\mathrm{T}}^{\mathrm{miss}}))}$, calculated from the missing transverse momentum and the p_{T} of the b-tagged jet, p_{T}^{b}, with the smallest azimuthal separation from $\vec{E}_{\mathrm{T}}^{\mathrm{miss}}$, is a useful discriminating variable to diminish the dominant $t\bar{t} \to (l\nu b)(qqb)$ background contribution. A large fraction of $t\bar{t}$ events are characterised by $M_{\mathrm{T}}^{\mathrm{b,min}}$ values peaking below the top quark mass, while signal events have large $M_{\mathrm{T}}^{\mathrm{b,min}}$ values, as can be seen in figure 5.16. Only events with $M_{\mathrm{T}}^{\mathrm{b,min}} > 175$ GeV

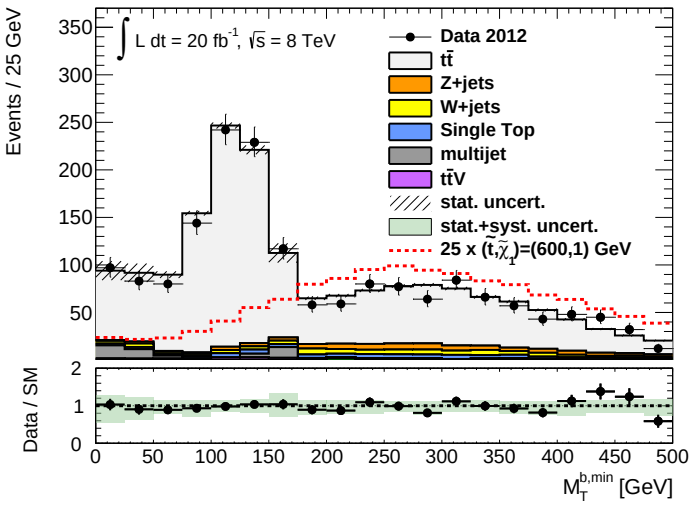

Figure 5.16: $M_{\mathrm{T}}^{\mathrm{b,min}}$ distribution of events passing the baseline selection together with the requirement of a b-tagged jet. The style convention is identical to figure 5.11.

and with moderately large missing transverse momentum, $E_{\mathrm{T}}^{\mathrm{miss}} > 275$ GeV,

are selected. The signal acceptance for SR2 is 3.1% for a signal sample with $(m_{\tilde{t}_1}, m_{\tilde{\chi}_1^0}) = (600, 1)$ GeV.

The distributions of the missing transverse energy and of the top candidate mass in SR2 are shown in figure 5.17(a) and 5.17(b), respectively.

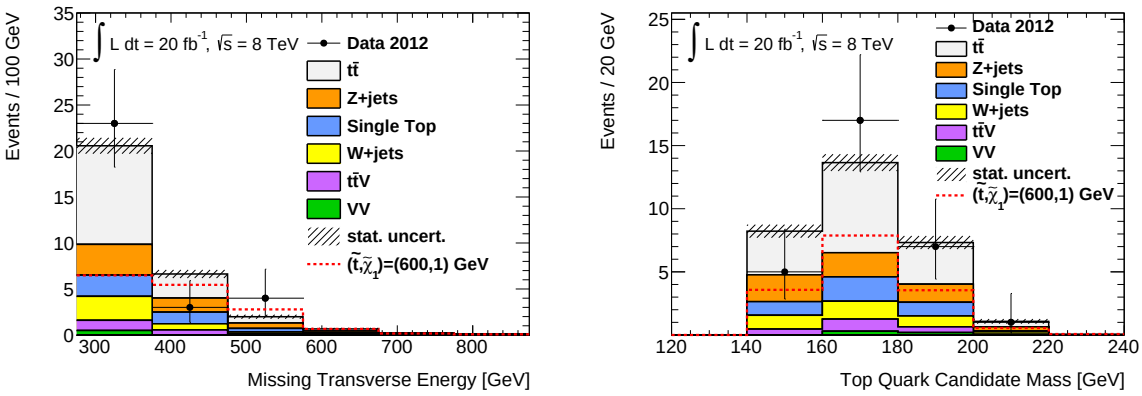

(a) (b)

Figure 5.17: SR2 distributions of $E_{\mathrm{T}}^{\mathrm{miss}}$ (a) and the HEPTopTagger candidate mass (b). The style convention is identical to figure 5.15.

Single large-R jet tagged by the HEPTopTagger: signal region SR3

If the sub-leading top quark has a transverse momentum even lower than 200 GeV, it can happen that no large-R jet can originate from its decay and the signature is characterised by only one tagged large-R jet associated to the leading top quark. The signature with only one reconstructed and tagged large-R jet per event occurs also if the two tops are so close to each other ($\Delta R < 2.0$) that only one large-R jet can be reconstructed. If one large-R jet is exclusively reconstructed and has $p_{\mathrm{T}} > 280$ GeV, the event might be selected for the third signal region, SR3. The $M_{\mathrm{T}}^{\mathrm{b,min}}$ and b-tagged jet requirements are the same as in SR2. However, the $E_{\mathrm{T}}^{\mathrm{miss}}$ selection criterion is tightened to reduce the background that in SR2 was rejected by the second large-R jet requirement. Only events with $E_{\mathrm{T}}^{\mathrm{miss}} > 400$ GeV are selected for SR3.

The fraction of selected signal events in SR3 is 2.2% in a signal sample with $(m_{\tilde{t}_1}, m_{\tilde{\chi}_1^0}) = (600, 1)$ GeV. The missing transverse energy and the top candidate mass distributions for SR3 are shown in figure 5.18.

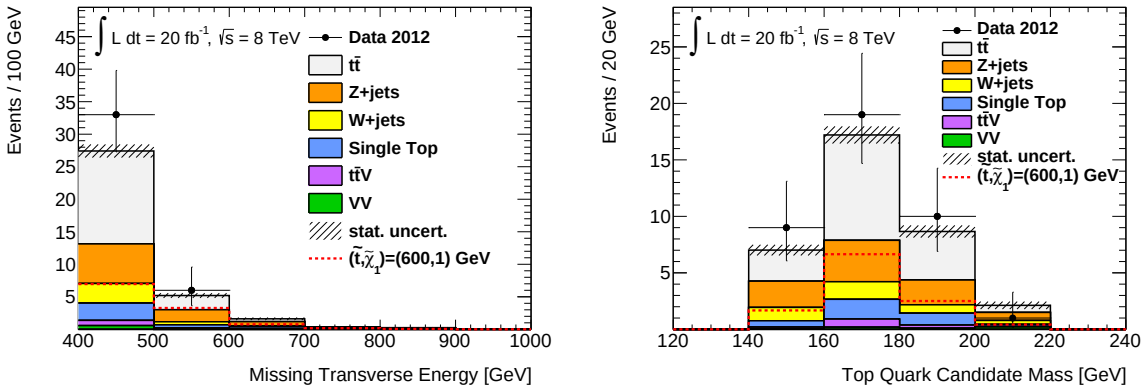

(a) (b)

Figure 5.18: SR3 distributions of $E_{\mathrm{T}}^{\mathrm{miss}}$ (a) and the HEPTopTagger candidate mass (b). The style convention is identical to figure 5.15.

The requirements of the three signal regions are summarised in table 5.4. The fraction of the events selected by the union of SR1, SR2, and SR3 is 6% in the signal sample with $(m_{\tilde{t}_1}, m_{\tilde{\chi}_1^0}) = (600, 1)$ GeV, and 12% with $(m_{\tilde{t}_1}, m_{\tilde{\chi}_1^0}) = (800, 1)$ GeV.

	SR1	SR2	SR3
$N_{\text{large-}R\text{ jet}}$	≥ 2	≥ 2	$= 1$
$N_{\text{top}}^{\text{cand.}}$	≥ 2	$= 1$	$= 1$
$E_{\mathrm{T}}^{\mathrm{miss}}$	≥ 275 GeV	≥ 275 GeV	≥ 400 GeV
M_{T2}	≥ 300 GeV	–	–
$N_{b\text{-jets}}$	≥ 0	≥ 1	≥ 1
$M_{\mathrm{T}}^{\mathrm{b,min}}$	–	≥ 175 GeV	≥ 175 GeV

Table 5.4: Summary of the selection criteria specific to each signal region.

In table 5.5, the number of observed events in each SR is compared to the expected number events, obtained from the normalisation of the processes to the theory cross section. Good agreement between the data and the SM expectation is observed. Since no significant data excess is found, a statistical evaluation is performed in section 5.7 aiming to set exclusion limits at 95% confidence level in the $(m_{\tilde{t}_1}, m_{\tilde{\chi}_1^0})$ parameter space.

5.3.2 Background estimation

The $t\bar{t} \to (l\nu b)(qqb)$ process constitutes the main background component in the three signal regions. If two top candidates are reconstructed as in SR1, the other irreducible background is the associated production of two top quarks with a Z decaying into a neutrino pair: the signature of $t\bar{t}Z$ is large missing transverse energy and two top quarks. If only one top candidate is reconstructed (SR2 and SR3),

Event number class	SR1	SR2	SR3
Observed	2	30	39
SM MC expected	1.33	30.24	34.96
Expected signal $(600, 1)$ GeV	3.55	15.63	11.26

Table 5.5: Event yields in each signal region (SR1, SR2, and SR3). The observed events are reported together with the expected SM background events. The expected signal events for one signal model with $(m_{\tilde{t}_1}, m_{\tilde{\chi}_1^0}) = (600, 1)$ GeV are presented.

Z+jets, W+jets and the single top production have a non-negligible contribution to the background.

The contribution of low cross section processes, like $t\bar{t}V$, single top and diboson, are evaluated by means of simulation. On the other hand, a semi-data-driven approach can be used to estimate the expected contribution of background sources like $t\bar{t}$ and V+jets (where $V = Z, W$), characterised by a large cross section. This method consists in employing the simulation to predict the background shape, while normalisation factors are extracted by comparing the number of simulated events to the data ones in control regions. This comparison allows the reduction of the background systematic uncertainties in the signal regions by constraining them in the control regions. The orthogonality to the signal regions and the enhancement of a specific background process with negligible signal contamination are the main aspects to consider in the definition of CRs. Moreover, a compromise has to be found in defining the CR event selection: it should contain enough events to result in a small statistical uncertainty on the background prediction, but at the same time it should be kinematically close to the SR.

Despite of being enriched in a specific process, a CR might present contamination from other processes with normalisation factors to be derived from other CRs. Therefore a fit is performed on all these regions simultaneously in order to take into account the cross contamination.

Three CRs are defined to estimate the $t\bar{t}$ and V+jets background processes. These are described in the following and their selection requirements are summarised in table 5.6.

The contribution from multijet processes due to misidentified top quarks is found to be negligible when large $E_{\mathrm{T}}^{\mathrm{miss}}$is required in association with two top tags, or one top tag and one b-tagged jet.

V+jets control region

The baseline requirements of section 5.2.3, apart from the HEPTopTagger candidate requirement, are applied in order to define the control region enriched in Z+jets and W+jets events. Thus, events with at least one large-R jet with $p_{\mathrm{T}} > 280$ GeV are

	V+jets CR	$t\bar{t}$ CR	μ +jets CR
Trigger	$E_{\mathrm{T}}^{\mathrm{miss}}$	$E_{\mathrm{T}}^{\mathrm{miss}}$	muon trigger
N_ℓ	0	0	1 ($\ell = \mu$)
$E_{\mathrm{T}}^{\mathrm{miss}}$	$\in (150, 275)$ GeV	$\in (150, 275)$ GeV	> 150 GeV
$\lvert\Delta\phi(\mathrm{jet}^{0,1,2}, \vec{E}_{\mathrm{T}}^{\mathrm{miss}})\rvert$	$> \pi/5$	$> \pi/5$	–
$N^{\text{ b-jet}}$	$=0$	≥ 1	≥ 0
$M_{\mathrm{T}}^{\mathrm{b,min}}$	–	> 100 GeV	–
leading large-R jet p_{T}	> 280 GeV	> 280 GeV	> 280 GeV
HEPTopTagger candidate	inverted	default	default
candidate mass	$\in (120, 240)$ GeV	$\in (120, 240)$ GeV	$\in (120, 240)$ GeV

Table 5.6: Selection criteria of the control regions defined to estimate the background of: associated production of a vector boson with jets in the V+jets CR; top quark pair production in the $t\bar{t}$ CR; $t\bar{t} \to (l\nu b)(qqb)$ and W+jets processes in the μ+jets CR. The HEPTopTagger candidate type is either the default one (explained in sections 5.2.3 and 3.1) or inverted if the requirements on the mass ratio variables $\arctan(m_{13}/m_{12})$ and m_{23}/m_{123} are complementary to the default ones, see figure 5.19(a).

selected. The orthogonality to the signal regions is respected with the requirement that the missing transverse momentum does not exceed 275 GeV.

As described in section 3.1, after the three exclusive subjets are reconstructed, the candidate is considered a top quark, if its subjet mass ratio variables lie in the A-shaped region of the $\arctan(m_{13}/m_{12})$ and m_{23}/m_{123} plane of figure 3.3, and if its mass is close to the top quark mass. The first requirement is very effective in rejecting large-R jets originating from light-quark/gluon hadronization. The majority of the V+jets events populate the low $\arctan(m_{13}/m_{12})$ and low m_{23}/m_{123} phase space, as can be seen in figure 5.19(a). A V+jets event purity of about 80% is achieved by vetoing b-tagged jets and inverting the HEPTopTagger requirements on the variables $\arctan(m_{13}/m_{12})$ and m_{23}/m_{123}, and thus enhancing the selection of fake top quarks. In particular, only selected regions in the $\arctan(m_{13}/m_{12})$ and m_{23}/m_{123} plane are considered, as illustrated by the black boxes of figure 5.19(a). The fake candidate selection, also referred to as *inverted* selection, is optimized to have negligible contribution from multi-jet events and to be kinematically close but complementary to the default top candidate selection. Events with the mass of the HEPTopTagger fake-top candidate (also referred to as pre-candidate) between 120 and 240 GeV are considered for the V+jets control region. The main variables used to define the CR, which are the fake-top candidate mass, the subjet mass ratio variables $\arctan(m_{13}/m_{12})$ and m_{23}/m_{123}, the missing transverse energy and the large-R jet transverse momentum are well described by the simulation within the statistical and systematic uncertainties, as shown in figures 5.19(b)-(f).

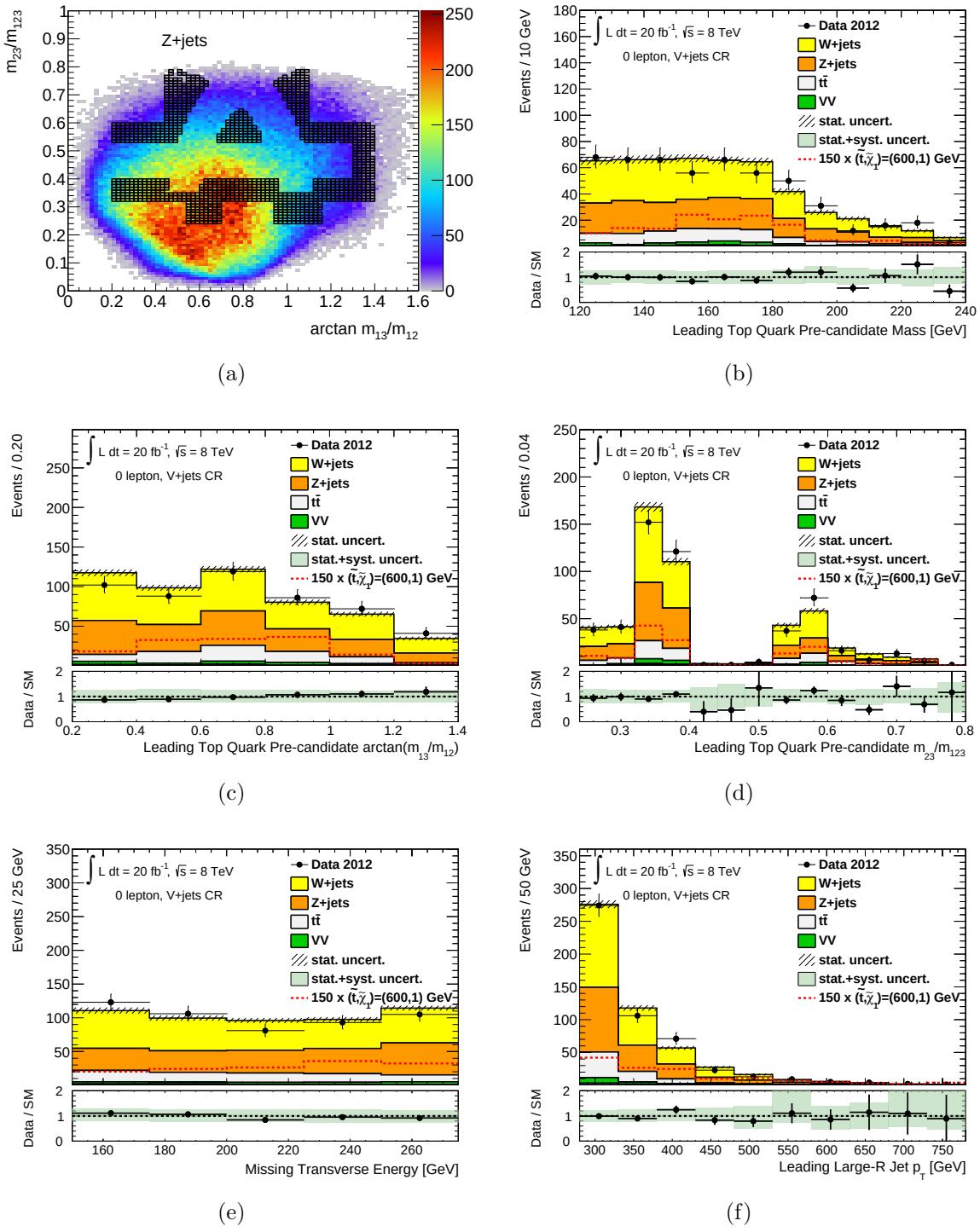

Figure 5.19: (a) Two-dimensional distribution of m_{23}/m_{123} versus $\arctan(m_{13}/m_{12})$ in the Z+jets background process. Overlaid are black squares which identify the part of the phase space used to define the inverted selection for the fake candidate reconstruction. V+jets CR distributions respectively of the mass (b), $\arctan(m_{13}/m_{12})$ (c) and m_{23}/m_{123} (d) reconstructed by the HEPTopTagger with the requirements of the inverted selection in the ($\arctan(m_{13}/m_{12})$, m_{23}/m_{123}) plane. Distributions of $E_{\mathrm{T}}^{\mathrm{miss}}$ (e) and of the highest transverse momentum large-R jet p_{T} (f). The style convention is identical to figure 5.11.

$t\bar{t}$ control region

The $t\bar{t}$ CR selection criteria are similar to the SR2 and SR3 ones. After the baseline selection of section 5.2.3, with a looser requirement on the top candidate mass, required within $(120, 240)$ GeV, events with at least one b-tagged small-R jet and a top tagged large-R jet with $p_{\mathrm{T}} > 280$ GeV are taken into account. A highly pure sample of $t\bar{t}$ events is selected, by loosening the $M_{\mathrm{T}}^{\mathrm{b,min}}$ lower limit down to 100 GeV.

As for the V+jets control region, the orthogonality to the signal regions is achieved by taking into account events with moderate missing transverse energy, between 150 and 275 GeV, figure 5.20(a). The distributions of $M_{\mathrm{T}}^{\mathrm{b,min}}$, of the tagged large-$R$ jet p_{T} and the HEPTopTagger variables are shown in figures 5.20(b)-(f). The $t\bar{t}$ simulation performs well in describing the data distributions.

μ+jets control region

An additional control region, called μ+jets, is taken into account. Its goal is to mimic the background of the signal regions and to reduce the uncertainty of the background normalisation factors by its inclusion in the simultaneous fit. The SR background contains at least one hadronically decaying top candidate, and other hadronic activity which is reconstructed as another large-R jet or a b-tagged jet. This hadronic activity in the case of $t\bar{t} \to (l\nu b)(qqb)$ and W+jets processes is often characterised by the presence of hadronically decaying τ leptons. The μ+jets CR aims to select the $t\bar{t} \to (l\nu b)(qqb)$ and W+jets processes in which a muon is produced instead of a τ.

The baseline selection for the events in this region is defined according to the muon channel strategy of chapter 4. Events are required to have one isolated muon with $p_{\mathrm{T}} > 25$ GeV, moderate $E_{\mathrm{T}}^{\mathrm{miss}}$, a small-$R$ jet close to the muon, and a reconstructed large-R jet, tagged by the HEPTopTagger with mass between 120 and 240 GeV. The requirement of a b-tagged small-R jet is excluded, in order to have a non-negligible contribution from W+jets.

In addition to this baseline selection, stringent requirements are applied on the p_{T} of the large-R jet, $p_{\mathrm{T}} > 280$ GeV, and on the missing transverse energy, $E_{\mathrm{T}}^{\mathrm{miss}} > 150$ GeV, to be closer to the SRs. The data missing transverse energy distribution, shown in figure 5.21(a), is well described by simulation within the systematic uncertainties. A small overestimation of the expected events with respect to the data is observed in the high p_{T} region tails of the muon transverse momentum in figure 5.21(b), and of the leading large-R jet p_{T} in figure 5.21(c). At high muon and large-R jet p_{T} the impact of the total systematic uncertainty increases comparing to the low p_{T} region. This slight disagreement with respect to the data is within the total systematic uncertainty. The top candidate mass distribution in figure 5.21(d) is characterised by the clear mass peak from hadronically decaying top quarks over a flat background distribution of W+jets events. Overall good agreement between data and MC prediction is observed.

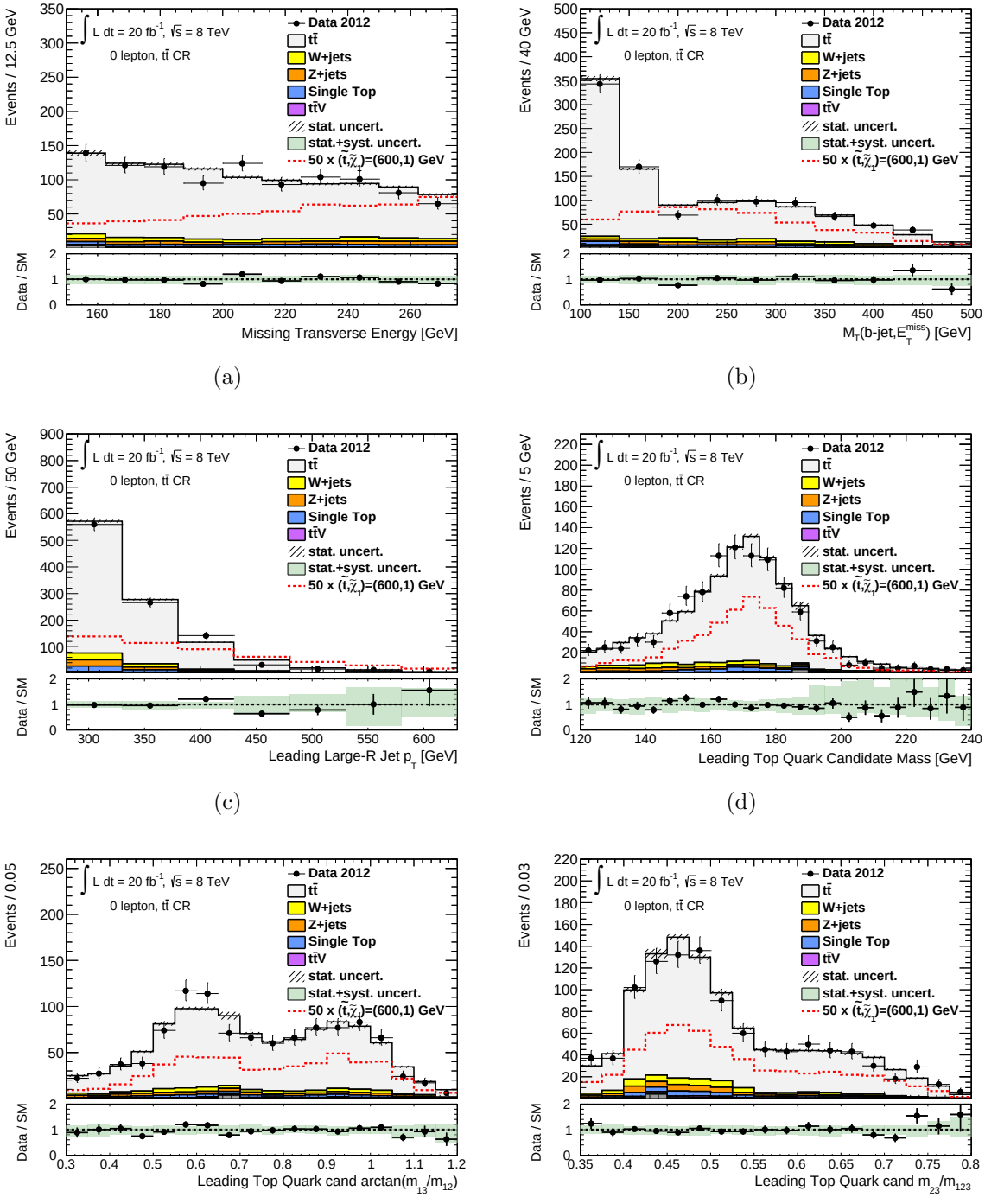

Figure 5.20: $t\bar{t}$ CR distributions of $E_{\mathrm{T}}^{\mathrm{miss}}$ (a), of $M_{\mathrm{T}}^{\mathrm{b,min}}$ (b) and of the highest transverse momentum large-R jet p_{T} (c). $t\bar{t}$ CR distributions respectively of the mass (d), $\arctan(m_{13}/m_{12})$ (e) and m_{23}/m_{123} (f) reconstructed by the HEPTopTagger. The style convention is identical to figure 5.11.

The SM background in this CR is composed of approximately 80% of $t\bar{t} \rightarrow (l\nu b)(qqb)$ events and 15% W+jets events, with a small remaining contribution from single top and diboson processes.

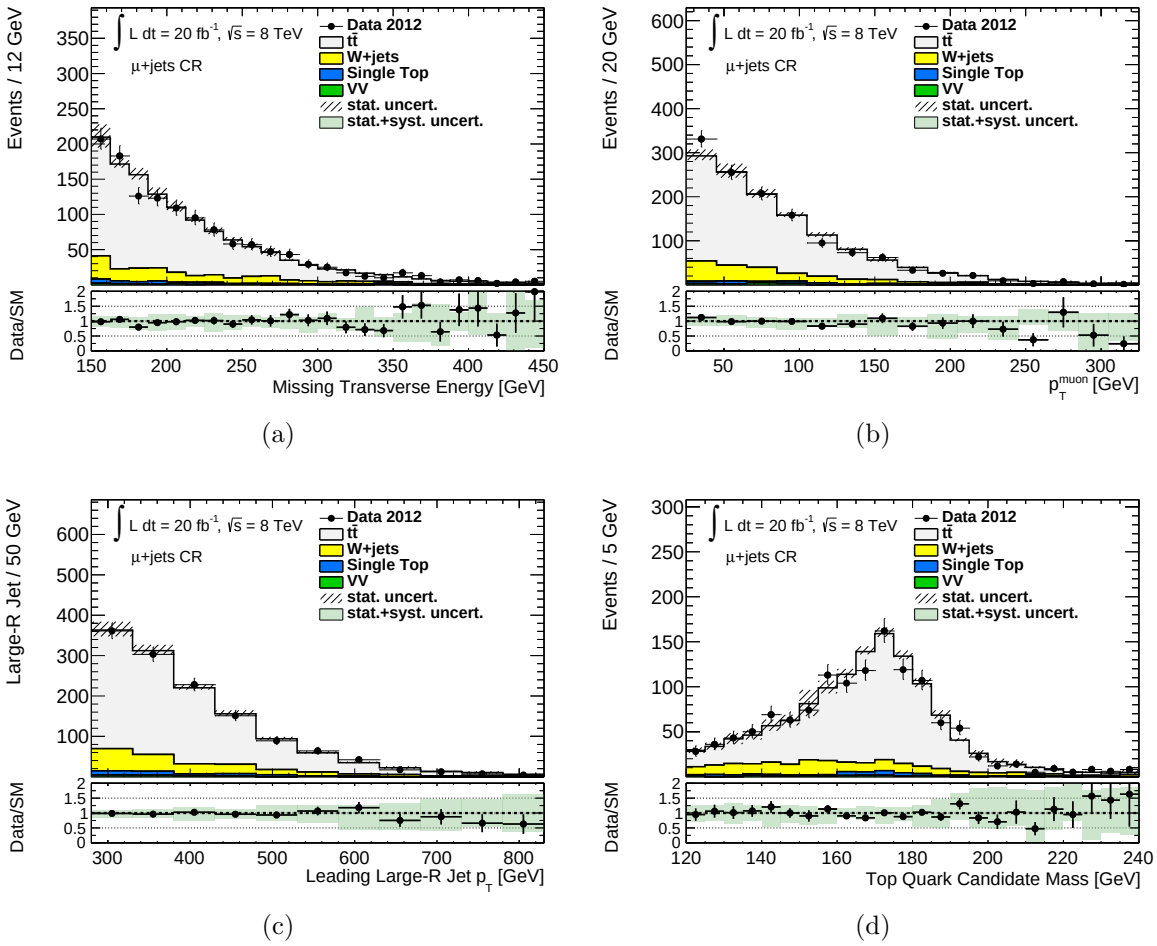

Figure 5.21: μ+jets CR distributions respectively of $E_{\mathrm{T}}^{\mathrm{miss}}$ (a), of the muon transverse momentum (b), of the highest transverse momentum large-R jet p_{T} (c) and of the top candidate mass (d). The SM background prediction is represented as a stacked histogram while the data distribution is overlaid as black points. The lower panel shows the ratio between the data and the SM prediction and overlaid is the impact of the systematic and statistical uncertainties added in quadrature.

5.3.3 Validation regions

In addition to the CR and the SR, a third class of events is collected in the validation region (VR). Its selection criteria are kinematically closer to the SR than the CR. In fact, the purpose of this region of phase space is to validate the background estimation, by verifying in this intermediate step the extrapolation of the background from the CR to the SR. Two validation regions are considered. The first (called

"2 HTTs VR") is defined to be close to SR1, by requiring two top candidates. These candidates can either be selected through the default top candidate definition or the inverted definition. This enhances the number of selected events, reducing the statistical uncertainty. The orthogonality with respect to SR1 is achieved by inverting the missing transverse energy requirement: events with $E_{\mathrm{T}}^{\mathrm{miss}}$ in the range $150 - 275$ GeV are selected. The M_{T2} distribution in this VR is shown in figure 5.22(a). Compatibility between the data and the SM expectation is observed.

The second VR (called "1 HTT VR") selects events kinematically close to the union of SR2 and SR3, but is orthogonal to the two SRs by requiring the single HEPTopTagger candidate for each event to be selected with the inverted candidate criteria. The missing transverse energy is required to be larger than 275 GeV as in SR2 and is displayed in figure 5.22(b). At high $E_{\mathrm{T}}^{\mathrm{miss}}$ an overestimation of the SM expectation with respect to the data is observed. This might be due to statistical fluctuation or overestimation of the small-R jet energy scale at high energies.

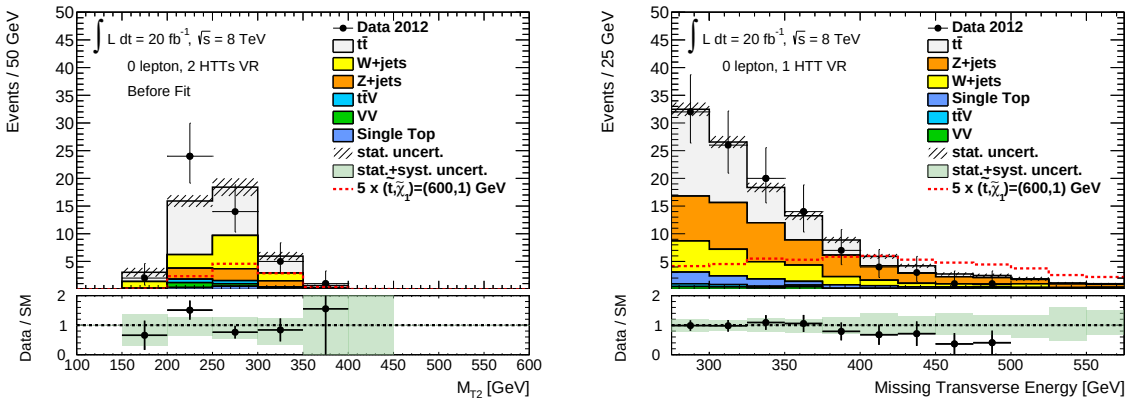

(a) (b)

Figure 5.22: M_{T2} distribution in 2 HTTs VR (a) $E_{\mathrm{T}}^{\mathrm{miss}}$distribution in 1 HTT VR (b). The style convention is identical to figure 5.11.

5.4 Statistical hypothesis testing

The goal of this analysis is to look for the top quark's supersymmetric partner. The observed data events might lead to the discovery or the exclusion of the signal presence. It is important to determine the consistency of the Standard Model hypothesis or the SUSY signal hypothesis given the experimental measurement.

This issue can be addressed with a *hypothesis testing* statistical tool. The main concepts [151, 152] relevant for this analysis are introduced in this section.

The *background-only hypothesis* is that the SM is the theory expected to be true and to govern the outcome of the data. It is complemented to an *alternative hypothesis*, consisting in the assumption of the presence of new particles, in this case the $\tilde{t}_1$ and $\tilde{\chi}_1^0$, predicted by SUSY models. This *signal-plus-background hypothesis*

depends on a free parameter, which is the signal strength μ_S. It is a normalisation factor applied to the nominal cross section of the signal. The signal-plus-background hypothesis concerning the nominal signal expectation corresponds to $\mu_S = 1$. The background-only hypothesis corresponds to $\mu_S = 0$.

A scalar quantity, called *test statistic* $q_{\mu_S^H}$, is needed for the hypothesis testing in order to evaluate the compatibility of the observed measurement $\mathbf{n}$ with an hypothesis characterised by a specific μ_S^H. Here the "H" superscript indicates that μ_S^H corresponds to the hypothesis undergoing test.

If the generic output of a measurement is given by a binned distribution with N bins, the expectation value of the observed data in bin i is the sum of the expected background events in bin i, b_i, and the expected signal events in bin i, s_i, times the signal strength: $\mu_S s_i + b_i$. The background and signal expectation may depend on a set of nuisance parameters $\boldsymbol{\theta}$: $s_i = s_i(\boldsymbol{\theta})$ and $b_i = b_i(\boldsymbol{\theta})$. Given the observed data distribution, $\mathbf{n} = (n_1, n_2, \cdots n_N)$, the likelihood function is defined as the product of the Poisson probabilities of observing n_i given the expectation value $\mu_S s_i(\boldsymbol{\theta}) + b_i(\boldsymbol{\theta})$:

$$L(\mathbf{n}|\mu_S, \boldsymbol{\theta}) = \prod_{i=1}^{N} \frac{(\mu_S s_i + b_i)^{n_i}}{n_i!} e^{-(\mu_S s_i + b_i)},$$

which depends on the signal strength μ_S and on the nuisance parameters $\boldsymbol{\theta}$.

The optimal choice for $q_{\mu_S^H}$, as stated by the Neyman-Pearson lemma, is based on the *likelihood ratio*,

$$q_{\mu_S^H} = -2\ln(Q(\mu_S^H)), \quad \text{with} \quad Q(\mu_S^H) = \frac{L(\mathbf{n}|\mu_S^H, \hat{\hat{\boldsymbol{\theta}}})}{L(\mathbf{n}|\hat{\mu}_S, \hat{\boldsymbol{\theta}})} \tag{5.4}$$

where the numerator and the denominator likelihoods are maximised separately by means of a fit procedure on the data distribution $\boldsymbol{n}$. The set $\hat{\hat{\boldsymbol{\theta}}}$ corresponds to the maximum likelihood estimator of $\boldsymbol{\theta}$, namely $\hat{\hat{\boldsymbol{\theta}}}$ is the set of values of the nuisance parameter set $\boldsymbol{\theta}$ maximising the numerator likelihood, given a fixed μ_S^H. The denominator, instead, is maximised with respect to μ_S and $\boldsymbol{\theta}$: $\hat{\mu}_S$ and $\hat{\boldsymbol{\theta}}$ are the values of μ_S and $\boldsymbol{\theta}$ which maximise the denominator likelihood.

The profile likelihood ratio $Q(\mu_S^H)$ ranges between 0 and 1. In fact, the condition $L(\mathbf{n}|\mu_S^H, \hat{\hat{\boldsymbol{\theta}}}) \leq L(\mathbf{n}|\hat{\mu}_S, \hat{\boldsymbol{\theta}})$ is always true because when the hypothesised μ_S^H is equal to the free parameter optimal choice $\hat{\mu}_S$, which maximises $L(\mathbf{n}|\hat{\mu}_S, \hat{\boldsymbol{\theta}})$, the two likelihoods have similar values and their ratio is close to 1. Since $\hat{\mu}_S$ is the result of the fit over the data distribution, the likelihood ratio close to 1 means that there is compatibility between the hypothesis, defined by the value μ_S^H, and the data, connected to the best choice $\hat{\mu}_S$ profiled on the measurement. On the contrary, if $\hat{\mu}_S$ and μ_S^H are very different, i.e. the data and the hypothesis are incompatible, the denominator maximised by the value $\hat{\mu}_S$ is greater than the numerator where μ_S^H is fixed, and thus the ratio $Q(\mu_S^H)$ is close to 0. Consequently, the larger the test $q_{\mu_S^H}$, the more incompatible the hypothesis, defined by the μ_S^H value, is with respect to the data.

To proceed with the hypothesis testing, the probability density function of $q_{\mu_S^H}$, $g(q_{\mu_S^H}|\mu_S)$, has to be calculated with respect to the hypothesis, described by the value μ_S, which is assumed in the distribution of the data. For example, as in the case of limit exclusion, the nominal signal-plus-background hypothesis is tested and the test statistic is q_1 (with $\mu_S^H = 1$). The distributions $g(q_1|\mu_S = 1)$ and $g(q_1|\mu_S = 0)$ are derived. They represent the probability density functions with respect to the variable q_1 under the hypothesis that the data are described by the signal-plus-background hypothesis or the background-only hypothesis, respectively. The $g(q_{\mu_S^H}|\mu_S)$ distribution is obtained by multiple pseudo-experiments or, according to the Wilks' theorem [153], it follows a χ^2 distribution in the case of a large statistics data sample (called the asymptotic regime).

Discovery, p-value and expected significance

To quantify the discrepancy between the measurement and an hypothesis, the *p-value* is computed.

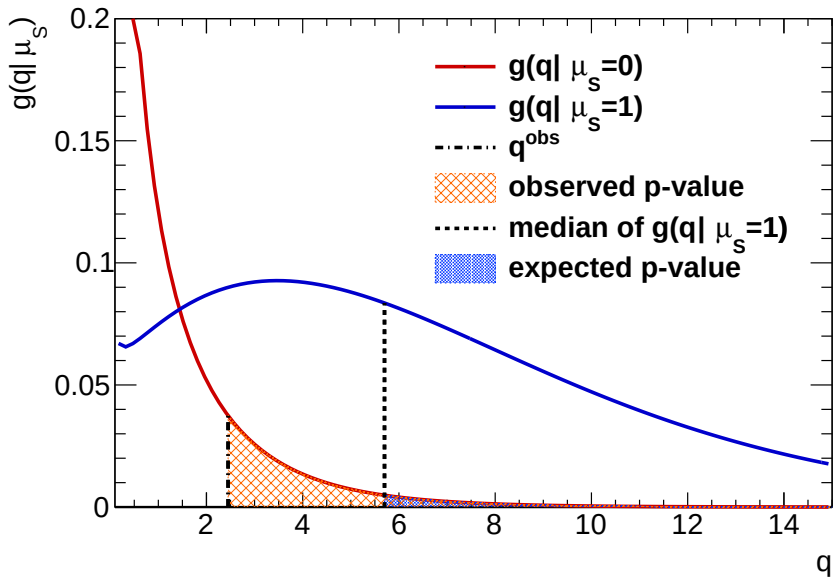

Figure 5.23: Example distribution of the q test statistic probability density function under the background-only hypothesis (red curve) and signal-plus-background hypothesis (blue line). The filled red area represent the observed p-value, while the small blue shaded area represent the expected p-value.

As represented in figure 5.23, the p-value, p_0, expresses the probability of measuring a value of q_0 greater or equal than the observed q_0^{obs} under the assumption of background-only hypothesis to be true:

$$p_0 = \int_{q_0^{\text{obs}}}^{\infty} g(q_0|\mu_S = 0)\, \mathrm{d}q_0 \tag{5.5}$$

This value estimates the probability of having an excess of events with respect to the background-only expectation, given that the corresponding hypothesis is true.

The p-value is used to quantify a *discovery*. The background-only hypothesis is rejected if the p_0 is smaller than 2.87×10^{-7}, equivalent to 5σ significance.

In order to evaluate the discovery sensitivity of a test, it is useful to know its *expected significance*. This indicates the expected deviation from the background-only hypothesis, under the assumption that the signal-plus-background hypothesis is true. The p-value, p_0^{exp}, calculated with respect to the median of $g(q_0|\mu_S = 1)$, instead of q_0^{obs} in equation 5.5, is the *expected confidence level* and gives information on the expected significance. Here $g(q_0|\mu_S = 1)$ represents the probability density function of the test statistic q_0 under the assumption of the signal-plus-background hypothesis with nominal signal strength.

Hypothesis exclusion

Similarly, the p-value, p_1, is calculated with respect to the signal-plus-background hypothesis with the signal cross section as predicted by the theory, $\mu_S = 1$:

$$p_1 = \int_{q_1^{\text{obs}}}^{+\infty} g(q_1|\mu_S = 1)\,\mathrm{d}q_1. \tag{5.6}$$

It quantifies the probability of excluding a signal hypothesis. For example, a p-value threshold of 5%, $p_1 < 0.05$, corresponds to a 95% confidence level (CL).

The expected significance of a test in the case of exclusion limits is related to the expected p-value, p_1^{exp}. This is defined as:

$$p_1^{\text{exp}} = \int_{q_1^{\text{exp}}}^{+\infty} g(q_1|\mu_S = 1)\,\mathrm{d}q_1 \tag{5.7}$$

where q_1^{exp} is the median of the background-only hypothesis probability density function. Having p_1^{exp} small suggests that, in case the background-only hypothesis is true, the typical experiment will be inconsistent with the signal-plus-background hypothesis.

If the signal contribution is small or the signal and background cannot be easily disentangled, $g(q_1|\mu_S = 1)$ and $g(q_1, \mu_S = 0)$ distributions are not well separated. In this case the experiment is close to the sensitivity limit, and if the data distribution is characterised by a downward fluctuation of the observed events with respect to the background-only hypothesis, the signal-plus-background hypothesis might be excluded, although there is no real sensitivity. The CL_S method [154] does not set an exclusion limit on p_1 itself but on the ratio $\text{CL}_S = p_1/(1 - p_0)$. Therefore the signal-plus-background hypothesis is rejected if $\text{CL}_S < 5\%$. This criterion is applied to set exclusion limits on the signal-plus-background hypothesis.

5.4.1 HistFitter and fit description

The statistical treatment of the measurement is performed using the *HistFitter* software framework [155]. It is configured to take into account control, signal and validation regions, with the scope of constraining, extrapolating and validating models

for the data description. These are treated by the tool with statistically rigorous methods using the Frequentist approach.

The extraction of information from the data is possible via the usage of probability density functions which model the expected distribution in the regions. In particular these probability density functions depend on free parameters which are adjusted to the data with a fit. Although separate probability density functions are used to model all the regions due to their statistical independence, the free parameters of the probability density functions are shared among the regions. Thus the fit needs to be simultaneous in all the regions in order to extract consistently the information of the background, the signal and the systematic uncertainties.

The parameters of interest are:

- the **normalisation factors**, $\boldsymbol{\mu_b}$, for the two main background sources, V+jets and $t\bar{t}$, used as a multiplicative parameter in front of the theory cross section;
- the **signal strength**, μ_{S}, normalisation factor with respect to the nominal signal cross section;
- the **nuisance parameters**, $\boldsymbol{\theta}$, which model the impact of the systematic uncertainties or of the MC statistical uncertainties. Each systematic uncertainty i is represented by the continuous parameter θ_i, such that the nominal expectation corresponds to $\theta_i = 0$ and the $\pm 1\sigma$ variations correspond to $\theta_i = \pm 1$.

The general form of the constructed likelihood used in equation 5.4 is parametrised by μ_{S}, $\boldsymbol{\mu_b}$, $\boldsymbol{\theta}$ and is given by the product of the Poisson measurements of the observed events $\boldsymbol{n}$ in the CR and SR,P_{CR} and P_{SR}, and the constraint term for the systematic uncertainties C_{syst}:

$$L(\boldsymbol{n}, \boldsymbol{\theta_0} | \mu_{\mathrm{S}}, \boldsymbol{\mu_b}, \boldsymbol{\theta}) = P_{\mathrm{SR}} \times P_{\mathrm{CR}} \times C_{syst}. \tag{5.8}$$

In case of independent nuisance parameters, the probability density function of the systematic uncertainties, C_{syst}, can be expressed as the product of Gaussians with unit width centred at $\theta_i - \theta_i^0$, with θ_i^0, being the central value of the auxiliary measurement, usually set to zero. The probability density function of the MC statistical uncertainties is represented by Poisson distributions.

Fit description

Three types of fits are considered in this analysis: the background-only fit, the model-independent signal fit and the model-dependent signal fit.

The *background-only fit* aims to estimate the background contribution in SRs and VRs. This is achieved by performing the fit only in the CRs and using the resulting fit parameters to extrapolate the background expectation to the SRs and VRs, being excluded from the fit.

The purpose of the *model-independent signal fit* is to set upper limits on the number of signal events in each SR. It is performed for every SR, taking into account all the CRs and only one SR at a time. To be model-independent, integrated event yields are used instead of distributions. The expected signal contribution is considered only in the SR under study and a possible signal contamination in the CRs is neglected. Once the fit is performed and the fit parameters are optimized with respect to the observation, several hypotheses with different signal strength values are tested and the CL_S is evaluated each time. The signal strength which leads to a CL_S at 5% represents the 95% CL upper limit on the number of signal events in a SR. Both the observed and expected upper limits, N_{obs}^{95} and N_{exp}^{95} are determined. The background-only hypothesis is also tested and the p-value, p_0, is calculated in order to quantify the significance of an event excess in a SR.

The goal of the *model-dependent signal fit* is to test a specific signal model. If no significant excess of events in each SR is found, exclusion limits are set on the signal model. The model-dependent signal fit takes into account the CRs together with the SRs. The signal contribution is considered in both types of regions and includes a signal contamination in the latter. The signal model is tested with its expected cross section. If the resulting CL_S is less than 5% the model is excluded. In general, better sensitivity is achieved by taking into account multiple SRs and their shape information. In fact, distributions of SRs help discriminating the signal from the background. In this analysis the fit is performed on the $E_{\text{T}}^{\text{miss}}$ distribution which provides a significant discrimination power between the signal and the background.

Extrapolation

The background prediction, which depends on the estimators of the systematic uncertainty nuisance parameters and of the background normalisation factors, is extrapolated to the SRs and VRs from the fit in the CRs. The extrapolation procedure is possible since the background parameters of the probability density function are shared among all the different regions.

Once the parameters are constrained in the CRs by means of the background-only fit, the values of the background normalisation factors and the θ_i central value of the systematic uncertainty, i, are used to estimate the contribution of all the SM processes in the SRs and VRs. The uncertainty, $\sigma_{b,\text{tot}}$, on the extrapolated background prediction, b, is estimated by error propagation:

$$\sigma_{b,\text{tot}}^2 = \sum_i^n \left(\frac{\partial b}{\partial \eta_i}\right)^2 \sigma_{\eta_i}^2 + \sum_i^n \sum_{j \neq i}^n \rho_{ij} \left(\frac{\partial b}{\partial \eta_i}\right) \left(\frac{\partial b}{\partial \eta_j}\right) \sigma_{\eta_i} \sigma_{\eta_j} \tag{5.9}$$

where η_i is the collection of all the free parameters (normalisation factors, $\boldsymbol{\mu_b}$, and the set of systematic uncertainty auxiliary measurements, $\boldsymbol{\theta}$) with standard deviation σ_{η_i}, and ρ_{ij} is the correlation coefficient between the parameters η_i and η_j.

5.5 Systematic uncertainties

The sources of the systematic uncertainties in this analysis are either experimental or come from modelling uncertainties of the SM processes.

The main detector-related uncertainties affect the energy scale of the HEPTopTagger subjets and the large-R jets. The uncertainty on the subjet energy resolution is included, since it has a non-negligible contribution before the fit. The contribution of the energy scale uncertainty of small-R jets is considered as well, as it influences the reconstruction of the missing transverse energy, while the uncertainty on the small-R jet resolution is found to be negligible. In the regions where a b-tagged jet is required, the corresponding uncertainties are included. The uncertainties related to the reconstruction of the soft term of the $E_{\mathrm{T}}^{\mathrm{miss}}$, coming from the energy deposits not associated with other particle objects, are found to be negligible.

Concerning the modelling uncertainties on the SM expectation, those on the cross section of the SM processes are considered. In addition, the modelling uncertainties of the V+jets and $t\bar{t}$ processes are estimated. The $t\bar{t}$ modelling uncertainties consist of parton shower, generator, ISR/FSR, PDF and renormalisation scale uncertainties.

All the systematic uncertainties and their estimate by means of auxiliary measurements are explained in section 2.7.

5.5.1 Systematic uncertainty profiling

The systematic uncertainties are introduced in the fit as nuisance parameters $\hat{\boldsymbol{\theta}}$ and are constrained in the CRs. They are modelled before the fit by a Gaussian centred at the origin ($\theta_0 = 0$), with unitary width. The uncertainties are constrained with the fit. In particular the preferred Gaussian mean value in units of the input σ are profiled on the CR data. The Gaussian mean and width, which result from the background-only fit are displayed in figure 5.24. The central values after fit of the systematic uncertainties related to b-tagged jets and of those on the theory cross sections are close to zero with unitary width.

The uncertainties, that benefit most from the profiling on the CR data, are those affecting the shape of the top quark mass peak: the $t\bar{t}$ modelling, subjet energy scale and resolution uncertainties. These are considerably constrained by the data distribution of the top candidate mass in the $t\bar{t}$ CR and μ+jets CR and they are reduced to 50% for the $t\bar{t}$ parton shower uncertainty and to 70%-80% for most of the others.

After extrapolating all the fit parameters to the SRs, the impact of each systematic uncertainty is estimated by fixing all the other parameters and propagating the error of the nuisance parameter under study to the background prediction.

SR1 is the signal region which is affected by the largest relative systematic uncertainty, 23%. SR2 and SR3 have systematic uncertainties of 11% and 13%, respec-

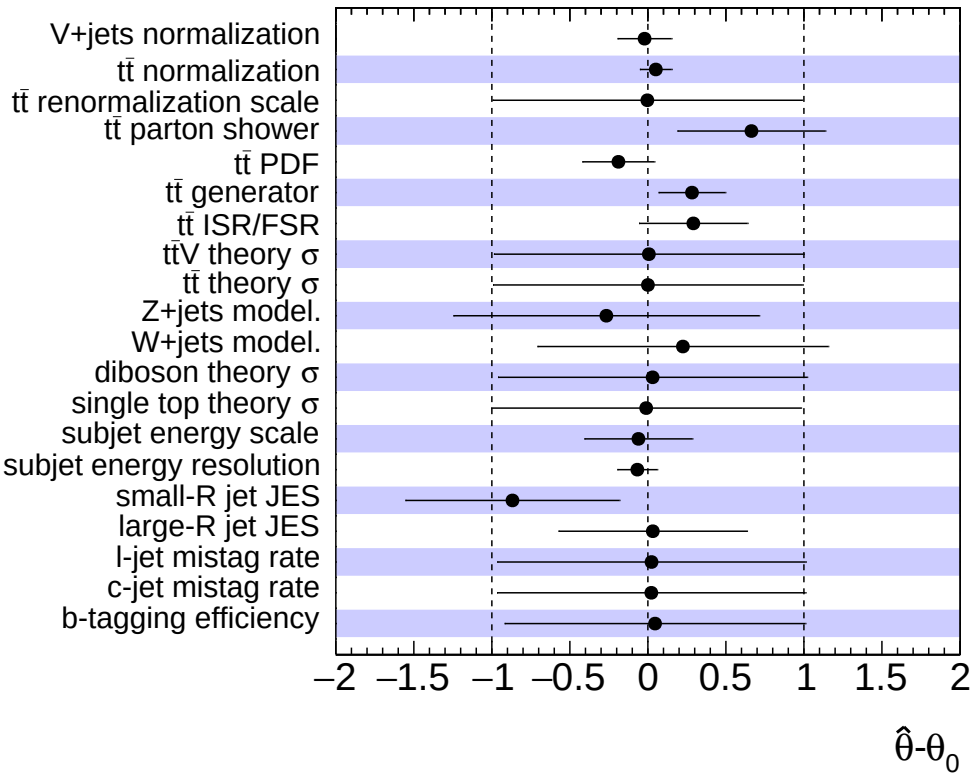

Figure 5.24: Fit values of the nuisance parameters associated to the systematic uncertainties. The shift of the fitted central value $\hat{\theta}$ with respect to initial parameter value θ_0 is represented on the x-axis for each source of uncertainty on the y-axis. θ_0 is by convention zero for all the uncertainties, apart from the normalisation factors whose central nominal value is $\theta_0 = 1$. The pre-fit variation of each uncertainty by $+1\sigma$ or -1σ corresponds to a pre-fit absolute error on θ_0 of 1. After the fit, the impact of each uncertainty is constrained by the observation and thus the error on $\hat{\theta}$ may be reduced.

tively.

The dominant uncertainty of SR1 is the one due to the limited MC statistics with an effect of 20%: the requirement of two top tags rejects a large fraction of simulated background events. The requirement of the second top candidate implies that the subjet energy scale, the $t\bar{t}$ normalisation and modelling have a large impact, each ranging from 3% to 9%. In fact, in events with only one hadronically decaying top quark, as for the $t\bar{t} \to (l\nu b)(qqb)$ process, one of the two top candidates is a fake top reconstructed from other hadronic activity combined in a large-R jet. The substructure properties of this jet heavily depend on the modelling of the additional hadronic activity in the event. These non-top jets are mostly characterised by low p_{T} subjets, whose energy scale uncertainty have a large impact on the total number of selected events.

Regarding SR2 and SR3, the uncertainties on the normalisation factors of $t\bar{t}$ and V+jets, on the $t\bar{t}$ parton shower and on the energy scale of small-R jets have the largest effect which ranges from 4% to 10%. The breakdown of all the systematic uncertainties for the three SRs is reported in appendix B.

5.5.2 Uncertainty correlations

To account for the total uncertainty in a certain region, the correlations between the fit parameters must be considered. The correlation matrix resulting from the background-only fit is represented in figure 5.25. A negative (positive) correlation between parameter θ_1 and θ_2 means that the increase in θ_1 is reflected in the fit by a decrease (increase) in θ_2.

A correlation of approximately -0.6 is found between the normalisation factor of the $t\bar{t}$ process and its theory cross section; and of -0.5 (-0.7) between the normalisation of the Z+jets (W+jets) and its modelling.

The normalisation factors are correlated with the estimate of the energy scale of the large-R jets and subjets. Under the hypothesis that the nominal energy scales are underestimated and the corresponding θ parameters are centred at positive values after fit, the number of events selected in the CRs increases. This effect has to be compensated by a decrease of the background normalisation factors. This explains the negative correlation which is around -0.4 between the above-mentioned uncertainties.

As explained in section 4.2, the uncertainty on the subjet energy scale has a direct effect on the top mass peak. If the scale were underestimated, and the best estimate would be close to the "up" variation of the uncertainty, the peak of the reconstructed top mass would shift to higher values and more large-R jets would be tagged. This uncertainty presents interesting correlations with other parameters. The largest value, 0.7, is with the $t\bar{t}$ ISR/FSR uncertainty. In fact the enhancement of the initial and final state radiation makes the event more busy, slightly decreasing the efficiency of top-tagging a large-R jet. An additional effect is to reconstruct the

top candidate with a mass lower than in top events with nominal conditions. This can be explained by the higher number of reconstructed protojets in the large-R jet and the consequent misidentification of one of the three subjets, representing the top quark decay products. The resulting shift to lower masses of the top candidate mass distribution related to the condition with enhanced ISR or FSR should be than compensated by higher energy scale applied to the subjets which moves to higher values the reconstructed mass.

The reason for a correlation of -0.5 between the uncertainties on the scale and the resolution of the subjet energy lies in the shape of the top candidate mass with the application of the resolution uncertainty variation. Protojets and subjets reconstructed by the HEPTopTagger algorithm are calibrated and a minimum p_{T} of 20 GeV is required. All the subjets and protojets are smeared before calibration. The lower the p_{T} of these jets is, the larger the applied smearing is. As a result, a larger number of protosubjets pass the 20 GeV threshold, which contribute to the final candidate mass. The top mass peak broadens with the smearing applied to the subjets. This effect could be partially compensated by a reduced energy calibration scale applied to the subjets.

The uncertainty correlation between the energy scale of the large-R jets and the one of the subjets is 0.3. If the central value of the first increases, the energy scale of the large-R jets becomes larger. Hence, large-R jets, which had transverse momentum just below the threshold of 280 GeV before the fit, are able to pass the p_{T} requirement. However, these are low p_{T} large-R jets whose HEPTopTagger mass is probably small, as one top decay product might not lie in the jet. Thus, the effect of increasing the scale of large-R jets is to enhance the low values of the top candidate mass distribution, which can be compensated by a larger estimate on the energy scale of the subjets.

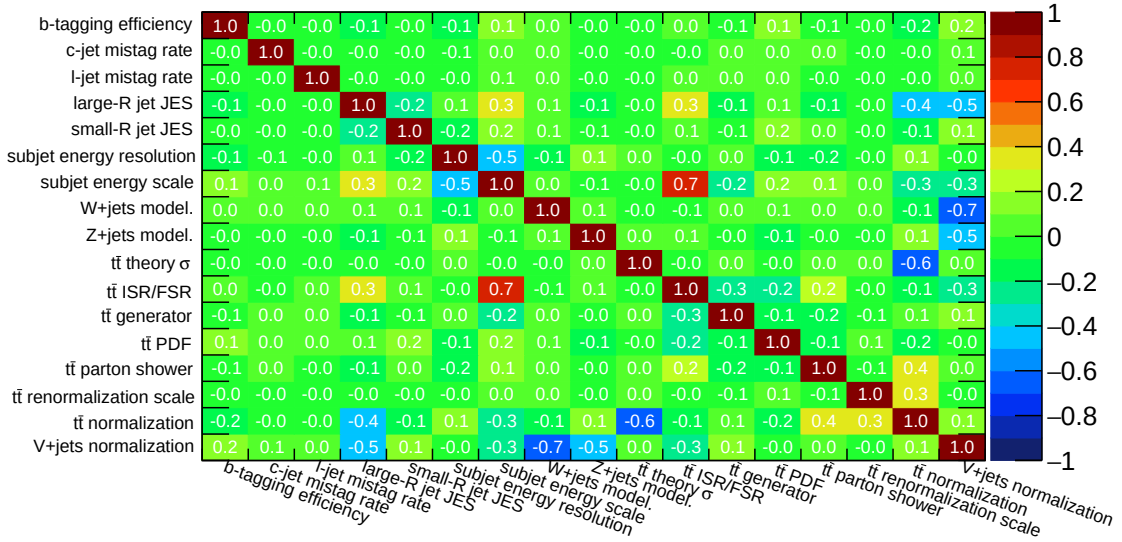

Figure 5.25: Correlation matrix of the systematic uncertainties from the background-only fit.

5.5.3 Systematic uncertainties on the signal process

The systematic uncertainties on the signal process are evaluated before the fit is applied and are reported in the following with respect to the sample with $\tilde{t}_1$ mass of 600 GeV and $\tilde{\chi}_1^0$ mass of 1 GeV.

The dominant experimental uncertainties are the subjet energy scale and resolution with a contribution of 2-8% and 6-9%, respectively. These uncertainties affect mainly SR1, due to the requirement of two reconstructed top quarks. The large impact of the subjet uncertainties is mitigated after the fit in the CRs. The uncertainty on the scale of small-R jets is about 3% for SR1 and SR2 and 6% for SR3, while the one on the large-R jet energy scale is non-negligible only for SR2, due to the requirement of a second large-R jet, with an effect of 3% on the signal yield. The uncertainty on the b-tagging efficiency related to SR2 and SR3 is of the order of 1%. All these detector-related systematic uncertainties are considered in the fit as correlated with the background ones.

The uncertainties on the theory modelling of the top squark production are not taken into account as nuisance parameters in the fit. Their impact is considered explicitly in the exclusion limit by performing independent hypothesis tests with modified nominal cross section according to the uncertainty.

5.6 Validation of the background extrapolation

The background contribution in the SRs and VRs is predicted by means of the extrapolation of the parameters resulting from the background-only fit of the CRs. The expectation of the $V+$jets (where $V = W$ or Z) and $t\bar{t}$ processes is corrected by the corresponding normalisation factor, summarised in table 5.7. The fitted value of these two factors is compatible with 1 within the uncertainty. The contribution of the other background processes is given by the simulation normalised to the theory cross section. The total background prediction depends not only on the normalisation factors, but also on the central values of the systematic uncertainties, included in the fit as nuisance parameters and profiled on the CR data.

Background Source	Normalisation Factor
$t\bar{t}$	1.05 ± 0.10
$V+$jets	0.98 ± 0.17

Table 5.7: Normalisation factors of the main background sources obtained from the background-only fit: $t\bar{t}$ and V+jets production (where $V = W$ or Z)

The number of expected events in the CRs before and after the fit is reported in table 5.8 together with the separated contribution of the different sources. The systematic uncertainties and their nuisance parameters are discussed in detail in section 5.5.

	V+jets CR	$t\bar{t}$ CR	μ+jets CR
Observed events	511	1045	1289
Fitted background events	513.06 ± 22.16	1048.97 ± 30.10	1282.71 ± 33.46
$t\bar{t}$	65.81 ± 11.78	905.60 ± 31.12	1019.68 ± 39.18
W+jets	251.23 ± 32.92	50.65 ± 7.93	201.48 ± 27.44
Z+jets	174.19 ± 27.73	40.06 ± 6.67	–
VV	15.53 ± 2.19	4.42 ± 0.56	15.94 ± 0.95
$t\bar{t}V$	0.96 ± 0.26	12.49 ± 2.77	12.92 ± 2.83
Single Top	5.34 ± 0.86	35.75 ± 3.28	32.69 ± 2.50
Expected events (before fit)	517.16	1056.91	1328.64
$t\bar{t}$	68.06	910.73	1069.06
W+jets	243.47	50.57	197.98
Z+jets	183.27	42.83	–
VV	16.25	4.49	15.94
$t\bar{t}V$	0.99	12.53	12.91
Single Top	5.12	35.77	32.76

Table 5.8: Number of events in the control regions after the background-only fit. Nominal simulation expectations (before fit) are given for comparison. The errors shown are the total systematic uncertainty.

The pull value, χ, is employed to validate the background extrapolation. χ is defined as the difference between the number of observed and predicted events, n_{obs} and n_{pred}, divided by σ_{tot}, which is the quadrature sum of the systematic uncertainty on the background prediction, σ_b, and the Poissonian statistical uncertainty σ_{stat} on n_{pred}:

$$\chi = \frac{n_{\text{obs}} - n_{\text{pred}}}{\sigma_{\text{tot}}} \qquad (5.10)$$
$$\sigma_{\text{tot}} = \sqrt{\sigma_b^2 + \sigma_{\text{stat}}^2}$$

The pull distributions for all the regions is shown in figure 5.26. The maximum deviation between the observation and the prediction in the VRs is 1.2σ.

The observed and predicted number of events in the two VRs are summarised in table 5.9.

5.7 Results, interpretation and limits

The three fit procedures, described in section 5.4.1, are used to interpret the observations with respect to the background-only hypothesis or to the background-plus-signal hypothesis. The signals considered are either a model-independent non-SM contribution or the direct $\tilde{t}_1$ pair production SUSY model in the $(t\tilde{\chi}_1^0)(\bar{t}\tilde{\chi}_1^0)$ final state.

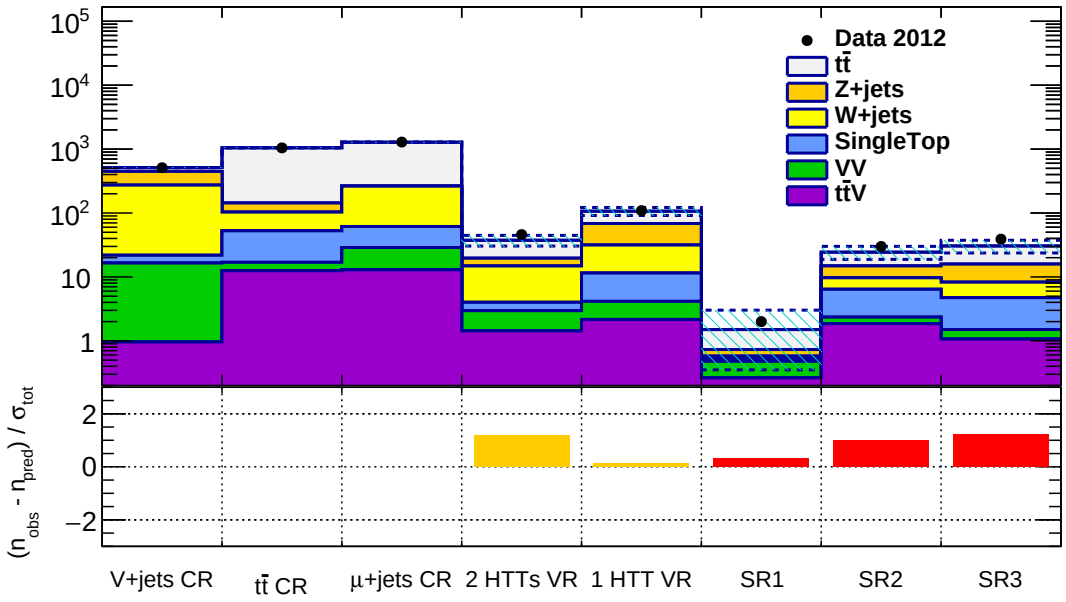

Figure 5.26: In the top panel the predicted number of events are represented by the stacked histogram and the observed ones by black points in CRs, VRs and SRs. The dashed lines correspond to the total systematic uncertainty added in quadrature with the statistical uncertainty. In the bottom panel the pull distribution of the observed yields with respect to the predicted yields is represented for CRs, VRs and SRs.

The estimate of the background prediction and the events observed in data in each SR are reported in table 5.10. The SM prediction is determined from the background-only fit and its error results from the propagation of the systematic uncertainties through the background extrapolation procedure.

The compatibility of the observation with the background-only hypothesis is tested as described in section 5.4.1. The p-value for each SR is calculated and reported in table 5.10. Since the smallest p_0 is 0.13, corresponding to 1.1σ deviation, no significant excess with respect to the SM expectation is observed. Upper limits on BSM contribution are set for each SR by means of the model-independent fit. The 95% CL upper limits on the number of expected and observed signal events, N^{95}_{exp} and N^{95}_{obs}, are summarised in table 5.10. These limits are derived using the CL_S method and calculated with the asymptotic formulae [152]. It has been verified that these results are in good agreement with those obtained from throwing multiple pseudo-experiments.

The signal model of direct $\tilde{t}_1$ pair production is tested against the SM-only assumption with the model-dependent signal fit and hypothesis test. A class of SUSY models is described in terms of the unknown mass parameters of the SUSY particles involved: the mass of the top squark, $m_{\tilde{t}_1}$, and the mass of the neutralino, $m_{\tilde{\chi}^0_1}$. This class is formed by a grid of signal samples with $\tilde{t}_1$ masses ranging from 250 GeV up to 800 GeV in steps of 50 GeV. Similarly the $\tilde{\chi}^0_1$ masses vary between 1 GeV up to

	2 HTTs VR	1 HTT VR
Observed events	46	109
Fitted background events	37.51 ± 3.68	106.80 ± 11.39
W+jets	10.81 ± 2.14	20.05 ± 4.07
Z+jets	4.79 ± 0.89	36.92 ± 7.28
$t\bar{t}$	17.90 ± 2.96	38.34 ± 3.57
VV	1.54 ± 0.19	1.98 ± 0.35
$t\bar{t}V$	1.43 ± 0.33	2.16 ± 0.49
Single Top	1.04 ± 0.13	7.35 ± 0.67

Table 5.9: Validation Regions: The fit results are obtained from the control regions using the background-only fit. The errors shown correspond to the total systematic uncertainty.

the allowed value for the decay $\tilde{t}_1 \to t\tilde{\chi}_1^0$ (i.e. $m_{\tilde{t}_1} > m_t + m_{\tilde{\chi}_1^0}$). Every point in this bi-dimensional grid is a SUSY model undergoing the hypothesis testing procedure. For each point, the fit is performed simultaneously in the SRs and the CRs, taking into account the specific signal contribution in every region. The three SRs are statistically independent and thus are combined in order to enhance the sensitivity of the test. The SR $E_{\mathrm{T}}^{\mathrm{miss}}$ distributions are displayed in figure 5.27. The background expectation is the result of the model-dependent fit, while the contribution of two representative signal models is obtained from the normalisation of the signal event yields to the nominal signal cross section. The asymptotic approximation is employed to calculate the $\mathrm{CL_S}$ for each $(m_{\tilde{t}_1}, m_{\tilde{\chi}_1^0})$ model. The compatibility of the asymptotic approximation with the results obtained from pseudo-experiments has been verified on one signal model.

A contour in the $(m_{\tilde{t}_1}, m_{\tilde{\chi}_1^0})$ plane delimits the region of the phase space which contains the models excluded at 95% CL. Several exclusion contours can be seen in figure 5.28. The *observed* limits are calculated from the data distributions with respect to models with nominal signal cross section for the central value or with $\pm\sigma_{\mathrm{theory}}^{\mathrm{SUSY}}$ variation on the signal theory uncertainties. The *expected* limits are obtained in the same way as the observed limits by substituting the data with the background expectation. The limit excursion due to the background systematic uncertainty variation by $\pm\sigma_{\mathrm{exp}}$ is also evaluated. Under the assumption of 100% branching ratio of the decay $\tilde{t}_1 \to t\tilde{\chi}_1^0$, models with top squark mass ranging from 250 GeV to 720 GeV are excluded if the neutralino mass is of the order of a few GeV. For neutralino masses less than 75 GeV, the observed limits are very close to the expected limits. The observation cannot exclude potential signals with $m_{\tilde{\chi}_1^0} > 140$ GeV, while the analysis was expected to be sensitive to exclude models with neutralino masses up to 200 GeV for $m_{\tilde{t}_1} \approx 600$ GeV. The reason for this difference is the following. For scenarios with the same top squark mass, the higher the $\tilde{\chi}_1^0$ mass is, the lower the missing transverse momentum of the signal events is on average. The $E_{\mathrm{T}}^{\mathrm{miss}}$ dis-

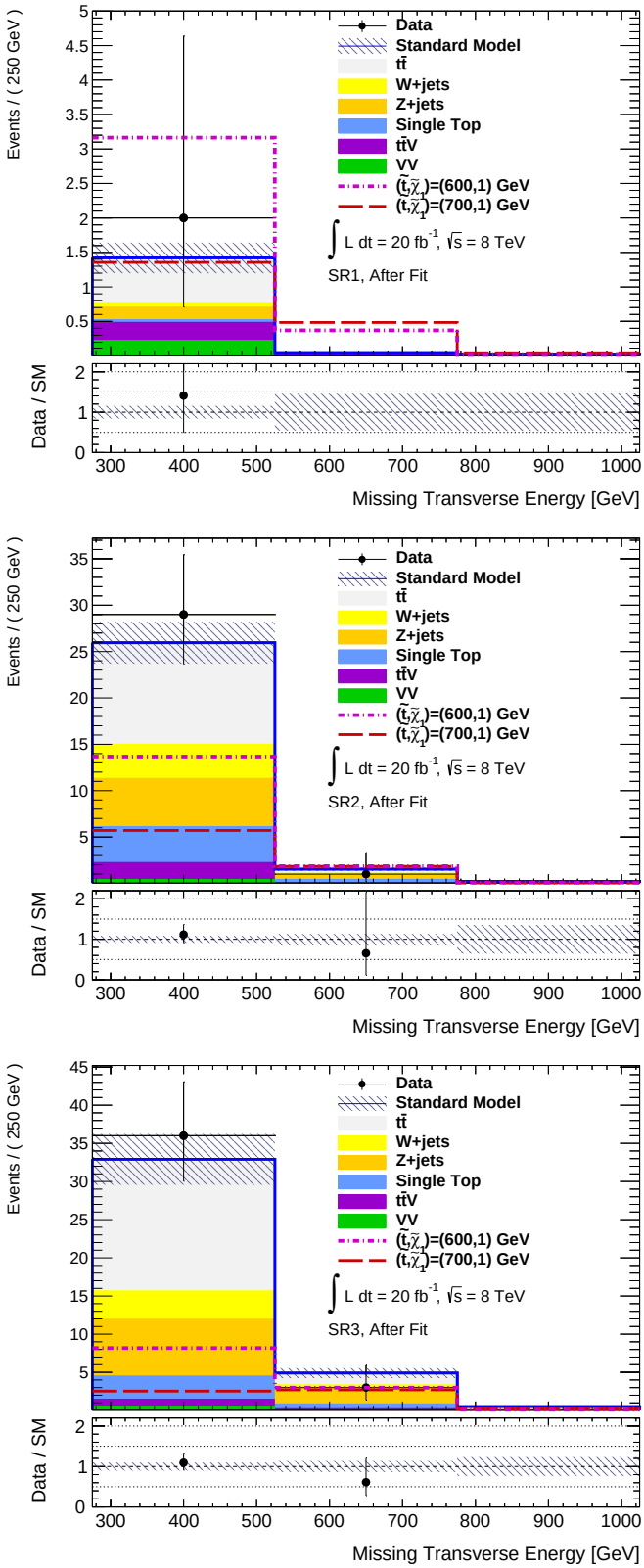

Figure 5.27: Missing transverse energy distributions for SR1 (top), SR2 (centre), and SR3 (bottom), after the model-dependent fit is performed. The SM background prediction is represented as a stacked histogram while the data distribution is overlaid as black points. The signal expectations for the samples with $(m_{\tilde{t}_1}, m_{\tilde{\chi}_1^0}) = (600, 1)$ GeV and $(m_{\tilde{t}_1}, m_{\tilde{\chi}_1^0}) = (700, 1)$ GeV are represented by a violet and purple dashed line respectively. The lower panel shows the ratio between the data and the SM prediction and overlaid is the after-fit impact of the systematic uncertainties.

	SR1	SR2	SR3
Observed events	2	30	39
Fitted background events	1.51 ± 0.35	24.36 ± 2.76	30.54 ± 4.10
$t\bar{t}$	0.78 ± 0.25	9.52 ± 2.30	14.69 ± 2.38
W+jets	0.05 ± 0.02	3.28 ± 0.62	3.54 ± 0.76
Z+jets	0.15 ± 0.05	5.16 ± 0.94	7.58 ± 1.61
VV	0.21 ± 0.07	0.47 ± 0.13	0.44 ± 0.17
$t\bar{t}V$	0.26 ± 0.08	1.86 ± 0.41	1.07 ± 0.25
Single Top	0.05 ± 0.02	4.06 ± 0.35	3.24 ± 0.37
Expected signal events $(m_{\tilde{t}_1}, m_{\tilde{\chi}_1^0})$			
$(600, 1)$ GeV	3.55	15.63	11.26
$(700, 1)$ GeV	1.87	7.60	5.44
N_{obs}^{95}	4.7	17.3	22.5
N_{exp}^{95}	$4.1^{+2.2}_{-1.1}$	$12.6^{+5.6}_{-3.6}$	$15.9^{+6.6}_{-4.6}$
p_0	0.35	0.17	0.13

Table 5.10: Event yields in each signal region (SR1, SR2, and SR3). The observed events are reported together with the simulated prediction after the discovery fit is performed. The predicted contribution of different background sources is summarised. The errors in the table correspond to the total systematic uncertainty, which is calculated taking into account all the correlations. The expected signal events before fit for two signal models are presented. For each signal region the 95% CL upper limits on the number of observed (expected) signal events, N_{obs}^{95} (N_{exp}^{95}) are included together with the observed p-value concerning the background-only hypothesis.

tributions of SR2 and SR3 are characterised by a small excess of data events with respect to the SM expectation in the lowest bin. This particular bin is populated by most of the events of signal models with large $\tilde{\chi}_1^0$ masses ($m_{\tilde{\chi}_1^0} \gtrsim 100$ GeV). Thus the signal-plus-background hypothesis is not incompatible with the observation and it cannot be rejected.

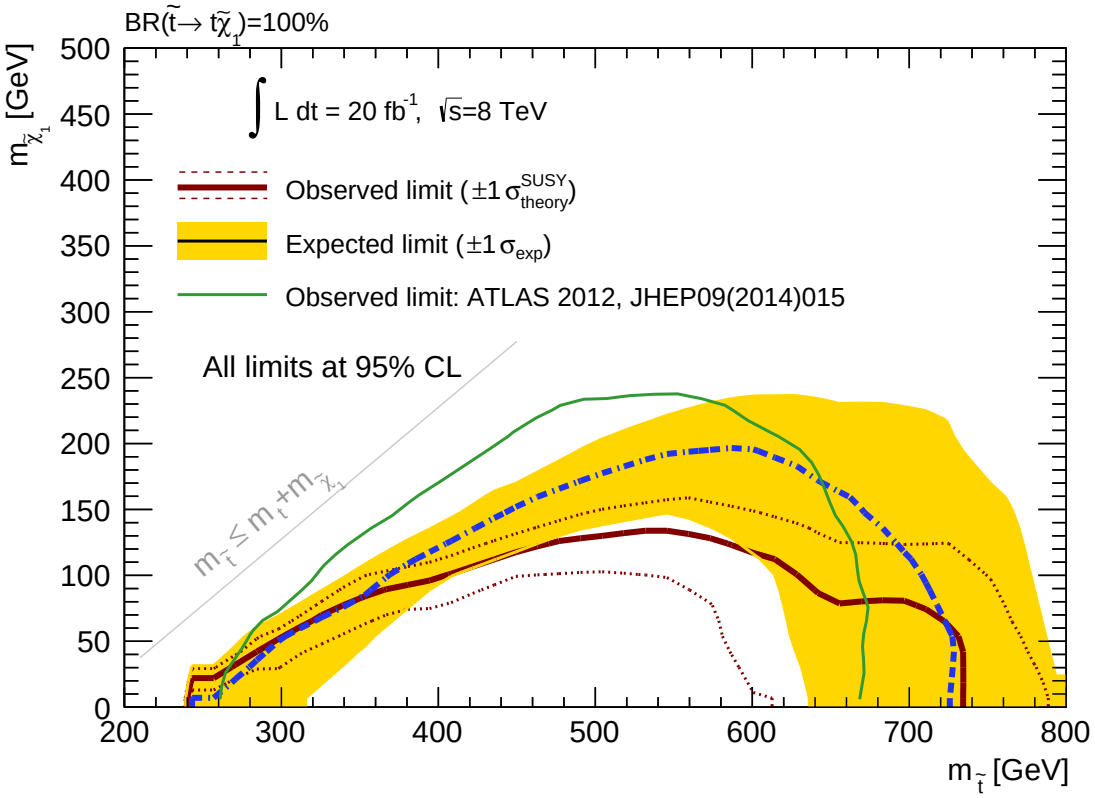

Figure 5.28: 95% CL expected and observed exclusion limits in blue dashed line and red solid line respectively in the mass plane $(m_{\tilde{t}_1}, m_{\tilde{\chi}_1^0})$. The yellow band represents the $\pm 1\sigma$ uncertainty on the expected limit, obtained by taking into account all the systematic and statistical uncertainties apart from the signal theory uncertainty whose impact on the limits is indicated by the dashed red lines. The observed contour from the published ATLAS analysis [7] is superimposed and represented by a green line.

5.8 Comparison with the published ATLAS analysis

The analysis reported so far makes use of the HEPTopTagger to search for direct production of a pair of the scalar top partners each decaying into a top quark and a neutralino. This strategy is sensitive to events with both top quarks decaying all-hadronically and to signal models where the $\tilde{t}_1$ mass is much larger than the $\tilde{\chi}_1^0$ mass, such that a non-negligible fraction of events have moderately boosted top quarks in the final state.

A different reconstruction approach of the hadronically decaying top quarks has been employed by the published ATLAS analysis [7]. In order to be sensitive to models with $\tilde{t}_1$ masses ranging from low to high values, i.e. $m_{\tilde{t}_1}$ between 250 GeV and 700 GeV, with $\tilde{\chi}_1^0$ masses in the interval $(0, m_{\tilde{t}_1} - m_t)$, resolved or semi-resolved techniques are used. The *resolved* approach is used for events with six or more small-R jets: a jet is reconstructed for each top quark decay product. Each of the two top

candidates is built by one b-tagged jet, and by two close jets in the $\eta - \phi$ plane, representing the W decay. Loose requirements on the reconstructed top masses are applied in order to provide high signal efficiency. The top candidate mass in the resolved signal region is required to be greater than 50 GeV.

The *semi-resolved* approach is applied as an alternative to the previous one to reconstruct higher p_{T} top quarks. In this case not all the decay products result in an individual small-R jet. The events selected for this category are thus characterised by four or five small-R jets. In order to associate a group of these jets to each top quark decay, they are reclustered by the anti-k_t algorithm with $R = 1.2$, i.e. the small-R jets themselves are used as input to the anti-k_t algorithm. A semi-resolved signal region is defined to select events with at least two reclustered $R = 1.2$ jets.

The probability of reconstructing at least one candidate, associated to a hadronically decaying top quark, is different for the three techniques and depends on the p_{T} of the associated top quark. The comparison between the three methods is shown in figure 5.29(a). The signal model with $(m_{\tilde{t}_1}, m_{\tilde{\chi}_1^0}) = (700, 1)$ GeV is employed for this and the following comparisons, unless stated otherwise. While the resolved technique is not suitable for high p_{T} top quarks, both the semi-resolved one and the HEPTopTagger algorithm aim to reconstruct top quarks in the moderately boosted regime. The HEPTopTagger has the best efficiency to identify top quarks with $p_{\mathrm{T}} > 300$ GeV.

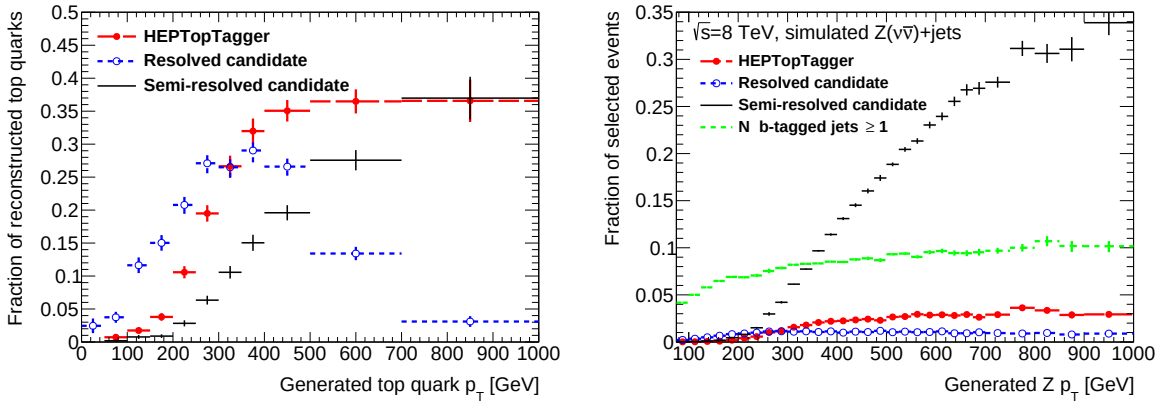

(a) (b)

Figure 5.29: Top tagging efficiency comparison in the signal sample $(m_{\tilde{t}_1}, m_{\tilde{\chi}_1^0}) = (700, 1)$ GeV (a), top tagging mis-tag fraction in the background $Z(\nu\bar{\nu})$+jets sample (b). A HEPTopTagger top tag is found if a top candidate with mass in the range $(140, 210)$ GeV is found. A top is reconstructed by means of the resolved method if the invariant mass of a b-tagged small-R jet and other two close-by small-R jets is within the range $(50, 250)$ GeV, as required in the analysis described in [7]. The leading top candidate reconstructed with the semi-resolved method is required to have mass in the range $(140, 500)$ GeV.

A simulation of Z+jets events with the Z boson decaying to neutrinos is used to calculate the fraction of events containing a fake top candidate for the different top

reconstruction techniques. This mis-tagged fraction is represented in figure 5.29(a) as a function of the generated Z boson transverse momentum. The HEPTopTagger and the resolved method have the best rejection power, with a fraction of selected events which increases with higher Z boson transverse momentum up to 3% and 1% respectively. It should be noticed that the resolved method has the implicit requirement of the reconstruction of at least one b-tagged jet per top candidate. The Z+jets simulation contains events with light and heavy flavour jets and the fraction of selected events by requiring at least one b-tagged jet is between 5 and 10%.

Without b-tag information, the rejection power of requiring two candidates reconstructed by the resolved or semi-resolved technique would not be enough to disentangle the signal from the background. Hence, additional requirements are applied to reject SM background. The most important ones are large missing transverse momentum, as required also in the HEPTopTagger analysis, and two b-tagged jets, with $M_{\mathrm{T}}^{\mathrm{b,min}} > 175$ GeV. On the contrary, the HEPTopTagger has the capability to reject a large fraction of background events not containing hadronically decaying top quarks and its application does not need the requirement of two b-tagged jet to acquire sensitivity to the signal process.

The comparison of the visible signal event fraction between the HEPTopTagger analysis and the published ATLAS analysis using the resolved and semi-resolved techniques is shown in figure 5.30 as a function of the minimum and maximum top quark transverse momentum in the event. It can be noticed that the signal acceptance of the HEPTopTagger analysis (SR1, SR2, SR3 combined) is about three times larger than the one that uses (semi-)resolved techniques. This difference is mainly caused by the requirement of two b-tagged jets, that have the advantage of rejecting a large fraction of the background, but the negative effect of discarding signal events. For comparison purposes, the amount of selected signal events with the additional requirement of two b-tagged jets in the HEPTopTagger analysis is shown in figure 5.30. The signal acceptance for this selection is higher than the one from the published analysis for events with boosted top quarks.

The final results of the two analyses are compared in figure 5.28, where the exclusion limits of the signal models are shown in the $(m_{\tilde{t}_1}, m_{\tilde{\chi}_1^0})$ plane. The observed exclusion contour of the published analysis reaches a $m_{\tilde{t}_1}$ value of 660 GeV for massless neutralinos, while the HEPTopTagger analysis is able to exclude models up to $m_{\tilde{t}_1} \approx 720$ GeV. On the other hand, the published analysis could exclude models with large $\tilde{\chi}_1^0$ masses, while the HEPTopTagger analysis has no sensitivity to reject these models. Similar limits are obtained by the two analyses for regions in the parameter space with small $\tilde{t}_1$ and $\tilde{\chi}_1^0$ masses. Thus, as expected, the HEPTopTagger analysis is the most suitable to test models with $m_{\tilde{t}_1} \gg m_{\tilde{\chi}_1^0}$ which are more likely to have boosted top quarks in the final state.

It is interesting to calculate the overlap between the (semi-)resolved analysis and the HEPTopTagger one. This estimate is performed by applying the analyses requirements on a signal model with $(m_{\tilde{t}_1}, m_{\tilde{\chi}_1^0}) = (700, 1)$ GeV. About 14% is the

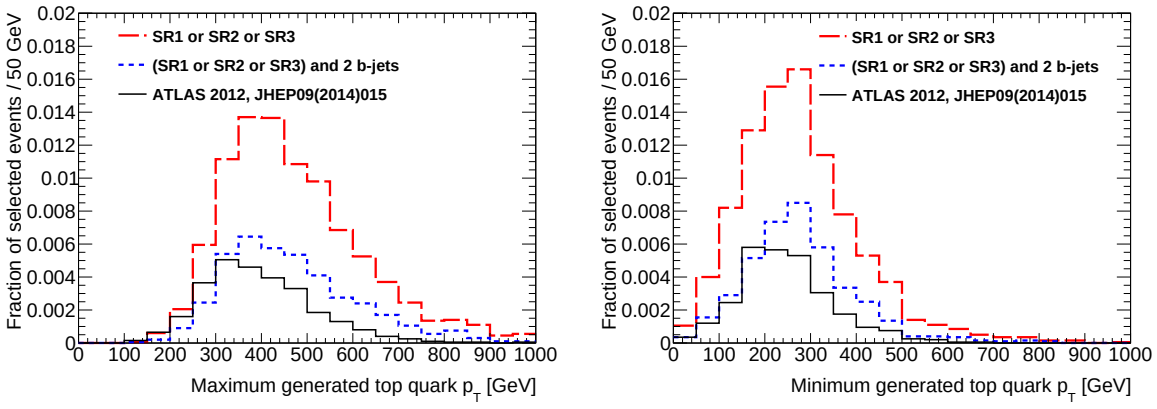

(a) (b)

Figure 5.30: Ratio of the number of signal events selected by the HEPTopTagger analysis, i.e. SR1, SR2 and SR3 combined, represented in red dashed line, over the number of total simulated signal events. The same ratio is represented in blue dashed line if the requirement of two b-tagged jet is added to the analysis selection. The fraction of signal events selected by the published analysis [7] is represented in solid black line. The fraction of selected events are represented as a function of the maximum and minimum generated top quark p_{T} in (a) and (b) respectively.

fraction of events selected by the HEPTopTagger analysis which are also contained in the signal regions of the published analysis. Even by requiring two b-tagged jets in the HEPTopTagger analysis the overlap reaches at most a level of 30%. The small overlap keeps open the option to create orthogonal signal regions between the HEPTopTagger and the published analyses for future $\tilde{t}_1$ searches at higher centre of mass energies.

Conclusions

In this thesis, a detailed analysis of the HEPTopTagger performance and its application in a search for the top squark in proton-proton collision data collected at a centre of mass energy of $\sqrt{s} = 8$ TeV by the ATLAS detector are reported. The dataset corresponds to an integrated luminosity of about 20 fb^{-1}.

The HEPTopTagger algorithm is validated in a sample enriched in top quarks, obtained by applying the ℓ+jets channel selection, which consists of one isolated electron or muon, b-tagged jets, and a large-R jet. It is shown that the four-momenta of the large-R jet (the input to the HEPTopTagger) and of the top quark candidate are very well described by the simulation of Standard Model processes.

In my work, an innovative technique is developed to measure in-situ the energy scale uncertainty of the subjets reconstructed within the HEPTopTagger. The subjet energy scale is one of the dominant sources of uncertainty, since the top quark candidate four-momentum is the result of the sum of the reconstructed and calibrated subjets. By comparing the mass of the top quark candidate reconstructed in data and simulation, the derived relative uncertainty on the subjet p_{T} is at most 10% for subjets with $p_{\mathrm{T}} = 20$ GeV and decreases to approximately 2-3% for high p_{T} subjets. A recipe for the evaluation of the contribution of this uncertainty has been developed for physics analyses.

The efficiency of tagging hadronically decaying top quarks is measured to vary from 10% for large-R jets with $p_{\mathrm{T}} \approx 200$ GeV to 45% for large-R jets with $p_{\mathrm{T}} \gtrsim 400$ GeV. The dominant systematic uncertainty is the modelling of the $t\bar{t}$ SM process. The measured and simulated efficiencies are consistent within few percent. The MC simulation has been verified to be a reliable tool to model and predict the output of the HEPTopTagger algorithm. The results of this work has been published in [6], together with the performance of other top tagging techniques.

The HEPTopTagger has been applied in the search for the direct production of a pair of supersymmetric top partners in the fully hadronic channel. Under the assumption that each top squark decays into a top and a neutralino with a branching ratio of 100%, the experimental signature consists of large missing transverse momentum and jets. The HEPTopTagger capability to discriminate between large-R jets originating from top quarks and those from light quarks or gluons, and to reconstruct the kinematics of top quarks, makes the algorithm a very valuable tool in this search. In a signal enriched region the reconstruction of two HEPTopTagger candidates is exploited to calculate the stransverse mass, M_{T2}, which carries information

about the mass of the top squark. Events with large missing transverse momentum and large M_{T2} are selected for a first signal region. The significance of the search is further enhanced by the use of two other signal enriched categories with only one top tag, at least one b-tag and large missing transverse momentum. Improvements in sensitivity to the top squark pair production is provided by the statistical combination of the three signal regions. No significant excess is observed over the expected SM background. Hence, exclusion limits are set in the plane defined by the mass of the top squark and the mass of the neutralino. Under the assumption that the top squark decays with 100% branching ratio into a top quark and a neutralino, top squark masses between $250 - 720$ GeV are excluded for small neutralino masses of a few GeV.

A comparison of these results with those from the analogous search published by ATLAS [7] is performed. The latter uses standard resolved techniques for top reconstruction. The usage of the HEPTopTagger extends the exclusion limits for signal models with large top squark masses and small neutralino masses. Thus, the HEPTopTagger improves the sensitivity in the search for heavy top squarks.

Since proton-proton collisions at higher centre of mass energy ($\sqrt{s} = 13$ TeV so far) and higher luminosities than in 2012 have been provided by the LHC since 2015, new regions in the parameter space of the top squark-neutralino masses are tested. As models with top squark masses close to the TeV scale are explored, a search strategy with top tagging techniques for high p_{T} top reconstruction is needed. In this thesis, the HEPTopTagger has been proven to be a well suited technique for this purpose. Thus, the combination of the two search strategies, one with events selected by the HEPTopTagger algorithm, and the other with top quarks reconstructed with resolved techniques, as described in [7], promises to be the best approach to reach high sensitivity in yet unexplored regions in the fully hadronic channel.

Appendix A

Fast Tracker

More than 25 fb^{-1} of proton-proton collision data have been recorded by the ATLAS detector from 2010 to 2012. During these three years, not only the energy increased from $\sqrt{s} = 7\,\text{TeV}$ to $\sqrt{s} = 8\,\text{TeV}$ but also the instantaneous luminosity by many orders of magnitude. The increasing number of colliding bunches and number of protons in each bunch brought the average number of distinct proton-proton interactions per bunch crossing up to 20-30 during 2012.

The event rate peak registered in 2012 was approximately 20 MHz. The ATLAS trigger system has been designed to select only a few hundred of possibly interesting events per second over the dominant soft interaction processes.

The LHC machine and experiments were upgraded during the Long Shutdown 1, in order to get closer to the design parameters. In 2015 the LHC Run 2 started and protons have been collided at a center of mass energy of $\sqrt{s} = 13\,\text{TeV}$. The design instantaneous luminosity peak of Run 2 has been raised up to $\mathcal{L} \sim 2 \times 10^{34}\,\text{cm}^{-2}\text{s}^{-1}$.

The Run 2 trigger system had to adjust not only to the new machine conditions but also to the evolved physics program. In fact, after the discovery of the Higgs boson and its observation in its bosonic decay modes, the main interest has moved towards the Higgs coupling to fermions. The most favourite channels are those involving the Higgs boson decaying into a τ pair or a b-quark pair.

In a similar way, beyond the Standard Model searches are characterised by the presence in the event of τ leptons, b-jets, top quarks or missing transverse momentum.

The selection of these events at the first stages of the trigger level is very challenging, due to the overwhelming multijet background. The tracking information, because of its fine resolution and granularity, plays a crucial role in disentangling interesting physics events from multijet ones. However, the processing time per event made it impossible in Run 1 to have the global track information at the early stages of the trigger. In Run 2 the installation of the Fast TracKer (FTK), hardware system with massively parallel processing, can permit the global reconstruction of tracks immediately after the first trigger level.

After the trigger system overview and comparison between Run 1 and Run 2

(section A.1), the illustration of the FTK and its performance are presented in section A.2 and A.2.1, respectively. The usage of the FTK track information in the missing transverse energy trigger is described in section A.2.2.

A.1 Trigger system

During Run 1, three distinct sequential trigger levels were used to reduce the rate of events to read out and store: the level 1 (L1), level 2 (L2) trigger and the event filter (EF), see section 2.4. The ATLAS Trigger and Data Acquisition System underwent limited changes accordingly to the new Run 2 conditions.

The maximum accepted rate of the L1 has increased from 75 kHz to 100 kHz. The High Level Trigger has a new architecture in which L2 and EF have been merged and run on the same processing unit with the reduction of the CPU and network usage. In addition, the trigger algorithms have been re-optimised on a processing time basis. The data bandwidth for the Readout System has been raised from 400 Hz to 1 kHz. A comparison between the Run 1 and the Run 2 trigger systems is illustrated in figure A.1.

High tracking performance can be very helpful in object reconstruction. The gain in event selection and trigger rate control is more efficient, the earlier the track information is available in the trigger sequence. In Run 1 the track reconstruction at the trigger level was performed twice: a first time at the L2 in a Region of Interest (RoI) based mode and a second time at the EF level with a software shared with the offline reconstruction. At the HLT of Run 2, a fast tracking stage using the Fast Track Finder seeds a subsequent precision tracking, with a reduction by a factor of three of the processing time with respect to Run 1. In addition to the improvement in the software tracking strategy, the installation of a new hardware track finder, the Fast TracKer (FTK) [156], will highly reduce the timing required for track reconstruction and will allow track related information, like primary vertex position, to be available at the earliest stages of the HLT just after the L1. This feature is crucial for selecting events with b-quark jets and taus.

At regime, the FTK will provide tracking information over the full detector coverage for the events accepted by the L1 with a latency of around 100 μs.

A.2 Fast Tracker

The Fast Tracker aims to provide the global track information at the early stages of the HLT trigger. During Run 2, this information is extracted using data from the ATLAS Inner Detector, composed of the pixel, the semiconductor tracker (SCT) and the Insertable B-Layer (IBL) pixel detector [157].

To perform global and fast track reconstruction and to deal with the large event rate selected by the L1, the FTK hardware system has been designed to be massively parallel. It consists of a combination of FPGA-based hardware and custom ASICs.

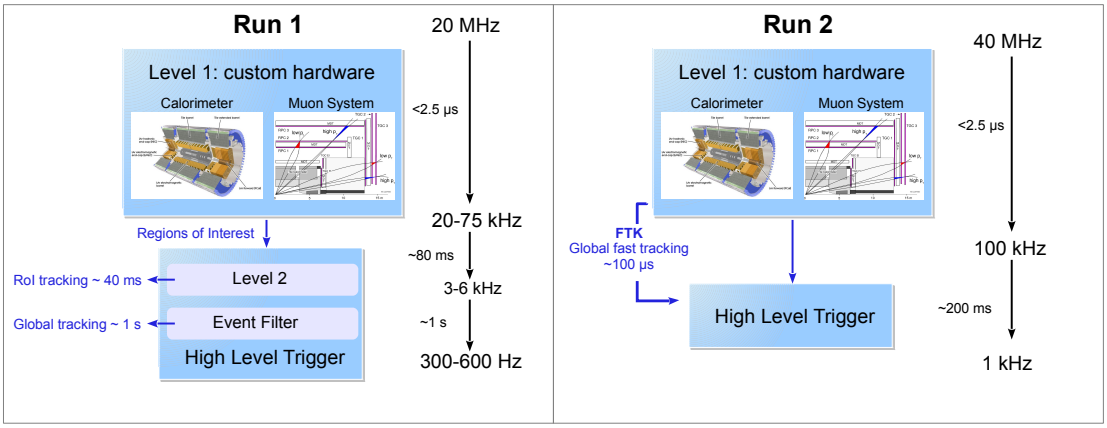

Figure A.1: Illustrative comparison of Run 1 and Run 2 trigger systems

FTK performs track reconstruction in two stages. In the first one, low precision tracks are found through pattern recognition, which uses only 8 Inner Detector layers. In the second step a linearised track fit is performed which makes use of the full hit resolution. Good tracks are extrapolated and the remaining 4 layers are added to the refined fit which gives the final track parameters.

The FTK system is composed of different boards and cards that perform different steps of the track reconstruction, illustrated in figure A.2. The data from the Inner Detector is duplicated by the *dual output HOLA* and sent to the FTK. The *Input Mezzanine* finds the clusters from the hits of the SCTs and pixels; the data are organised into 64 $\eta - \phi$ regions by the *Data Formatter* and sent to 64 pairs of Processing Units, each pair corresponding to one $\eta - \phi$ region. The segmentation in multiple geometrical regions, which overlap in the ϕ direction, characterises the highly parallel structure of the FTK. Each Processing Unit is composed of the *Auxiliary (AUX) Card*, which contains the *Data Organizer*, the *Track Fitter* and the *Hit Worrior*, and by the *Associative Memory* (AM) boards. The conversion of the cluster centroids to coarse resolution superstrips is performed by the Processing Unit. These silicon detector wide strips are the input to the Associative Memory boards, which are custom associative memory chips designated to perform pattern recognition.

As can be seen from Figure A.3, coarse resolution tracks are found using only 8 silicon detector layers by comparing the superstrip collection with patterns, defined as a set of eight superstrips consistent with charged particle trajectory. One billion patterns are obtained from single-muon simulation and they are stored in the Associative Memory chips. Afterwards compatibility of the clusters in the superstrips with the found pattern is verified.

The track helical fit is replaced by a simple linear fit in the local hit position in each silicon layer.

The Track Fitter performs a linearised track fit in the local cluster position

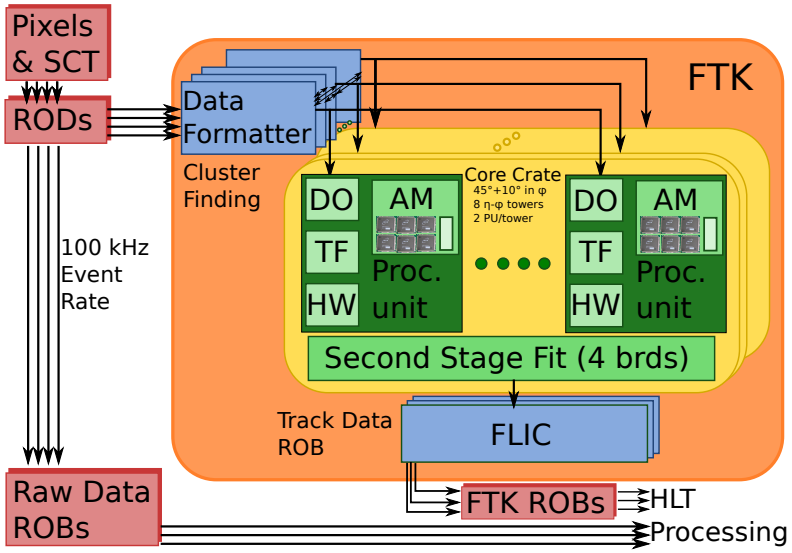

Figure A.2: Sketch of FTK. AM is the Associative Memory, DO is the Data Organizer, FLIC is the FTK-to-Level-2 Interface Crate, HW is the Hit Warrior, ROB is the ATLAS Read Out input Bu er, ROD is a silicon detector Read Out Driver, and TF is the Track Fitter. Second Stage Fit stands for the Second Stage Board. Figure from [156].

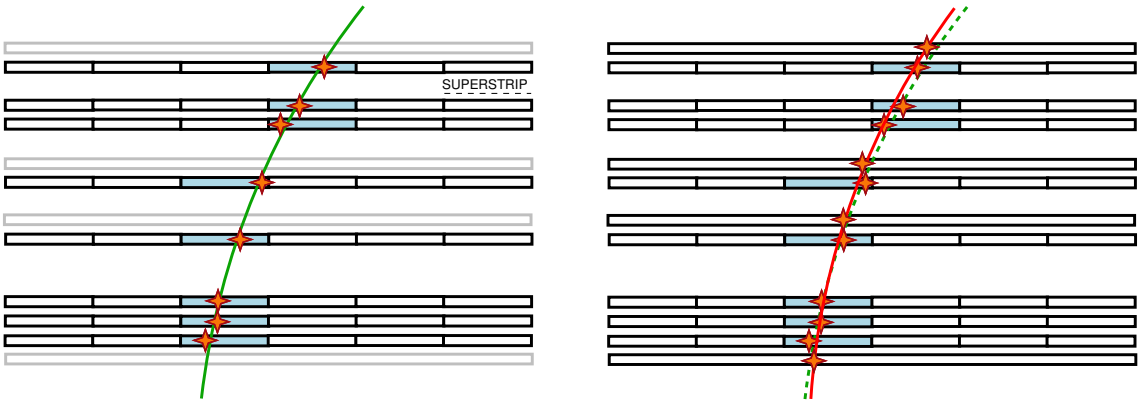

Figure A.3: Simplified sketch of the track reconstruction process. On the left, a coarse resolution track, defined by the collection of the light blue superstrips, is found in the pattern recognition stage using 8 silicon detector layers only. A linearised fit is performed using the cluster position in the previous selected superstrips. The resulting track candidate is shown in green. On the right plot, a second fit is performed using the 12 layer information and a refined track candidate, red line, is found.

belonging to those superstrips of the coarse resolution track in each silicon layer. Helix parameters and χ^2 are estimated from linear calculations, defined by a set of scalar products of the cluster centroid coordinates and precalculated constants taking into account the detector geometry and alignment.

Those full resolution tracks, which has $\chi^2 < 6$, are sent to the *Second Stage Board*. The track candidates from the previous stages are extrapolated to the 4 remaining silicon layers and a second fit is performed. Good tracks with $\chi^2 < 4$ and $p_{\mathrm{T}} > 1$ GeV undergo duplicate removal. Two tracks are both kept if they don't share more than 6 cluster centroids.

The cluster coordinates, 5 helix parameters and the χ^2 of the good tracks are sent to the HLT. The FTK tracks can be used as seed in the HLT tracking, or can be refitted in particular RoIs.

At $3 \times 10^{34} cm^{-2} s^{-1}$ instantaneous luminosity with 25 ns bunch spacing around 300 tracks per event can be found by FTK.

A software emulation is used to estimate the FTK track reconstruction performance [156]. Since FTK is a massively parallel hardware system, it is not possible to perform a bit-by-bit simulation. The hardware behaviour is reproduced with a functional emulation of each stage of the FTK processing, and the result is converted into trigger or general data formats. The software and the simulation configuration are in continuous development. The setup used for the study presented in this appendix is described in [156].

A.2.1 Fast Tracker performance

The main part of my service task is related to the integration of part of the FTK emulation into the software validation framework of the inner detector trigger. This trigger validation framework produces performance plots to verify that changes in the software do not affect the performances of the trigger. The framework is used to validate that developments in part of the FTK emulation code do not affect dramatically the FTK performance.

As an example of the output after the FTK integration into the trigger validation framework, the efficiency and resolution of the FTK track reconstruction is obtained in a single muon sample. This sample is simulated without pileup and with a flat distribution in the particle helix parameters: η, ϕ, $|d_0| < 1.5$ mm, $|z_0| < 120$ mm and curvature. The ATLAS detector geometry includes the IBL. The track reconstruction efficiency is defined as the fraction of generated muons with $p_{\mathrm{T}} > 1$ GeV matched to a reconstructed track. The matching criterion is defined in terms of the angular separation between the track and the generated muon, which has to be smaller than 0.05 ($\Delta R < 0.05$). In figure A.4, the track-finding efficiency for the FTK tracks is compared to the one for the HLT muon track, labelled as muon trigger object, as a function of the muon pseudorapidity and of the muon transverse momentum. The FTK efficiency increases with the muon transverse momentum, ranging from about

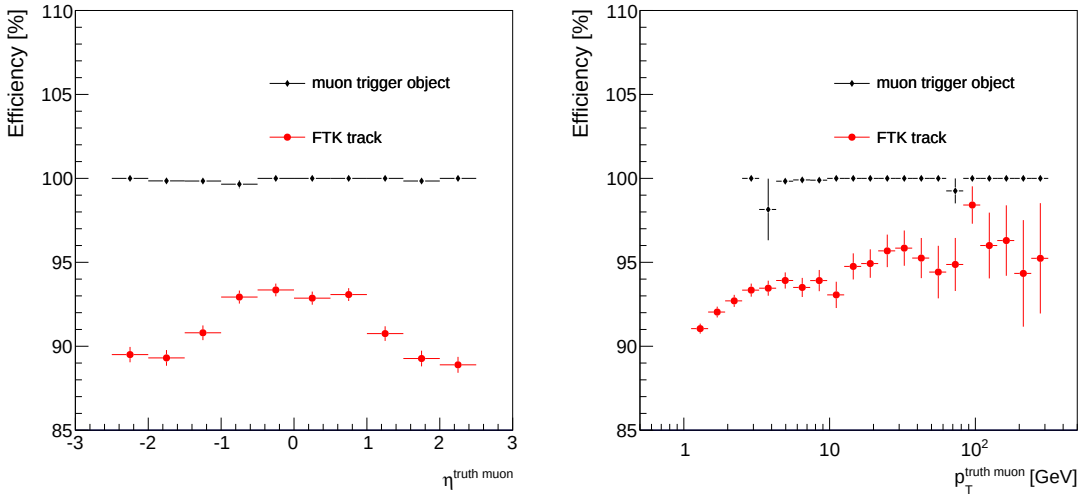

(a) (b)

Figure A.4: Track-finding efficiency for the FTK and the HLT in a single muon sample with no pileup as a function of the muon pseudorapidity (a) and the muon transverse momentum (b).

90% for low p_{T} muons, up to 95% for high p_{T} muons, and is higher in the central pseudorapidity region ($|\eta| < 1.0$).

The track reconstruction performance is also evaluated in terms of the resolution of track kinematic variables. The resolution is defined as the root mean square of the difference between the reconstructed and generated variable in a range containing 95% of the events. In figure A.5, the resolution of ϕ, of η, of the impact parameter, d_0, and of the curvature, q/p_{T}, as a function of the curvature is compared for the HLT reconstructed muons, for the FTK tracks and for FTK tracks refitted using the HLT tracking software. The resolution of the refitted FTK tracks is very close to the HLT one. The ϕ, d_0 and $1/p_{\mathrm{T}}$ resolution of the original FTK track reconstruction is similar to the refitted one for large absolute values of curvature. The resolution of these transverse quantities is dominated by multiple scattering in the low p_{T} regime. At low curvature, the FTK track resolution is worse than the HLT one due to the worse FTK hit resolution and worse fit precision.

A.2.2 $E_{\mathrm{T}}^{\mathrm{miss}}$ trigger with the Fast Tracker

The global track information at the very early stages of the HLT is very important to discriminate at the trigger level not only events containing b-jets and τ-leptons, but also events with missing transverse energy, $E_{\mathrm{T}}^{\mathrm{miss}}$.

As described in section 2.5.6, the missing transverse energy is the opposite of the vectorial sum of the transverse momentum of reconstructed objects, which could be physics objects, like jets, photons or charged leptons, contributing to the so called *hard term* but also generic tracks or calorimeter clusters, contributing to the soft term. In Run 2 at the offline level, the missing transverse energy is calculated using

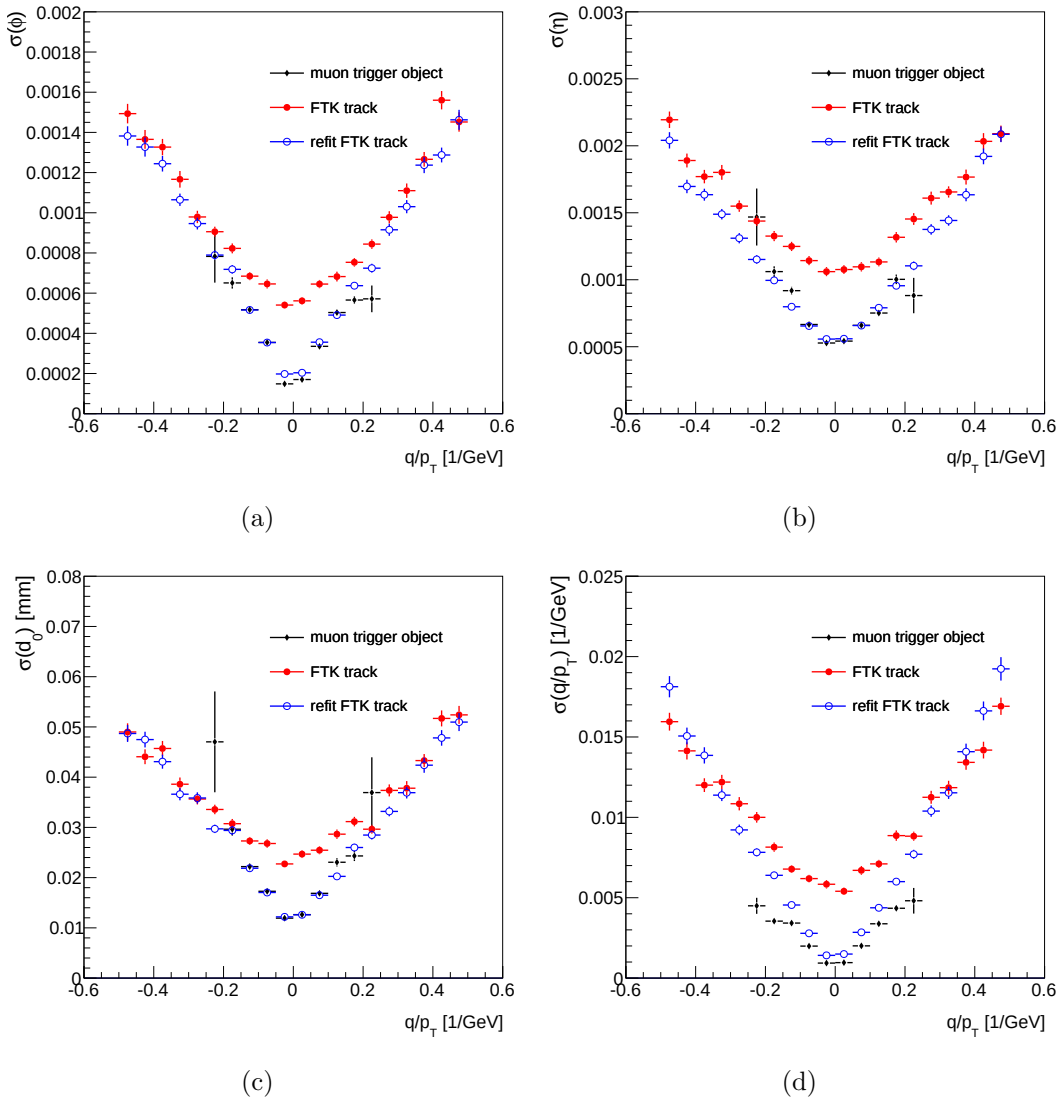

Figure A.5: Resolution of ϕ (a), η (b), d_0 (c) and curvature (d) as a function of the curvature for the HLT muon trigger objects, the FTK tracks, and the refitted FTK tracks.

the reconstructed physics objects as in Run 1, but with tracks instead of low-p_{T} calorimeter energy deposits for the soft term contribution. To avoid double counting, the tracks matched to the high-p_{T} physics objects are not included in the soft term. The usage of tracks associated to the primary vertex to evaluate the soft term leads to a reduction from the pileup contribution.

The signal acceptance of physics analyses heavily depends on the trigger efficiency. The wider the overlap between the trigger selection and the offline selection, the larger the signal acceptance is with respect to a constant rate of triggered background events.

In Run 1, the L2 $E_{\mathrm{T}}^{\mathrm{miss}}$ was calculated from the transverse momentum of calorimeter cells. In Run 2, the reconstructed objects at the HLT used for the $E_{\mathrm{T}}^{\mathrm{miss}}$ calcula-

tion are either topological clusters calibrated at the hadronic scale (LCW) or jets.

As the FTK provide a global track information at the beginning of the HLT, missing transverse energy triggers can be defined in every similar way to the offline $E_{\mathrm{T}}^{\mathrm{miss}}$ calculation, reducing the impact of pileup effects by only using tracks associated to the primary vertex. Two approaches are proposed to improve the missing transverse energy trigger at the HLT. The first approach, referred to as FTK+JET $E_{\mathrm{T}}^{\mathrm{miss}}$, consists in the direct usage of tracks not associated to jets for the soft term calculation and the jets for the hard term. The second more sophisticated approach, referred to as FTK PFlow $E_{\mathrm{T}}^{\mathrm{miss}}$, exploits the high resolution of a new collection of jets for the jet term calculation: the particle flow jets; the soft term is calculated with FTK tracks not associated to particle flow jets. The performance of the trigger defined with this approach has been studied in the second part of my service task in comparison to the Run 2 missing transverse energy triggers and FTK+JET $E_{\mathrm{T}}^{\mathrm{miss}}$ trigger.

After a brief explanation of the Particle Flow algorithm, the performance of jets reconstructed from different types of constituents, particle flow objects or calorimeter clusters, is compared. Afterwards, the performance of $E_{\mathrm{T}}^{\mathrm{miss}}$ reconstruction with different jet collections and the consequent improvements in the trigger definition are presented.

Particle flow algorithm

The particle flow (PFlow) algorithm [158] has been implemented in order to combine track and calorimeter measurements to achieve the best performance of the energy momentum measurement and the reduction of pileup effects.

Neutral and charged particles are detected as energy deposits in the calorimeter. Before reaching the calorimeter, charged particle passing through the inner detector are reconstructed as tracks. In order to avoid double-counting the energy of charged particles, its signal in the calorimeter has to be identified and removed. For low energy charged particles, the track momentum resolution is better than the calorimeter energy resolution; hence the track measurement is kept and the calorimeter measurement is removed.

Good quality tracks, with $p_{\mathrm{T}} < 40$ GeV, are extrapolated by the PFlow algorithm to the second layer of the EM calorimeter. The charged shower associated to the track is subtracted at the calorimeter cell level. The remaining cells are combined again by the topological cluster algorithm (see section 2.5.4). For these studies, the resulting topological clusters are used at the electromagnetic (EM) scale (the local hadronic calibration is not applied). The result is a collection of particle flow objects: the charged ones, corresponding to tracks; the neutral ones, corresponding to the remaining topological clusters. Each PFlow object ideally represents an individual particle.

By considering in an event only those charged PFlow objects associated to the primary vertex, the calorimeter energy deposits coming from in-time pileup interac-

tions are substantially reduced in the jet and $E_{\mathrm{T}}^{\mathrm{miss}}$reconstruction.

Particle flow jet performance

FTK and offline tracks are used as input to the Pflow algorithm, for the HLT and offline reconstruction of PFlow objects called FTK PFlow objects and offline PFlow objects, respectively. At the HLT and offline together with PFlow objects, topological clusters are available.

Different jet collections are reconstructed from these kinds of constituents. In this study, four jet collections are considered:

- **standard jets at the LC scale**: anti-k_{T} R=0.4 jets built from topological clusters with local hadron calibration;
- **standard jets at the EM scale**: anti-k_{T} R=0.4 jets built from clusters at the electromagnetic scale;
- **offline PFlow jets**: anti-k_{T} R=0.4 jets built from PFlow objects exploiting the full offline reconstructed track information, and the remaining clusters at the EM scale;
- **FTK PFlow jets**: anti-k_{T} R=0.4 jets built from PFlow objects exploiting the FTK reconstructed track information, and the remaining clusters at the EM scale.

Jets are calibrated with different calibration constants, derived for each jet collection in simulated multijet events. The performance of the jet collections is compared in terms of the jet p_{T} resolution. The resolution is the width of a Gaussian fit of the transverse momentum ratio of the reconstructed jet and of the geometrically matched truth jet.

The resolutions of the four jet collections as a function of the truth jet p_{T} are shown in figure A.6 for jets reconstructed over the full detector area (figure A.6(a)), and for jets reconstructed within $|\eta| < 1.1$ (figure A.6(b)). Offline PFlow jets give the best resolution, and FTK PFlow jets give a better resolution than Standard jets for $p_{\mathrm{T}} \lesssim 100$ GeV. The resolution improvements in momentum reconstruction with PFlow jets is enhanced in the central detector region.

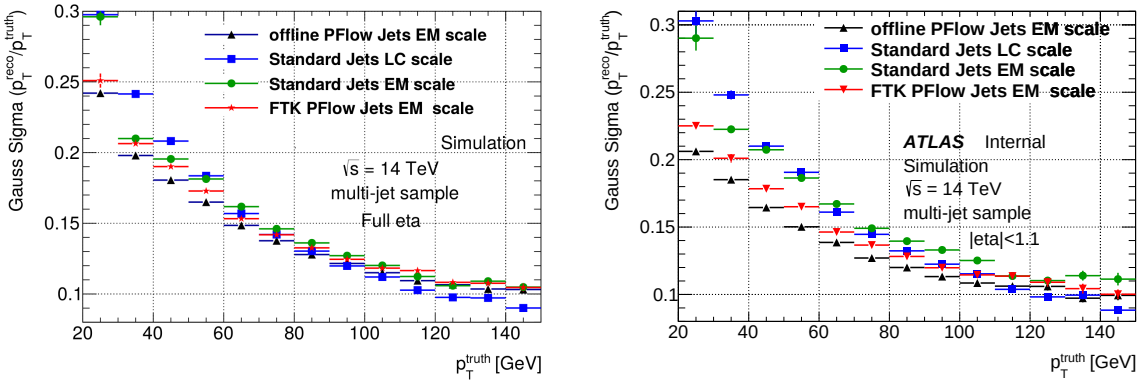

(a) (b)

Figure A.6: Jet energy resolution as a function of the transverse momentum of the truth jet for the four jet collections over the full detector region (a) and the $|\eta^{\text{jet}}| < 1.1$ region (b): standard jets at the LC scale (blue), standard jets at the EM scale (green), FTK PFlow jets (red), and Offline PFlow jets (black). The multi-jet sample is used for this study.

$E_{\text{T}}^{\text{miss}}$ performance

The four jet collections described above can be used in the jet term calculation of the missing transverse energy. In this section, several types of missing transverse energy algorithms are compared.

At the offline level two methods are available depending on the jet collections used for the jet term. If standard calorimeter jets are used, the *Offline Hybrid* $E_{\text{T}}^{\text{miss}}$ is reconstructed. If PFlow jets are employed, the Offline PFlow $E_{\text{T}}^{\text{miss}}$ is obtained.

At the HLT, the $E_{\text{T}}^{\text{miss}}$ algorithm does not take into account the contribution of the soft term, and uses standard jets for the hard term.

With the FTK global track information, two additional $E_{\text{T}}^{\text{miss}}$ definitions can be considered at the HLT: one using standard jets in the jet term and FTK tracks in the soft term, Jet+FTK $E_{\text{T}}^{\text{miss}}$; and one using PFlow jets for the jet term calculation and charged PFlow objects, corresponding to FTK tracks, in the soft term. The tracks used for the soft term calculation are not geometrically associated to jets with $p_{\text{T}} > 20$ GeV. The definitions are summarised in Table A.1.

The performance is studied for the different $E_{\text{T}}^{\text{miss}}$ reconstructions by looking at the difference between the reconstructed and generated x component of the missing transverse momentum in a signal process with $E_{\text{T}}^{\text{miss}}$ due to undetected particles and in a background process with fake $E_{\text{T}}^{\text{miss}}$, due to jet mismeasurement. The signal and background samples are ZH $\rightarrow \nu\nu$bb and multi-jet processes, respectively, with 60 average number of interactions per bunch crossing.

The difference between the reconstructed $E_{\text{x}}^{\text{miss}}$ and the truth $E_{\text{x}}^{\text{miss}}$ in the signal and background samples is shown in Figure A.7. Particle Flow $E_{\text{T}}^{\text{miss}}$ algorithms perform better than the standard $E_{\text{T}}^{\text{miss}}$ algorithms.

In Figure A.8, the correlations among different $E_{\text{T}}^{\text{miss}}$ definitions is compared.

	Jet hard term	Soft term
Offline Hybrid $E_{\mathrm{T}}^{\mathrm{miss}}$	standard jets	offline tracks
Offline PFlow $E_{\mathrm{T}}^{\mathrm{miss}}$	Offline PFlow jets	charged PFlow obj. (offline tracks)
FTK PFlow $E_{\mathrm{T}}^{\mathrm{miss}}$	FTK PFlow jets	charged PFlow obj. (FTK tracks)
Jet+FTK $E_{\mathrm{T}}^{\mathrm{miss}}$	standard jets	FTK tracks
Jet $E_{\mathrm{T}}^{\mathrm{miss}}$	standard jets	-

Table A.1: Definition of $E_{\mathrm{T}}^{\mathrm{miss}}$ reconstruction according to jet term and objects used as input to the $E_{\mathrm{T}}^{\mathrm{miss}}$ algorithm.

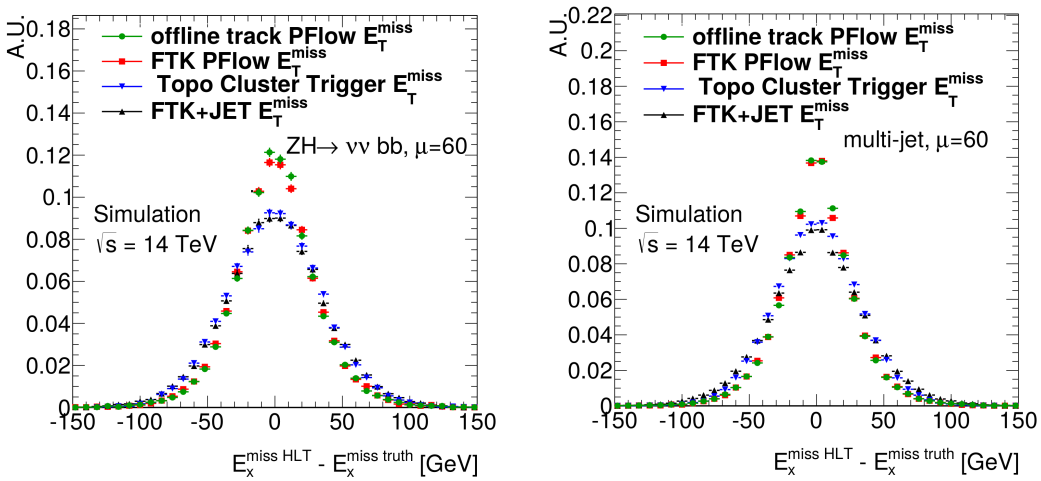

(a) (b)

Figure A.7: Differences between the reconstructed and the truth $E_{\mathrm{x}}^{\mathrm{miss}}$ for various algorithms. The ZH signal (a) and multi-jet background (b) samples are used for this study.

The JET+FTK $E_{\mathrm{T}}^{\mathrm{miss}}$ is highly correlated to the offline Hybrid $E_{\mathrm{T}}^{\mathrm{miss}}$ (figure A.8(a)). This correlation is stronger than the correlation between the FTK PFlow $E_{\mathrm{T}}^{\mathrm{miss}}$ and its offline PFlow $E_{\mathrm{T}}^{\mathrm{miss}}$ counterpart (figure A.8(e)). This difference can be attributed to the fact that the first pair uses the same jet collection for the jet hard term, while the second pair uses similar but not exactly the same PFlow jet collection.

To compare the trigger efficiency, the threshold for each $E_{\mathrm{T}}^{\mathrm{miss}}$ trigger has to be defined. The Run 2 $E_{\mathrm{T}}^{\mathrm{miss}}$ HLT with 80 GeV threshold, based on the vectorial sum of topological clusters, is used as a reference. The threshold value for each other $E_{\mathrm{T}}^{\mathrm{miss}}$ HLT definition is set such that the $E_{\mathrm{T}}^{\mathrm{miss}}$ HLT selects the same rate of background events passing the L1 $E_{\mathrm{T}}^{\mathrm{miss}}$ trigger with 50 GeV threshold, as the topocluster $E_{\mathrm{T}}^{\mathrm{miss}}$ trigger with 80 GeV threshold. For $E_{\mathrm{T}}^{\mathrm{miss}}$ triggers, the background rate is dominated by multijet events. The threshold values are summarised in Table A.2.

The performance of the $E_{\mathrm{T}}^{\mathrm{miss}}$ HLT triggers are compared in terms of efficiency curves. The $E_{\mathrm{T}}^{\mathrm{miss}}$ HLT efficiency is defined as the fraction of events selected by the

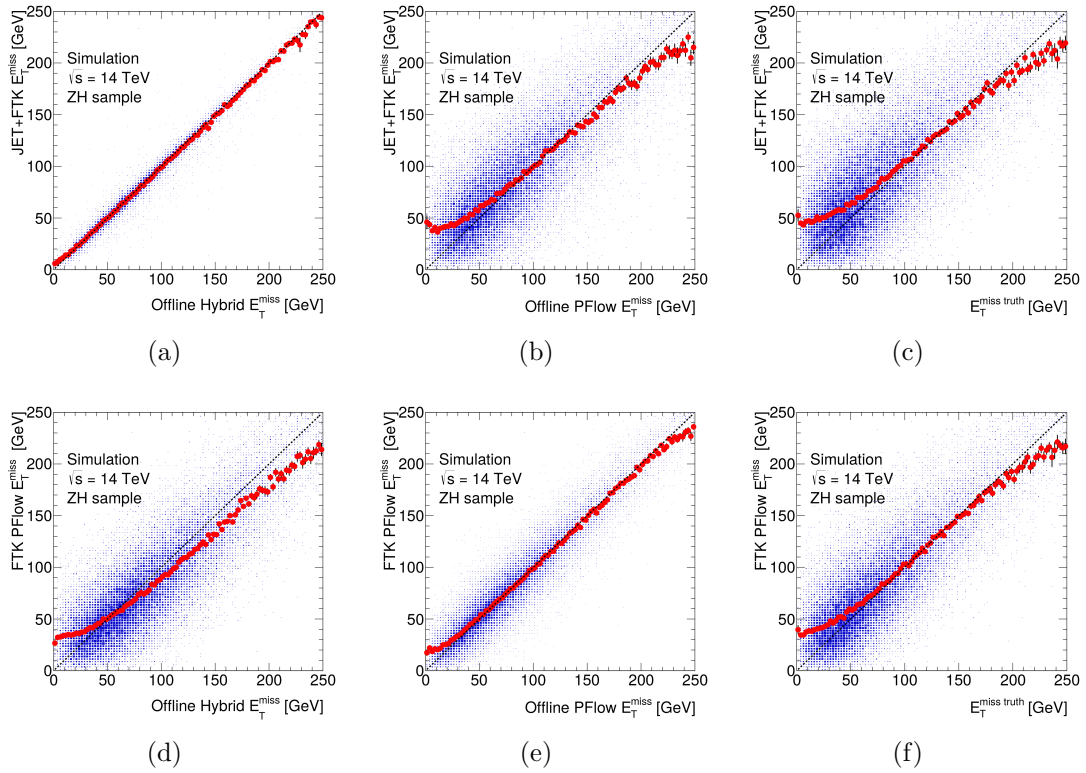

Figure A.8: Correlations among different $E_{\mathrm{T}}^{\mathrm{miss}}$ definitions: between the trigger JET+FTK $E_{\mathrm{T}}^{\mathrm{miss}}$ and Hybrid $E_{\mathrm{T}}^{\mathrm{miss}}$ (a), offline PFlow $E_{\mathrm{T}}^{\mathrm{miss}}$ (b), truth $E_{\mathrm{T}}^{\mathrm{miss}}$; (f) between the trigger FTK PFlow $E_{\mathrm{T}}^{\mathrm{miss}}$ and Hybrid $E_{\mathrm{T}}^{\mathrm{miss}}$ (d), offline PFlow $E_{\mathrm{T}}^{\mathrm{miss}}$ (e), truth $E_{\mathrm{T}}^{\mathrm{miss}}$ (c). The ZH signal sample is used for this study.

	threshold (GeV)
Topo Cluster $E_{\mathrm{T}}^{\mathrm{miss}}$ (current reference)	80.0
Jet+FTK based $E_{\mathrm{T}}^{\mathrm{miss}}$	106.0
Jet based $E_{\mathrm{T}}^{\mathrm{miss}}$	107.0
FTK PFlow $E_{\mathrm{T}}^{\mathrm{miss}}$	96.0

Table A.2: Threshold values for various $E_{\mathrm{T}}^{\mathrm{miss}}$ definitions which give the same background rate.

L1 $E_{\mathrm{T}}^{\mathrm{miss}}$ trigger which pass the HLT with the threshold values reported in table A.2. The efficiencies for the $ZH \to \nu\bar{\nu}b\bar{b}$ sample for the three different $E_{\mathrm{T}}^{\mathrm{miss}}$ definitions and the Run 2 topo cluster $E_{\mathrm{T}}^{\mathrm{miss}}$ HLT are shown in Figure A.9 as a function of (a) the truth $E_{\mathrm{T}}^{\mathrm{miss}}$, (b) the offline Hybrid $E_{\mathrm{T}}^{\mathrm{miss}}$, and (c) the offline PFlow $E_{\mathrm{T}}^{\mathrm{miss}}$. With the respect to the true $E_{\mathrm{T}}^{\mathrm{miss}}$, the FTK PFlow $E_{\mathrm{T}}^{\mathrm{miss}}$ has a steeper efficiency curve than the other two definitions, and reaches the plateau sooner than the other HLTs. The JET+FTK $E_{\mathrm{T}}^{\mathrm{miss}}$ performs best with respect to the offline hybrid $E_{\mathrm{T}}^{\mathrm{miss}}$ (figure A.9(b)) and the FTK PFlow performs best with respect to the offline PFlow (figure A.9(c)).

These results show that the FTK track reconstruction is very useful for $E_{\mathrm{T}}^{\mathrm{miss}}$ high level triggers, as it provides the possibility to define a $E_{\mathrm{T}}^{\mathrm{miss}}$ HLT algorithm

highly correlated to the offline $E_{\mathrm{T}}^{\mathrm{miss}}$ reconstruction.

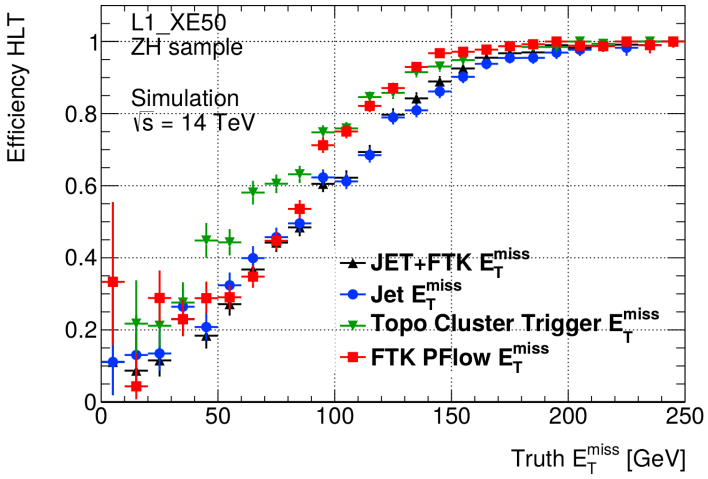

(a)

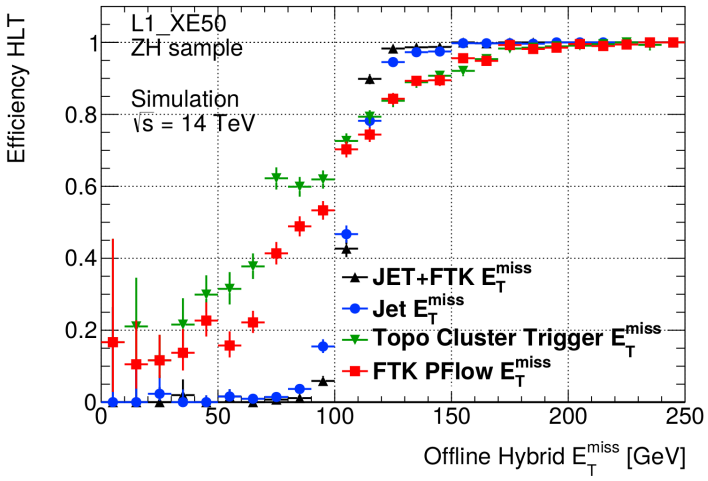

(b)

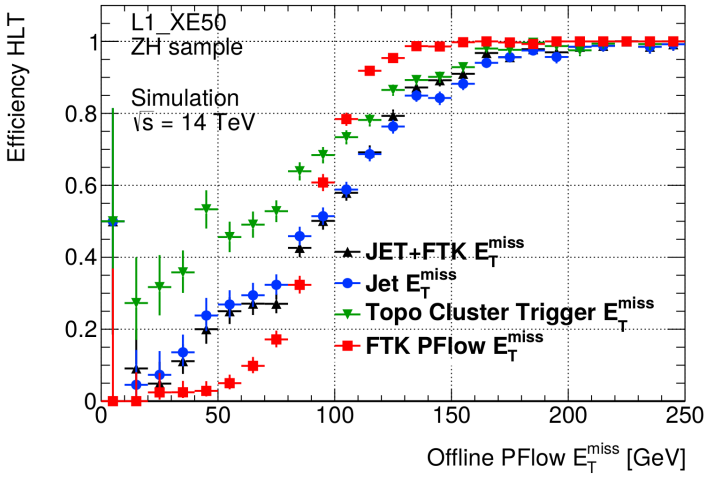

(c)

Figure A.9: Efficiency curve of four HLT $E_{\mathrm{T}}^{\mathrm{miss}}$ definitions with respect to the truth $E_{\mathrm{T}}^{\mathrm{miss}}$ (a) and the offline $E_{\mathrm{T}}^{\mathrm{miss}}$ (b) and (c) for the $ZH \rightarrow \nu\bar{\nu}b\bar{b}$ signal sample.

Appendix B

Systematic uncertainties breakdown

The breakdown of the dominant systematic uncertainties on the number of predicted events are reported in table B.1, B.2 and B.3 for SR1, SR2 and SR3, respectively.

It has to be noticed that the individual uncertainties can be correlated, and do not necessarily add up quadratically to the total background uncertainty.

Uncertainty of channel	SR1
Total background expectation	1.51
Total statistical ($\sqrt{N_{\text{exp}}}$)	$\pm$1.23
Total background systematic	$\pm$0.35 [22.94%]
MC statistics	$\pm$0.30 [19.9%]
subjet energy scale	$\pm$0.14 [9.3%]
$t\bar{t}$ PDF	$\pm$0.13 [8.6%]
$t\bar{t}$ ISR/FSR	$\pm$0.09 [6.0%]
$t\bar{t}$ normalization	$\pm$0.08 [5.3%]
small-R jet JES	$\pm$0.07 [4.6%]
$t\bar{t}V$ theory σ	$\pm$0.06 [4.0%]
$t\bar{t}$ generator	$\pm$0.05 [3.3%]
$t\bar{t}$ theory σ	$\pm$0.05 [3.3%]
V+jets normalization	$\pm$0.04 [2.6%]
Z+jets theory model.	$\pm$0.03 [2.0%]
$t\bar{t}$ renormalization scale	$\pm$0.02 [1.3%]
diboson theory σ	$\pm$0.01 [0.7%]
W+jets theory model.	$\pm$0.01 [0.7%]
subjet energy resolution	$\pm$0.01 [0.7%]

Table B.1: Breakdown of the dominant systematic uncertainties on background estimates in SR1. Note that the individual uncertainties can be correlated, and do not necessarily add up quadratically to the total background uncertainty. The percentages show the size of the uncertainty relative to the total expected background.

Uncertainty of channel	SR2
Total background expectation	24.36
Total statistical ($\sqrt{N_{\text{exp}}}$)	±4.94
Total background systematic	±2.76 [11.31%]
$t\bar{t}$ parton shower	±2.42 [9.9%]
V+jets normalization	±1.49 [6.1%]
small-R jet JES	±1.42 [5.8%]
Z+jets theory model.	±1.04 [4.3%]
$t\bar{t}$ generator	±0.97 [4.0%]
$t\bar{t}$ normalization	±0.92 [3.8%]
$t\bar{t}$ PDF	±0.81 [3.3%]
large-R jet JES	±0.79 [3.2%]
$t\bar{t}$ ISR/FSR	±0.77 [3.2%]
W+jets theory model.	±0.60 [2.5%]
$t\bar{t}$ theory σ	±0.57 [2.3%]
$t\bar{t}$ renormalization scale	±0.56 [2.3%]
subjet energy scale	±0.51 [2.1%]
$t\bar{t}V$ theory σ	±0.41 [1.7%]
b-tagging efficiency	±0.40 [1.6%]
l-jet mistag rate	±0.35 [1.4%]
single top theory σ	±0.27 [1.1%]
c-jet mistag rate	±0.24 [1.0%]
MC statistics	±0.17 [0.7%]
diboson theory σ	±0.12 [0.5%]
subjet energy resolution	±0.02 [0.1%]

Table B.2: As for table B.1, breakdown of the dominant systematic uncertainties on background estimates in SR2.

Uncertainty of channel	SR3
Total background expectation	30.54
Total statistical ($\sqrt{N_{\text{exp}}}$)	±5.53
Total background systematic	±4.10 [13.42%]
small-R jet JES	±3.01 [9.9%]
V+jets normalization	±1.96 [6.4%]
Z+jets theory model.	±1.53 [5.0%]
$t\bar{t}$ normalization	±1.42 [4.6%]
$t\bar{t}$ parton shower	±1.40 [4.6%]
$t\bar{t}$ ISR/FSR	±1.17 [3.8%]
$t\bar{t}$ theory σ	±0.87 [2.8%]
$t\bar{t}$ renormalization scale	±0.85 [2.8%]
$t\bar{t}$ PDF	±0.81 [2.7%]
b-tagging efficiency	±0.81 [2.7%]
W+jets theory model.	±0.64 [2.1%]
l-jet mistag rate	±0.51 [1.7%]
subjet energy scale	±0.34 [1.1%]
c-jet mistag rate	±0.32 [1.0%]
subjet energy resolution	±0.31 [1.0%]
MC statistics	±0.28 [0.9%]
$t\bar{t}V$ theory σ	±0.23 [0.8%]
$t\bar{t}$ generator	±0.22 [0.7%]
single top theory σ	±0.21 [0.7%]
large-R jet JES	±0.08 [0.3%]
diboson theory σ	±0.02 [0.1%]

Table B.3: As for table B.1, breakdown of the dominant systematic uncertainties on background estimates in SR3.

Bibliography

[1] ATLAS Collaboration, *Observation of a new particle in the search for the Standard Model Higgs boson with the ATLAS detector at the LHC*, Phys. Lett. **B716** (2012) 1–29, arXiv:1207.7214 [hep-ex].

[2] CMS Collaboration, *Observation of a new boson at a mass of 125 GeV with the CMS experiment at the LHC*, Phys. Lett. **B716** (2012) 30–61, arXiv:1207.7235 [hep-ex].

[3] T. Plehn, G. P. Salam, and M. Spannowsky, *Fat Jets for a Light Higgs Boson*, Phys. Rev. Lett. **104** (2010) 111801, arXiv:0910.5472 [hep-ph].

[4] T. Plehn, M. Spannowsky, M. Takeuchi, and D. Zerwas, *Stop reconstruction with tagged tops*, JHEP **1010** (2010) 078, arXiv:1006.2833 [hep-ph].

[5] S. Schaetzel and M. Spannowsky, *Tagging highly boosted top quarks*, Phys. Rev. **D89** no. 1, (2014) 014007, arXiv:1308.0540 [hep-ph].

[6] ATLAS Collaboration, *Identification of high transverse momentum top quarks in pp collisions at $\sqrt{s}$ = 8 TeV with the ATLAS detector*, JHEP **06** (2016) 093, arXiv:1603.03127 [hep-ex].

[7] ATLAS Collaboration, *Search for direct pair production of the top squark in all-hadronic final states in proton-proton collisions at $\sqrt{s} = 8$ TeV with the ATLAS detector*, JHEP **1409** (2014) 015, arXiv:1406.1122 [hep-ex].

[8] T. Plehn, M. Spannowsky, and M. Takeuchi, *Stop searches in 2012*, JHEP **08** (2012) 091, arXiv:1205.2696 [hep-ph].

[9] S. L. Glashow, *Partial Symmetries of Weak Interactions*, Nucl. Phys. **22** (1961) 579–588.

[10] S. Weinberg, *A Model of Leptons*, Phys. Rev. Lett. **19** (1967) 1264–1266.

[11] A. Salam, *Elementary Particle Theory*. ed. N. Svartholm (Almquist and Wiksells, Stockholm), 1969.

[12] S. L. Glashow, J. Iliopoulos, and L. Maiani, *Weak Interactions with Lepton-Hadron Symmetry*, Phys. Rev. **D2** (1970) 1285–1292.

[13] F. Englert and R. Brout, *Broken Symmetry and the Mass of Gauge Vector Mesons*, Phys. Rev. Lett. **13** (1964) 321–323.

[14] P. W. Higgs, *Broken symmetries, massless particles and gauge fields*, Phys. Lett. **12** (1964) 132–133.

[15] P. W. Higgs, *Broken Symmetries and the Masses of Gauge Bosons*, Phys. Rev. Lett. **13** (1964) 508–509.

[16] D. J. Griffiths, *Introduction to elementary particles; 2nd rev. version*. Physics textbook. Wiley, New York, NY, 2008. https://cds.cern.ch/record/111880.

[17] *The BEH-Mechanism, interactions with short range forces and scalar particles*, Nobel Media AB (2014). http://www.nobelprize.org/nobel_prizes/physics/laureates/2013/.

[18] A. Bettini, *Introduction to elementary particle physics*. Cambridge Univ. Press, Cambridge, 2008. https://cds.cern.ch/record/1111396.

[19] F. Mandl and G. G. Shaw, *Quantum field theory; 2nd ed.* Wiley, New York, NY, 2010. https://cds.cern.ch/record/1236742.

[20] M. E. Peskin and D. V. Schroeder, *An Introduction to Quantum Field Theory; 1995 ed.* Westview, Boulder, CO, 1995. https://cds.cern.ch/record/257493.

[21] K.A. Olive *et al.* (Particle Data Group), *2015 Review of Particle Physics*, Chin. Phys. C **38** (2014) 090001 and 2015 update. http://pdg.lbl.gov/2015/reviews/contents_sports.html.

[22] G. Altarelli and G. Parisi, *Asymptotic Freedom in Parton Language*, Nucl. Phys. **B126** (1977) 298–318.

[23] Y. L. Dokshitzer, *Calculation of the Structure Functions for Deep Inelastic Scattering and e^+ e^- Annihilation by Perturbation Theory in Quantum Chromodynamics.*, Sov. Phys. JETP **46** (1977) 641–653. [Zh. Eksp. Teor. Fiz.73,1216(1977)].

[24] V. N. Gribov and L. N. Lipatov, *Deep inelastic e p scattering in perturbation theory*, Sov. J. Nucl. Phys. **15** (1972) 438–450. [Yad. Fiz.15,781(1972)].

[25] GEANT4 Collaboration, S. Agostinelli et al., *GEANT4—a simulation toolkit*, Nucl. Instrum. Meth. **A506** (2003) 250–303.

[26] ATLAS Collaboration, *The ATLAS Simulation Infrastructure*, Eur. Phys. J. **C70** (2010) 823–874, arXiv:1005.4568 [physics.ins-det].

[27] CDF Collaboration, F. Abe et al., *Observation of top quark production in $\bar{p}p$ collisions*, Phys. Rev. Lett. **74** (1995) 2626–2631, arXiv:hep-ex/9503002 [hep-ex].

[28] D0 Collaboration, S. Abachi et al., *Observation of the top quark*, Phys. Rev. Lett. **74** (1995) 2632–2637, arXiv:hep-ex/9503003 [hep-ex].

[29] ATLAS Collaboration, *Measurement of the top quark mass in the $t\bar{t} \to$ dilepton channel from $\sqrt{s} = 8$ TeV ATLAS data*, Phys. Lett. **B761** (2016) 350–371, arXiv:1606.02179 [hep-ex].

[30] ATLAS, CMS Collaboration, *Combined Measurement of the Higgs Boson Mass in pp Collisions at $\sqrt{s} = 7$ and 8 TeV with the ATLAS and CMS Experiments*, Phys. Rev. Lett. **114** (2015) 191803, arXiv:1503.07589 [hep-ex].

[31] D. E. Morrissey, T. Plehn, and T. M. P. Tait, *Physics searches at the LHC*, Phys. Rept. **515** (2012) 1–113, arXiv:0912.3259 [hep-ph].

[32] S. P. Martin, *A Supersymmetry primer*, arXiv:hep-ph/9709356 [hep-ph]. [Adv. Ser. Direct. High Energy Phys.18,1(1998)].

[33] LHC New Physics Working Group Collaboration, *Simplified models for LHC new physics searches*, Journal of Physics G: Nuclear and Particle Physics **39** no. 10, (2012) 105005. http://stacks.iop.org/0954-3899/39/i=10/a=105005.

[34] W. Beenakker, R. Hopker, and M. Spira, *PROSPINO: A Program for the production of supersymmetric particles in next-to-leading order QCD*, arXiv:hep-ph/9611232 [hep-ph].

[35] M. Kramer, A. Kulesza, R. van der Leeuw, M. Mangano, S. Padhi, T. Plehn, and X. Portell, *Supersymmetry production cross sections in pp collisions at $\sqrt{s} = 7$ TeV*, arXiv:1206.2892 [hep-ph].

[36] W. Beenakker, M. Kramer, T. Plehn, M. Spira, and P. M. Zerwas, *Stop production at hadron colliders*, Nucl. Phys. **B515** (1998) 3–14, arXiv:hep-ph/9710451 [hep-ph].

[37] W. Beenakker, S. Brensing, M. Kramer, A. Kulesza, E. Laenen, and I. Niessen, *Supersymmetric top and bottom squark production at hadron colliders*, JHEP **08** (2010) 098, arXiv:1006.4771 [hep-ph].

[38] W. Beenakker, S. Brensing, M. n. Kramer, A. Kulesza, E. Laenen, L. Motyka, and I. Niessen, *Squark and Gluino Hadroproduction*, Int. J. Mod. Phys. **A26** (2011) 2637–2664, arXiv:1105.1110 [hep-ph].

[39] ATLAS Collaboration, *ATLAS Run 1 searches for direct pair production of third-generation squarks at the Large Hadron Collider*, Eur. Phys. J. **C75** no. 10, (2015) 510, arXiv:1506.08616 [hep-ex]. [Erratum: Eur. Phys. J.C76,no.3,153(2016)].

[40] L. Evans and P. Bryant, *LHC Machine*, JINST **3** (2008) S08001.

[41] TeVI Group, *Design Report Tevatron 1 project*, FERMILAB-DESIGN-1984-01.

[42] *HERA - A Proposal for a Large Electron Proton Colliding Beam Facility at DESY*, Hamburg Desy - DESY HERA 81-10 (81,REC.AUG.) 292p (1981).

[43] ATLAS Collaboration, *The ATLAS Experiment at the CERN Large Hadron Collider*, JINST **3** (2008) S08003.

[44] CMS Collaboration, *The CMS experiment at the CERN LHC*, JINST **3** (2008) S08004.

[45] LHCb Collaboration, *The LHCb Detector at the LHC*, JINST **3** (2008) S08005.

[46] ALICE Collaboration, *The ALICE experiment at the CERN LHC*, JINST **3** (2008) S08002.

[47] Schörner-Sadenius, Thomas, ed., *The Large Hadron Collider*. Springer, Berlin, 2015. http://www.springer.com/gb/book/9783319150017.

[48] *LEP design report*. CERN, Geneva, 1984. https://cds.cern.ch/record/102083.

[49] F. Marcastel, *CERN's Accelerator Complex. La chaine des accelerateurs du CERN*,. https://cds.cern.ch/record/1621583.

[50] ATLAS Collaboration, "Luminosity Public Results." https://twiki.cern.ch/twiki/bin/view/AtlasPublic/LuminosityPublicResults.

[51] ATLAS Collaboration, "ATLAS Experiment @ 2016 CERN." http://atlasexperiment.org/photos/index.html.

[52] ATLAS Collaboration, M. Kayl, *Tracking Performance of the ATLAS Inner Detector and Observation of Known Hadrons*, in *Hadron collider physics. Proceedings, 22nd Conference, HCP 2010, Toronto, Canada, August 23-27, 2010*. 2010. arXiv:1010.1091 [physics.ins-det].

[53] J. Pequenao, *Computer generated image of the ATLAS Muons subsystem*, Mar, 2008. http://cds.cern.ch/record/1095929.

[54] ATLAS Collaboration, *Performance of the ATLAS Trigger System in 2010*, Eur. Phys. J. **C72** (2012) 1849, arXiv:1110.1530 [hep-ex].

[55] ATLAS Collaboration, *Performance of the ATLAS Inner Detector Track and Vertex Reconstruction in the High Pile-Up LHC Environment*, ATLAS-CONF-2012-042. https://cds.cern.ch/record/1435196.

[56] ATLAS Collaboration, *Tracking Results and Comparison to Monte Carlo simulation at* $\sqrt{s} = 900$ *GeV*, ATLAS-CONF-2010-011. https://cds.cern.ch/record/1276323.

[57] ATLAS Collaboration, *Performance of primary vertex reconstruction in proton-proton collisions at* $\sqrt{s} = 7$ *TeV in the ATLAS experiment*, ATLAS-CONF-2010-069. http://cds.cern.ch/record/1281344.

[58] ATLAS Collaboration, *Electron efficiency measurements with the ATLAS detector using the 2012 LHC proton-proton collision data*, ATLAS-CONF-2014-032. http://cdsweb.cern.ch/record/1706245.

[59] ATLAS Collaboration, *Electron reconstruction and identification efficiency measurements with the ATLAS detector using the 2011 LHC proton-proton collision data*, Eur. Phys. J. **C74** no. 7, (2014) 2941, arXiv:1404.2240 [hep-ex].

[60] ATLAS Collaboration, *Electron performance measurements with the ATLAS detector using the 2010 LHC proton-proton collision data*, Eur. Phys. J. **C72** (2012) 1909, arXiv:1110.3174 [hep-ex].

[61] W. Lampl, S. Laplace, D. Lelas, P. Loch, H. Ma, S. Menke, S. Rajagopalan, D. Rousseau, S. Snyder, and G. Unal, *Calorimeter Clustering Algorithms: Description and Performance*, ATL-LARG-PUB-2008-002. https://cds.cern.ch/record/1099735.

[62] T. Cornelissen, M. Elsing, S. Fleischmann, W. Liebig, E. Moyse, and A. Salzburger, *Concepts, Design and Implementation of the ATLAS New Tracking (NEWT)*, ATL-SOFT-PUB-2007-007. https://cds.cern.ch/record/1020106.

[63] T. G. Cornelissen, M. Elsing, I. Gavrilenko, J.-F. Laporte, W. Liebig, M. Limper, K. Nikolopoulos, A. Poppleton, and A. Salzburger, *The global* χ^2 *track fitter in ATLAS*, Journal of Physics: Conference Series **119** no. 3, (2008) 032013. http://stacks.iop.org/1742-6596/119/i=3/a=032013.

[64] ATLAS Collaboration, *Improved electron reconstruction in ATLAS using the Gaussian Sum Filter-based model for bremsstrahlung*, ATLAS-CONF-2012-047. https://cds.cern.ch/record/1449796.

[65] ATLAS Collaboration, *Measurement of the muon reconstruction performance of the ATLAS detector using 2011 and 2012 LHC proton-proton collision data*, Eur. Phys. J. **C74** no. 11, (2014) 3130, arXiv:1407.3935 [hep-ex].

[66] ATLAS Collaboration, *Topological cell clustering in the ATLAS calorimeters and its performance in LHC Run 1*, arXiv:1603.02934 [hep-ex].

[67] S. Catani, Y. L. Dokshitzer, M. Olsson, G. Turnock, and B. R. Webber, *New clustering algorithm for multi - jet cross-sections in e+ e- annihilation*, Phys. Lett. **B269** (1991) 432–438.

[68] S. D. Ellis and D. E. Soper, *Successive combination jet algorithm for hadron collisions*, Phys. Rev. **D48** (1993) 3160–3166, arXiv:hep-ph/9305266 [hep-ph].

[69] S. Catani, Y. L. Dokshitzer, M. Seymour, and B. Webber, *Longitudinally invariant $k_\perp$ clustering algorithms for hadron hadron collisions*, Nucl. Phys. **B406** (1993) 187–224.

[70] M. Cacciari, G. P. Salam, and G. Soyez, *The anti-k_t jet clustering algorithm*, JHEP **0804** (2008) 063, arXiv:0802.1189 [hep-ph].

[71] Y. L. Dokshitzer, G. Leder, S. Moretti, and B. Webber, *Better jet clustering algorithms*, JHEP **9708** (1997) 001, arXiv:hep-ph/9707323 [hep-ph].

[72] M. Wobisch and T. Wengler, *Hadronization corrections to jet cross-sections in deep inelastic scattering*, pp. , 270–279. 1998. arXiv:hep-ph/9907280 [hep-ph].

[73] M. Cacciari, G. P. Salam, and G. Soyez, *FastJet User Manual*, Eur. Phys. J. **C72** (2012) 1896, arXiv:1111.6097 [hep-ph].

[74] ATLAS Collaboration, *Jet energy measurement with the ATLAS detector in proton-proton collisions at $\sqrt{s} = 7$ TeV*, Eur. Phys. J. **C73** no. 3, (2013) 2304, arXiv:1112.6426 [hep-ex].

[75] ATLAS Collaboration, *Pile-up subtraction and suppression for jets in ATLAS*, ATLAS-CONF-2013-083. http://cds.cern.ch/record/1570994.

[76] M. Cacciari and G. P. Salam, *Pileup subtraction using jet areas*, Phys. Lett. **B659** (2008) 119–126, arXiv:0707.1378 [hep-ph].

[77] ATLAS Collaboration, *Jet energy measurement and its systematic uncertainty in proton-proton collisions at $\sqrt{s}$=7 TeV with the ATLAS detector*, Eur. Phys. J. **C75** (2015) 17, arXiv:1406.0076 [hep-ex].

[78] ATLAS Collaboration, *Performance of b-Jet Identification in the ATLAS Experiment*, JINST **11** no. 04, (2016) P04008, arXiv:1512.01094 [hep-ex].

[79] ATLAS Collaboration, *Performance of algorithms that reconstruct missing transverse momentum in $\sqrt{s} = 8$ TeV proton-proton collisions in the ATLAS detector*, arXiv:1609.09324 [hep-ex].

[80] S. Frixione, P. Nason, and G. Ridolfi, *A positive-weight next-to-leading-order Monte Carlo for heavy flavour hadroproduction*, JHEP **0709** (2007) 126, arXiv:0707.3088 [hep-ph].

[81] P. Nason, *A new method for combining NLO QCD with shower Monte Carlo algorithms*, JHEP **0411** (2004) 040, arXiv:hep-ph/0409146 [hep-ph].

[82] S. Frixione, P. Nason, and C. Oleari, *Matching NLO QCD computations with parton shower simulations: the POWHEG method*, JHEP **0711** (2007) 070, arXiv:0709.2092 [hep-ph].

[83] S. Alioli, P. Nason, C. Oleari, and E. Re, *A general framework for implementing NLO calculations in shower Monte Carlo programs: the POWHEG BOX*, JHEP **1006** (2010) 043, arXiv:1002.2581 [hep-ph].

[84] T. Sjostrand, S. Mrenna, and P. Z. Skands, *PYTHIA 6.4 physics and manual*, JHEP **0605** (2006) 026, arXiv:hep-ph/0603175 [hep-ph].

[85] ATLAS Collaboration, *Measurements of normalized differential cross sections for $t\bar{t}$ production in pp collisions at $\sqrt{s} = 7$ TeV using the ATLAS detector*, Phys. Rev. **D90** no. 7, (2014) 072004, arXiv:1407.0371 [hep-ex].

[86] ATLAS Collaboration, *Search for the Standard Model Higgs boson produced in association with top quarks and decaying into $b\bar{b}$ in pp collisions at $\sqrt{s} =$ 8 TeV with the ATLAS detector*, Eur. Phys. J. **C75** no. 7, (2015) 349, arXiv:1503.05066 [hep-ex].

[87] *The simulation principle and performance of the ATLAS fast calorimeter simulation FastCaloSim*, ATL-PHYS-PUB-2010-013. http://cds.cern.ch/record/1300517.

[88] S. Frixione and B. R. Webber, *Matching NLO QCD computations and parton shower simulations*, JHEP **0206** (2002) 029, arXiv:hep-ph/0204244 [hep-ph].

[89] S. Frixione, P. Nason, and B. R. Webber, *Matching NLO QCD and parton showers in heavy flavor production*, JHEP **0308** (2003) 007, arXiv:hep-ph/0305252 [hep-ph].

[90] G. Corcella, I. Knowles, G. Marchesini, S. Moretti, K. Odagiri, et al., *HERWIG 6: an event generator for hadron emission reactions with interfering gluons (including supersymmetric processes)*, JHEP **0101** (2001) 010, arXiv:hep-ph/0011363 [hep-ph].

[91] J. Butterworth, J. R. Forshaw, and M. Seymour, *Multiparton interactions in photoproduction at HERA*, Z. Phys. **C72** (1996) 637–646, arXiv:hep-ph/9601371 [hep-ph].

[92] B. P. Kersevan and E. Richter-Was, *The Monte Carlo event generator AcerMC versions 2.0 to 3.8 with interfaces to PYTHIA 6.4, HERWIG 6.5 and ARIADNE 4.1*, Comput. Phys. Commun. **184** (2013) 919–985, arXiv:hep-ph/0405247 [hep-ph].

[93] ATLAS Collaboration, *Measurement of $t\bar{t}$ production with a veto on additional central jet activity in pp collisions at $\sqrt{s} = 7$ TeV using the ATLAS detector*, Eur. Phys. J. **C72** (2012) 2043, arXiv:1203.5015 [hep-ex].

[94] M. Cacciari, M. Czakon, M. Mangano, A. Mitov, and P. Nason, *Top-pair production at hadron colliders with next-to-next-to-leading logarithmic soft-gluon resummation*, Phys. Lett. **B710** (2012) 612–622, arXiv:1111.5869 [hep-ph].

[95] M. Beneke, P. Falgari, S. Klein, and C. Schwinn, *Hadronic top-quark pair production with NNLL threshold resummation*, Nucl. Phys. **B855** (2012) 695–741, arXiv:1109.1536 [hep-ph].

[96] P. Baernreuther, M. Czakon, and A. Mitov, *Percent-Level-Precision Physics at the Tevatron: Next-to-Next-to-Leading Order QCD Corrections to $q\overline{q} \to t\bar{t} + X$*, Phys. Rev. Lett. **109** (2012) 132001, arXiv:1204.5201 [hep-ph].

[97] M. Czakon and A. Mitov, *NNLO corrections to top-pair production at hadron colliders: the all-fermionic scattering channels*, JHEP **1212** (2012) 054, arXiv:1207.0236 [hep-ph].

[98] M. Czakon and A. Mitov, *NNLO corrections to top pair production at hadron colliders: the quark-gluon reaction*, JHEP **1301** (2013) 080, arXiv:1210.6832 [hep-ph].

[99] M. Czakon, P. Fiedler, and A. Mitov, *Total Top-Quark Pair-Production Cross Section at Hadron Colliders Through $O(\alpha_s^4)$*, Phys. Rev. Lett. **110** (2013) 252004, arXiv:1303.6254 [hep-ph].

[100] M. Czakon and A. Mitov, *Top++: A program for the calculation of the top-pair cross-section at hadron colliders*, Comput. Phys. Commun. **185** (2014) 2930, arXiv:1112.5675 [hep-ph].

[101] S. Frixione, E. Laenen, P. Motylinski, B. R. Webber, and C. D. White, *Single-top hadroproduction in association with a W boson*, JHEP **0807** (2008) 029, arXiv:0805.3067 [hep-ph].

[102] N. Kidonakis, *Next-to-next-to-leading logarithm resummation for s-channel single top quark production*, Phys. Rev. **D81** (2010) 054028, arXiv:1001.5034 [hep-ph].

[103] N. Kidonakis, *Two-loop soft anomalous dimensions for single top quark associated production with a W^- or H^-*, Phys. Rev. **D82** (2010) 054018, arXiv:1005.4451 [hep-ph].

[104] N. Kidonakis, *Next-to-next-to-leading-order collinear and soft gluon corrections for t-channel single top quark production*, Phys. Rev. **D83** (2011) 091503, arXiv:1103.2792 [hep-ph].

[105] ATLAS Collaboration, *Measurement of the charge asymmetry in top quark pair production in pp collisions at $\sqrt{s} = 7$ TeV using the ATLAS detector*, Eur. Phys. J. **C72** (2012) 2039, arXiv:1203.4211 [hep-ex].

[106] ATLAS Collaboration, *Measurements of top quark pair relative differential cross-sections with ATLAS in pp collisions at $\sqrt{s} = 7$ TeV*, Eur. Phys. J. **C73** no. 1, (2013) 2261, arXiv:1207.5644 [hep-ex].

[107] T. Gleisberg, S. Hoeche, F. Krauss, M. Schonherr, S. Schumann, F. Siegert, and J. Winter, *Event generation with SHERPA 1.1*, JHEP **02** (2009) 007, arXiv:0811.4622 [hep-ph].

[108] S. Catani, L. Cieri, G. Ferrera, D. de Florian, and M. Grazzini, *Vector boson production at hadron colliders: a fully exclusive QCD calculation at NNLO*, Phys. Rev. Lett. **103** (2009) 082001, arXiv:0903.2120 [hep-ph].

[109] A. Martin, W. Stirling, R. Thorne, and G. Watt, *Parton distributions for the LHC*, Eur. Phys. J. **C63** (2009) 189–285, arXiv:0901.0002 [hep-ph].

[110] ATLAS Collaboration, *Further search for supersymmetry at $\sqrt{s}$=7 TeV in final states with jets, missing transverse momentum, and isolated leptons with the ATLAS detector*, Phys. Rev. D **86** (2012) 092002. http://link.aps.org/doi/10.1103/PhysRevD.86.092002.

[111] ATLAS Collaboration, *Search for pair-produced third-generation squarks decaying via charm quarks or in compressed supersymmetric scenarios in pp collisions at $\sqrt{s} = 8$ TeV with the ATLAS detector*, Phys. Rev. D **90** (2014) 052008. http://link.aps.org/doi/10.1103/PhysRevD.90.052008.

[112] J. M. Campbell, R. K. Ellis, and C. Williams, *Vector boson pair production at the LHC*, JHEP **07** (2011) 018, arXiv:1105.0020 [hep-ph].

[113] J. Alwall, M. Herquet, F. Maltoni, O. Mattelaer, and T. Stelzer, *MadGraph 5: Going Beyond*, JHEP **06** (2011) 128, arXiv:1106.0522 [hep-ph].

[114] J. M. Campbell and R. K. Ellis, *$t\bar{t}W^{+-}$ production and decay at NLO*, JHEP **07** (2012) 052, arXiv:1204.5678 [hep-ph].

[115] M. V. Garzelli, A. Kardos, C. G. Papadopoulos, and Z. Trocsanyi, Z^0 - *boson production in association with a top anti-top pair at NLO accuracy with parton shower effects*, Phys. Rev. **D85** (2012) 074022, arXiv:1111.1444 [hep-ph].

[116] M. Bahr, S. Gieseke, M. Gigg, D. Grellscheid, K. Hamilton, et al., *Herwig++ physics and manual*, Eur. Phys. J. **C58** (2008) 639–707, arXiv:0803.0883 [hep-ph].

[117] P. Z. Skands, *Tuning Monte Carlo generators: The Perugia tunes*, Phys. Rev. **D82** (2010) 074018, arXiv:1005.3457 [hep-ph].

[118] H.-L. Lai, M. Guzzi, J. Huston, Z. Li, P. M. Nadolsky, et al., *New parton distributions for collider physics*, Phys. Rev. **D82** (2010) 074024, arXiv:1007.2241 [hep-ph].

[119] ATLAS Collaboration, *New ATLAS event generator tunes to 2010 data*, ATL-PHYS-PUB-2011-008. http://cds.cern.ch/record/1345343.

[120] J. Pumplin, D. Stump, J. Huston, H. Lai, P. M. Nadolsky, et al., *New generation of parton distributions with uncertainties from global QCD analysis*, JHEP **0207** (2002) 012, arXiv:hep-ph/0201195 [hep-ph].

[121] ATLAS Collaboration, *Improved luminosity determination in pp collisions at* $\sqrt{s} = 7$ TeV *using the ATLAS detector at the LHC*, Eur. Phys. J. **C73** no. 8, (2013) 2518, arXiv:1302.4393 [hep-ex].

[122] ATLAS Collaboration, *Performance of jet substructure techniques for large-R jets in proton-proton collisions at* $\sqrt{s} = 7$ *TeV using the ATLAS detector*, JHEP **1309** (2013) 076, arXiv:1306.4945 [hep-ex].

[123] ATLAS Collaboration, *Boosted top quark identification in pp collisions at* $\sqrt{s}$ *= 8 TeV with the ATLAS detector*, Tech. Rep. ATL-COM-PHYS-2014-1492, CERN, Geneva, Nov, 2014. https://cds.cern.ch/record/1971108.

[124] S. Schaetzel, *Jet pT resolution for HEPTopTagger Jets in ATLAS*, ATL-COM-PHYS-2012-1463. https://cds.cern.ch/record/1483229.

[125] ATLAS Collaboration, *Single hadron response measurement and calorimeter jet energy scale uncertainty with the ATLAS detector at the LHC*, Eur. Phys. J. **C73** no. 3, (2013) 2305, arXiv:1203.1302 [hep-ex].

[126] M. Botje, J. Butterworth, A. Cooper-Sarkar, A. de Roeck, J. Feltesse, et al., *The PDF4LHC Working Group Interim Recommendations*, arXiv:1101.0538 [hep-ph].

[127] A. Martin, W. Stirling, R. Thorne, and G. Watt, *Uncertainties on α_S in global PDF analyses and implications for predicted hadronic cross sections*, Eur. Phys. J. **C64** (2009) 653–680, arXiv:0905.3531 [hep-ph].

[128] J. Gao, M. Guzzi, J. Huston, H.-L. Lai, Z. Li, et al., *CT10 next-to-next-to-leading order global analysis of QCD*, Phys. Rev. **D89** no. 3, (2014) 033009, arXiv:1302.6246 [hep-ph].

[129] R. D. Ball, V. Bertone, S. Carrazza, C. S. Deans, L. Del Debbio, et al., *Parton distributions with LHC data*, Nucl. Phys. **B867** (2013) 244–289, arXiv:1207.1303 [hep-ph].

[130] J. Butterworth, E. Dobson, U. Klein, B. Mellado Garcia, T. Nunnemann, J. Qian, D. Rebuzzi, and R. Tanaka, *Single Boson and Diboson Production Cross Sections in pp Collisions at sqrts=7 TeV*, ATL-COM-PHYS-2010-695. https://cds.cern.ch/record/1287902.

[131] M. V. Garzelli, A. Kardos, C. G. Papadopoulos, and Z. Trocsanyi, *$t\,\bar{t}\,W^{+-}$ and $t\,\bar{t}\,Z$ Hadroproduction at NLO accuracy in QCD with Parton Shower and Hadronization effects*, JHEP **11** (2012) 056, arXiv:1208.2665 [hep-ph].

[132] J. M. Butterworth, A. R. Davison, M. Rubin, and G. P. Salam, *Jet Substructure as a New Higgs-Search Channel at the Large Hadron Collider*, Phys. Rev. Lett. **100** (2008) 242001, arXiv:0802.2470 [hep-ph].

[133] ATLAS Collaboration, *A search for $t\bar{t}$ resonances using lepton-plus-jets events in proton-proton collisions at $\sqrt{s} = 8$ TeV with the ATLAS detector*, JHEP **08** (2015) 148, arXiv:1505.07018 [hep-ex].

[134] CMS Collaboration, *Search for direct pair production of supersymmetric top quarks decaying to all-hadronic final states in pp collisions at $\sqrt{s} = 8$ TeV*, Eur. Phys. J. **C76** no. 8, (2016) 460, arXiv:1603.00765 [hep-ex].

[135] CMS Collaboration, *Exclusion limits on gluino and top-squark pair production in natural SUSY scenarios with inclusive razor and exclusive single-lepton searches at 8 TeV*, CMS-PAS-SUS-14-011.

[136] CMS Collaboration, *Search for direct pair production of scalar top quarks in the single- and dilepton channels in proton-proton collisions at $\sqrt{s} = 8$ TeV*, JHEP **07** (2016) 027, arXiv:1602.03169 [hep-ex]. [Erratum: JHEP09,056(2016)].

[137] CMS Collaboration, *Search for top-squark pair production in the single lepton final state in pp collisions at 8 TeV*, CMS-PAS-SUS-13-011.

[138] CMS Collaboration, *Searches for third-generation squark production in fully hadronic final states in proton-proton collisions at* $\sqrt{s} = 8$ *TeV*, JHEP **06** (2015) 116, arXiv:1503.08037 [hep-ex].

[139] ATLAS Collaboration, *Search for the Supersymmetric Partner of the Top Quark in the Jets+*$E_{\mathrm{T}}^{\mathrm{miss}}$ *Final State at* $\sqrt{s} = 13$ *TeV*, ATLAS-CONF-2016-077.

[140] ATLAS Collaboration, *Search for top squarks in final states with one isolated lepton, jets, and missing transverse momentum in* $\sqrt{s} = 13$ *TeV pp collisions with the ATLAS detector*, ATLAS-CONF-2016-050.

[141] CMS Collaboration, *Search for supersymmetry in events with jets and missing transverse momentum in proton-proton collisions at 13 TeV*, CMS-PAS-SUS-16-014.

[142] CMS Collaboration, *Search for new physics in the all-hadronic final state with the MT2 variable*, CMS-PAS-SUS-16-015.

[143] CMS Collaboration, *An inclusive search for new phenomena in final states with one or more jets and missing transverse momentum at 13 TeV with the AlphaT variable*, CMS-PAS-SUS-16-016. https://cds.cern.ch/record/2205163.

[144] CMS Collaboration, *Search for direct top squark pair production in the fully hadronic final state in proton-proton collisions at* $\sqrt{s} = 13$ TeV *corresponding to an integrated luminosity of 12.9/fb*, CMS-PAS-SUS-16-029.

[145] CMS Collaboration, *Search for supersymmetry in the all-hadronic final state using top quark tagging in pp collisions at* $\sqrt{s} = 13$ TeV, CMS-PAS-SUS-16-030.

[146] CMS Collaboration, *Search for direct top squark pair production in the single lepton final state at* $\sqrt{s} = 13$ TeV, CMS-PAS-SUS-16-028.

[147] C. G. Lester and D. J. Summers, *Measuring masses of semiinvisibly decaying particles pair produced at hadron colliders*, Phys. Lett. **B463** (1999) 99–103, arXiv:hep-ph/9906349 [hep-ph].

[148] A. Barr, C. Lester, and P. Stephens, *m(T2): The Truth behind the glamour*, J. Phys. **G29** (2003) 2343–2363, arXiv:hep-ph/0304226 [hep-ph].

[149] C. Lester and A. Barr, *MTGEN: Mass scale measurements in pair-production at colliders*, JHEP **12** (2007) 102, arXiv:0708.1028 [hep-ph].

[150] H.-C. Cheng and Z. Han, *Minimal Kinematic Constraints and m(T2)*, JHEP **12** (2008) 063, arXiv:0810.5178 [hep-ph].

[151] Behnke, Olaf and Kröninger, Kevin and Schott, Gregory and Schörner-Sadenius, Thomas, *Data analysis in high energy physics: a practical guide to statistical methods*. Wiley-VCH, Weinheim, 2013. https://cds.cern.ch/record/1517556.

[152] G. Cowan, K. Cranmer, E. Gross, and O. Vitells, *Asymptotic formulae for likelihood-based tests of new physics*, Eur. Phys. J. **C71** (2011) 1554, arXiv:1007.1727 [physics.data-an]. [Erratum: Eur. Phys. J.C73,2501(2013)].

[153] S. S. Wilks, *The Large-Sample Distribution of the Likelihood Ratio for Testing Composite Hypotheses*, Annals Math. Statist. **9** no. 1, (1938) 60–62.

[154] A. L. Read, *Presentation of search results: The CL(s) technique*, J. Phys. **G28** (2002) 2693–2704. [,11(2002)].

[155] M. Baak, G. J. Besjes, D. Cote, A. Koutsman, J. Lorenz, and D. Short, *HistFitter software framework for statistical data analysis*, Eur. Phys. J. C **75** no. arXiv:1410.1280, (2014) 153. 35 p. https://cds.cern.ch/record/1953093.

[156] ATLAS Collaboration, *Fast TracKer (FTK) Technical Design Report*,. https://cds.cern.ch/record/1552953.

[157] ATLAS Collaboration, *ATLAS Insertable B-Layer Technical Design Report*,. https://cds.cern.ch/record/1291633.

[158] M. Hodgkinson, D. Tovey, and R. Duxfield, *Energy Flow Reconstruction with the eflowRec Combined Reconstruction Software in Athena 15.6.9.8*, Tech. Rep. ATL-PHYS-INT-2011-031, CERN, Geneva, Apr, 2011.